Dissertation
submitted to the
Combined Faculties of the Natural Sciences and Mathematics
of the Ruperto-Carola University of Heidelberg, Germany
for the degree of
Doctor of Natural Sciences

Put forward by
Pooja Surajbali M.Sc. (Astrophysics)
Born in: Mauritius
Oral examination: 8th July 2020

Observing Large-scale Structures in the Gamma-ray Sky

Referees: Prof. Dr. J. A. Hinton
apl. Prof. Dr. S. J. Wagner

Zusammenfassung

Der Kern dieser Doktorarbeit besteht aus der Entwicklung und Anwendung neuartiger Datenanalyse- und Modellierungstechniken für Beobachtungen des High Altitude Water Cherenkov (HAWC) Gammastrahlen-Observatoriums. Diese Arbeit gliedert sich in drei Hauptteile und kulminiert in der Untersuchung ausgedehnter sehr hochenergetischer Quellen wie den *Fermi*-Blasen.

Wir entwickeln zuerst einen neuartigen Diskriminator zur Unterscheidung gammastrahleninduzierter und protoneninduzierter Luftschauer. Unser Diskriminator ist unabhängig von der Rekonstruktion des Schauerkerns und ist nützlich, zur Verbesserung der Genauigkeit der Detektorsimulation. Zweitens haben wir ein neues Untergrundmodell entwickelt, das die Anisotropie der kosmischen Strahlung einbezieht, die gesamte verfügbare Statistik ausnutzt und schnelle Berechnungszeiten hat. Drittens stellen wir einen Profile-Likelihood-Ansatz zur Berechnung der Signifikanz und des Flusses von jeder beliebigen Region des Himmels vor, der die Kombination von Daten aus verschiedenen Schauergrößen ermöglicht, während ihre relativen Beiträge konsistent berücksichtigt werden.

Mit diesen Werkzeugen führen wir eine Blindsuche nach großräumigen Strukturen am TeV-Gammastrahlenhimmel durch. Wir finden einen Kandidaten für eine Quellregion mit einer Signifikanz von bis zu $5,30\sigma$ auf einer Integrationsskala von $16°$, bei der es sich um einen TeV-Halo handeln könnte, der mit einem Pulsar, Molekülwolken oder einem galaktischen Ausfluss assoziiert ist. Da von der nördlichen *Fermi*-Blase und ihrer Basis kein signifikantes Signal ausgeht, berechnen wir schließlich ihre Obergrenzen für des Integralen Flusses auf einem Konfidenzniveau von 95% und präsentieren ein hadronisches Modell mit einer geschätzten Protonen-Cut-off-Energie von 85 TeV.

Abstract

The essence of this doctoral research constitutes the development and application of novel data analysis and modelling techniques to observations from the High Altitude Water Cherenkov (HAWC) gamma-ray observatory. This thesis is organised in three main parts, culminating in the study of extended very-high-energy sources such as the *Fermi* bubbles.

We first develop a novel discriminator to distinguish between gamma-ray-induced and proton-induced atmospheric showers. Our discriminator is independent of core reconstruction and is useful for enhancing the accuracy of the detector simulation. Secondly, we developed a new background model which incorporates the cosmic-ray anisotropy, exploits all statistics available and has fast computation times. Thirdly, we present a profile likelihood approach to calculate the significance and flux from any region of the sky, which allows the combination of data from different shower sizes while consistently accounting for their relative contributions.

With the above tools, we perform blind searches for large-scale structures in the TeV gamma-ray sky. We find a candidate source region with significance up to 5.30σ at $16°$ integration scale, which could be a TeV halo associated with a pulsar, molecular clouds or a galactic outflow. Finally, with no significant signal from the north *Fermi* bubble and its base, we compute their integral flux upper limits, at 95% confidence level and present a hadronic model with an estimated proton cut-off energy at 85 TeV.

Acknowledgements

For this unique endeavour, one that brings together the astrophysics and particle physics communities, I would like to thank first and foremost the members of the thesis committee: **Prof. Dr. Jim A. Hinton** (MPIK), as director and thesis advisor, for the opportunity to pursue my doctoral research at MPIK, Heidelberg and for his support and mentorship throughout the years, **apl. Prof. Dr. Stefan J. Wagner** (LSW) for the scientific guidance and advice, especially for asking some interesting, leading questions, **Dr. Harm Schoorlemmer** (MPIK) for his meticulous supervision. He never fails to motivate or criticise as every detail matters, whether it is for bug fixes in my codes, accurate writing or the interpretation of all the information a figure provides which improved the quality of the work presented in this thesis.

An enormous thank you to the secretary of the MPIK division 4, **Mrs. Ruth Crespo López-Urruthia**, for she is absolutely indispensable in navigating bureaucracy. She helped me a countless number of times in reading most of my letters, the actions I needed to take and literally how to handle the German system. I would also like to thank **Dr. Christian Fendt** (MPIA) and the International Max Planck Research School for Astronomy and Cosmic Physics at the University of Heidelberg (IMPRS-HD) for the multifaceted support and the opportunity to study in Heidelberg.

I am very grateful for the patience and help of **Dr. Vincent Marandon** (MPIK) who answered my endless stream of questions, assisted in debugging codes and performed cross-checks of my results. Also for reading through and checking some chapters, I thank **Prof. Werner Hofmann** (MPIK), **Dr. Carlo Romoli** (MPIK), **Dr. Brian Reville** (MPIK) and **Dr. rer nat. Alison M. W. Mitchell** (UZH, Zurich). I thank **Dr. rer. nat. Axel Donath** (MPIK) for his assistance with python scripting. I could trouble him more than once on the shortcomings of codes in use. I thank **Dr. rer. nat. Sabina Puerckhauer** and **Dr. Felix Werner** for their invaluable help in translating my abstract. I also thank **Dr. Joachim Hahn**, **Dr. Rubén López-Coto** (INFN), **Prof. Dr. Richard Tuffs** (MPIK), **Prof. Dr. Konrad Bernlöhr** (MPIK) and **Dr. R. D. Parsons** (MPIK) for valuable input to the thesis through many interesting and fruitful discussions.

I am thankful for the insightful discussions and input regarding the *Fermi* Bubbles with **Dr. Roland Crocker** (ANU), **William Taylor** (ANU), **Dr. Dmitry Malyshev** (ECAP), **Dr. Philipp Mertsch** (RWTH, Aachen), **Dr. Gwenael Giacinti** (MPIK), **Andrew Taylor** (DESY), **Prof. Dr. Felix Aharonian** (MPIK), **Prof. Dr. Subir Sarkar** (Oxford) and **Mattias Sormani** (ITA). Moreover, I thank **Dr. Eric Charles** (SLAC), **Dr. Luigi Tibaldo** (IRAP) and **Dr. Quentin Remy** (MPIK) for quick access to sky maps from Fermi-LAT and different surveys including dust, Hα and CO.

As a member of the HAWC collaboration, I thank everyone for their amazing work, especially **Dr. Hugo A. Ayala Solares** (PSU), **Dr. Matthew Rosenberg** (PSU), **Dr. Israel Martinez-Castellanos** (UMD), **Dr. Henrike Fleischhack** (MTU) and **Dr. John Pretz** for insightful discussions on HAWC analysis and map-making procedures. I would like to thank **Michael Schneider** (UMD), **Robert Scott De Lay** (UMD) and **Dr. Hao Zhou** (Los Alamos) for an excellent on-site shifter team. I am incredibly grateful to the MPIK IT team, especially **Dominik Weinmann**, **Stefanie Kolb**, **Kevin Zink** and **Thomas Khim** (**Mizzi**).

Contents

List of Figures

xiv

List of Tables

List of Abbreviations

3FGL	**3**rd *Fermi*-LAT **G**amma-ray **S**ource **Cat**a**l**o**gu**e
ACD	**A**nti**c**oincidence **D**etector
ACT	**A**tmospheric **C**herenkov **T**elescope
AERIE	**A**nalysis and **E**vent **R**econstruction **I**ntegrated **E**nvironment
AGN	**A**ctive **G**alactic **N**uclei
ASPD	**A**ir **S**hower **P**article **D**etector
ATNF	**A**ustralia **T**elescope **N**ational **F**acility
BATSE	**B**urst **A**nd **T**ransient **S**ource **E**xperiment
CANGAROO	**C**ollaboration **B**etween **A**ustralia and **N**ippon for a **G**amma **R**ay **O**bservatory
CGRO	**C**ompton **G**amma-**r**ay **O**bservatory
CL	**C**onfidence **L**evel
CMB	**C**osmic **M**icrowave **B**ackground
CMZ	**C**entral **M**olecular **Z**one
CNN	**C**onvolutional **N**eural **N**etwork
COM	**C**entre **o**f **M**ass
COMPTEL	Imaging **Comp**ton **Tel**escope
CORSIKA	**Co**smic **r**ay **Si**mulation for **KA**SKADE
COS	**C**osmic **O**rigins **S**pectograph
CR	**C**osmic **R**ay
CTA	**C**herenkov **T**elescope **A**rray
DAQ	**D**ata **A**c**q**uisition
DI	**D**irect **I**ntegration
DoF	**D**egree **o**f **F**reedom
EAS	**E**xtensive **A**ir **S**hower(s)
ECL	**E**mitter-**C**oupled **L**ogic
EGRET	**E**nergetic **G**amma-**r**ay **E**xperiment **T**elescope
EHE	**E**xtremely **H**igh **E**nergy
EM	**E**lectro**m**agnetic
FADC	**F**ast **A**nalog-to-**D**igital **C**onverter
FEB	**F**ront-**E**nd-**B**oard
FFT	**F**ast **F**ourier **T**ransform
FoV	**F**ield **o**f **V**iew
GBM	**G**amma **B**urst **M**onitor
GC	**G**alactic **C**entre
GLAST	**G**amma-ray **L**arge **A**rea **S**pace **T**elescope
GMST	**G**reenwich **M**ean **S**idereal **T**ime

GP	**G**round **P**arameter
GPS	**G**lobal **P**ositioning **S**ystem
GRB	**G**amma-**r**ay **B**urst
GTC	**G**PS **T**iming and **C**ontrol
GZK	**G**reisen-**Z**atsepin-**K**uzmin
HA	**H**our **A**ngle
HAWC	**H**igh **A**ltitude **W**ater **C**herenkov
HE	**H**igh **E**nergy
HEALPix	**H**ierarchical **E**qual **A**rea and iso-**L**atitude **Pix**elation
HEGRA	**H**igh **E**nergy **G**amma-**r**ay **A**stronomy
H.E.S.S.	**H**igh **E**nergy **S**pectroscopic **S**ystem
HiSCORE	**H**undred***i** **S**quare-km **C**osmic **OR**igin **E**xplorer
HV	**H**igh **V**oltage
IACT	**I**maging **A**mospheric **C**herenkov **T**elescope
IC	**I**nverse **C**ompton
INTEGRAL	**INTE**rnational **G**amma-**r**ay **A**strophysics **L**aboratory
IRAS	**I**nfra**r**ed **A**stronomical **S**atellite
ISM	**I**nter**s**tellar **M**edium
ISRF	**I**nter**s**tellar **R**adiation **F**ield
KN	**K**lein-**N**ishina
LAT	**L**arge **A**rea **T**elescope
LDF	**L**ateral **D**istribution **F**unction
LE	**L**ow **E**nergy
LH	**L**ikeli**h**ood
LHAASO	**L**arge **H**igh **A**ltitude **A**ir **S**hower **O**bservatory
LMST	**L**ocal **M**ean **S**idereal **T**ime
MAGIC	**M**ajor **A**mospheric **G**amma **I**maging **C**herenkov Telescopes
MB	**M**odel **B**ackground
MC	**M**onte **C**arlo
MHD	**M**agneto**h**ydro**d**ynamics
NFB	**N**orth *Fermi* **B**ubble
NKG	**N**ishimura-**K**amata-**G**reisen
NN	**N**eural **N**etwork
NPS	**N**orth **P**olar **S**pur
OSO	**O**rbiting **S**olar **S**ystem
OSSE	**O**riented **S**cintillation **S**pectrometer Experiment
PINC	**P**arameter for **I**dentifying **N**uclear **C**osmic rays
PE	**P**hoto**e**lectron
PMT	**P**hoto**m**ultiplier **T**ube
PSF	**P**oint **S**pread **F**unction
PSR	**P**ul**s**a**r**
QE	**Q**uantum **E**fficiency
RA	**R**ight **A**scension
ROI	**R**egion **o**f **I**nterest
SFCF	**S**uper **F**ast **C**ore **F**it
SN	**S**uper**n**ova
SNR	**S**uper**n**ova **R**emnant

SWGO	**S**outhern **W**ide-Field **G**amma-Ray **O**bservatory
TDC	**T**ime-to-**D**igital **C**onverter
TOT	**T**ime **O**ver **T**hreshold
TS	**T**est **S**tatistic
UHE	**U**ltra **H**igh **E**nergy
VERITAS	**V**ery **E**nergetic **R**adiation **I**maging **T**elescope **A**rray **S**ystem
VHE	**V**ery **H**igh **E**nergy
WCD	**W**ater **C**herenkov **D**etector

Physical Constants

Speed of Light	$c = 2.99792458 \times 10^{8}$ m s^{-1}
Elementary charge	$e = 1.602176634 \times 10^{-19}$ C
Vacuum electric permittivity	$\epsilon_0 = 8.854187813 \times 10^{-12}$ F m^{-1}
Electron mass	$m_\mathrm{e} = 9.109383701 \times 10^{-31}$ kg (0.511 MeV/c^2)
Proton mass	$m_\mathrm{p} = 1.672621924 \times 10^{-27}$ kg (938 MeV/c^2)
Boltzmann constant	$k_\mathrm{B} = 1.380649 \times 10^{-23}$ J K^{-1}
Planck constant	$h = 6.62607004 \times 10^{-34}$ J s
Thomson scattering cross-section	$\sigma_\mathrm{T} = 6.652458\ldots \times 10^{-29}$ m^2
Vacuum magnetic permeability	$\mu_0 = \mathrm{N}/\mathrm{A}^2$
Fine structure constant	$\alpha = 1/137$

List of Symbols

Symbol	Name	Units
E	energy	eV
ν	frequency	Hz
λ	wavelength	m
T	temperature	K
X_{max}	atmospheric depth where number of particles is maximum	$\mathrm{g/cm^2}$
p	momentum	$\mathrm{kg\,m\,s^{-1}}$
θ	pitch angle	$^\circ$
γ	Lorentz factor	–
v	velocity/speed	$\mathrm{m\,s^{-1}}$
N	number of particles	–
α	spectral index	–
t_{esc}	time-taken by a particle to escape a medium	s
E_e	electron energy	eV
m	mass	kg
n	number density of gaseous medium	$\mathrm{cm^{-3}}$
X_0	radiation length	$\mathrm{g/cm^2}$
τ	lifetime of particle	yr
U_{mag}	magnetic energy density	$\mathrm{eV/cm^3}$
B	magnetic field strength	μG
U_{rad}	density of photon fields	$\mathrm{eV/cm^3}$
σ_{IC}	inverse-Compton scattering cross-section	$\mathrm{m^2}$
F	photon flux	$\mathrm{cm^2/s}$
Z	electric charge	C
L	size of astrophysical object	m
x	column density	$\mathrm{g/cm^3}$
E_{c}	critical energy	eV
E_{s}	transverse energy scale	eV
ρ	density	$\mathrm{g/cm^3}$
n	refractive index of medium	–
h	height in the atmosphere	m
R	rigidity	GV
τ	spin down age of pulsar	kyr
N_e	shower size	m

s	shower age	–
t	shower duration	s
r	length scale for lateral distribution	m
K	kinetic energy	J
$\mathcal{W}$	work function	J
X	slant depth	g/cm^2
z	altitude	m
θ	zenith angle	°
$\vec{x}_{COM}$	centre of mass shower core location	m
q_i	electric charge of a triggered PMT	C
x_i	PMT location	m
ψ	angle between the simulated and reconstructed directions	°
$\mathcal{B}$	nHit bins	–
$\mathcal{C}$	COMPACT gamma/hadron separator	–
$\mathcal{P}$	PINC gamma/hadron separator	–
$R_{d/\gamma}$	likelihood ratio, the TankLHR gamma/hadron separator	–
P	probability density distribution	–
ϵ	efficiency of shower acceptance	–
S/N	signal-to-noise ratio	–
TS	test statistic	–
N_{side}	HEALPix resolution	–
$\mathcal{G}$	gamma-like events	–
$\mathcal{H}$	hadron-like events	–
B_{DI}	Direct Integration background	–
$\mathcal{R}(t)$	integrated rate array	s^{-1}
$\mathcal{A}$	acceptance map	–
HA	hour angle	°
dec or δ	declination	°
a	a-factor	–
$\mathcal{D}_{NS}$	fractional deviation in North/South a-factor	–
b	b-factor	–
$\mathcal{S}_{G}$	Gaussian smoothing function	–
$\mathcal{Y}$	product of a and b factors	–
B_{DI}	Model Background	–
$\mathcal{E}$	excess	–
$\mathcal{E}_{rel}$	relative excess	–
$\mathcal{S}_{\mathcal{B}}$	bin significance	–
N_{on}	measured counts in *on* region	–
N_{off}	measured counts in *off* region	–
α	*on* source to *off* source ratio	–
$\overline{N}_{on}$	expected counts in *on* region	–
$\overline{N}_{off}$	expected counts in *off* region	–
$\mathcal{L}$	likelihood function	–
$\mathcal{F}$	differential flux	$TeV^{-1}\,cm^{-2}\,s^{-1}$
$\mathcal{C}$	Cash statistic	–
l	galactic longitude	°
b	galactic latitude	°

$\mathcal{F}_7$	differential flux at 7 TeV	$\mathrm{TeV}^{-1}\,\mathrm{cm}^{-2}\,\mathrm{s}^{-1}$
$\mathcal{W}_{\mathrm{CR}}$	cosmic-ray energy density	$\mathrm{eV/cm}^{-3}$
$\mathcal{L}_\gamma$	gamma-ray luminosity	erg/s
d_{PSR}	pulsar distance	pc
τ_{p}	characteristic cooling timescale from pp-interactions	s
σ_{pp}	pp-interaction cross-section	m^2
f	coefficient of inelasticity	–
n	number density	cm^{-3}
Γ	spectral index	–
ϵ	cut-off energy	TeV
β_{A}	Alfvén wave velocity relative to c	–
η	ratio of turbulent to mean magnetic field	–
λ_{max}	maximum Alfvén wavelength relative to L	–
q	index of MHD turbulence	–
r_g	gyration radius	km

List of Units

Abbreviation	Name	Equivalence
m	metre	–
s	second	–
kg	kilogram	–
eV	electronvolt	$1.60 \times 10^{-19} \text{ kg m}^2 \text{ s}^{-2}$
erg	ergon	$0.624\,15 \text{ TeV}$
Hz	hertz	1 s^{-1}
pc	parsec	$3.086 \times 10^{16} \text{ m}$
yr	year	$3.154 \times 10^7 \text{ s}$
ly	light year	$0.306\,601 \text{ pc} \equiv 9.46 \times 10^{15} \text{ m}$
sr	steradian	$41\,252.96 \text{ deg}^2$
arcmin	arcminute	$1/60\,°$
arcsec	arcsecond	$1/3\,600\,°$

List of Prefixes

Abbreviation	Prefix	Equivalence
Z	Zeta	10^{21}
E	Exa	10^{18}
P	Peta	10^{15}
T	Tera	10^{12}
G	Giga	10^{9}
M	Mega	10^{6}
k	kilo	10^{3}
c	centi	10^{-2}
m	milli	10^{-3}
μ	micro	10^{-6}
n	nano	10^{-9}
p	pico	10^{-12}

Camille Flammarion, L'atmosphère: météorologie populaire (1888)

"When you have eliminated the impossible, then whatever remains, however improbable, must be the truth..."

Sir Arthur Conan Doyle, The Case Book of Sherlock Holmes

ॐ

भूर्भुवः स्वः
तत्सवितुर्वरेण्यं
भर्गो देवस्य धीमहि
धियो यो नः प्रचोदयात् ॥

To my Maa & Paa . . .

Introduction

Context and Motivation

The Universe is home to numerous exotic and beautiful phenomena, some of which can generate almost inconceivable amounts of energy; Supermassive black holes, merging neutron stars, streams of hot gas moving close to the speed of light... These are but a few of the cosmic marvels that generate gamma-ray radiation, the most energetic form of radiation, millions of times more energetic than the type of light visible to our eyes. What are the physical mechanisms underlying the production of such massive amounts of energy? What happens to the astrophysical environments surrounding these phenomena? How will studying these energetic objects contribute to our understanding of the inherent nature of the Universe and how it behaves? These are a few questions which drive the curious mind into probing the gamma-ray sky.

At the frontiers of gamma-ray astronomy and particle physics lies the interdisciplinary field of *astroparticle physics* or *particle astrophysics*. Therein, we study elementary particles of astrophysical origin and while it is a relatively new branch, it has undergone rapid development over the past few decades and has led us to the following open questions:

1. What can we learn about our Universe from cosmic rays?

2. What is the nature of dark matter and dark energy?

3. Can gravity be incorporated in the Standard Model of Particle Physics?

4. Why are the neutrino masses so small and what can neutrinos teach us about the matter/anti-matter asymmetry?

5. Is there physics beyond the Standard Model of Particle Physics?

Within the scope of contributing to elucidate some of the aforementioned open questions, we provide the following instrumental context for gamma-ray detection. HAWC

is a ground-based gamma-ray observatory that samples particles of extensive air showers over a large collection area. With the Earth's atmosphere acting as part of the detector, HAWC takes a slice along the longitudinal development of a photon- or hadron-induced atmospheric shower, through the use of water Cherenkov detectors. The array of water tanks is instrumented with photomultiplier tubes (PMTs) calibrated to read-out Cherenkov light, which is emitted when particles move faster than the speed of light in a medium. This approach allows us to continuously survey the sky within the entire field of view of the instrument. Besides unveiling galactic and extragalactic particle accelerators, with HAWC or HAWC-like detectors, for instance SWGO, we further aim towards monitoring of the transient sky at very high energies, probing particle physics beyond the Standard Model, and the characterisation of the cosmic ray flux. The underlying objective is to improve our understanding of violent astrophysical phenomena and extreme environments, such as supernovae, gamma-ray bursts and the turbulent neighbourhood of supermassive blackholes, via the study of gamma and cosmic rays.

Structure of this thesis

Our primary undertaking to probe large-scale structures was motivated by the wide field of view of HAWC. However, given our detector type, we face a few obstacles and we need to understand our measurements and assess the impact of uncertainties, before making any claims about the nature of any process driving these large-scale structures. The organisation of this thesis, therefore, follows the methodology adopted to analyse our measurements, as described below.

Chapter 1 introduces the basic concepts and terminology of high-energy gamma-ray astrophysics, starting with a brief historical review of observational gamma-ray astronomy. A list of the key science goals of HAWC is then provided, followed by a description of cosmic rays and their acceleration mechanisms. This chapter also outlines the various processes involved in the production of high-energy gamma-ray emission and a concise description of plausible acceleration sites.

Chapter 2 provides an in-depth description of the key aspects of ground-based particle detection techniques, as relevant to this thesis. It subsequently reviews the essential physical concepts underlying electromagnetic air showers and outlines the main observables of interest to this work. The remaining sections of this chapter cover the atmospheric production of muons, the distinctive features of hadron-induced air showers, compared to gamma-ray initiated showers, and the main processes involved in atmospheric shower physics. The final part of this chapter reviews the various ground-based detection methods.

Chapter 3 covers the essential details of the water Cherenkov detectors of HAWC, such as their set-up and configuration. It presents the instrumentation aspects involving the data-acquisition system, with a description of its calibration and performance. A brief summary of the outrigger array of HAWC is also provided for the sake of completeness, with the subsequent sections outlining the use of Monte Carlo simulations, the impact of primary energy, zenith angle and detection altitude on simulated air showers for a HAWC-like instrument.

Chapter 4 details reconstruction process in HAWC and follows-up with a discussion of the technique developed in this thesis to differentiate between gamma-ray induced showers and their cosmic-ray induced counterparts, i.e. gamma/hadron separation, which will be employed in future HAWC analyses. Other novel algorithms, developed recently or still currently in development for the next PASS (PASS 5) of HAWC data are also described.

Chapter 5 entails the generation of different maps from HAWC data, with particular focus on the methodology employed. Some examples of these maps include the ones that pass gamma selection of events, maps that pass hadron selection of events, the conventional HAWC background map, a new background map, excess maps and exposure maps. The potential applications of such maps are also detailed.

Chapter 6 ensues with the mathematical formalism for significance computation through the profile likelihood approach. A blind search for large-scale structures in the HAWC sky map is performed and the results are discussed extensively. The differential flux of a few gamma-ray sources, computed through the aforementioned approach, are listed.

Chapter 7 presents a literary review of the *Fermi* bubble, from observed multiwavelength sky maps to searches performed to constrain the gamma-ray emission mechanism(s). Thereon, we derive templates that describe the northern *Fermi* bubble (and its base) and use them to search for an emission signal at very high energies with HAWC.

The thesis culminates with with Chapter 8 which summarises the salient aspects and conclusions drawn from this doctoral work, and provides an outlook for impending improvement on the detector, methods and analysis approach used, while highlighting potential promising avenues for future investigations.

We provide supplementary material to some of the above chapters in the appendices. As supplement to Chapters 1 and 2, Appendix A contains a summary of gamma-ray sources of high significance, such as the Crab nebula. Further mathematical background pertaining to the lateral distribution of secondary particles in electromagnetic air showers is also provided. We end with a description of the geomagnetic field.

Appendix B presents further details complementary to the description of the HAWC observatory, as laid out in Chapter 3. The instrumental aspect of photomultiplier tubes

(PMTs), cable propagation and the data and aquisition (DAQ) system are described in more depth, followed by an investigation of the lateral distribution of muons.

Appendix C supplies detailed information concerning air shower reconstruction and gamma/hadron discrimination, as described in Chapter 4. Moreover, it contains the complete sets of figures for different shower bins and PMTs, complementary to the ones illustrated in Chapter 4 and ends with a brief summary of some other gamma/hadron separators.

Appendix D provides the gamma/hadron cuts, as employed in Chapter 5, for the novel background modelling method developed in this thesis. The relevant gamma-like event maps, hadron-like event maps and background maps for all nHit bins are also illustrated, along with the variation of significance with declination.

Appendix E complements the literature review on the *Fermi* bubbles, as provided in Chapter 7. In particular, it covers the essential aspects involved in the derivation of the integral flux upper limits of the north *Fermi* bubbles.

1

Non-thermal Astrophysics

In this chapter, we provide a basic review of the electromagnetic spectrum and the distinct energy regimes of observational gamma-ray astronomy to lay down the terminology employed throughout this thesis. The structure of this chapter is organised as follows: We provide a brief historical review of gamma-ray astronomy in Section 1.2, followed by an introductory description of cosmic rays in Section 1.3, with their acceleration mechanisms outlined in Section 1.4. The various processes involved in the production of high-energy gamma-ray emission are subsequently described in Section 1.5. This chapter concludes with a brief description of a list of plausible acceleration sites, i.e. potential sources of gamma-ray emission, in Section 1.6.

1.1 Introduction to Gamma-ray Astronomy

Astronomy is a science dealing with the study of celestial objects and phenomena that allows us to understand the nature of astronomical objects. Gamma-ray astronomy is the study of astrophysical gamma-rays and relies on their detection and the reconstruction of their arrival direction and energies.

1.1.1 Electromagnetic Spectrum

To understand the regime of astrophysics studied in this work, a basic notion of the electromagnetic (EM) spectrum is prerequisite. The EM spectrum defines the range of frequencies of electromagnetic radiation and their corresponding wavelengths and photon

---

[1]Available from: http://chandra.harvard.edu/resources/em_radiation.html
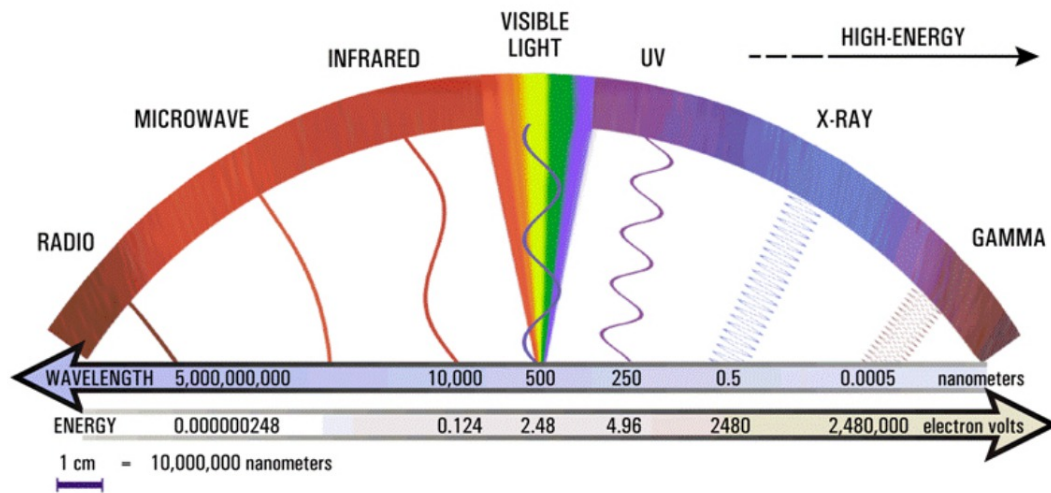
FIGURE 1.1: Electromagnetic spectrum depicting the high-energy astrophysics regime, with the gamma region of the spectrum being of particular relevance to this thesis. Figure from Chandra X-ray mission, CfA.[1]

energies, divided into distinct bands, as illustrated in Figure 1.1. Each band has a specific name attributed to it, with particular characteristics. The gamma portion of the EM spectrum lies at the high-energy end, i.e. high-frequency and short wavelength regime ($E = h\nu = hc/\lambda$) and provides a window to study extremely energetic non-nuclear processes, such as acceleration of cosmic rays, gamma rays from galactic and extragalactic origin, and high-energy neutrinos. Together, the above constitute the field of high-energy astrophysics (e.g. Longair, 2011).

Processes emitting EM radiation may be characterised as *thermal* or *non-thermal* in nature. The former concerns conventional observational astronomy dealing primarily with photons emitted thermally by astrophysical objects at high temperatures, with the most extreme environments producing photons in the range of a few hundreds of keV ($E = k_{B}T$). Nevertheless, the emission of even higher energy gamma-ray photons would require non-thermal processes. Attaining these energies via thermal emission would necessitate the black-body temperature of the given astrophysical object to be of the order of that only present in the very early Universe, shortly after the Big Bang. In essence, non-thermal radiation implies that the properties of the emitted radiation do not depend on the temperature of the astrophysical source.

1.1.2 Energy Regimes of Gamma-ray Astronomy

Gamma-rays are used as probes to study the production and acceleration of cosmic ray particles in extreme astrophysical environments. Such particles are deprived of their

TABLE 1.1: Definition of the distinct energy regimes of observational gamma-ray astronomy.

Energy regime	Energy range
Low Energy (LE)	1 MeV to 30 MeV
High Energy (HE)	30 MeV to 50 GeV
Very High Energy (VHE)	50 GeV to 100 TeV
Ultra High Energy (UHE)	100 TeV to 100 PeV
Extremely High Energy (EHE)	>100 PeV

directional information when propagating through the galactic and extragalactic environments on their way to Earth, resulting in an isotropic measured flux. Being charged particles, however, they interact with the surrounding medium to produce high-energy gamma-rays, whose trajectories are not deflected by the magnetic fields since they are neutral. As such, they retain the directional information of the source locations and serve as excellent messengers to probe the source environments of the highest energy cosmic accelerator sites. As depicted in Figure 1.1, the gamma-ray band covers a significant portion of the EM spectrum from ~ 1 MeV to the highest energies. Observational gamma-ray astronomy can be divided into different regimes, depending on the energy of the observed gamma-rays, as listed in Table 1.1. This is because the approach for detection is different across the energy regimes. The energy domain most relevant to this thesis concerns the VHE regime.

1.2 Brief History of Gamma-ray Astronomy

From time immemorial, humanity has been inherently driven by astronomical quests, with Galileo Galilei being the quintessential embodiment of this desire to peer into the cosmos, when he first pointed a telescope towards the sky to observe a narrow spectrum of visible frequencies, around the beginning of the XVII$^{\text{th}}$ century (Singer, 2013). This heralded the dawn of the era of observational astronomy, which, during the following 350 years, subsequently evolved from the optical band to extend across the whole electromagnetic spectrum.

The essence of this thesis lies in very high energy non-thermal astrophysics, with the main focus being ground-based gamma-ray astronomy. We outline the key milestones which have marked the development of gamma-ray astronomy during the past century. For a thorough historical review of gamma-ray astronomy, we refer the interested reader to Lorenz and Wagner (2012), Hillas (2013), and Funk (2015).

1.2.1   Discovery of Cosmic Rays

The first detection of cosmic rays, around a century ago, involves the pioneering work of two key figures: the Austrian-American physicist Victor F. Hess (Hess, 1912) and the Italian physicist Domenico Pacini in two independent experiments (De Angelis, Giglietto, and Stramaglia, 2010). Hess, while in a balloon flight, observed the ionisation rate, i.e. an increase in the density of ionised particles, to increase with altitude. This ionising radiation, consequently, was deduced to be emanating from a source beyond the Earth's atmosphere, a discovery which eventually earned Hess the Nobel prize in physics in 1936. This extraterrestrial source was subsequently referred to as *cosmic rays*. Around the same time, Pacini also found the radiation strength to decrease with the depth of water in both a lake and the sea, when moving from the water surface to a few metres underwater. An in-depth introduction to cosmic rays is provided in Section 1.3. This groundbreaking discovery was the starting point of the study of the non-thermal Universe. Gamma-ray instruments can be divided into ground-based and space-based detectors, with the primary detection techniques pertaining to ground-based observations, as relevant to this work, outlined in Chapter 2.

1.2.2   Space-based Detection

Initial attempts to detect cosmic gamma-rays with balloon-borne detectors were unsuccessful, as a result of the contamination from the high level of secondary gamma rays produced by cosmic rays in the atmosphere (De Angelis and Mallamaci, 2018). The end of the 1960s then witnessed the launch of the first gamma-ray satellites: The OSO-3 (Orbiting Solar System) satellite (1967-1968) provided remarkable tangible evidence that the Milky Way was a bright source of gamma-rays above 50 MeV. This was followed by SAS-2 (1972-1973, $E > 35$ MeV), which unveiled the diffuse emission of the Milky Way and led to the discovery of the Crab and Vela pulsar wind nebulae and the periodic signals from their pulsars. COS-B (1975-1982, $E > 100$ MeV) subsequently compiled a catalogue of 25 sources, including one extragalactic source (quasar 3C 273) (Swanenburg et al., 1981).

In the 1980s, the Compton Gamma-ray Observatory (CGRO, Gehrels et al., 1993; Gehrels, Chipman, and Kniffen, 1994) was launched, recording data from 1991 until 2000, which represented a key phase in the growth of gamma-ray astronomy. It was composed of four instruments that covered the electromagnetic spectrum across six orders of magnitude, from 30 keV to 30 GeV: the Burst And Transient Source Experiment (BATSE, Fishman et al., 1992), the Oriented Scintillation Spectrometer Experiment (OSSE, Johnson et al., 1993), the Imaging Compton Telescope (COMPTEL, Schoenfelder et al., 1993), and the Energetic Gamma Ray Experiment Telescope (EGRET, Fichtel et al., 1993), each with a specific energy range, detection technique and scientific goal (see, for e.g., De Angelis
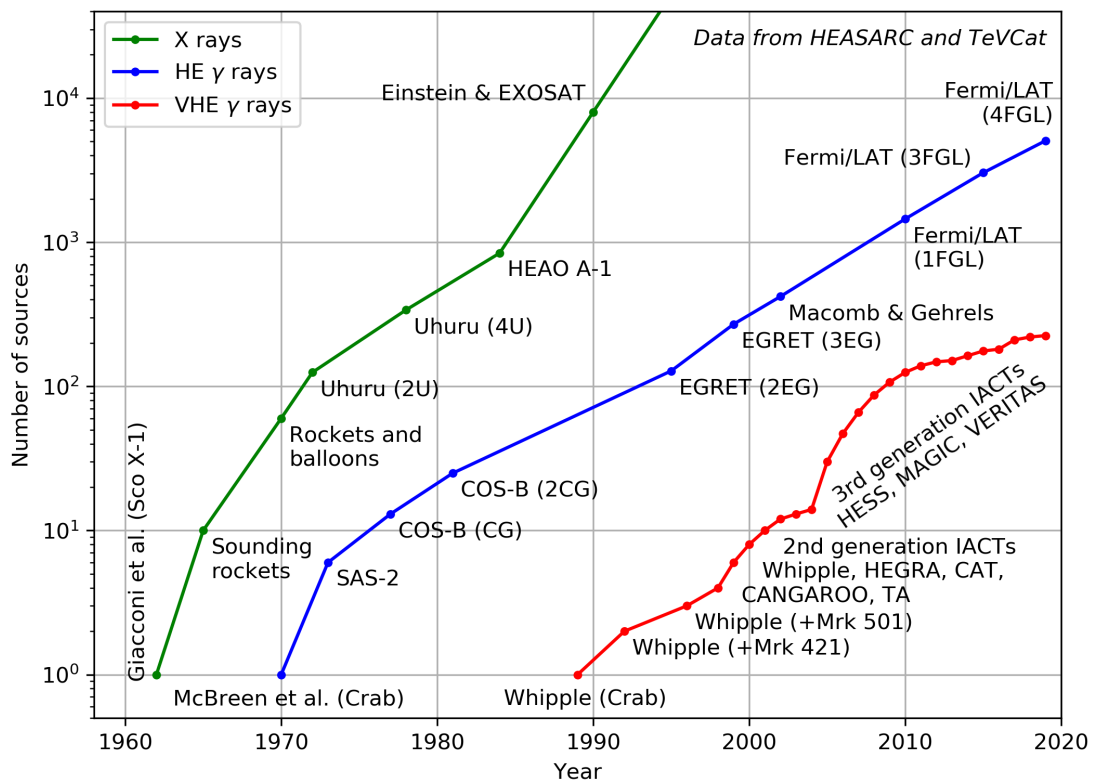
FIGURE 1.2: Variation of integral number of high-energy astrophysical sources detected with year of detection, the so-called "Kifune plot". Figure from Stephen Fegan.[2]

and Mallamaci, 2018; Di Sciascio, 2019b, for technical specifications). The third EGRET catalogue, yielding 271 sources, including several active galactic nuclei (AGN), led the way to extragalactic gamma-ray astronomy at high energies (Hartman et al., 1999).

The launch of the *Fermi* gamma-ray telescope (formerly known as Gamma-ray Large Area Space Telescope, or GLAST) in June 2008 marked the onset of a new era for space-based gamma-ray astronomy. Currently in operation, it remains the largest space-based detector and most sensitive gamma-ray telescope in orbit, powered by particle physics technology. Its sensitivity outperforms that of its predecessor, the INTErnational Gamma-Ray Astrophysics Laboratory (INTEGRAL, Teegarden and Sturner, 1999), launched in 2002. *Fermi* consists of two primary instruments: the Large Area Telescope (LAT, Atwood et al., 2009), as a successor to EGRET, and the Fermi Gamma Burst Monitor (GBM, Meegan et al., 2009). More details about the *Fermi*-LAT ensemble are provided in Chapter 7, Section 1.2.2. The third catalogue of high-energy gamma-ray sources (3FGL, Fermi-LAT

---

[2]Available from: `https://github.com/sfegan/kifune-plot`

Collaboration et al., 2015) produced by LAT contains 3033 sources above 4σ significance within the 100 MeV - 300 GeV range. The fourth catalogue was recently released and has twice the exposure as the third catalogue, and contains more than 5000 sources with significance above 4σ (Thompson, 2019). The rising number of observed high-energy astrophysical sources is illustrated in Figure 1.2, the so-called "Kifune plot" (Kifune, 1996), which depicts the integral number of high-energy astrophysical sources detected as a function of year of detection. *Fermi* also made important observations of gamma-ray bursts (GRBs), which are extremely intense and relatively short bursts of gamma radiation (e.g. Fermi-LAT Collaboration et al., 2009), with the LAT detection of GRB 130427A currently one of the highest energy outputs ever recorded (Fermi-LAT Collaboration et al., 2014a).
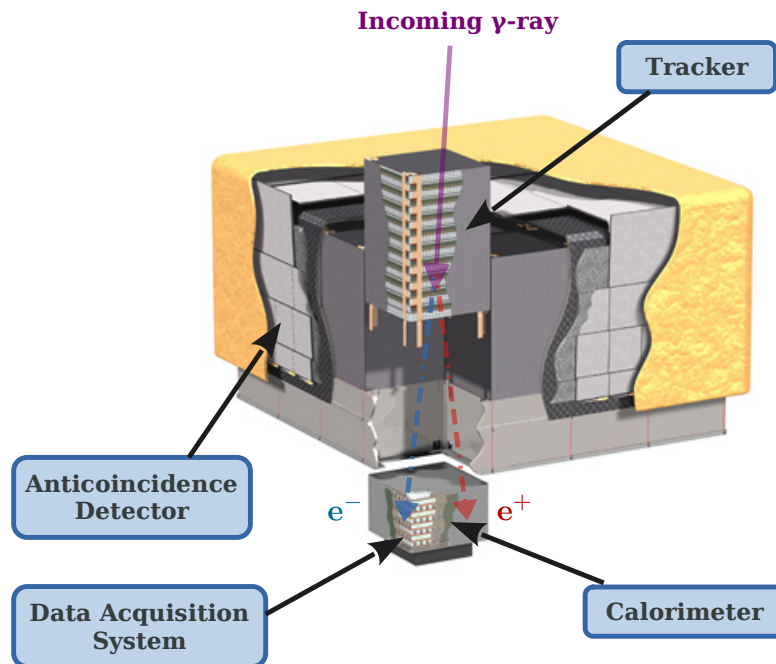
*Fermi***-LAT**

FIGURE 1.3: Schematic of the *Fermi*-LAT, illustrating the different instruments involved in the detection of gamma-rays. The trajectory of an incoming gamma-ray photon is depicted, along with the tracks of the resulting electron and positron formed via pair production. Figure adapted from Atwood et al. (2009).

The *Fermi*-LAT is an imaging high-energy gamma-ray telescope (Atwood et al., 2009). It is a pair production instrument with a large field of view. The LAT has four sub-systems that work together to detect gamma-rays and to reject signals from the intense bombardment of CRs. For every gamma-ray that enters the LAT, it will have to filter out 100 000 to one million CRs, charged particles that resemble the particles produced by gamma-rays.

The four main subsystems of the *Fermi*-LAT telescope are: tracker, calorimeter, anticoincidence detector (ACD), and data acquisition system (DAQ), with their respective tasks outlined in Appendix A.

In essence, the above instruments make a series of measurements to determine the energy of the electron-positron pair produced by a gamma-ray, which can subsequently be used to infer the primary photon energy and reconstruct the shower profile, while rejecting CRs. The overall detection process may be summarised as follows: An incoming gamma-ray photon first goes through the ACD and interacts in one of the tungsten sheets, yielding an electron and positron via pair production (cf. Section 2.2.1). The paths of the latter particles are measured by the tracker using silicon strips to infer the arrival direction of the incoming gamma-ray. The electron and positron then enter the calorimeter which determines the energy of the gamma-ray photon via the measurement of the respective energies of these particles. Undesired CR particles will produce a flash of light in the ACD, which alerts the DAQ system to discard the signal. The DAQ system is also designed to reject gamma-rays that originate in the atmosphere, which are not of interest, based on their arrival direction. A schematic of the above detection pipeline is illustrated in Figure 1.3.

Data released by the *Fermi*-collaboration are publicly available,[3] along with standard analysis software, from NASA's Fermi Science Support Center.[4]

1.2.3 Ground-based Detection

Ground-based experiments, as detailed in Chapter 2, aim to detect the Cherenkov radiation of charged particles in air (imaging atmospheric Cherenkov technique) or indirectly detect the extensive air shower (particle detection technique) via the charged particles reaching the ground (De Angelis and Mallamaci, 2018).

Imaging Atmospheric Cherenkov Technique

In 1952, Cherenkov light emission induced by cosmic rays in the atmosphere was first detected by Galbraith and Jelley (1953), leading to pioneering studies by Chudakov and Nesterova (1958). Cocconi (1960) proposed, in 1959, to measure gamma-ray sources in the TeV energy range and predicted that the Crab nebula was a rich source of TeV gamma-rays which could be detected using an instrument with sufficiently large angular resolution to reject the isotropic cosmic ray background. Zatsepin and Chudakov (1961), motivated by this idea, then suggested to use Cherenkov radiation, eventually leading

---

[3]https://www-glast.stanford.edu/pub_data/
[4]https://fermi.gsfc.nasa.gov/ssc/

to the construction of the first Atmospheric Cherenkov Telescope (ACT), designed for gamma-ray observations, in Crimea. This was followed by the ACT Whipple in 1968 on Mount Hopkins in Arizona, another landmark for gamma-ray astronomy. The latter was then upgraded in 1983 to employ a 37 pixel imaging camera proposed by Weekes (1981), resulting in the first Imaging ACT (or IACT).

The seminal detection of TeV gamma rays from the Crab nebula in 1989 by the Whipple Collaboration (Weekes et al., 1989), as a result of an imaging analysis developed by Hillas (1985) for background rejection of cosmic rays, unlocked a new observational window onto the Universe: VHE gamma-ray astronomy. They observed an excess of photons with energies ≥ 500 GeV emanating from the direction of the Crab nebula,[5] to establish the latter as a 'stationary' and continuous source of photons with energy in the range of 0.5 TeV to 10 TeV (Hillas, 2013). Subsequent observations by other experiments corroborated this claim, with this steady-state flux of photons now used as a standard candle to improve instrumental and data analysis aspects. It is used to calibrate flux from detectors, cross-calibrate ground-based detectors, perform stability tests and assess the sensitivity of a given experiment (Di Sciascio, 2019b).

The development and implementation of IACTs changed the landscape of gamma-ray astronomy. The second generation of IACTs was composed of High Energy Gamma Ray Astronomy (HEGRA, Mirzoyan et al., 1994) on the Canary Islands and Collaboration between Australia and Nippon for a Gamma Ray Observatory in the Outback (CANGAROO, Kubo et al., 2004) in Australia. Some highly successful experiments of the current generation include the High Energy Stereoscopic System (H.E.S.S., Hofmann, 2000), Major Atmospheric Gamma Imaging Cherenkov Telescopes (MAGIC, Baixeras, 2003) and Very Energetic Radiation Imaging Telescope Array System (VERITAS, Weekes et al., 2002), which led to important breakthroughs in the field, as reviewed in Aharonian and Casanova (2018). The next-generation ground-based observatory is the Cherenkov Telescope Array (CTA, Cherenkov Telescope Array Consortium et al., 2019), with over 100 telescopes located in the northern and southern hemispheres, and will be the world's largest very-high-energy gamma-ray observatory, with an order of magnitude improvement in sensitivity relative to current-generation detectors (e.g. Maier et al., 2019; Mazin, 2019).

Air Shower Particle Detection Technique

The first observation of TeV photons via a Air Shower Particle Detector (ASPD) array was achieved in 1999 by Tibet AS-γ (Amenomori et al., 1992) using a sparse array of

---

[5]See Appendix A for more details.

scintillator-based detectors. This was followed by observations from Milagro (The Milagro Collaboration, 2004), a water-Cherenkov instrument, and ARGO-YBJ (ARGO-YBJ Collaboration et al., 2002), an array of resistive plate counters, which demonstrated the potential of shower arrays for the detection of gamma-ray sources and flaring emissions from extra-galactic sources (Di Sciascio, 2019b). This laid the groundwork and substantiated the investment in the construction of the next-generation ASPD High Altitude Water Cherenkov (HAWC, HAWC Collaboration et al., 2013) gamma-ray observatory, Large High Altitude Air Shower Observatory (LHAASO, Di Sciascio and LHAASO Collaboration, 2016) and Hundred*i Square-km Cosmic ORigin Explorer (HiSCORE, Tluczykont et al., 2014). The HAWC observatory is of particular relevance to this thesis, with an in-depth description of its instrumental features, data acquisition and analysis pipelines provided in Chapters 3 and 4. A forthcoming next-generation instrument is the Southern Wide-field Gamma-ray Observatory (SWGO, SWGO Collaboration et al., 2019).

Science Goals of HAWC

HAWC has a wide instantaneous FoV of ~ 2 sr and high duty cycle of about 95% which covers 8.4 sr on the daily sky, making it a powerful survey and monitoring experiment. As shown in Figure 1.4, half of the Galactic plane is seen by HAWC, with the GC being on the edge of the FoV as it lies close to the horizon of HAWC and is seen for a very small fraction of the day.
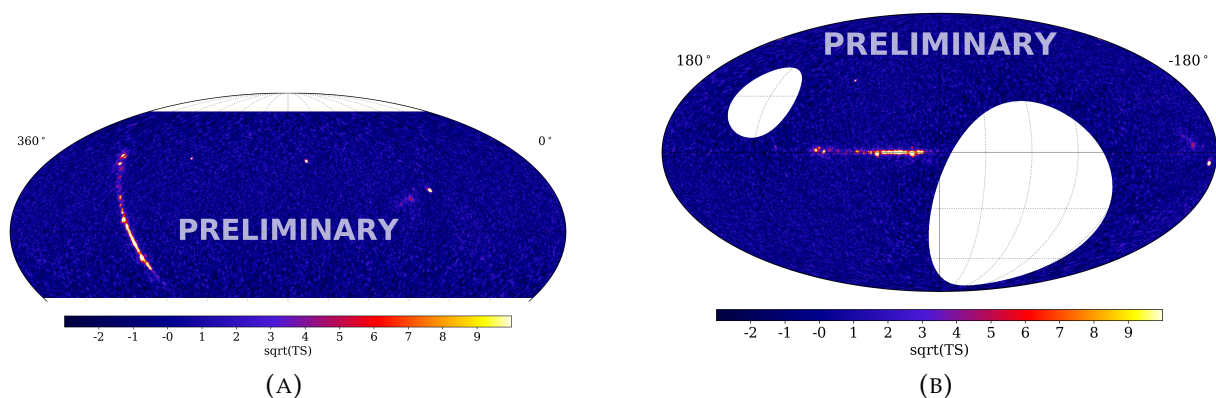
FIGURE 1.4: HAWC sky maps; the left panel (A) shows equatorial coordinates while the right panel (B) displays galactic coordinates.

The angular resolution of HAWC (40% containment) is $\sim 0.1°$ above 10 TeV and has differential point source sensitivity as illustrated in Figure 1.5. The sensitivity decreases with increasing zenith angles because the incoming shower has to travel through a larger layer of the atmosphere before reaching the detector. Thus, the sensitivity of HAWC is

dependent on declination, the optimal being for sources transiting through the zenith
(19°).
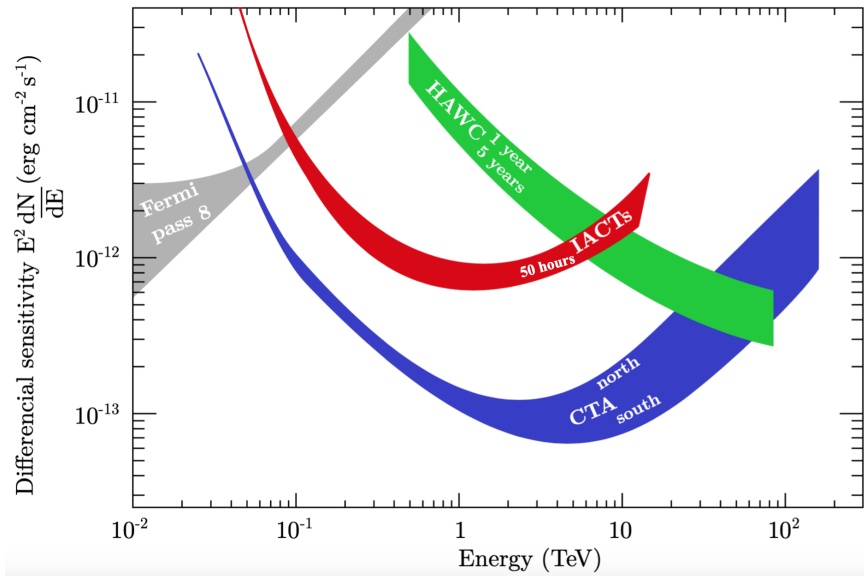
FIGURE 1.5: Differential sentitivity of HAWC compared to other detectors. Figure adapted from Jardin-Blicq (2019), https://www.cta-observatory.org/science/gamma-rays-cosmic-sources/.

The scientific aims associated with the HAWC gamma-ray observatory are:

1. Understanding of high energy particle acceleration and propagation from galactic, for instance SNRs, and extra-galactic sources;

2. Detection and monitoring of transients such as AGNs, GRBs, flares from PWN and binary systems as part of a real-time alert system;

3. Probing and study of extended sources such as the *Fermi* bubbles and galactic diffuse emission;

4. Contributing to constrain fundamental physics problems, such as dark matter[6] or Lorentz invariance violation, within the scope of multimessenger astrophysics;

5. Study of the local CR anisotropy which provides an additional lens with which to probe our local CR environment.

In line with the work presented in this thesis, the study of extended astrophysical sources is of primary interest. Characterising their morphology and gamma-ray energy spectra provides a pathway to elucidate the claims regarding the dominant processes at the acceleration site.

---

[6]The measurement of gamma-ray emission from low luminosity, high mass galaxies can provide clues for dark matter particles with masses of ~ 1 TeV (VERITAS Collaboration et al., 2012; Scott et al., 2010)

1.3 Introduction to Cosmic Rays

The discovery of cosmic rays (CRs) by Victor Hess, as outlined in Section 1.2.1, triggered a series of community-wide efforts to understand their origin and nature. The work of Bothe and Kolhörster (1929) elucidated the corpuscular nature of CRs as charged particles emanating from outer space. The following decade helped to shape our understanding of Extensive Air Showers (EASs) initiated by CRs, as a result of the work of Pierre Auger, and culminated in deducing the ~PeV energies of the primary CR particles. Through the observation of EASs and/or the direct detection of CRs, the energy spectrum of CRs, as depicted in Figure 1.6, has been measured by several experiments over a period spanning several decades.

1.3.1 Cosmic Ray Spectrum

The primary CR all-particle energy spectrum, i.e. the number of nuclei as a function of total energy, displays some distinctive features, as labelled on Figure 1.6:

- An initial $\sim E^{-2.7}$ power-law behaviour until a small and smooth drop in energy, known as the "*knee*" around a few PeV;

- A subsequent $\sim E^{-3.1}$ power-law behaviour until a further slight dip around 10^{17} eV, usually referred to as the "*second knee*";

- A transition to the initial $\sim E^{-2.7}$ power-law behaviour around 10^{18} eV, the so-called "*ankle*";

- A cut-off around 10^{20} eV, with the most probable explanation being due to extra-galactic CR interactions with the cosmic microwave background (CMB), also known as the *Greisen-Zatsepin-Kuzmin (GZK) effect* (Greisen, 1966; Zatsepin and Kuz'min, 1966).

The above features encode fundamental information pertaining to the key unresolved mystery of CR origin. Understanding the origin of the knee is essential to piece together a comprehensive picture of the origin of CRs up to the ankle. The location of the knee, in particular, depends on the particle species since the larger the charge of a given particle, the higher is its peak in energy. Below the knee, the CR origin is believed to be of galactic nature, with supernova remnants (SNRs) being a plausible source. Above 10^{15} eV energies, however, CRs are no longer restrained by the magnetic fields and length scales of galactic objects and consequently escape, such that the energy scale coincides with the transition from galactic to extragalactic origin. The second knee is subsequently attributed to the transition to heavy primary particles (Particle Data Group et al., 2018),
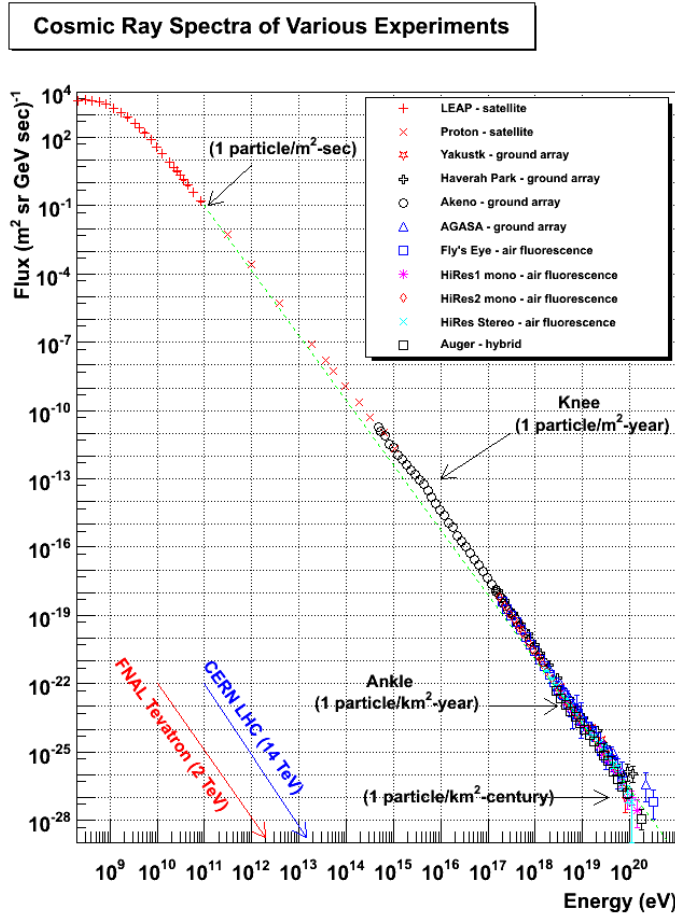
(A)
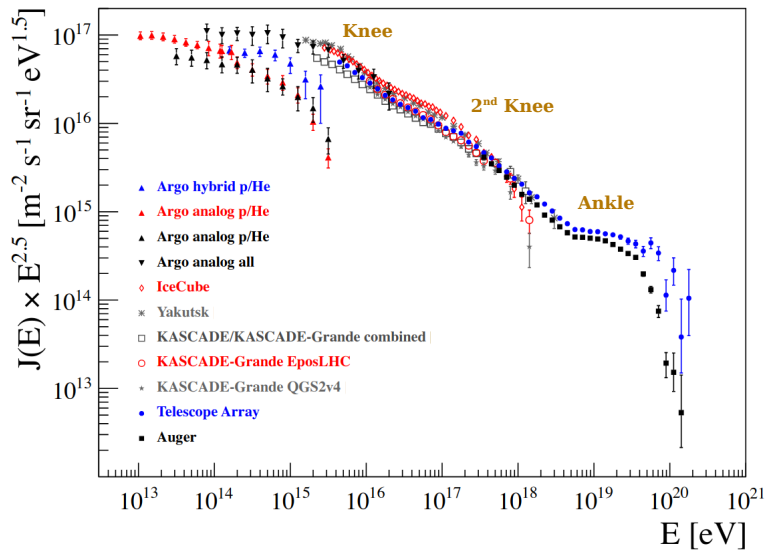
(B)

FIGURE 1.6: The top panel displays the spectrum of primary CRs, as a function of energy per nucleus, as measured by several experiments, figure obtained from https://www.physics.utah.edu/~whanlon/spectrum.html. The characteristic features depicted in the bottom panel include the knee, second knee and the ankle. Figure adapted from Di Sciascio (2019a).

with an interesting interpretation by Lemoine (2005) and Kotera and Lemoine (2008) asso-
ciating this transition to a suppression of the extragalactic CR spectrum due to magnetic
horizon effects, which are insignificant for energies below the second knee, such that the
galactic contribution dominates in that regime. The eventual ankle indicates the highest-
energy CRs which are most likely of extragalactic origin. The flux suppression, as seen in
the tail of the CR spectrum at the highest energies, can be explained by the GZK effect.
The latter attributes this cut-off to the interaction of CRs with the CMB, resulting in a
horizon at 50 Mpc as the distance that CRs of energies $> 10^{20}$ eV can travel.

1.3.2 Composition of Cosmic Rays
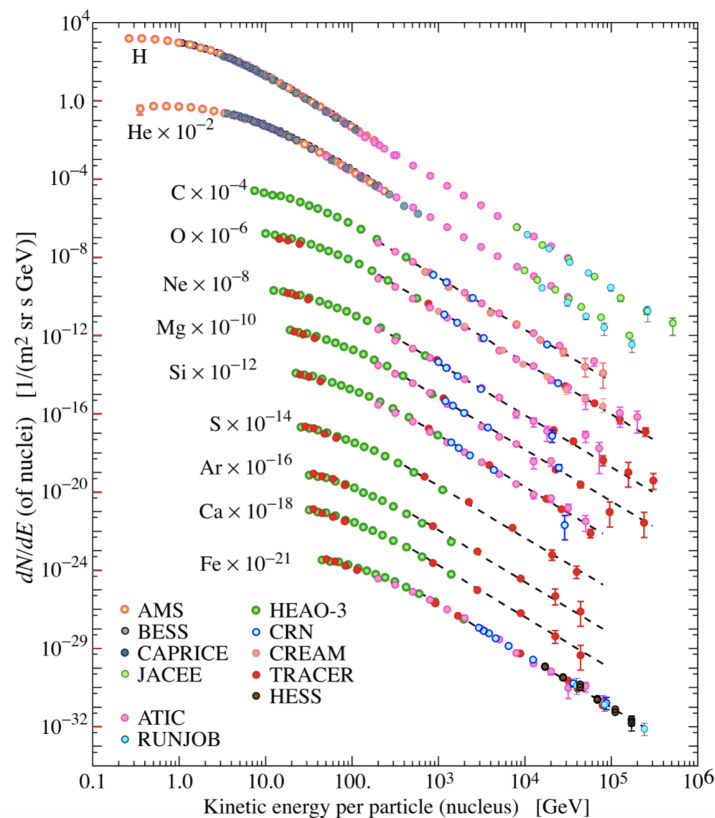
FIGURE 1.7: Energy spectra of the distinct elements in cosmic rays, measured by various
experiments over an extended energy range. Figure from Particle Data Group et al. (2012).

It is important to note that the exact locations of the aforementioned transitions, corre-
sponding to the different features in the CR energy spectrum, and their respective origins
are not yet known with certainty due to their dependence on the mass composition of the
CR spectrum. Figure 1.7 illustrates the energy spectrum of the various elements making
up the composition of CRs.

At low energies below 10^{14} eV, it is possible to directly measure the composition of cosmic rays, which consists predominantly of atomic nuclei, with a fraction of charged leptons such as electrons and positrons. At higher energies, direct measurements are no longer possible and as such, we can detect only the secondary particles resulting from the interactions with the atmosphere. Therefore, experiments are specifically designed to cover a large area to detect these secondaries, such that the reconstruction of the air shower will yield an estimate of the CR composition.

The key observables in studying the composition of CRs are the mean and variance, $\langle X_{\max} \rangle$ and $\sigma(X_{\max})$, respectively, where $X_{\max}$ corresponds to the atmospheric depth at which the number of particles in the EAS is maximum, this is described further in Chapter 2, Section 2.1.1. These two observables are typically employed to discuss experimental composition results for energies above $\sim$PeV.

1.4   Fermi Acceleration Mechanisms

In this section, we outline the astrophysical acceleration mechanisms of high energy CRs, relativistic charged particles, which are accelerated to high energies in extreme astrophysical systems. In essence, the acceleration of CRs is due to the recurring crossing of charged particles through shock boundaries (or shock fronts). In particular, we describe the first and second order Fermi acceleration framework, which depend on the properties of the moving plasma while other acceleration mechanisms are outlined in Appendix A.

Second order Fermi Acceleration

The Fermi acceleration mechanism, as proposed by Fermi (1949), is capable of accelerating particles to very high energies via collisions with a magnetised shock front. The seminal model entails the scattering of charged particles due to irregularities in the structure of the magnetic field. We briefly review the mathematical formalism underlying the second order Fermi acceleration.

We consider the random motion of scattering centres which "reflect" a given incident particle with energy and momentum, E_i and $\boldsymbol{p}_i$, respectively, prior to the collision, with E_f and $\boldsymbol{p}_f$ being the corresponding quantities after the collision. The energy and momentum are defined in the reference frame of the cloud. Denoting the incident angle of the particle by θ_i and the angle after scattering as θ_f and performing a boost into the cloud reference frame yields:

$$E_i' = \gamma E_i (1 - \beta \cos \theta_i) \, , \tag{1.1}$$

where $\beta = v/c$, v is the speed of propagation of the cloud and $\gamma \equiv (1 - \beta^2)^{-1}$ is the Lorentz factor. The energy of the particle, after leaving the cloud, is:

$$E_f = \gamma E'_f (1 + \beta \cos \theta'_f) . \tag{1.2}$$

Conservation of energy in the cloud reference frame implies $E'_i = E'_f$. The energy gain after each subsequent scattering of a CR by the magnetised centre can be conveniently expressed as (e.g. Protheroe, 1999):

$$\frac{\Delta E}{E} \equiv \frac{E_f - E_i}{E_i} = \gamma \frac{E'_f}{E'_i} (1 - \beta \cos \theta_i + \beta \cos \theta'_f - \beta^2 \cos \theta_i \cos \theta'_f) - 1 . \tag{1.3}$$

Since the scattering of CRs by the irregular patterns in the magnetic field is an approximately random process, we obtain the average energy gain by performing an average over the angles θ_i and θ'_f. The random scattering of the particles in all directions in the cloud reference frame implies that $\langle \cos \theta'_f \rangle = 0$, whilst the average value of θ_i is dependent on the geometry of the scattering. Under the assumption of azimuthal symmetry, the probability of collision depends only on θ_i. Considering ultrarelativistic particles, i.e. $v \to c$, the averaging over all angles from 0 to π leads to:

$$\langle \cos \theta_i \rangle = \frac{\int_{-1}^{1} dx \, x(1 + \beta x)}{\int_{-1}^{1} dx \, (1 + \beta x)} = -\frac{\beta}{3} , \tag{1.4}$$

where $x \equiv \cos \theta_i$. In the non-relativistic limit, i.e. $\beta << 1$, the average energy gain simplifies to:

$$\left\langle \frac{\Delta E}{E} \right\rangle \approx \frac{4}{3} \beta^2 . \tag{1.5}$$

This constitutes the second order Fermi mechanism, so-called because the energy gain is proportional to the second power of β, i.e. the square of the velocity of the cloud. Nevertheless, this energy gain is small, with the resulting spectrum following a power law, $N(E) = E^{-\alpha}$, where $N(E)$ corresponds to the number of particles and $\alpha = -(1/E)(dE/dt)t_{\text{esc}}$ is the spectral index, with t_{esc} being the time-taken by the CR to escape the cloud. A more detailed description of the above mechanism can be found in Longair (2011).

First order Fermi Acceleration

The first order Fermi acceleration, also known as *diffusive shock acceleration*, involves the propagation of powerful shock waves, as non-linear disturbances, in the interstellar medium (ISM), which transfer energy and momentum to the particles.

As mentioned above, second order Fermi acceleration cannot attain very high energy gains. Consequently, the framework of the more efficient first order mechanism was formulated (Axford, Leer, and Skadron, 1977; Krymskii, 1977; Bell, 1978a; Bell, 1978b; Blandford and Ostriker, 1978). Conceptually similar to the second order mechanism (cf. equations (1.1) and (1.2)), the first order framework involves particles moving with velocity v_p which interact with the shock front moving with v_s. As in the second order scenario, CR particles gain energy via interactions with the irregular features of the magnetic field. In a nutshell, a given particle gains energy as it crosses the shock front and is subsequently scattered or isotropised in the gas rest frame on a particular side of the shock, such that it loses all sense of its original direction. This consequently results in multiple crossings of the shock front. The average energy gain in one round trip (i.e. two shock crossings) can be expressed as (e.g. Longair, 2011):

$$\left\langle \frac{\Delta E}{E} \right\rangle \approx \frac{4}{3}\beta \; . \tag{1.6}$$

Analogous to its second order counterpart, the terminology of first order Fermi acceleration is due to the energy gain being linearly proportional to the velocity of the shock. The differential spectrum may be written as (e.g. Longair, 2011):

$$\frac{\mathrm{d}N(E)}{\mathrm{d}E} \propto E^\alpha \; . \tag{1.7}$$

Acceleration via the above diffusive shock framework is feasible in supernovae up to PeV energies or even higher, depending on when the shock wave dissipates. For particles to be accelerated to EeV energies, as in the case of the most energetic CRs observed, other factors, such as the properties of the magnetic field, which will extend the duration of particle confinement to the accelerator site, must be considered.

1.5 Gamma-ray Emission Mechanisms

Gamma-rays are produced via the interaction of highly energetic charged CR particles with the different environments they encounter. Due to the distinct types of charged particles and ambient astrophysical media, the nature of the interaction is not unique and lead to different gamma-ray emission mechanisms. A proper understanding of these mechanisms is essential to obtain insights about the origin, type and propagation of CR particles in different media. The origin of gamma-rays is either hadronic or leptonic, while possible forms of media are matter, radiation or magnetic fields. As such, there are two primary scenarios of gamma-ray emission processes: leptonic (bremsstrahlung,
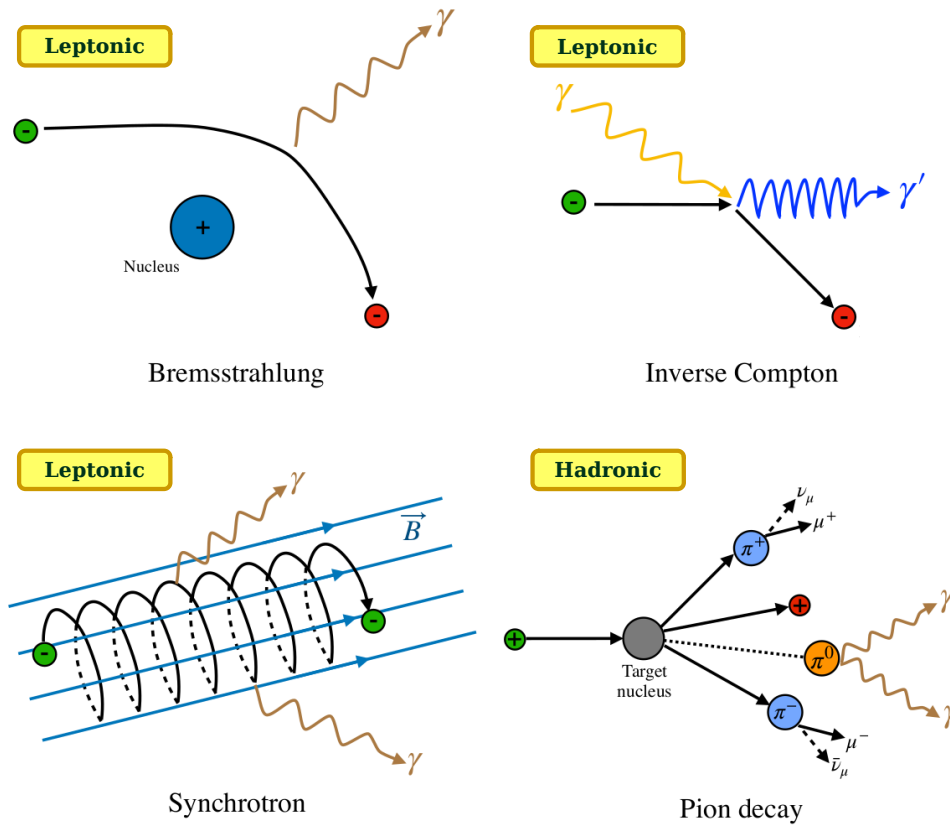
FIGURE 1.8: Schematic illustrating the primary channels of gamma-ray emission, namely the bremsstrahlung, synchrotron, inverse Compton and pion decay mechanisms. Figure adapted from López-Coto (2015) and Joshi (2019).

synchrotron[7] and inverse Compton scattering) and hadronic (pion decay), as depicted in Figure 1.8, with the spectral energy distribution of their respective gamma-ray emission displayed in Figure 1.9. These mechanisms are discussed below, with more detailed descriptions found in Blumenthal and Gould (1970), Rybicki and Lightman (1986), and H.E.S.S. Collaboration et al. (2004).

1.5.1 Bremsstrahlung

The energy loss of electrons, as they are decelerated while passing in the vicinity of atomic nuclei and ions and subsequently emit a gamma-ray photon (cf. top left panel of Figure 1.8), is known as "*bremsstrahlung*" (or braking radiation). The corresponding rate of energy loss of the electrons can be expressed as:

$$-\frac{\mathrm{d}E_e}{\mathrm{d}t} = \frac{cm_{\mathrm{p}}n}{X_0}E_e \, , \tag{1.8}$$

---

[7]The mass of electron is much lower than that of proton, consequently the contribution from electrons is dominant and this emission mechanism is treated as leptonic
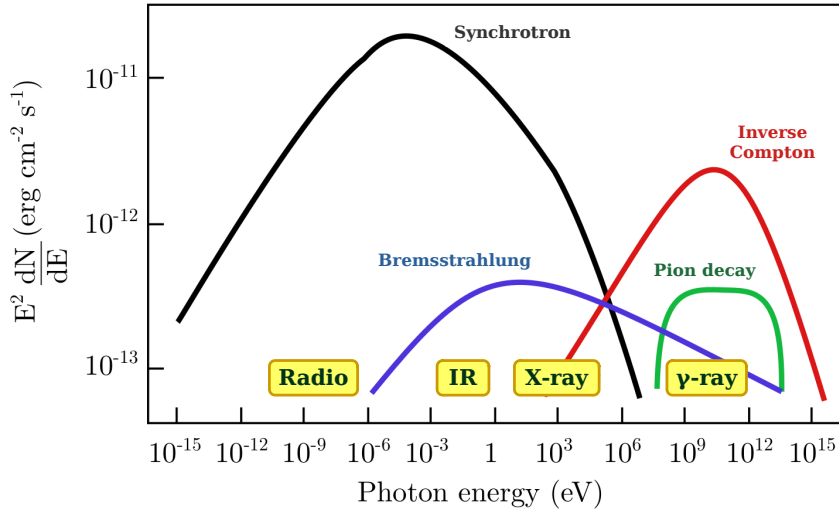
FIGURE 1.9: Spectral energy distribution of gamma-ray emission by bremsstrahlung, synchrotron, inverse Compton and neutral pion decay mechanisms. Figure adapted from Jardin-Blicq (2019) and is solely for the purpose of illustrating the shape and energy range of the emission mechanisms of interest.

where E_e denotes the electron energy, m_p is the proton mass, c is the speed of light in vacuum, with n being the number density of the ambient gaseous medium, while X_0 corresponds to the radiation length, a specific property of the medium, which characterises the mean distance over which an ultrarelativistic electron loses $1/e$ of its energy via bremsstrahlung. The lifetime τ_br of electrons with energy E_e varies with the energy loss rate as:

$$\tau_\mathrm{br} = \frac{E_e}{-\mathrm{d}E_e/\mathrm{d}t} \approx 4 \times 10^7 (n/\mathrm{cm}^{-3})^{-1}\mathrm{yr}\,. \tag{1.9}$$

Since the energy loss rate is proportional to the electron energy, i.e. $-\mathrm{d}E_e/\mathrm{d}t \propto E_e$ the lifetime is independent of the electron energy. This implies that energy losses due to bremsstrahlung only do not influence the shape of the electron spectrum. With the energy loss rate being directly proportional to the surrounding gas density, bremsstrahlung becomes particularly significant for gamma-ray production at MeV energies in dense gaseous environments, but at very high energies it becomes subdominant to the processes described below.

1.5.2   Synchrotron Radiation

Electrons with relativistic velocities moving in a magnetic field spiral around the magnetic field lines (cf. bottom left panel of Figure 1.8) due to the perpendicular component of their velocity to the magnetic field lines. As a result of this circular motion, electrons experience an acceleration and emit photons in a process known as *synchrotron radiation*.

In analogous fashion, electrons moving along curved magnetic field lines are also accelerated and emit EM radiation in a mechanism known as *curvature radiation*. The average rate of energy loss due to synchrotron emission is given by:

$$-\frac{\mathrm{d}E_e}{\mathrm{d}t} = \frac{4}{3}\sigma_{\mathrm{T}}cU_{\mathrm{mag}}\left(\frac{v}{c}\right)^2\gamma^2\,, \tag{1.10}$$

where σ_{T} is the Thomson scattering cross-section, $U_{\mathrm{mag}} = B^2/2\mu_0$ is the energy density of the surrounding magnetic field of strength B with μ_0 being the magnetic permeability in vacuum. The corresponding lifetime of electrons emitting synchrotron radiation can be written as:

$$\tau_{\mathrm{sync}} = \frac{E_e}{-\mathrm{d}E_e/\mathrm{d}t} \propto \frac{1}{B^2}\frac{1}{E_e}\,, \tag{1.11}$$

which implies a reduced lifetime for high-energy electrons in strong magnetic fields. Hence, the lifetime of such electrons is much shorter than the observed lifespan of extremely energetic astrophysical objects such as the Crab nebula, which, in turn, entails continuous acceleration of electrons within such sources. The synchrotron emission by a given population of electrons with energy E_e has a continuous spectrum with a peak at a characteristic energy of:

$$E_{\mathrm{sync}} \simeq 0.2\left(\frac{B}{10^{-5}\mathrm{G}}\right)\left(\frac{E_e}{\mathrm{TeV}}\right)^2\mathrm{eV}\,, \tag{1.12}$$

which translates to synchrotron radiation of roughly 1 keV energy for 100 TeV electrons in a 5 μG magnetic field (Aharonian, Atoyan, and Kifune, 1997). Note that for any charged particle of mass m, the energy loss rate $\propto 1/m^4$ due to $\sigma_{\mathrm{T}} \propto 1/m^2$. Consequently, lighter particles will produce more intense synchrotron emission via a larger energy loss, implying that electrons will result in several orders of magnitude more energy loss than protons, such that the observed synchrotron radiation is mainly attributed to CR electrons.

1.5.3 Inverse Compton Scattering

The scattering of a photon by a charged particle, usually an electron, is known as Compton scattering, which typically yields an energy loss and gain, respectively, of the photon and electron. The converse process is known as *inverse Compton* (IC) scattering, whereby a high-energy electron scatters off a low-energy photon, such that the latter gains energy while the incident particle loses energy (cf. top right panel of Figure 1.8). Interactions of CR electrons with ambient radiation fields such as the CMB, star light or the infrared

background, may, therefore, scatter photons to much higher gamma-ray energies via such IC processes.

The IC scattering cross-section, σ_{IC}, is defined in terms of the electron energy E_e and initial photon energies of ω_0, and subsequently the ratio $\epsilon_0 = \omega_0/E_e$, using the *Klein-Nishina* (KN) formula (Klein and Nishina, 1929) as follows:

$$\sigma_{\text{IC}} = \frac{3\sigma_{\text{T}}}{8\epsilon_0} \left[\left(1 - \frac{2}{\epsilon_0} - \frac{2}{\epsilon_0^2} \right) \ln\left(1 + 2\epsilon_0\right) + \frac{1}{2} + \frac{4}{\epsilon_0} - \frac{1}{2(1 + 2\epsilon_0)^2} \right] . \qquad (1.13)$$

Note that the rest frame electron energy is $E_e = m_e c^2$, where m_{e} is the electron's rest mass. The ratio ϵ_0 characterises two distinct regimes of IC scattering: $\epsilon_0 << 1$, for non-relativistic electron energies, is the so-called Thomson regime, whilst $\epsilon_0 >> 1$ is referred to as the KN regime.

The energy loss rate via IC scattering in the Thomson regime may be expressed as:

$$-\frac{\mathrm{d}E_e}{\mathrm{d}t} = \frac{4}{3}\sigma_{\text{T}} c U_{\text{rad}} \left(\frac{v}{c} \right)^2 \gamma^2 , \qquad (1.14)$$

where U_{rad} denotes the density of ambient photon fields. The energy loss rate is $\propto E_e^2$ in the Thomson regime, but is independent of E_e in the KN regime. The lifetime of electrons due to energy losses via IC scattering is as follows:

$$\tau_{\text{IC}} = \frac{E_e}{-\mathrm{d}E_e/\mathrm{d}t} \propto \begin{cases} \frac{1}{E_e}, & \text{(Thomson regime)} \\ E_e, & \text{(KN regime)} \end{cases} \qquad (1.15)$$

which implies that higher energy electrons will cool down faster than lower energy ones in the Thomson regime.

For a given population of electrons with energy E_e, IC scattering results in the following characteristic photon energy of:

$$E_{\text{IC}} \simeq 5 \left(\frac{\omega_0}{\text{MeV}} \right) \left(\frac{E_e}{\text{TeV}} \right)^2 \text{GeV} , \qquad (1.16)$$

which implies that IC scattering of 100 TeV electrons off the CMB, with typical photon energy 6×10^{-4} eV, yields photons of approximately 30 TeV (Aharonian, Atoyan, and Kifune, 1997). Assuming that photons up-scattered by synchrotron and IC processes are due to the same parent electron population, we can relate their respective characteristic

energies using equations (1.12) and (1.16) as:

$$\frac{E_{\text{sync}}}{\text{keV}} \simeq 0.07 \left(\frac{E_{\text{IC}}}{\text{TeV}} \right) \left(\frac{B}{10^{-5}\text{G}} \right). \tag{1.17}$$

From equations (1.10) and (1.14), we obtain the following relation between the emitted photon flux due to synchrotron and IC emission, denoted by F_{sync} and F_{IC}, respectively, which depends only on the magnetic field,

$$\frac{F_{\text{sync}}}{F_{\text{IC}}} = \frac{U_{\text{mag}}}{U_{\text{rad}}} \simeq 0.1 \left(\frac{B}{10^{-5}\text{G}} \right)^{-2}. \tag{1.18}$$

The above relation therefore allows us to estimate the magnetic field strength within a particular astrophysical environment, by comparing measured flux, which also implies that synchrotron emission is the dominant component only if the magnetic field strength is higher than 3.2μG threshold. Moreover, as in the case of synchrotron radiation, the mass dependence of the energy loss rate implies that IC scattering of protons will result in ~ 13 orders of magnitude lower energy loss relative to electrons, rendering this process less significant for hadrons. Hence, this is usually referred to as a leptonic scenario of gamma-ray emission.

1.5.4 Pion Decay

The primary process involved in the hadronic scenario of gamma-ray production is the neutral *pion decay* (Ginzburg and Syrovatskii, 1964). Pions are the by-products of proton-proton or proton-nuclei collisions, induced by the hadronic CR particles travelling through the dense interstellar environments. The probability of occurrence of both the charged (π^+, π^-) pions and the neutral (π^0) pion are the same. The threshold energy required to produce neutral pions from protons is ~ 280 MeV. Charged pions decay mainly into muons and neutrinos via the weak interaction, whilst the neutral pions decay by emitting a photon pair, i.e. $\pi^0 \rightarrow \gamma + \gamma$ (cf. bottom right panel of Figure 1.8), with a much shorter mean lifetime of $\tau = 8.4 \times 10^{-17}$s (Martin and Shaw, 2008). In dense regions where protons are relativistic in nature, the pions resulting from the collisions are highly energetic and their decay, therefore, yields VHE gamma-ray emission. If hadronic interactions are dominant in a given astrophysical environment, then the VHE gamma-ray spectrum displays a characteristic "pion bump" at GeV-TeV energies indicative of the hadronic gamma-ray production, as shown in Figure 1.9.

1.5.5 Other Secondary Mechanisms

Electron-Positron Pair Annihilation

An important process at lower energies is the annihilation of electron-positron pairs, i.e. $e^+ + e^- \rightarrow 2\gamma$, which yields an emission line at 0.511 MeV. This process depends on two primary factors: the number density of electrons in the astrophysical medium and the degree of influx of relativistic positrons (Aharonian, 2004).

Nuclear Emission

There are two astrophysical nuclei processes which can lead to gamma-ray production, namely the decay of radioactive nuclei resulting from nucleosynthesis and the de-excitation of nuclei induced by CRs (Kozlovsky, Murphy, and Ramaty, 2002; Diehl, Prantzos, and von Ballmoos, 2006). The characteristic energy of gamma-ray emission of radioactive nuclei, which are expelled by astrophysical objects during explosive nucleosynthesis, is $\sim$ 10-100 MeV per nucleon.

1.6 Acceleration Sites

The acceleration of CRs via the Fermi mechanism, as outlined in Section 1.4, occurs in various known astrophysical environments. A rudimentary but fundamental requirement for CR acceleration was derived by Hillas (1984), whereby the particle's Larmor radius of gyration in the magnetic fields surrounding a given source cannot be larger than the physical size of the source for the particle to be confined. The Larmor radius, in essence, corresponds to the radius of a charged particle's circular motion in a uniform magnetic field. In this framework, the maximum energy (E_{max}) attainable by a particle is given by:

$$E_{\mathrm{max}} = Z\beta_{\mathrm{s}} B L \,, \tag{1.19}$$

for a particle with charge Z, moving with velocity β_{s} in a magnetic field with strength B of an astrophysical object with physical size L. This condition yields the so-called "Hillas plot", illustrated in Figure 1.10, which depicts the distinct acceleration sites and their associated magnetic fields with respect to their physical size. This is an extremely useful tool to characterize the candidates responsible for CR acceleration. According to this plot, the acceleration of CR particles with $E \sim 10^{20}$ eV necessitates an extremely efficient mechanism ($\beta_{\mathrm{s}} \sim 1$) as present in extreme astrophysical systems such as neutron stars, active galactic nuclei (AGNs) and jets of radio galaxies.
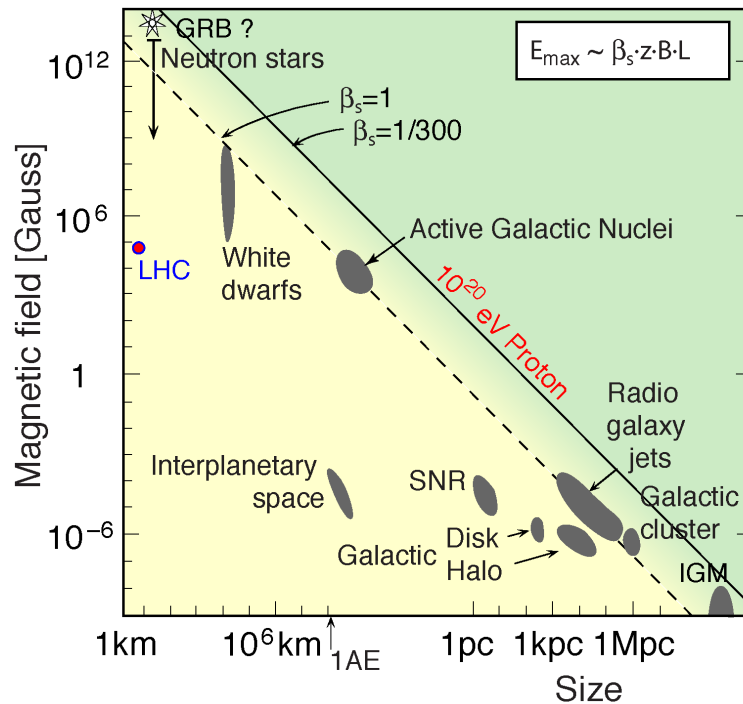
FIGURE 1.10: The *Hillas plot* illustrating the size and magnetic field strength of various astrophysical systems as potential particle acceleration sites. The different lines depict the Hillas condition as the maximum energy attainable for the distinct particle species with respect to source size and magnetic field, with the sources above the lines satisfying this condition. Figure from Blümer and Kampart (2000), which is an adaptation of Hillas (1984).

We now provide a brief description of a series of small and large extended known sources of gamma-ray emission in the following subsections. We provide a list comprising both potential and confirmed sources which could be transients or steady state. Sources of galactic origin are primarily comprised of pulsars and pulsar wind nebulae (PWN), supernova remnants (SNRs) and stellar binary systems, whilst extragalactic sources predominantly include gamma-ray bursts (GRB), active galactic nuclei (AGN) and starburst galaxies.

Supernova Remnants

Supernova remnants (SNRs) are the relics of the explosion of massive stars in supernovae (SNe) and are surrounded by an expanding shock wave resulting from the interaction between the material ejected by the SN explosion and the ISM. The emerging shock front consequently acts as a CR acceleration site, producing VHE gamma-rays with their origin generally thought to be of hadronic nature (Naito and Takahara, 1994; Gaisser, Protheroe, and Stanev, 1998).

Pulsars and Pulsar Wind Nebulae

Pulsars are rapidly-rotating neutron stars with a strong dipole magnetic field, first discovered by Jocelyn Bell in 1967 (Hewish et al., 1968). Such highly magnetised objects induce strong magnetic potentials that are capable of accelerating CRs to UHE to produce VHE gamma-ray emission (MAGIC Collaboration et al., 2008). The interaction of the accelerated particles with their surroundings leads to the formation of the pulsar wind nebula. Subsequent interactions with the ISM produce shocks capable of accelerating particles, such as electrons, to PeV energies, yielding gamma-ray emission via the leptonic scenario. The Crab nebula is an established strong source in the gamma-ray sky as mentioned in Appendix A.

Stellar Binary Systems

There are many known stellar binary systems in the Milky Way, but to date only six of them are known to produce gamma-ray emission, with the latest system (SS 443) recently seen at TeV energies with the HAWC observatory (HAWC Collaboration et al., 2018b). Such systems typically consist of a massive star and a heavy and compact companion such as a neutron star or black hole. Several explanations of the gamma-ray emission have been put forward, as reviewed in (Dubus, 2013), such as the accretion of mass from the massive companion star to produce a jet as a particle acceleration site, or the interaction between the winds of the pulsar and those of the massive star to form a shock where particle acceleration occurs.

Galactic Centre

The Galactic centre (GC) hosts the radio source *Sgr A**, but is also an important gamma-ray source. It has a bright point-like appearance with a diffuse ridge-like emission constituting the surrounding envelope. Recently, it was shown that the GC source accelerates protons to PeV energies (H.E.S.S. Collaboration et al., 2016). The conditions in the GC, with high supernova rates, strong magnetic fields, intense radiation fields, and large amounts of dense molecular gas in the central molecular zone, promote bright gamma-ray emission via interactions between such an augmented ISM and cosmic rays (Yoast-Hull, Gallagher, and Zweibel, 2014).

Central Molecular Zone

Within the inner few parsecs, the GC hosts the galaxy's most active star forming region known as the *Central Molecular Zone* (CMZ).[8] The CMZ extends approximately from

---

[8]More details can be found at `https://web.archive.org/web/20140219030646/http://www.phys.unsw.edu.au/mopracmz/`

galactic longitude 1.7° to −0.7° and ±0.2° in galactic latitude. It consists of 5% of the to-tal molecular content of the Galaxy and is thus prominent in molecular emission which suggests the presence of extensive star formation. The conditions prevailing within the CMZ is quite different compared to molecular clouds, with significantly higher temper-atures, densities and turbulent velocities. According to the Mopra[9] CMZ molecular line mapping survey, typical temperatures are 30 K to 60 K but can rise to 200 K, compared to 10 to 20 K in giant molecular clouds. Moreover, the densities exceed $10^4 cm^{-3}$ through-out, and turbulent velocities are as high as 15 to 50 km/s compared to $\sim$ 5 km/s in giant molecular clouds. Thus, the CMZ is a strong source of gamma-ray emission.

Diffuse Emission

The interaction of leptonic and hadronic CRs with the gas of the ISM and photon fields yields the galactic diffuse gamma-ray emission (Aharonian et al., 2008; Fermi-LAT Col-laboration et al., 2012) via mechanisms such as pion decay, bremsstrahlung and inverse compton scattering. This diffuse emission is the primary constituent of the gamma-ray sky in the energy range of 200 Mev to 100 GeV, as seen with *Fermi*-LAT, thereby allowing us to probe the distribution and propagation of CRs in the Milky Way.

Giant Molecular Clouds

There is an approximately uniform distribution of atomic (HI) hydrogen in the Milky Way, with a higher concentration in the Galactic plane, while molecular hydrogen (H_2) is generally clustered in dense clouds. As outlined in Section 1.4, the inelastic scattering of hadronic CRs off the gas of the ISM produces gamma-ray emission. As such, molecular clouds are potentially a source of particularly intense and localised gamma-ray emission in the presence of hadronic CRs. Giant molecular clouds can also be considered as a form of diffuse emission, providing a means to study the galactic CR flux and distribution in distant regions of the galaxy (Casanova et al., 2010; Yang, de Oña Wilhelmi, and Aharo-nian, 2014).

Massive Stellar Clusters

The formation of massive stars within giant molecular clouds often end as dense gravita-tionally bound stellar clusters (Williams, Blitz, and McKee, 2000). With most ($\sim$ 70%) of the massive stars are bound in binary systems (de Mink et al., 2014), the interactions re-sult in colliding wind binaries, which, along with collective stellar winds and supernova explosions within stellar clusters, are potential CR acceleration sites.

---

[9]The Mopra Telescope is a radio telescope located about 450 km north-west of Sydney, Australia.

Fermi **Bubbles**

Fermi bubbles are large structures emanating from the central region of our galaxy, which have been detected with *Fermi*-LAT gamma-ray instrument in the MeV range (Su, Slatyer, and Finkbeiner, 2010). These bubble-like structures have motivated various studies and simulations to shed some light on their origin and gamma-ray production mechanisms. A search for these bubbles and other large-scale structures at TeV energies constitutes a significant part of this thesis, and as such, the *Fermi* bubbles are described and discussed in depth in Chapter 7.

Gamma-ray Bursts

Gamma-ray bursts (GRBs), while relatively short-lived, constitute some of the most spectacularly bright extragalactic objects in the sky, as a result of extremely energetic gamma-ray outbursts. They have long been proposed as highly probable sites of CR acceleration (Vietri, 1995; Waxman, 1995) and are classified as short (< 2s) and long (> 2s) duration GRBs. The origin of this dichotomy stems from the physical mechanisms responsible for the energetic emission, respectively, through the merger of two compact objects or the hypernova explosion of a very massive star. In all scenarios, there is an initial almost instantaneous emission of gamma-rays, followed by an eventual afterglow emission across the EM spectrum (Kumar and Zhang, 2015). For instance, GRB 190114C was observed at TeV energies (MAGIC Collaboration et al., 2019) and GRB 180720B at hundreds of GeV (H.E.S.S. Collaboration et al., 2019a).

Active Galactic Nuclei

Galaxies with a central nucleus as the brightest region of the galaxy, hosting a supermassive black hole, are known as active galactic nuclei (AGNs). Past observations have shown powerful collimated jets of relativistic charged particles emanating from the central galactic region, resulting in non-thermal emission in radio to gamma-rays (Fabian, 2012; Netzer, 2015) and can be further categorised as blazars, radio galaxies and quasars, depending on the viewing angle.

Starburst Galaxies

The distinctive feature of starburst galaxies is an exceptionally high star-formation rate, which consequently yields a high SN explosion rate, in turn leading to a high CR density. These CRs are then responsible for producing VHE gamma-ray emission (Ohm, 2016; Owen et al., 2019). Such galaxies are also observed to drive powerful nuclear outflows

(or "magnetised winds"), which are potential sites of high-energy particle acceleration (Anchordoqui, Romero, and Combi, 1999).

Galaxy Clusters

Galaxy clusters, as the largest bound objects in the Universe, have inevitably been considered as plausible sites of CR production (Kang, Rachen, and Biermann, 1997; Ryu et al., 2003). Despite their moderate magnetic fields, they are extended over several Mpc, such that they are capable of confining particles to extremely high energies (Fang and Olinto, 2016). Galaxy clusters may also host sites of CR acceleration, such as AGNs with jets (Murase, Inoue, and Nagataki, 2008; Kotera et al., 2009; Fang and Murase, 2018).

2

Ground-based Particle Detection Techniques for Very High Energy Gamma-ray Astronomy

This chapter describes the essential aspects of ground-based particle detection techniques. In the following section, we review the physics of extensive air showers (EAS) and outline the key observables as relevant to this thesis. The remainder of this chapter is then organised as follows: The production of muons in the atmosphere, which leaves a distinct observational footprint, is covered in Section 2.1.3. We then describe the particular characteristics of hadron-induced air showers, in contrast to gamma-ray initiated counterparts, in Section 2.1.2. The following Section 2.2 elaborates on the processes involved in atmospheric shower physics, with the last part of this chapter, Section 2.3, providing a description of the various ground-based detection methods.

2.1 Extensive Air Showers

Since gamma-rays interacts with the Earth's atmosphere, the observation of gamma-rays from the ground must inevitably rely on indirect detection methods. The interaction of highly energetic primary gamma-ray photons or CR particles with the nuclei present in the atmosphere initiates a cascade of particle collisions, scattering and decay interactions, resulting in secondary particles. This cascade process is known as *extensive air showers*

(EAS) and is a crucial aspect of ground-based observations. Different methods, as explained in the sections below, can be employed to reconstruct the properties of the EAS detected in order to determine the nature, energy and direction of the primary particle.
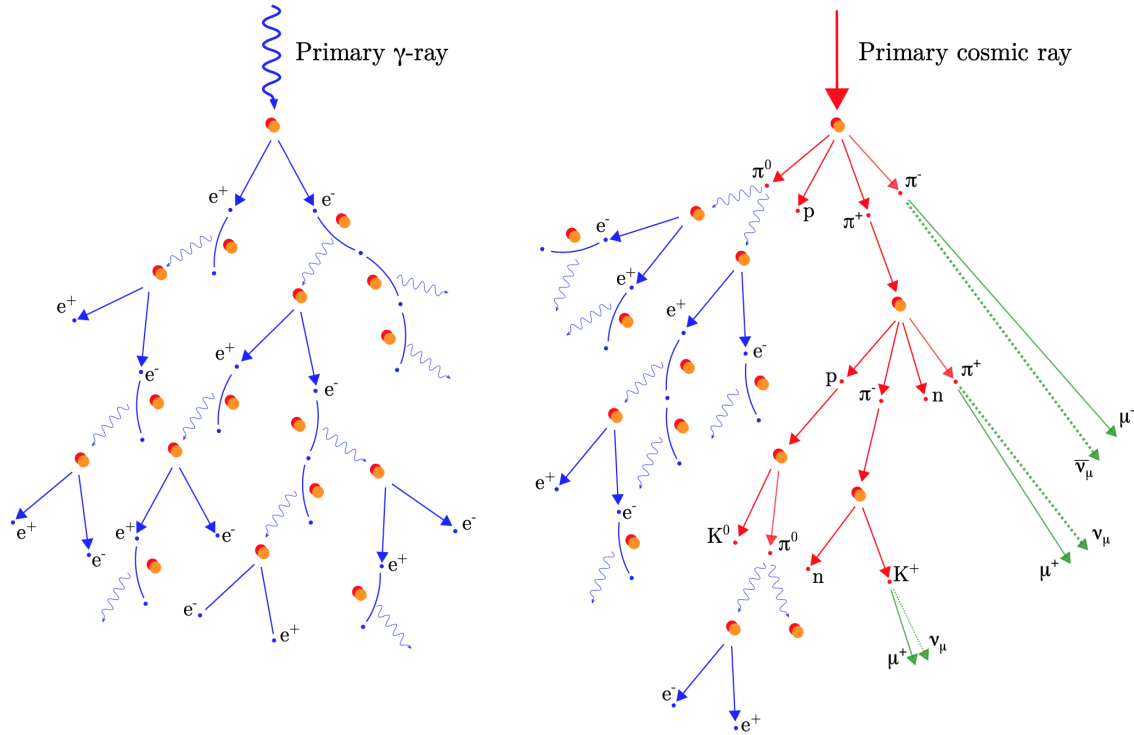
FIGURE 2.1: Schematics of a gamma-induced shower (*left panel*) and proton-induced shower (*right panel*). Figure from Jardin-Blicq (2019).

2.1.1   Electromagnetic Showers

EAS may be broadly classified as hadronic or electromagnetic (EM) showers, depending on whether they were initiated by a charged hadronic particle (proton-dominated, cf. Section 2.1.2) or an energetic photon or lepton (both electrons and positrons), respectively, as illustrated in Figure 2.1. EM showers induced by either gamma-ray photons or leptons are nearly identical, with the sole difference being the average height of first interaction. Leptons (mostly electrons) will interact at earlier times than gamma-ray photons of similar energy since the former have a larger interaction cross-section.

The principal physical mechanisms driving the development of an EM air shower are bremsstrahlung (cf. Chapter 1.5.1), pair production (cf. Section 2.2.1 below), Compton scattering and photo/electro-nuclear interactions. For production of secondary particles through pair production to occur, usually in the vicinity of a nucleus, the original energy of the gamma-ray photon should exceed the sum of the rest mass energy of the electron-position pair, i.e. $E_\gamma > 2m_\mathrm{e}c^2 \sim 1.02$ MeV. The production of secondary photons occurs
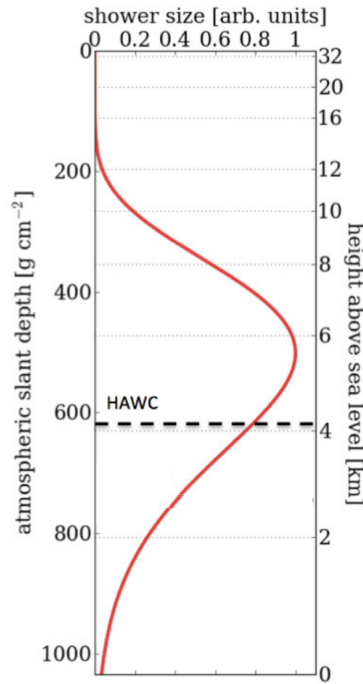
FIGURE 2.2: Variation of shower size of a typical TeV gamma-ray air shower with height above sea level. The horizontal dashed line indicates the altitude of the HAWC observatory. Figure reproduced from S. BenZvi.

via bremsstrahlung emission of a charged particle deflected when moving through the Coulomb field of a nucleus. This process is defined by a particular length scale, X_0, known as the *radiation length*, encoded in the following relation between the particle energy and the column density, x in g/cm^2, covered:

$$E(x) = E_0 e^{-x/X_0} , \tag{2.1}$$

where E_0 is the original energy of the primary particle. As such, X_0 is the distance covered by an electron, after which its initial energy is reduced by a factor of $1/e$. The typical value for electrons emitting bremsstrahlung radiation in air is $X_0 \sim 37 - 38$ g/cm^2, while for the mean free path for photons undergoing pair production is $X_{0,\gamma} = 9/7 X_0$.

A simplified model of shower developement is the *Heitler* model (Bhabha and Heitler, 1937), which encodes three basic assumptions (Matthews, 2005):

- The radiation length of bremsstrahlung and pair production are the same;

- Bremsstrahlung and pair production are the only dominant mechanisms;

- Energy is distributed equally among the secondary particles (or gamma-ray photons) at every step.

The earliest interaction of an air shower occurs typically at an altitude of around 10-20 km above sea level (a.s.l). The development of the shower entails the production of secondary particles, such that the shower expands along the forward (or longitudinal) direction. As a result of scattering and particle decays with transverse moment component, the lateral distribution of the shower also widens. The shower size is dictated by the energy of the primary particle, the incident zenith angle and the height of the initial interaction. The maximum depth of shower development, X_{max}, measured from the uppermost layer of the atmosphere, gets deeper with increasing energy.

According to the above Heitler model, an interaction occurs once per radiation length, with the number of particles as a function of distance travelled given by $N(x) = 2^{x/X_0}$, where each particle has an energy of $E(x) = 2^{-x/X_0} E_0$. The number of secondary particles rises until it attains the maximum shower depth in the atmosphere at:

$$X_{\text{max}} = \frac{\ln E_0/E_c}{\ln 2} X_0 \,, \tag{2.2}$$

where $E_c \sim 80$ MeV corresponds to the critical energy, at which the energy losses due to bremsstrahlung and ionisation are the same. After attaining X_{max}, the shower size is gradually reduced due to the ionisation losses. The profile of shower size (or number of particles) as a function of height above sea level is illustrated in Figure 2.2, which shows that HAWC collects particles close to the shower maximum for ~ 1 TeV gamma-ray induced vertical showers.

The length scale for the lateral distribution of different types of particles is quantitatively characterised by:

$$r = \frac{x}{\rho} \frac{E_s}{E_c} \,, \tag{2.3}$$

where E_s denotes the transverse energy scale, and ρ corresponds to the density of the atmosphere at a given height. For EM showers, the most commonly adopted length scale for the lateral distribution of secondary particles is the so-called *Molière radius*, r_{M}, obtained by substituting x by X_0, the radiation length. In essence, the Molière radius characterises the scale of the transverse dimension of the EAS, with this radius containing on average 90% of the energy deposited by the shower. The Molière radius, at the altitude of HAWC (4 100 m a.s.l), is ~ 124 m, using the following typical values of the relevant quantities in the above equation: $X_0 = 36.08$ g/cm^2, E_c in air ~ 84 MeV, $E_s = \sqrt{4\pi/\alpha} m_e c^2 \sim 21$ MeV, $\rho_{\text{air}} \sim 7 \times 10^{-4}$ g/cm^3 (at the altitude of HAWC).

The direction of the incident primary particle, extrapolated to ground level, defines the *shower axis*, around which the development of the EAS is centered. The secondary particles produced in the shower lie in concentrated regions close to the shower development axis. The largest amount of energy is, hence, deposited at the intersection of the shower
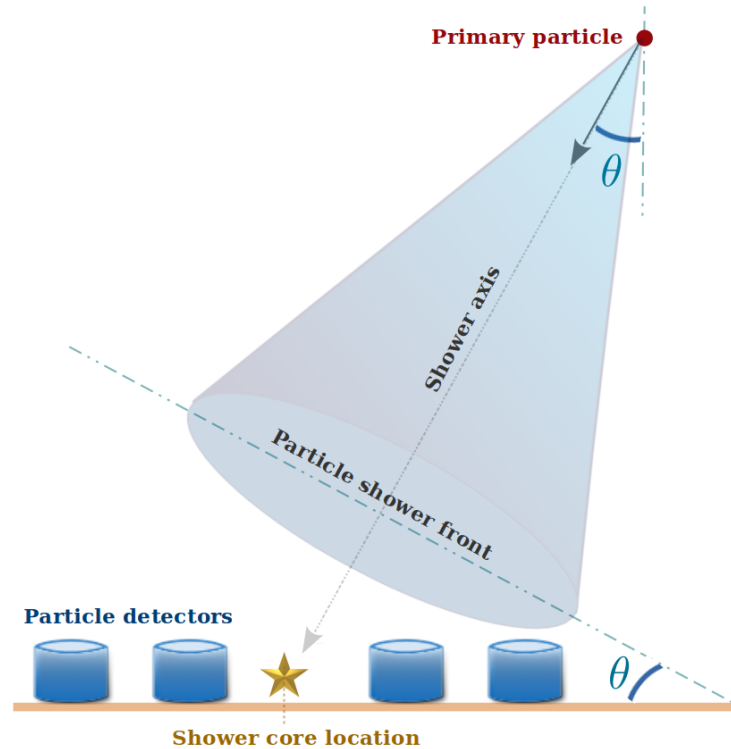
FIGURE 2.3: Schematic of an EAS, illustrating the interaction of a primary particle with the Earth's atmosphere, which subsequently leads to a shower of secondary particles as depicted by the resulting Cherenkov flash cone in the particle shower front. The intersection of the shower axis, where the incoming zenith angle is denoted by θ with the ground defines the core location indicated using a golden star.

axis with the ground, with this location defined as the *core* of the air shower. A schematic of an EAS depicting the shower axis and core location is illustrated in Figure 2.3. To determine the direction and energy of the primary particle initiating the air shower, a crucial step is core reconstruction, i.e. estimating the core location of the EAS. The evolution of the longitudinal distribution of the EAS around the shower axis depends on the type of the primary particle, such that this property can be used to distinguish between EM and hadronic showers, as elaborated in Section 2.1.2.

The lateral distribution of the secondary particles from the EAS depends on the type and energy of the primary particle, and is usually characterised by the lateral distribution function (LDF). In particular, the LDF of a given air shower event describes the observed charge distribution as a function of distance from the shower axis, commonly referred to as the impact distance. An analytical approximation to the LDF is given by the so-called *Nishimura-Kamata-Greisen* (NKG) function, which depends on key parameters such as shower age and shower size, as detailed in Appendix A.

2.1.2   Hadronic Showers

In the hadron-induced showers, the early phase of the shower development involves primarily strong interactions between the primary CR particle and the nuclei present in the atmosphere. The major fraction of the secondary products consists of mesons (typically pions and kaons, cf. Section 2.1.3), which subsequently decay into muons. The latter constitutes a penetrating component of the shower. The transverse component of the momentum transferred to the secondary particles produced in such interactions exceeds that in EM interactions (usually Coulomb scattering). Moreover, the presence of hadronic particles in hadron-induced showers yields several sub-showers.The vast majority of EAS are not initiated by VHE gamma-rays but by hadronic CR particles.Fortunately, this undesirable hadronic background may be mitigated by exploiting the inherent contrasting characteristics of lepton- and hadron-induced EAS.

As a result of the above two factors, a hadron-induced EAS displays a substantially larger lateral spread, which is also reflected in the properties of the Cherenkov signal, such as the particle arrival time and lateral distribution, observed on the ground. In contrast to the irregular distribution of the Cherenkov light for a hadronic shower with several light pools,[1] the Cherenkov emission emanating from an air shower initiated by a VHE gamma-ray has an arrival time within a few nanoseconds at a particular radial distance from the shower core. A gamma-induced shower, therefore, yields a single regular light pool which is much more concentrated around the shower axis. The respective characteristic signatures of gamma and hadronic showers are illustrated in Figure 2.4. The discrimination of VHE gamma-ray events from hadronic ones is usually referred to as *gamma-hadron separation*, and this constitutes the crux of Chapter 4 and is described partially in Section 3.6 in Chapter 3.

2.1.3   Atmospheric Muon Production

A substantial component of the background events observed by a Cherenkov detector, both by IACTs and WCDs, is composed of relativistic muons producing Cherenkov light. The production of muons occurs predominantly in hadronic air showers from incident CRs, at the first interaction height. When these primary CRs interact with the atmosphere, such charged particles fragment into smaller nuclei to produce charged mesons, such as pions and kaons. The latter mesons subsequently decay to form atmospheric muons,

---

[1]Cherenkov light pool is explained in Section 2.2.2.

Proton (5 TeV)   Photon (1 TeV)

charged particles

Cherenkov light and particles on ground
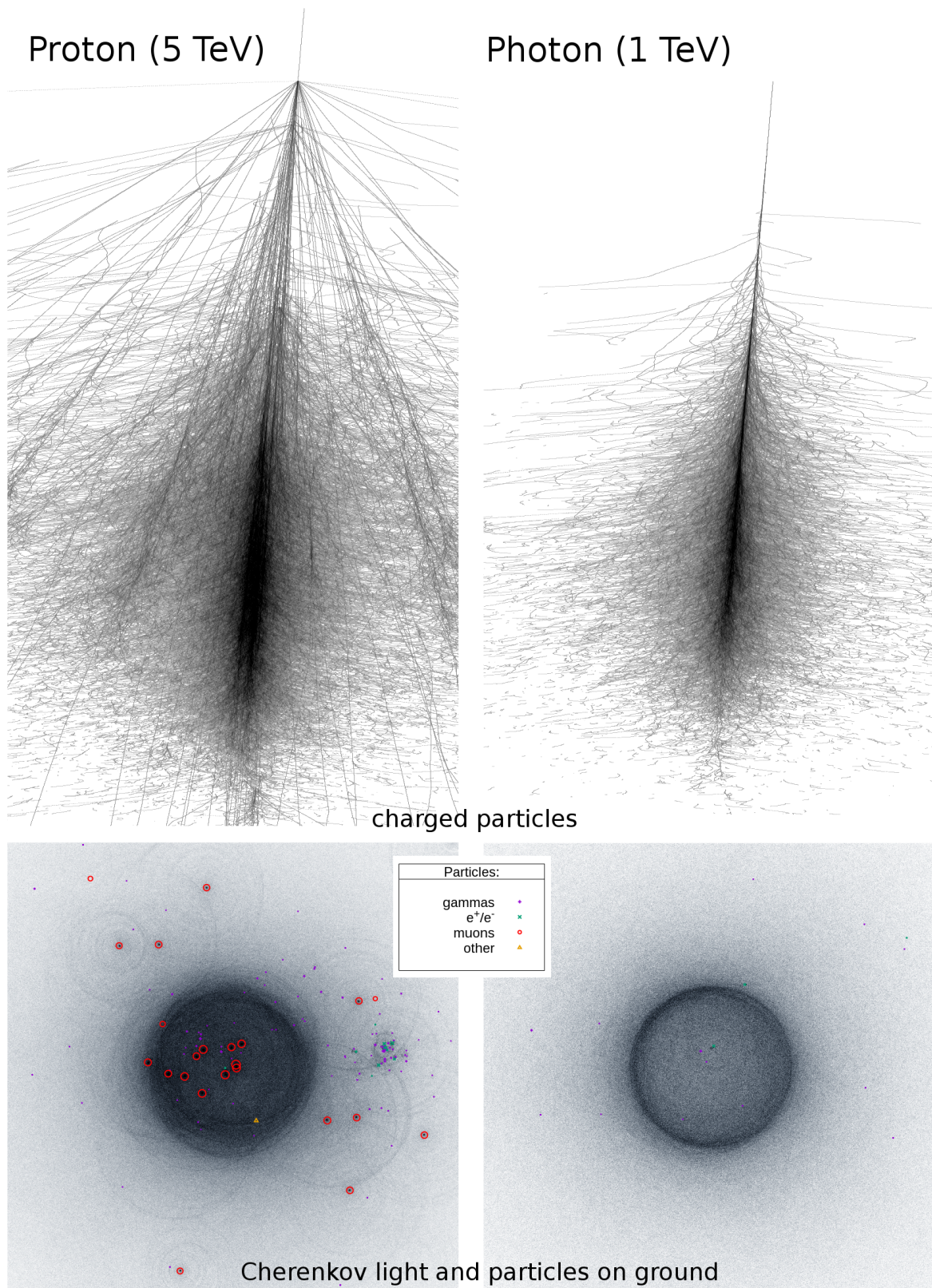
FIGURE 2.4: Contrast between the longitudinal (*top panels*) and lateral (*bottom panels*) distributions of electromagnetic (*right panels*) and hadronic showers (*left panels*). The primary distinctive features of the hadronic shower are the presence of several sub-showers, resulting in a significantly larger lateral spread. Figure from Bernlöhr (2018).

primarily via the following decay chains:

$$\pi^{\pm} \rightarrow \mu^{\pm} + \nu_{\mu}(\bar{\nu}) \qquad\qquad (\sim 100\%) \qquad\qquad (2.4)$$

$$K^{\pm} \rightarrow \mu^{\pm} + \nu_{\mu}(\bar{\nu}) \qquad\qquad (\sim 63.5\%) \qquad\qquad (2.5)$$

with their corresponding branching ratios indicated in parentheses. The lifetime of muon decay is $\simeq 2.2 \times 10^{-6}$ s, which is sufficient for relativistic muons to reach the ground, unlike for their non-relativistic counterparts (Martin and Shaw, 2008). Muons constitute a penetrating component of EAS, travelling for longer duration and covering larger distances between two successive scattering interactions. Highly energetic muons maintain the light cone structure around their direction of propagation and they typically possess a significantly large transverse momentum component, therefore they can be separated with relative ease from the parent air shower. This is in stark contrast to heavier charged leptons which have a much faster decay rate and also lighter leptons which are blended with other shower constituents and thus much harder to isolate.

2.2 Processes in Atmospheric Shower Physics

This section describes the crucial processes involved in atmospheric shower physics, pair production and Cherenkov light production, respectively.

2.2.1 Pair Production

The interaction of a photon with the Coulomb field of a nucleus results in the production of electron-positron pairs in a process known as *pair production*, $\gamma \rightarrow e^+ + e^-$. This process can only occur at energies higher than the sum of the rest masses of the respective electron and positron (1.02 MeV). Most of the remainder of the energy is then shared between the two leptons in the form of kinetic energy, with the momentum conservation accounted for by the nucleus.

2.2.2 Cherenkov Light Production

The propagation of a charged particle through a dielectric medium, such as air or water, results in *Cherenkov radiation*. The first discovery of this effect was made by Pavel Cherenkov (Cherenkov, 1934), which eventually led to him being awarded the Nobel Prize in physics in 1958. The motion of the charged particle induces a net polarisation in the medium due to the surrounding atoms and molecules moving accordingly to compensate for its presence. This results in a net dipole field in the medium around the
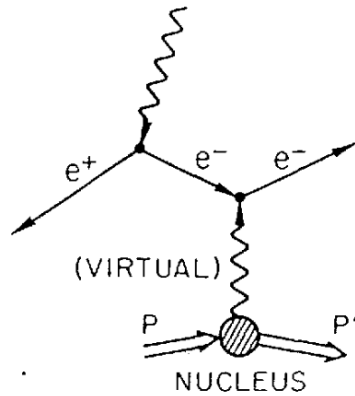
FIGURE 2.5: Schematic of pair production process. Diagram adapted from Donahue and Nelson (1991).
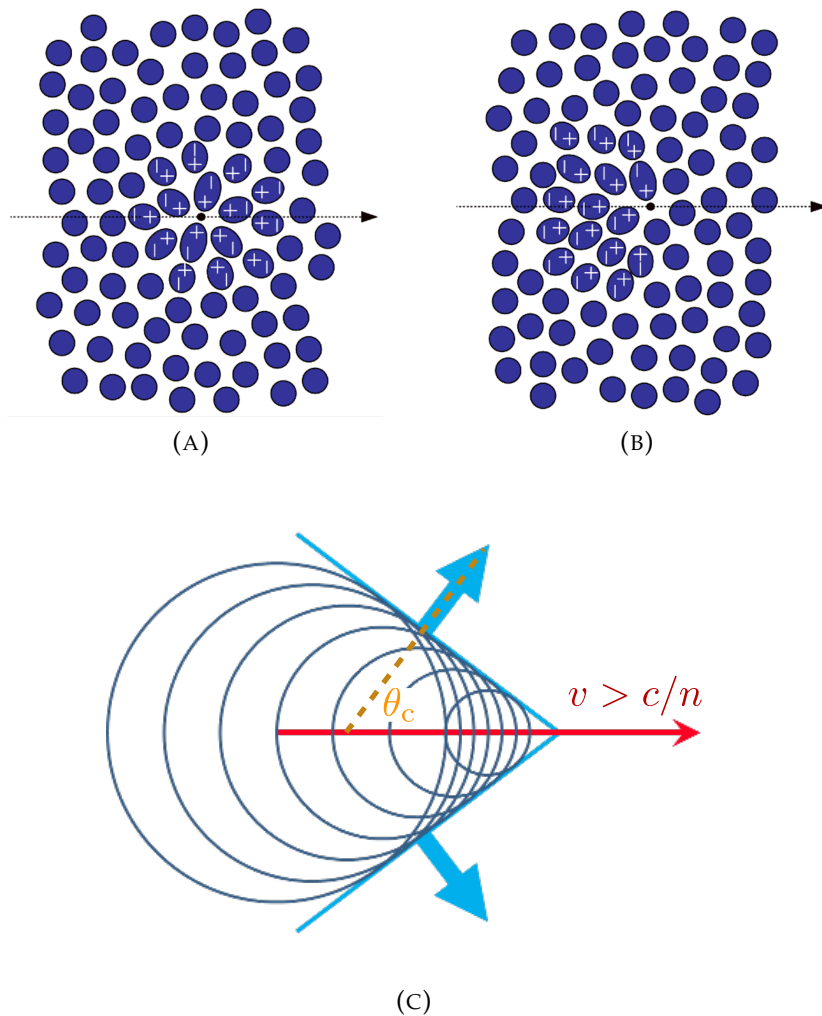
FIGURE 2.6: *Panels* (A) and (B) depicts the passage of a charged particle through a medium; (A) is the case where $v < c/n$ and (B) is the case where $v > c/n$. *Panel* (C) is a schematic illustrating the production of Cherenkov radiation at an angle θ_c to the trajectory of the charged particle moving with speed v. The coherent addition of the emission forms a conical wavefront which moves outwards.

particle. The former subsequently relaxes once the particle has passed, leading to the occurrence of dipole transitions, which are responsible for the emission of EM radiation. If the charged particle is sufficiently energetic, it will travel faster than the phase velocity of light in that medium, such that, in accordance with Huygen's construction, the radiation will add coherently along an angle θ_c, as illustrated in Figure 2.6. In the case of non-relativistic particles, however, there is the destructive interference of the EM radiation produced from the particles.

The energy of secondary particles in EAS is sufficiently high for them to be relativistic, with their velocity v exceeding that of light in the medium, $c_{\mathrm{medium}} = c/n$, where n denotes the refractive index of the medium and c is the speed of light in vacuum. The overall collection of the Cherenkov radiation emitted by each particle around its trajectory yields Cherenkov emission in a cone along the shower axis, with an opening angle θ_c of:

$$\cos \theta_c = \frac{c}{vn} \ . \tag{2.6}$$

A particle of mass m_0 should have a threshold energy, E_{min}, to emit Cherenkov radiation, which is given by:

$$E_{\mathrm{min}} = \gamma_{\mathrm{min}} m_o c^2 = \frac{m_0 c^2}{\sqrt{1 - n^{-2}}} \ , \tag{2.7}$$

where γ_{min} is the corresponding Lorentz factor of the moving charged particle. Thus, less massive particles will have a lower threshold energy and consequently are the dominant component of Cherenkov radiation. The number of photons produced per unit wavelength λ by an ultrarelativistic particle, as a function of distance covered x, is characterised by the *Frank-Tamm* formula (Frank and Tamm, 1937):

$$\frac{\mathrm{d}^2 N}{\mathrm{d}x \mathrm{d}\lambda} = 2\pi\alpha Z^2 \lambda^{-2} \left(1 - \frac{1}{\beta^2 n^2(\lambda)}\right) \ , \tag{2.8}$$

with $\alpha \approx 1/137$ being the fine structure constant, while Z is the particle charge. The above formula, by virtue of the wavelength dependence, also describes the peak of Cherenkov emission, typically occurring in the range of blue to ultraviolet wavelengths. The emitted and observed Cherenkov spectra are different because of attenuation from Rayleigh scattering with air molecules, aerosols and so on as illustrated in Figure 2.7.

Cherenkov radiation generated by an EAS occurs in a cone along the shower axis to produce an illuminated area on the ground, usually referred to as the *Cherenkov light pool*, which typically lasts a few nanoseconds, roughly the duration of the air shower. The edge of the light pool is defined by the overall cone produced along the shower axis, corresponding to the collective sum of the individual emissions. The fuzzy edge (cf. Figure 2.4) and the filled interior of the ring on the ground are due to the shower
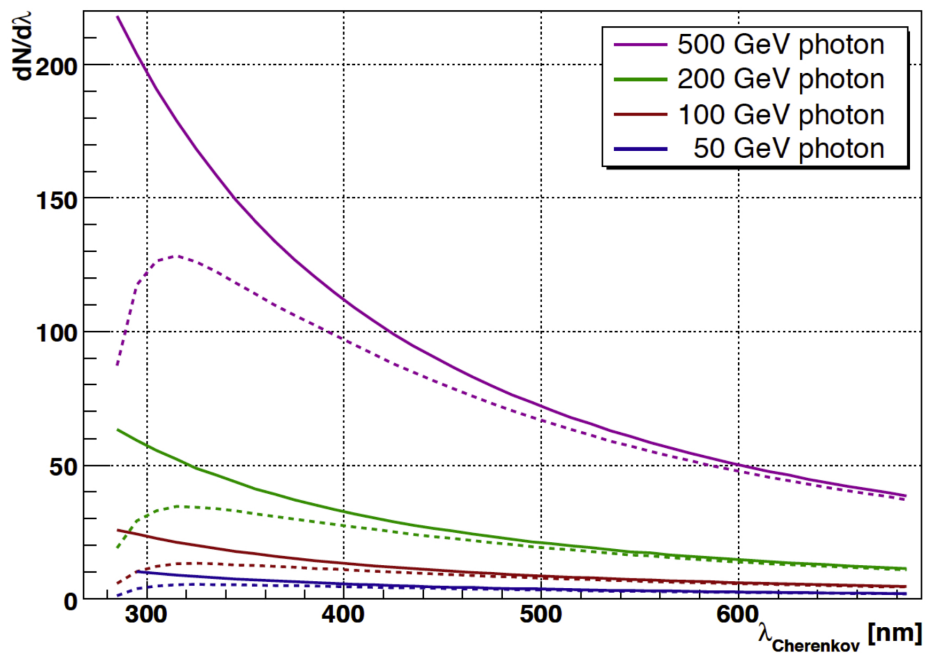
FIGURE 2.7: Cherenkov spectra for gamma-ray showers of different initial energies. The solid lines correspond to the emitted spectra at 10 km height while the dashed lines correspond to detected spectra at 2.2 km a.s.l. Figure from López-Coto (2015).

particles being scattered around the shower axis, thereby producing Cherenkov emission at slightly varying angles with respect to the shower axis. The refractive index n of the atmosphere is related to the height h via:

$$n(h) = 1 + n_0 \exp^{-h/h_0} , \qquad (2.9)$$

where $h_0 = 7250$ m and $n_0 = 0.000\,29$. The above height dependence of the atmospheric refractive index causes θ_c and $E_{\min}$ to vary with height (cf. equations (2.6) and (2.7), respectively). As a consequence, the radius of the Cherenkov light pool will depend on the height of original emission and on the altitude at which the detection is made.

2.3 Detection Methods

This section describes the two main techniques for the observation of EAS, which rely, to a great extent, on the Cherenkov radiation (cf. Section 2.2.2) emitted by charged particles. A summary of a comprehensive overview of the various ground-based observational techniques pertaining to EAS is illustrated in Figure 2.8. Space-based detection methods, including a brief historical account, were outlined in Chapter 1.2.2. Charged particles also produce light through *fluorescence* whereby atoms absorb photons of one wavelength

First collision (usually several 10 km high)

Particle cascade developing

Only very few of the particles make it to the ground due to energy loss and decay

Measurement of Cherenkov light with telescopes

Measurement of fluorescence light

Measurement of particles with scintillation counters or water Cherenkov counters

Non−imaging Cherenkov counters

Measurement of particle tracks in Cosmic Ray Tracking detectors

Measurement with Geiger−Müller counters

Low−energy muons after a few meters of shielding

High−energy muons measured deep under ground (or in water or ice)

Measurement of radio waves

FIGURE 2.8: Schematic illustrating the various detection techniques of signals emanating from EAS. Figure adapted from Bernlöhr (2018).

and emit photons at a longer wavelength. With fluorescence detectors, the longitudinal development of EAS can be studied. Lastly, air showers composed of moving charged particles generate coherent radio emission which has two origins: A charge excess mechanism and deflection by the geomagnetic field. Using antennas and fast data acquisition systems, the radio signals can also be used to infer information obtained about the EAS.

2.3.1 Imaging Atmospheric Cherenkov Telescopes

The direct observation EAS is possible via the measurement of the number, energy and type of particles within the shower. A particularly key approach is the so-called *imaging atmospheric Cherenkov technique*, which we briefly review in this section. An EAS illuminates an area on the ground, as outlined in Section 2.1 above, with the light emanating from different heights within the air shower displaying a slight variation in emission angle. This light may then be reflected by telescopes with large mirror dishes onto an imaging camera in the focal plane. Such cameras should possess fast recording capability as the typical duration of an EAS is $\sim \mathcal{O}(10 \text{ ns})$ in order to distinguish the weak transient signal from the night sky background[2] flux. The reflection angle will depend on the incident angle, which implies that light from distinct regions of an EAS will have

---

[2]The night sky background is airglow with emission lines mostly from atomic oxygen, hydroxide and sodium in the atmosphere.
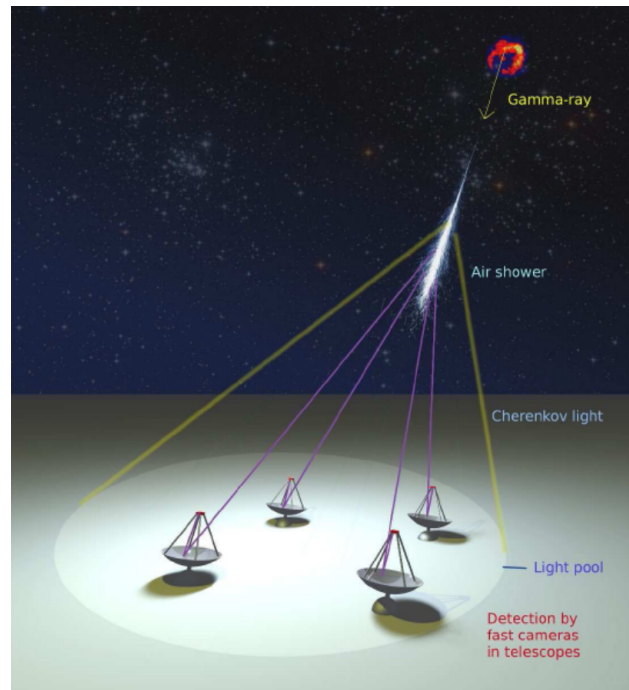
FIGURE 2.9: Schematic depicting the operation of an IACT. The Cherenkov light pool produced in the atmosphere, originating from a primary gamma-ray, illuminates an array of imaging telescopes on the ground. Figure from Antonelli et al. (2009).

varying reflection angles. As such, an EAS induced by gamma-ray photon will produce a characteristic elliptical image which is recorded by the camera. In comparison, hadronic showers will produce irregular images by virtue of the presence of sub-showers and massive secondary particles (cf. Figure 2.4). As a consequence of the relativistic nature of the particles, the secondary particles produced move along trajectories which deviate slightly from that of the primary particle in EM showers. The use of such images from an array of IACTs allows the reconstruction of the direction of the shower axis from the Cherenkov light emitted by the secondary particles.

The above technique is employed by Imaging Atmospheric Cherenkov Telescopes (IACTs). The historical development of IACTs, including various examples, such as the currently operating H.E.S.S. (Hofmann, 2000), MAGIC (Baixeras, 2003) and VERITAS (Weekes et al., 2002), and the forthcoming CTA (Cherenkov Telescope Array Consortium et al., 2019), is reviewed in Chapter 1.2.3.

2.3.2 Air Shower Particle Detector Arrays

Another class of detection methods involves the detection of the secondary particles produced in an EAS. This has led to the development of ASPD arrays, which are complementary to the IACTs, as highlighted in the following section. Such arrays are deployed
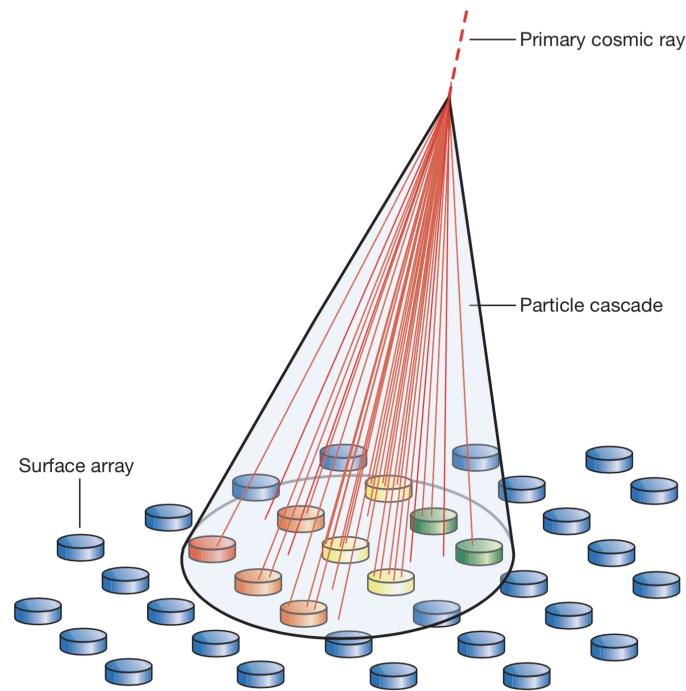
FIGURE 2.10: Schematic illustrating the operation of an ASPD array. The cascade of secondary particles are indicated as the solid red lines within the cone. An array of Cherenkov particle detectors on the ground detects the arrival of the particles, which allows shower reconstruction to be performed. The cascade footprint at ground level may extend over tens of square kilometres. Distinct colours in the schematic indicate different arrival times of the particles, here, green denotes first arrival. Figure from Bauleo and Rodríguez Martino (2009).

at high altitudes to maximise the collection of particles by being close to the maximum shower depth (cf. Section 2.1). A schematic of such an array of ASPDs is illustrated in Figure 2.10.

The Cherenkov effect occurs in any medium, which is denser than vacuum and transparent to UV-optical light. This property has been exploited using water by various experiments, resulting in Water Cherenkov Detectors (WCDs). Photomultiplier tubes (PMTs) are used to detect the Cherenkov light produced by the secondary particles in water. The shower properties are subsequently estimated from the time and charge information of the signal recorded by the PMTs. Another method to detect the secondary particles involves scintillation counters, where PMTs are used to detect the light from scintillation.

An example of a WCD currently in operation is HAWC (HAWC Collaboration et al., 2013), which is the most relevant in the context of this thesis, and is described in depth in Chapter 3. An upcoming WCD is the Southern Wide-Field Gamma-Ray Observatory (SWGO, SWGO Collaboration et al., 2019), a next-generation instrument with sensitivity to the VHE band which will provide wide-field coverage of a significant fraction of the

southern sky. A brief historical overview pertaining to the development of ASPD arrays is outlined in Chapter 1.2.3.

2.3.3 Complementarity of Ground-based Detection Techniques

The two broad classes of ground-based detectors, as outlined in the two previous sections, are, nevertheless, complementary to each other in various aspects:

- *VHE range* - IACTs are suited for observations in the range of few tens of GeV to tens of TeV (50 GeV - 50 TeV), whilst ASPD arrays are more effective at few TeV to few hundreds of TeV (1 TeV - 100 TeV);

- *Angular and energy resolution* - IACTs have both a higher angular and energy resolution than ASPD arrays, such that the former are more suitable for spectral and morphological studies. For instance, at a median energy of 2 TeV, HAWC has an angular (energy) resolution of $0.4°$ (~ 1.4) while that of H.E.S.S. is $0.1°$ (< 0.15);

- *Duty cycle* - IACTs, being optical instruments, are limited to operating only in dark nights (with moonlight also being a nuisance), whereas ASPD arrays have a nearly 100% duty cycle, such that they are ideal for surveying purposes;

- *Field of view (FoV)* - IACTs have a limited FoV but an enhanced pointing capability, such that they are better suited for deep observations. But to observe extended sources, the wide FoV of ASPD arrays is better suited.

In a nutshell, both classes of techniques are essential for an extensive and thorough observation of the gamma-ray sky and they have both played a key role in detecting a rich gamma-ray source population (e.g. Di Sciascio, 2019b).

3

High Altitude Water Cherenkov (HAWC) Gamma-ray Observatory

The High Altitude Water Cherenkov (HAWC) gamma-ray observatory is an Air Shower Particle Detector (ASPD), located at an altitude of 4 100 metres a.s.l., close to Pico de Orizaba, Mexico, with the coordinates being 97.3°W and 19.0°N. HAWC was inaugurated in March 2015 and the HAWC Collaboration consists of over 100 scientists from institutions in Costa Rica, Germany, Mexico, Poland, and the United States. HAWC consists of an array of water tanks that function as Water Cherenkov Detectors (WCD) designed to operate in the gamma-ray energy range of 100 GeV to 100 TeV. HAWC comprises of a main array of densely packed steel tanks and a sparser array of outrigger plastic tanks as shown in Figure 3.1.

This chapter is structured as follows: Details of the WCDs, more specifically, the rationale underlying their configuration and instrumentation are described in Section 3.1. The details of the data-acquisition system are laid out in Section 3.2. Calibration and performance are described in Section 3.3. The outrigger array was fully deployed by end of 2018 and its operation integrated that of the main array by mid 2019. Hence, this thesis involves work done using the main array only, which will be described in more details. Nevertheless, a brief summary for the outrigger array is provided in Section 3.4 for the sake of completeness. The significance of Monte Carlo simulations is highlighted in Section 3.5. Finally, in Section 3.6, we present the effects of simulated showers (gamma-ray and proton initiated) on the lateral distribution of muons detected with a HAWC-like instrument. The incoming particle energies, zenith angles and altitudes of the detector were

varied one at a time, with the results presented and discussed.

FIGURE 3.1: HAWC main and outrigger array. The Electronics building for data and acquisition lies at the centre of the main array.

3.1   Water Cherenkov Detectors

HAWC employs the water Cherenkov method to sample the secondary particles of EAS originated from high-energy gamma rays and cosmic rays. An array of 300 corrugated steel tanks, that would function as WCDs, were built on an area of approximately $22\,000\,\text{m}^2$ of pre-flattened land with a total filling factor of 60%. These tanks make up the HAWC main array, each of which are 7.3 m in diameter and 5 m in height. As shown in the left panel of Figure 3.2, each tank contains a light-tight bladder which holds approximately 188 kL of initially purified water. Only 294 tanks were instrumented with photomultiplier tubes (PMTs) which are anchored at fixed positions to the bottom of the bladder.

The width of the WCD was chosen based on the depth of the water body, ensuring that the PMT response is uniform as a function of radius out to the edge of the WCD. The right panel of Figure 3.2 depicts a schematic of the tank dimensions. Cherenkov radiation is relatively efficient in water due to its high refractive index. The emitted Cherenkov light forms a light cone with an opening angle of 41°. Moreover, water is transparent to photons over the operating range of the PMTs.

The actual height of the water body amounts to 4 m only. The tank height is sufficiently large that the EM particles of an air shower attenuates in the water before reaching the bottom of the tank. In this way, there is a direct proportionality between the total light yield in the tank and the total EM energy in the shower. Given this 4 m of overburden
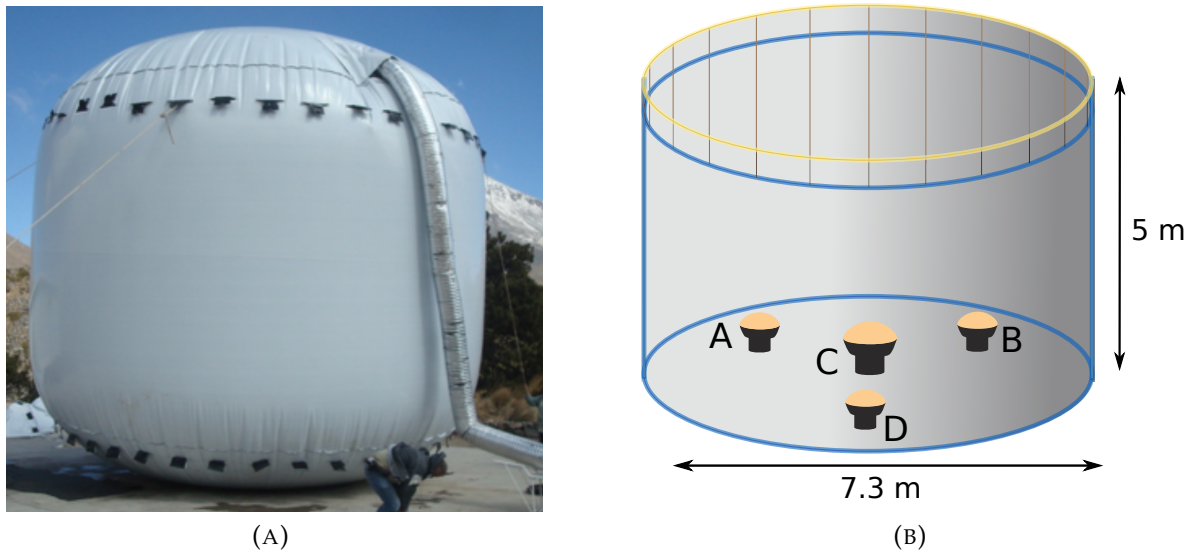
FIGURE 3.2: The *left panel* (A) shows the light tight bladder which holds the water in each WCD. The *right panel* (B) is a schematic of the dimensions of the WCD. The bottom consists of 4 PMTs arranged in an equilateral triangle configuration of side length 3.2 metres.

above the PMTs, muons from hadronic showers produce an asymmetric response from the four PMTs when their final position on the tank floor is near one of the PMTs, resulting in a large light yield in a single PMT far from the shower axis. This is not expected in gamma-ray air showers where the lateral energy distribution is both highly peaked near the shower axis and has a relatively smooth profile, as will be discussed in future sections. This provides a way of discriminating hadron-induced atmospheric showers from gamma-induced ones using light levels detected with the PMTs in a tank relative to each other. This approach is further discussed in Chapter 4.

Each HAWC main array tank has 4 PMTs at the bottom, facing upward as illustrated in Figures 3.2 and 3.3. One 10″ Hamamatsu PMT (R7081) with high ($\sim$ 40%) quantum efficiency lies at the centre and is referred to as PMT C while the other 3 PMTs are placed in an equilateral triangle about the central one and are referred to as PMTs A, B and D. They are approximately 2 m from the tank edge and 1.6 m from the central PMT. These peripheral PMTs are 8″ Hamamatsu PMTs (R5912) reused from the Milagro experiment with a manufacturer-quoted peak quantum efficiency of $\sim$ 25%. The PMTs are sensitive to light in the wavelength range of 300 nm to 500 nm. The PMTs have large collection areas and are sensitive enough to detect single photons and have extremely fast response speeds on the order of tens of nanoseconds. More details about the functioning of PMTs are described in Appendix B.

The PMT read-out is transmitted back to a centrally located electronics building using RG-59 coaxial cables which provide the high voltage to the PMT, and carry the signal

(A)   (B)
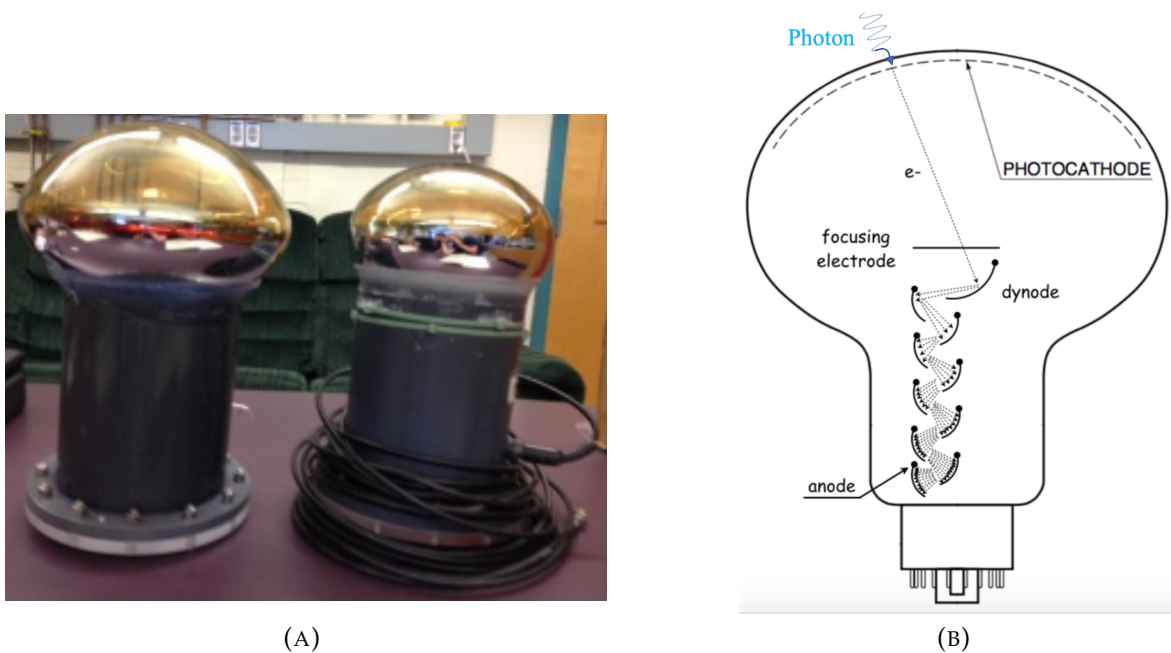
FIGURE 3.3: The *left panel* (A) shows a 10″ Hamamatsu PMT to the left and an 8″ Hamamatsu PMT with cabling to the right. The *right panel* (B) is a schematic of a PMT demonstrating the amplification process. This schematic was adapted from Wood (2016).

back to the data acquisition (DAQ) system.

3.2 Data Acquisition System

The main DAQ system records air shower events. The essential aspects of the DAQ processing pipeline are elaborated in the following subsections. Figure 3.4 illustrates the different steps involved in the DAQ system. The DAQ system receives PMT signals with a set of analog front-end electronics boards (FEBs) and applies two signal thresholds. The next DAQ component is a set of digital FEBs to merge low and high threshold outputs from the analog FEBs to a single digital waveform. This waveform is subsequently recorded by a group of time-to-digital converters (TDCs) which transmit the results to an on-site computing cluster for air shower reconstruction and analysis.

A set of analog FEBs attach to the coaxial cables leading to PMTs through lightning protection spark gaps. The FEBs were recycled from the Milagro experiment and process signal from 16 PMT channels. They amplify and apply two thresholds, a low threshold and a high threshold, to the PMT pulse. They are also responsible for distributing HV provided by an external HV power supply to each PMT.
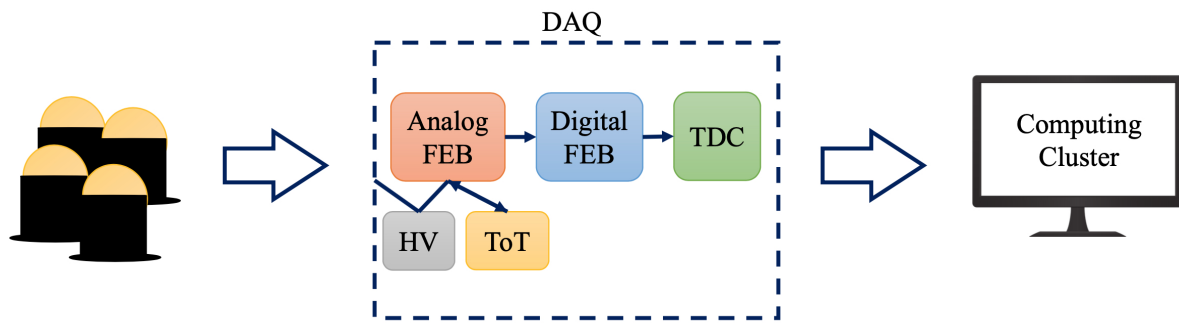
FIGURE 3.4: Overview of the DAQ system. The DAQ is composed of all the electronics that process and analyse the signal from the PMTs.

Time Over Threshold

The analog FEBs shape and amplify the signal pulses by comparing to two reference voltages: -30 mV and -50 mV. This results in two time over threshold (TOT) measurements, the so-called low TOT and high TOT. An emitter-coupled logic (ECL) is used to generate a pulse that begins when the signal voltage drops below the reference voltage and ends when the signal rises above the reference voltage. In this way, the square pulse created has a width that equals the time the original pulse was below the reference threshold as shown in Figure 3.5. This width is referred to as the *time-over-threshold* (TOT) and is typically shortened to LoTOT and HiTOT when referring to TOT from the low and high threshold circuits, respectively. The time-stamps when the pulses cross these thresholds are recorded by TDCs with a 100 ps time resolution, these are then used to estimate the number of PEs. The TOTs are thus used to measure the PMT signal amplitude (charge in PEs) and time (in ns) for data reconstruction. The amplitude corresponds approximately to 0.25 PE and 5 PE signals prior to amplification.

Time-to-Digital Converters

Ten CAEN VX1190A TDCs, each with 128 channels, are used to record the waveforms output by the digital FEBs. Each TDC channel records the rising and falling edges of the digital waveforms with an absolute time precision of 100 picoseconds and a minimum edge pair resolution of 5 ns. TDCs are kept synchronised by an external time clock.

The DAQ reads out PMT signals during a 2 μs window after a multiplicity trigger condition is met. HAWC is implemented with a condition for recording the number of PMT signals, which is satisfied by having at least 28 PMTs triggered in a 150 ns trigger window with at least 90% of active PMTs in the main array. The event rate for HAWC is thus 23.5 kHz leading to a 2 TB of raw data per day. This rate fluctuates by approximately
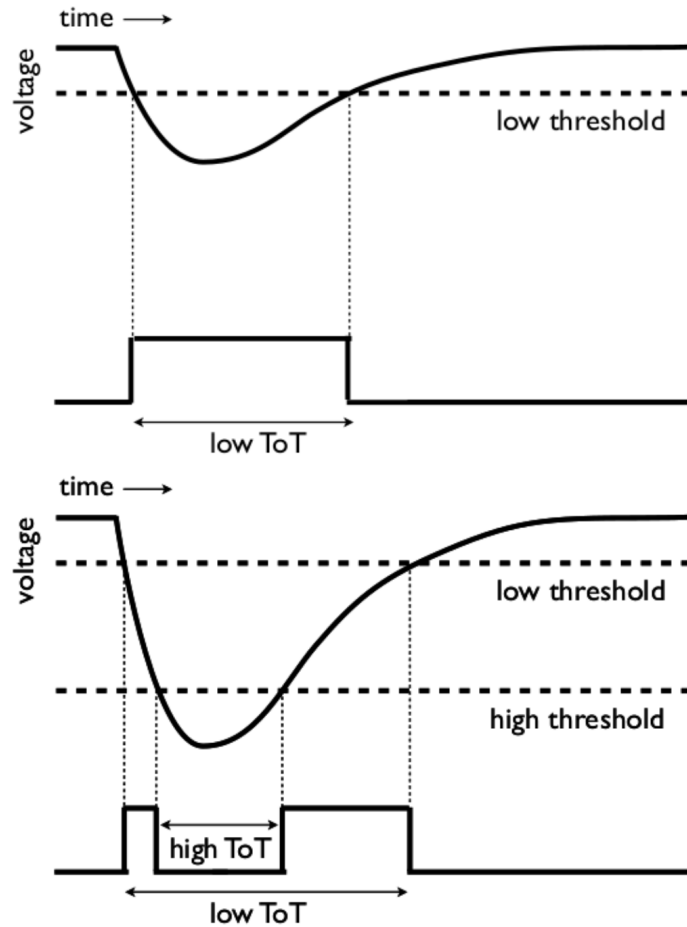
FIGURE 3.5: Time-over-Threshold processing. Figure adapted from Zhou (2015).

10% over the course of each day as atmospheric pressure variations change the amount of atmospheric overburden above HAWC.

3.3 Calibration

The aim of having a calibration system is to convert the amplitude of PMT waveforms as saved by TOT to the corresponding number of PE from the original waveform. Moreover, we have to correct for amplitude dependent timing offsets, referred to as *slewing*. Slewing occurs when large amplitude pulses, having faster rise times, cross the low and high threshold levels faster than smaller amplitude pulses. To do the calibration, a 532 nm wavelength laser with a 1 ns pulse-width is used to send light through optical fibers to a diffuser located 3 m above the central $10''$ PMT of each HAWC tank. The light level simulates the Cherenkov light from air showers and is controlled to produce distributions of charge as a function of TOT. The PMTs record the calibration light and transmit the signal to DAQ as in the case of real air shower events.

Using neutral density filters, the light level in all 1 200 PMTs can vary up to over 7 orders of magnitude, thus allowing amplitude calibration from a single PE to several thousand PEs. Although PMTs are calibrated prior to deployment, other effects can influence measured signals. For instance, the water quality within WCDs influences the attenuation and scattering length of emitted Cherenkov light, changing the number of photons incident on PMT cathodes. Hence, there is a need for re-calibration and regular monitoring.

Time calibration is done to account for the time difference arising from different optical path lengths which occurs because of the use of different splitters and fibers and can be measured on site.

3.4 Outriggers

The outrigger array consists of a sparse array of smaller WCDs surrounding the main array over an area 4 times the size of the main array. There are 345 plastic water tanks, each being 1.65 m high and 1.55 m in diameter as illustrated in Figure 3.6. Each tank is instrumented with a single 8″ PMT placed at the bottom centre of the tank facing upwards. The purpose of deploying such an array was to improve HAWC's performance above 10 TeV. Air showers above $\sim$ 10 TeV have a footprint bigger than the size of the main array. If the core of such a shower falls within the main array, it can be correctly reconstructed. However, in the case where the core of the shower is outside the main array, it might be spuriously reconstructed as a shower of lower energy, with a wrong core location and an erroneous arrival direction.

The outrigger array is divided into five independent sections named A to E, each with 69 tanks, for read-out purposes as depicted in Figure 3.7. Each section has its own electronics building, called node, for DAQ purposes. Similar to the main array, RG-59 coaxial cables were used to transmit PMT signals to the electronics building. However, in the outrigger case, the system is different. It has a set of pick-off modules that distribute HV and receive the PMT signals from 69 PMT channels. Ethernet cables are then used to transmit the signals to a set of Fast Analogue to Digital Converter (FADC) cards. The FADC cards perform the combined functions of the analog and digital FEBs. A White Rabbit LEN is then used to synchronise the signals to the central GPS time server. A a more in-depth description is provided in Jardin-Blicq (2019).

A multiplicity trigger condition for data acquisition is to have at least 2 outrigger tanks triggering above a threshold of 1 PE within a time window of 160 ns. This results in an approximate rate of 4 500 events per second. Events that trigger the main array and/or the outrigger array, according to their respective trigger conditions, are recorded
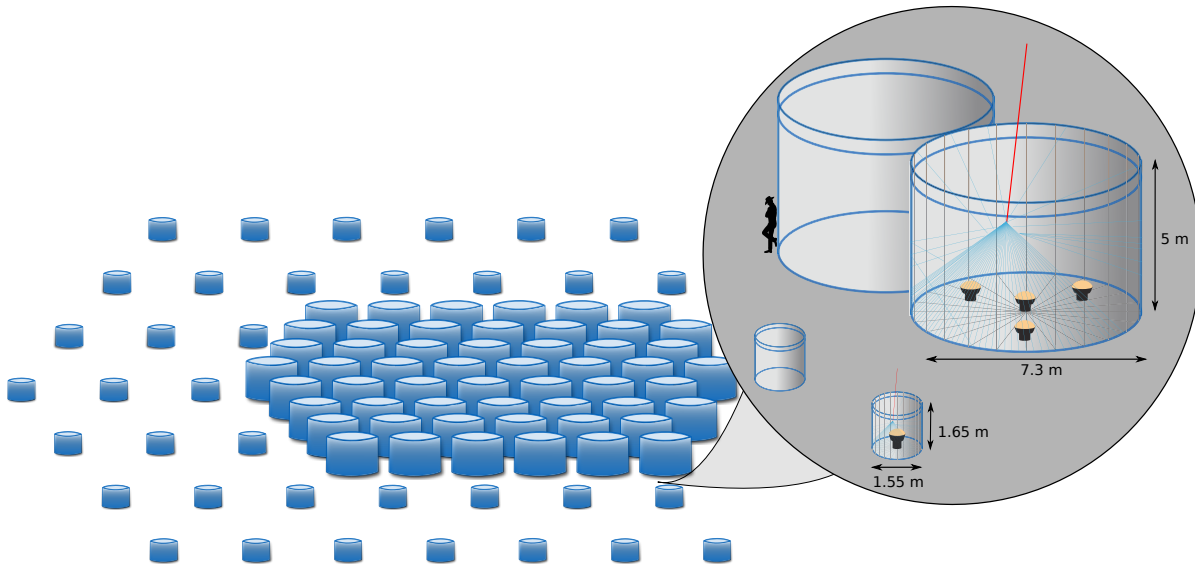
FIGURE 3.6: Schematic showing dimensions of the HAWC WCDs. The zoomed inset displays the size of the tank relative to the standard human height. Image credit: A. Jardin-Blicq.
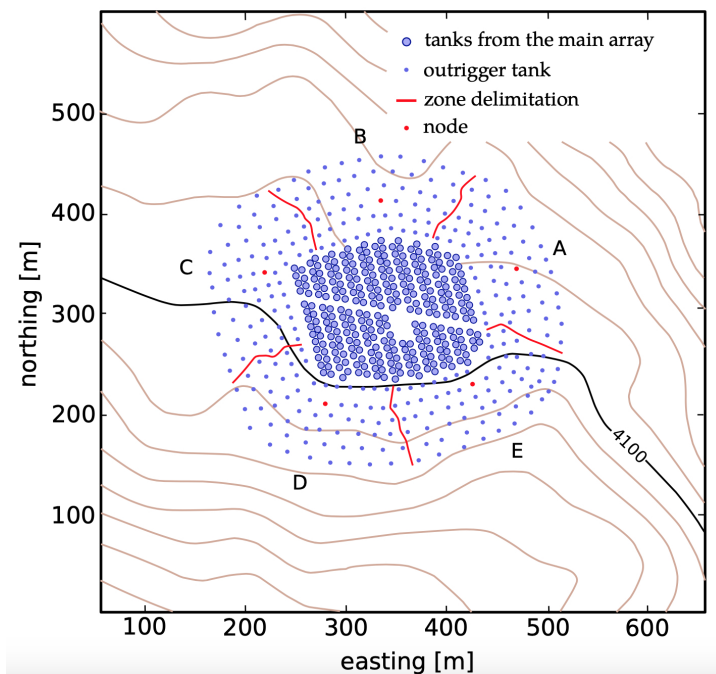
FIGURE 3.7: Sectioning of the outrigger array for read-out purposes. Figure adapted from Jardin-Blicq (2019).

independently. Then, if an outrigger event is found to be between 500 ns and 1 μs of a main array event, the corresponding data sets are merged.

3.5   Monte Carlo Simulation

To assess and improve the performance of reconstruction algorithms and to understand the measurements made, simulation of the entire process is essential. It also allows one to minimise the disagreement between simulated events and measurements, thereby minimising systematic errors. Figure 3.8 summarises the relevance of simulations in this context. Monte Carlo simulations are carried out in two steps: The first one involves the simulation of the air shower, while the second step relates to the simulation of the detector response.
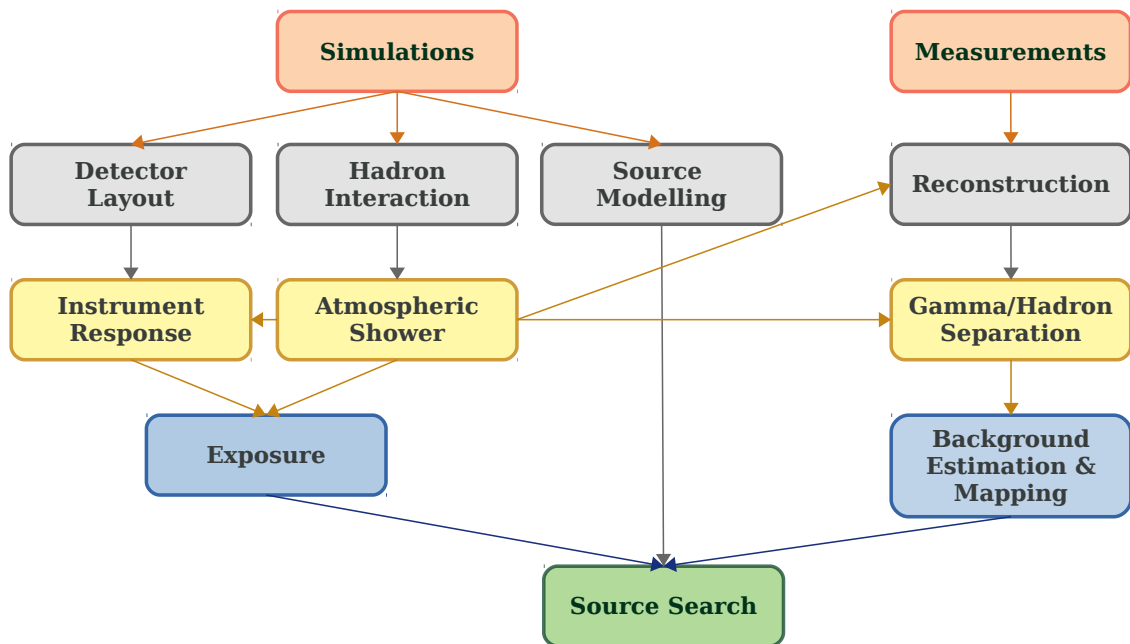
FIGURE 3.8: Relevance of simulation with respect to data. Although measurements alone can reflect a lot in a study, simulations can assist at different levels.

For air shower simulation, the software for COsmic Ray SImulations for KAscade (CORSIKA) were utilised (Heck et al., 1998). CORSIKA simulates the interactions between particles and tracks the development of secondary particles in EAS from different primary particles. Gamma-ray photons and CR particle species (H, He, C, O, Ne, Mg, Si and Fe) are simulated. The primary particles are injected from zenith angles 0° through 75° and are simulated up to 10 m above the HAWC WCDs. A power-law spectrum (with index

2[1]) is employed for the simulation of photons with energy 5 GeV to 500 TeV and 5 GeV to 2 PeV hadrons.

The geometry and tracking package, GEANT4 (Agostinelli et al., 2003; Allison et al., 2006; Allison et al., 2016) is used to simulate the passage of CORSIKA simulated particles through HAWC WCDs. The GEANT4 library contains the simulations of particle interactions in water and Cherenkov light production. Together with PMT time and charge response, CORSIKA and GEANT4 can be used to derive the HAWC detector response as a function of declination, which can then be used to derive an exposure model as described in Section 5.4 of Chapter 5. In this thesis, we use the results from CORSIKA and GEANT4 to simulate a distribution of all observable parameters, such as charge density and timings, that would be recorded had the air shower been induced by a photon or hadron. This list of observable parameters subsequently serves as the foundation for the reconstruction work described in Chapter 4.

3.6   Lateral Distribution of Muons

Photons, electrons (positrons) and muons (μ^- & μ^+) carry the bulk of energy of an EAS to the ground. While gamma-ray-induced showers have an eminent photon dominance, a considerable fraction of the bulk energy is carried by muons in the case of hadron-induced showers. The number of muons (N_{muon}) is, therefore, relevant. From both parent pions and decay process, muons gain significant transverse moment and are usually found at large distances from the shower core, as shown in the top panels of Figure 3.9, which leads this study of the lateral distribution of muons.

For the remainder of this section, we compare gamma-induced showers to proton-induced showers as the CR flux is dominated by protons. Furthermore, heavier elements interact higher in the atmosphere than protons, implying that they contribute fewer particles at ground level. Thus, the input of muons from heavier elements would only add marginally to the lateral distributions shown.

We performed over ten thousand simulations to find the average number of muons in gamma-ray induced and hadron-induced showers, respectively, by separately changing the incoming zenith angles of the primary particle, its energy and the altitude of detector. The middle panels of Figure 3.9 depict the distribution of the number of muons as a function of lateral distance (d) from the simulated shower core. The muons were counted in concentric rings around the simulated shower core every 10 m increment in radial distance from the shower axis to a radial distance of 1 000 m. The bottom panels illustrate

---

[1]A spectrum harder than typical astrophysical spectra is used to provide sufficient statistics on high-energy particles.

(A)

(B)

(C)

(D)

(E)

(F)
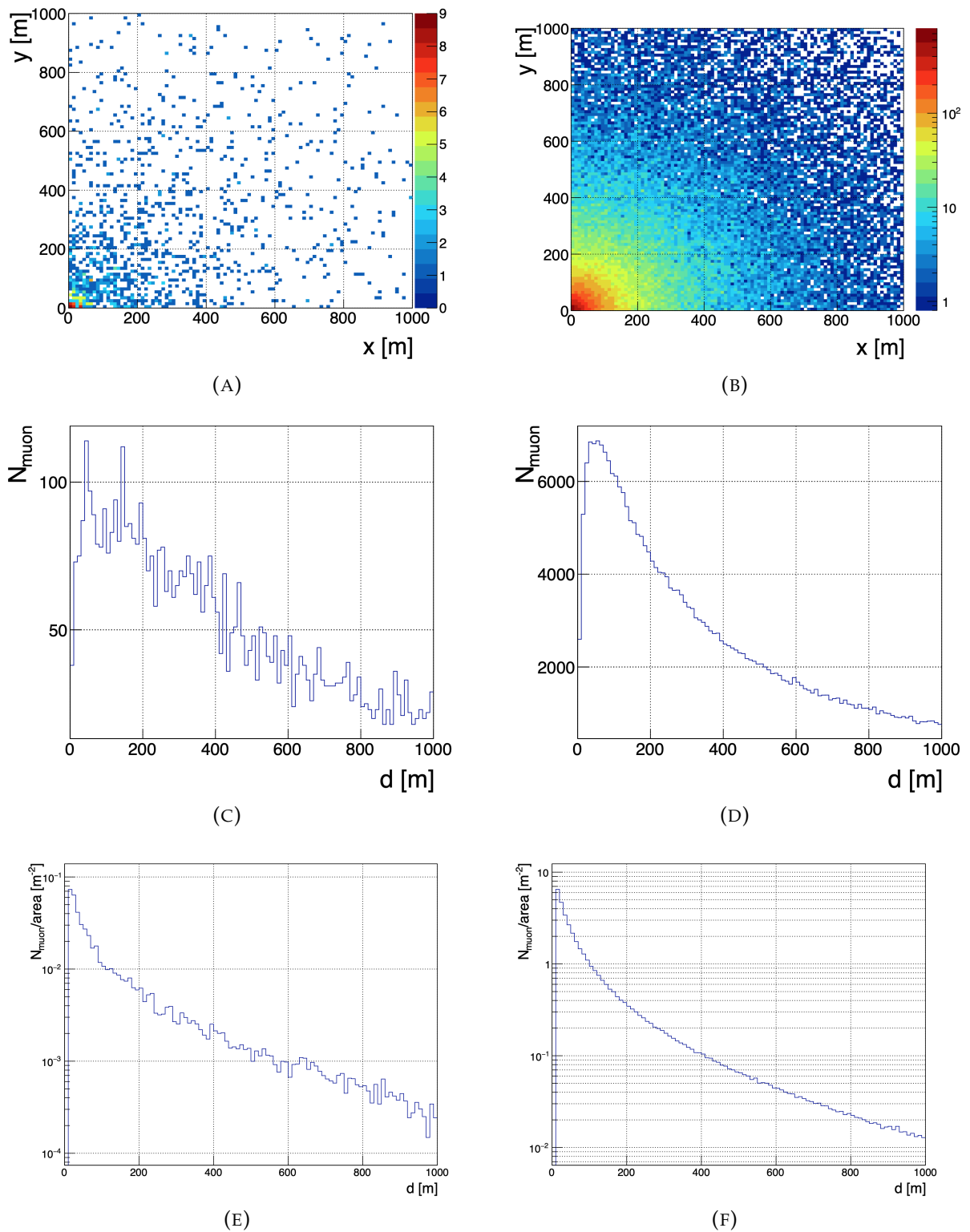
FIGURE 3.9: The *top panels* display the muon spread in a quadrant of an EAS. The *left* and *right panels* depict gamma-ray induced and proton-induced showers, respectively. As the proton-induced shower involves far more muons than the gamma-induced shower, the colour scale in the former case is given in log-scale to emphasise the gradient in muon numbers across the quadrant. The *middle panels* indicate the number of muons in concentric rings around the shower core as a function of lateral distance, with the *bottom panels* showing this number of muons normalised by the area of the corresponding ring. The showers used had an initial energy of 1 TeV, an incoming zenith angle of 0° and detection was set at an altitude of 5000 m.

the muon density in the rings as a function of lateral distance. Muons hold the potential to discriminate between gamma-induced and hadron-induced showers. The number of muons reaching the ground as well as the lateral extent are key for an effective discrimination.

An ASPD at 5 000 m a.s.l is approximately 5.5 radiation lengths below the shower maximum of a 1 TeV gamma-ray induced shower. This implies that few particles reach the ground with large fluctuations in observables. The low count of muons in gamma-induced showers result in relatively large error bars as shown in Figure 3.10 which depicts the distribution of the cumulative number of muons per event as a function of lateral distance from the shower core. With a random flux of muons passing through the detector and a limited detection probability for muons, we cannot rely on the association of a single muon for gamma/hadron discrimination. We show in Figure 3.11 the fraction of showers (out of the 10 000) that had a cumulative muon count greater than 2, 5, 8 and 11 at any given lateral distance d.

(A)

(B)
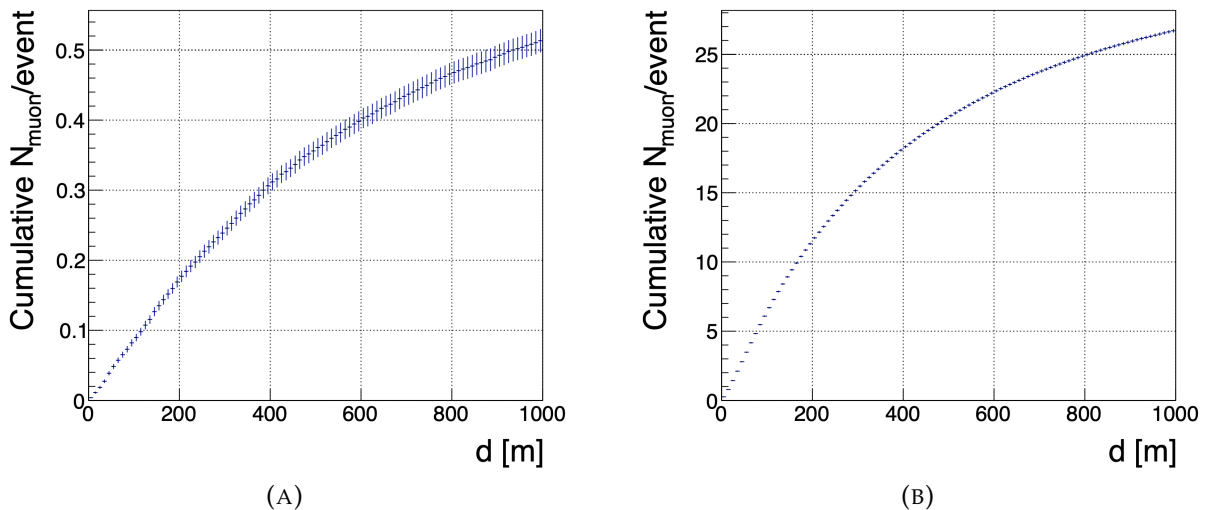
FIGURE 3.10: Distribution of the cumulative number of muons per event as a function of lateral distance for a gamma-ray induced shower (*left panel*) and proton-induced shower (*right panel*). The showers used had an initial energy of 1 TeV, an incoming zenith angle of 0° and detection was set at an altitude of 5 000 m.

3.6.1   Investigating the Energy, Zenith Angle and Altitude Dependencies on Number of Muons

The variation in the distribution of the cumulative number of muons as a function of lateral distance from simulated shower core for both gamma-ray-induced and proton-induced showers is shown in Figure 3.12 for different primary energies (A & B), incoming
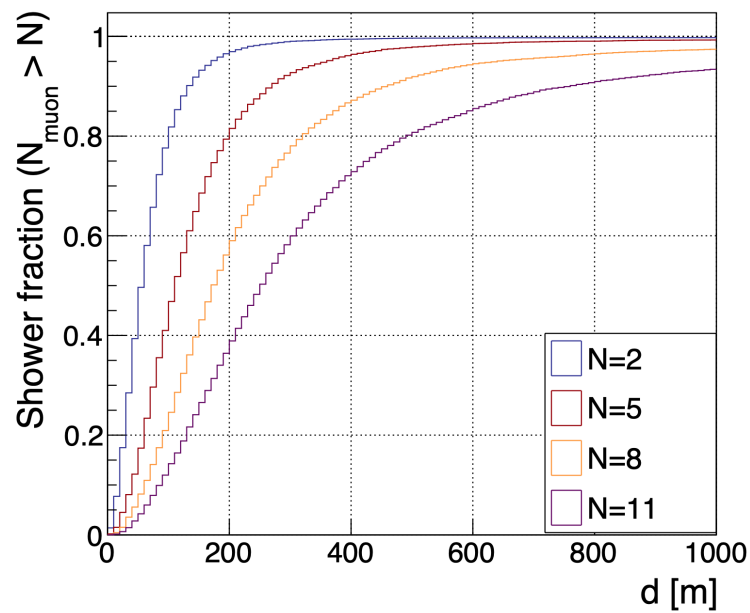
FIGURE 3.11: Fraction of showers (out of the 10 000) that had a cumulative muon count greater than N at any given lateral distance d. Showers are proton-initiated, incoming from zenith $= 0°$, with energy of 1 TeV and detected at an altitude $= 5 000$ a.s.l.

zenith angles (C & D) and altitudes for detection (E & F). In the case of energy dependence, we simulated showers with an incoming zenith angle of $0°$ and detection was set at an altitude of 5 000 m while the energy of the primary particles were set to 0.05 TeV, 0.1 TeV, 0.5 TeV, 1 TeV or 5 TeV. The top panels illustrate that the higher the energy, the larger the number of muons which is expected as the more energetic the primary particle, the deeper it penetrates the atmosphere. For the zenith dependence, as depicted in the middle panel, we simulated showers with an initial energy of 1 TeV and detection was set at an altitude of 5 000 m while the incoming zenith angles were binned equally in solid angles. Alternatively, we have in the Appendix B the same but for zenith angles binned equally in degrees for a detection altitude of 4 100 m. Lastly, for the altitude dependence, we simulated showers with an initial energy of 1 TeV, an incoming zenith angle of $0°$ and detection was set at an altitude of 5 000 m or 4 100 m as displayed in the bottom panel.

The behaviour of the lateral distribution of muons in both the zenith angle study and the altitude study are as expected. The higher the incoming zenith angle and/or the lower the altitude, the thicker is the layer of atmosphere that the shower encounters. This "longer" path implies that the muons can travel further from the shower axis or even decay before reaching the ground. These two factors, zenith and altitude, may be combined into a single one, the *slant depth*, the illustration of which is given in Appendix B.

(A)

(B)

(C)

(D)

(E)

(F)
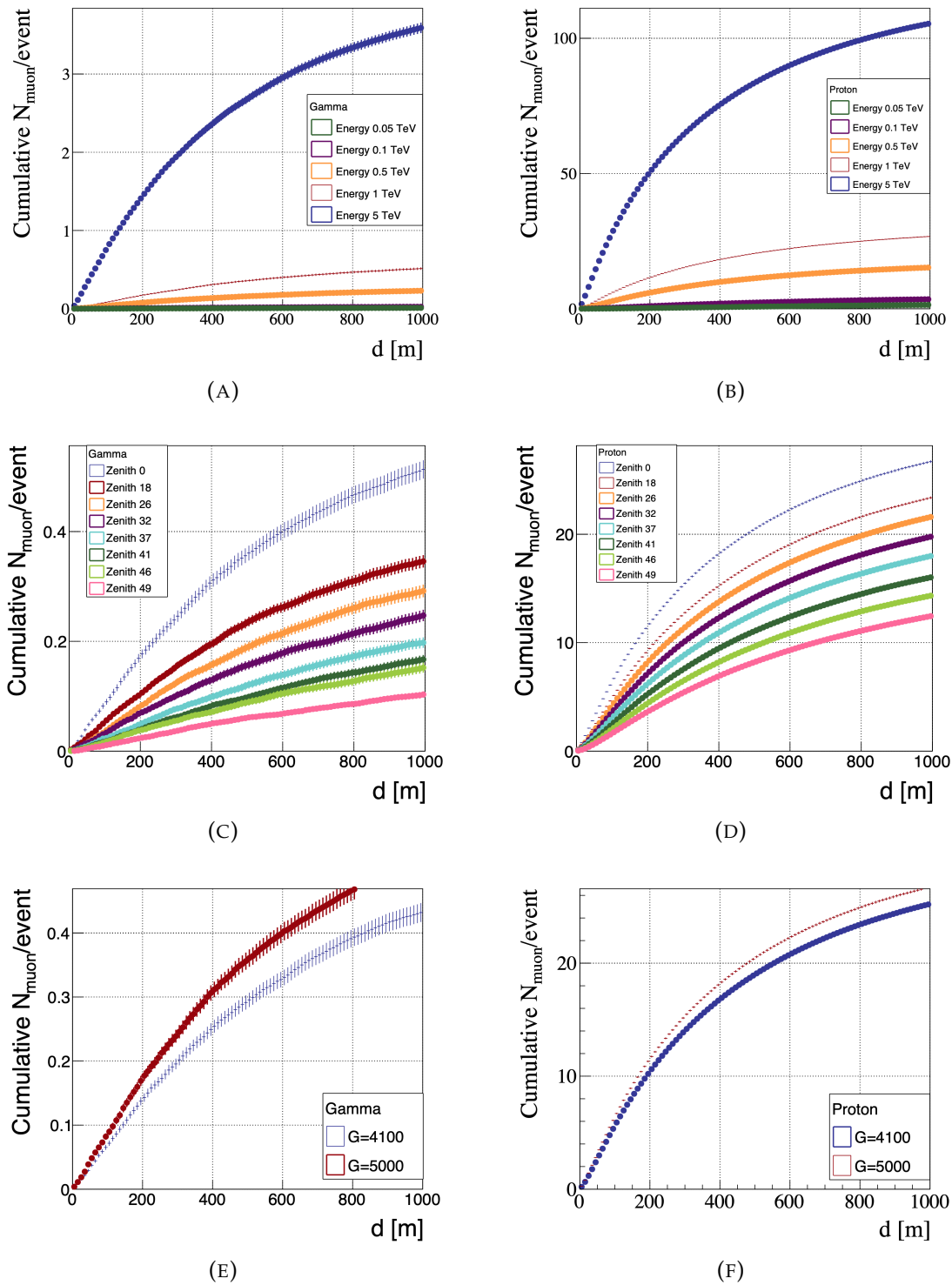
FIGURE 3.12: The variation in the distribution of the cumulative number of muons as a function of lateral distance from simulated shower core for both gamma-ray-induced showers (*left panel*) and proton-induced showers (*right panel*). The *top panels* are showers with an incoming zenith angle of 0° and detection was set at an altitude of 5 000 m while the energy of the primary particles are 0.05 TeV, 0.1 TeV, 0.5 TeV, 1 TeV or 5 TeV. The *middle panels* depict showers with an initial energy of 1 TeV and detection was set at an altitude of 5 000 m while the incoming zenith angles were binned equally in solid angles. The *bottom panels* illustrate showers with initial energy of 1 TeV, an incoming zenith angle of 0° and detection was set at an altitude of 5 000 m or 4 100 m.

3.6.2 Muons as Discriminator between Gamma-ray-induced Showers and Proton-induced Showers

As depicted in Figure 3.11, $N = 2$ has the highest shower fraction at all radial distances. We compare in Figure 3.13, the lateral distributions of the fraction of showers for which the muon count exceeds 2, i.e. $N_{\mathrm{muon}} > 2$, for different primary energies, incoming zenith angles, altitudes for detection and types of particle using the same set of showers as above. According to our simulations, Figure 3.13 (D) illustrates that a muon count as low as 2, in principle, is already very effective in discriminating gamma-ray-induced vertical showers from proton-induced vertical showers at 1 TeV and an altitude of 5 000 m a.s.l.

The rationale behind testing an altitude of 5 km is to be as close to the shower maximum as possible, while it is particularly problematic to find a suitable site for ground-based detection above that altitude. From the above studies, having an unambiguous muon identification is crucial to effectively discriminate between gamma-ray induced and proton-induced showers and should be considered in designing future HAWC-like observatories.

3.7 Summary

We detailed the instrumental set-up of HAWC and discussed the various aspects involving photomultiplier tubes and the data-acquisition system, with a description of their calibration and performance. The impact of primary energy, zenith angle and detection altitude on simulated air showers for a HAWC-like instrument was demonstrated for both gamma-ray initiated and proton initiated showers. Finally, we showed that a muon count as low as 2 can be very effective in discriminating between gamma-ray-induced and proton-induced vertical showers.

(A)

(B)

(C)

(D)
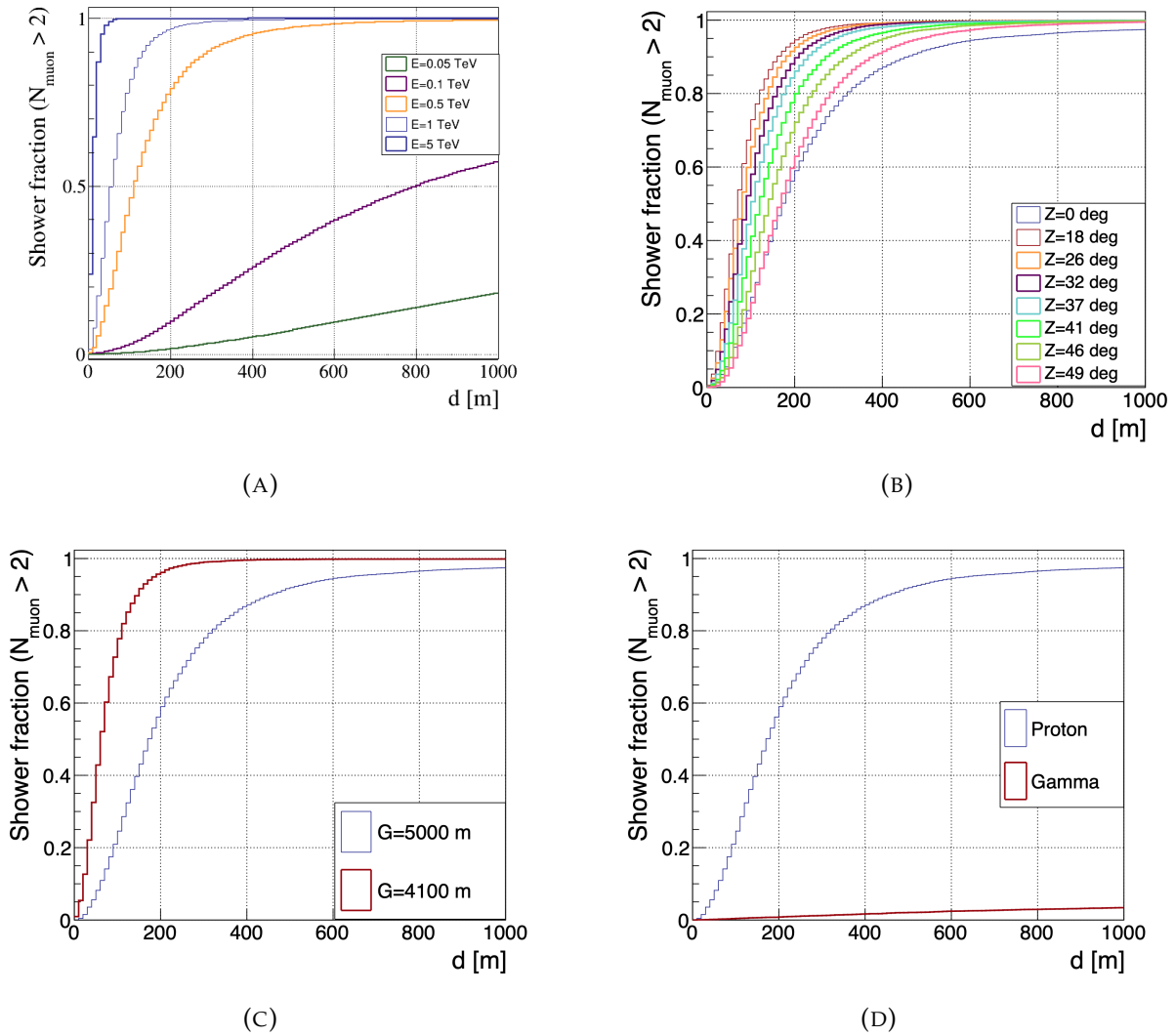
FIGURE 3.13: Distribution of shower fraction where muon number is larger than two, i.e. $N_{\text{muon}} > 2$, for different energies (A), incoming zenith angles (B), altitudes (C) and incoming particle types (D). A muon count as low as 2 is very effective in discriminating gamma-ray-induced vertical showers from proton-induced vertical showers at 1 TeV and an altitude of 5 000 m a.s.l.

4

Air Shower Reconstruction & Gamma/Hadron Discrimination in HAWC

In this chapter, we first describe the reconstruction process in HAWC and then discuss the technique that has been developed to differentiate between gamma-ray induced showers and cosmic-ray induced showers, i.e. gamma/hadron separation, which will be employed in future HAWC analyses. Throughout this chapter, we also mention the algorithms that have been recently developed and are still being processed to be included in the next PASS (PASS 5) of HAWC data. PASS 5 is basically a reconstruction of all the data acquired to date using enhanced software to better interpret the observations.

4.1 Reconstruction of Air Showers in HAWC

An air shower event record consists of a number of measurable quantities, for instance, the photomultiplier tubes (PMTs) triggered in a predefined time window, the charge deposited at each PMT, the time at which the PMTs triggered, amongst others, as introduced in Chapter 3. Reconstruction of an event encompasses a set of tasks to estimate air shower parameters like the core location, the incoming direction, the energy and the primary particle causing the shower. Being a survey instrument that operates practically 24 × 7, the

data influx in HAWC is huge. To efficiently deal with this amount of data, HAWC employs two modes of reconstruction: (i) online reconstruction which happens on-site basically for identification of transient events, and (ii) offline reconstruction. In both cases, dedicated algorithms are collected in a framework called `AERIE` (Analysis and Event Reconstruction Integrated Environment), to process real and simulated events. `AERIE` also contains advanced functionalities, such as map-making, which are outlined in Chapter 5.

4.1.1 Core Reconstruction

The location of the shower core is an important parameter that enables direction and energy reconstruction, as well as gamma/hadron separation. As introduced in Chapter 2, closer to a shower core implies a higher particle density, such that PMTs read out higher light signals. The shower core is therefore the maximum point in a distribution of charge versus distance from a reference point in the detector array, as illustrated in Figure 4.1.
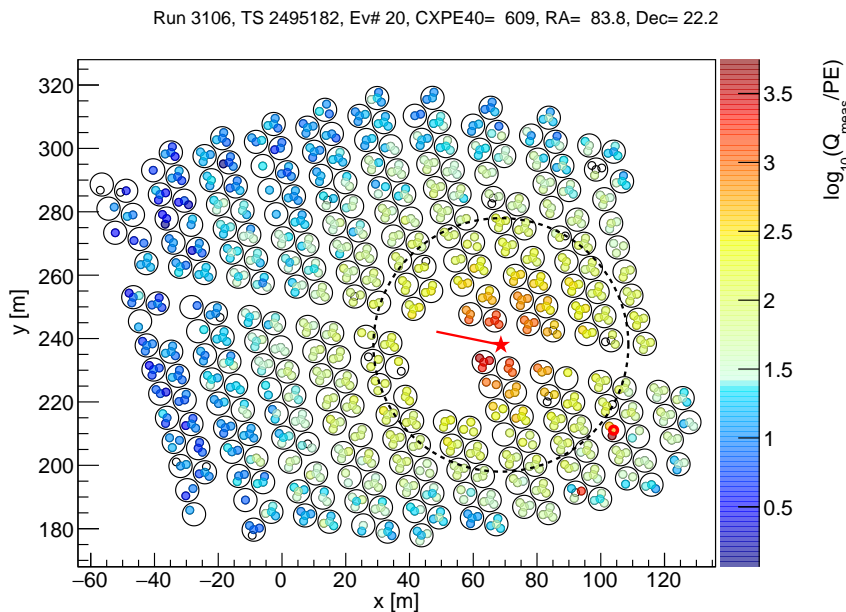
FIGURE 4.1: Distribution of charge in triggered HAWC PMTs for an event reconstructed from the Crab nebula. The red line comes from direction reconstruction and is discussed in the following section. The dotted black circle is a demarcation of 40 m[1] lateral distance from the reconstructed core. The red circle denotes a tank/tanks that received the highest charge deposition beyond a radius of 40 m from the reconstructed core. Lastly, the red star is the location of the reconstructed core.

---

[1] Motivation for 40 m is detailed in Section 4.1.3.

Super Fast Core Fit

Currently, HAWC employs the Super Fast Core Fit (SFCF) algorithm which minimises the χ^2 distribution of charges for the main array (HAWC Collaboration et al., 2017c). It requires an initial guess for the core location, $\vec{x}_{\text{COM}}$, which is the centre of mass (COM) of charges from the various triggered PMTs (N):

$$\vec{x}_{\text{COM}} = \frac{1}{Q} \sum_{i=0}^{N} \vec{x}_i q_i , \tag{4.1}$$

where q_i is the charge from a triggered PMT, $Q = \sum_{i=0}^{N} q_i$, and $\vec{x}_i$ is the location of the triggered PMT. SFCF uses a functional form that was optimised to fit the lateral spread of particles further away from the COM core. For smaller radial distances, a Gaussian fit is preferentially used to avoid the asymptotic behaviour of NKG functions and optimise the computation time. Using several iterations, a converging solution for the location of the core and a fit for the lateral spread of particles from that reconstructed core are obtained as shown in Figure 4.2.
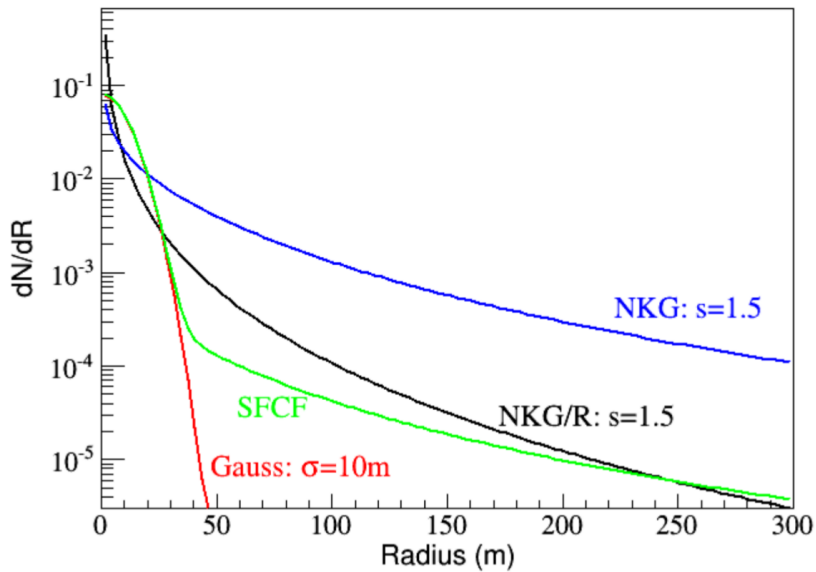
FIGURE 4.2: Comparison of distributions of charges from various triggered PMTs for core localisation. In blue and black, NKG and NKG/R distributions, respectively, both with shower age, $s = 1.5$. In red, a Gaussian distribution with $\sigma = 10$ and in green, the SFCF hybrid curve. Plot taken from Hampel-Arias (2017).

LH Method

A novel method to localise the shower core is to use MC template-based reconstruction, with a likelihood (LH) approach. The lateral amplitude distribution of an observed shower is fitted to an expected probability distribution template. MC simulations of air showers and the detector simulations are used to generate the respective probability distributions. This method has been developed to incorporate the reconstruction of the outrigger array to the main array and also to improve the reconstruction of archival data. A more in-depth description is provided in Joshi (2019).

4.1.2   Direction Reconstruction

As a shower propagates through the atmosphere, the air shower particles can be assumed to travel on a plane, defined by the speed of light and direction of the primary particle, called the shower front. The time of trigger for each PMT within a predefined time window can thus be used in the reconstruction of the incoming direction of a primary particle causing the shower. Figure 4.3 (A) displays the trigger time of PMTs in the HAWC main array for an event reconstructed to be from the Crab nebula region. From the gradient, it can be deduced that the shower front reached the array from the left hand side.
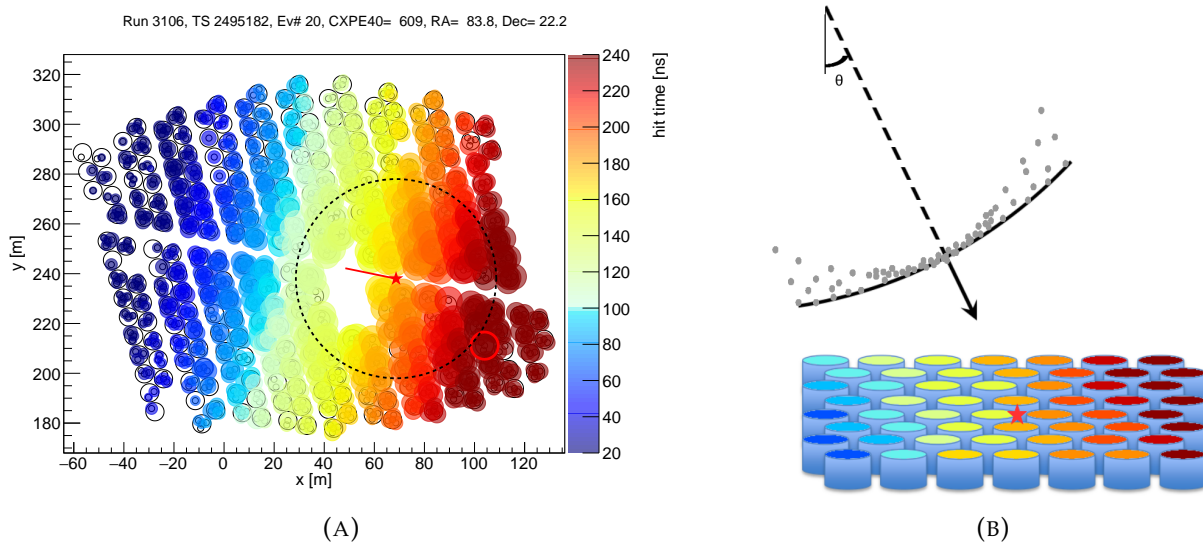
FIGURE 4.3: The *left panel* (A) shows the time gradient for triggered PMTs for an event reconstructed to be from the Crab nebula region. The red line indicates the direction from which the shower front came and its length is a measure of the projected zenith angle, θ. The *right panel* (B) is a schematic of the incoming zenith angle and shower front of the particle causing the shower from (A). (B) also shows the increase in the thickness of the shower front at the edges. The other annotations are the same as in Figure 4.1.

Since the incoming particle is at a large but finite distance, the secondary particle trajectories are not parallel, making the shower front slightly curved. During the shower development, however, some particles are deflected at large angles, resulting in larger path lengths, and therefore arrive at the observational level several nanoseconds later. Moreover, since the number of particles decreases with increasing distance from the shower core, there are fewer PMTs that trigger away from the core. This decrease in sampling in particle arrival time leads to a delay in the measured arrival time of the shower. Thus, particles at the shower edge cause more fluctuations in time measurements than those travelling along the trajectory of the original primary particle (Stanev, 2010). As a result, the thickness of the shower front is not constant, it is relatively thin in time close to the shower core and considerably thicker further away as shown in Figure 4.3 (B). With an iterative core reconstruction procedure, the incoming zenith angle, θ, is also iteratively reconstructed. During each iteration, each PMT is given a weight depending on its measured charge and a fit is applied using χ^2 minimisation to extract the incoming direction of the primary particle.

Point Spread Function

The point spread function (PSF) describes the instrument response to a point source. In other words, it characterises the accuracy of the reconstructed arrival direction (HAWC Collaboration et al., 2017c). In HAWC, it is approximated by a linear combination of two normalised 2D Gaussian functions, of type $G_i = \frac{1}{2\pi\sigma_i^2} \exp\left(-\frac{\psi^2}{2\sigma_i^2} \right)$, through:

$$\text{PSF}(\psi) = \alpha G_1(\psi) + (1 - \alpha) G_2(\psi) \,. \tag{4.2}$$

In equation (4.2), α is a weight assigned to the 2D function. This PSF varies with ψ, defined as the angle difference between the simulated and reconstructed directions of the incoming particle. Conventionally, angular resolution is taken as the 68% containment radius of the fitted PSF. The HAWC PSF was measured using the Crab nebula in HAWC Collaboration et al. (2017c) and was found to increase from 0.17° at higher nHit bins to 1.03° at lower ones. The PSF intrinsically depends on declination of the source. This is due to the fact that a shower encounters a different thickness of atmosphere based on the arrival direction of the primary particle. Therefore, the measured PSF at the position of the Crab nebula cannot be extrapolated to other declinations. However, the simulation can be used to predict the shape of the PSF at any declination.

4.1.3   Energy Reconstruction

The size of air shower events are classified in analysis bins, called nHit bins ($\mathcal{B}$), depending on the fraction of the PMTs triggered in the main array. The nHit binning scheme is shown in Table 4.1. Typically, an incoming particle with higher energy will trigger more PMTs than one with lower energy. However, the nHit bins are weakly correlated with energy and is more about event and reconstruction quality. In $\mathcal{B} = 9$, for instance, all PMT triggers and an nHit bin-based energy proxy saturates. This means that it is impossible to distinguish 30 TeV events from 100 TeV events in bin $\mathcal{B} = 9$ (which contains events above approximately 30 TeV). The nHit bins are known to have overlapping true energies as illustrated in Figure 4.4 (Figure 3 from HAWC Collaboration et al., 2017c)). Recently, two new energy estimators have been developed for HAWC (HAWC Collaboration et al., 2019), which are outlined below for sake of completeness.

TABLE 4.1: Table detailing the percentage of PMTs triggered in the main array for each nHit bin.

nHit bin ($\mathcal{B}$)	Percentage of main array PMTs triggered (%)
0	4.4 - 6.7
1	6.7 - 10.5
2	10.5 - 16.2
3	16.2 - 24.7
4	24.7 - 35.6
5	35.6 - 48.5
6	48.5 - 61.8
7	61.8 - 74.0
8	74.0 - 84.0
9	84.0 - 101.0[2]

Ground Parameter

For showers of the similar energy, the fluctuations are minimal. This was used as a criterion for finding the lateral distance from the reconstructed shower core at which the uncertainty in the shower energy density is lowest. To determine this optimal distance, the lateral distribution of charge is fit to a modified version of the NKG function for several shower ages as shown in Figure 4.5 (Figure 2 in HAWC Collaboration et al., 2019)). The

---

[2]Multiple hits are possible per PMT.
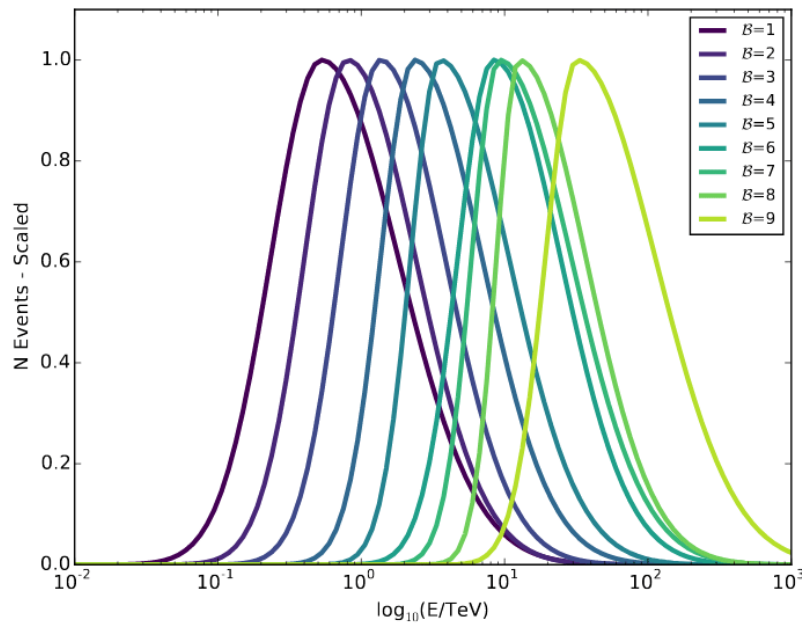
FIGURE 4.4: Normalised true energy distribution of photons summed across a transit of a source at a declination of 20° N and with spectral form of type $E^{-2.63}$ for $\mathcal{B}$: 1 - 9. Figure taken from HAWC Collaboration et al. (2017c).

optimal distance for HAWC was found to be 40 m from the shower core, independent of the incoming particle energy or zenith. Hence, the Ground Parameter (GP) method employs the charge density at that fixed distance to yield an energy proxy:

$$\log_{10} \hat{E} = m(\theta)\zeta_{40} + c(\theta) . \tag{4.3}$$

In equation (4.3), $m(\theta)$ and $c(\theta)$ are chosen empirically and are linear and quadratic piecewise functions, respectively (HAWC Collaboration et al., 2019). ζ_{40} is the PMT signal evaluated using a lateral distribution function (LDF) provided in equation (1) of HAWC Collaboration et al. (2019), therein referred to as sig_{40}. The GP method enhances the energy resolution of the HAWC gamma-ray observatory, enabling measurement of gamma-ray energies beyond 100 TeV (HAWC Collaboration et al., 2020).

Neural Network

A Neural Network (NN) is a complicated function mapping several quantities associated with an event (input variable) to some regression target (output variable), in this case $\log_{10} \hat{E}$. This function is characterised by many free parameters called weights, the optimal values of which are determined during data training (Marinelli, 2016) for minimisation of an error function (HAWC Collaboration et al., 2019). Input variables that capture characteristics of a shower are:
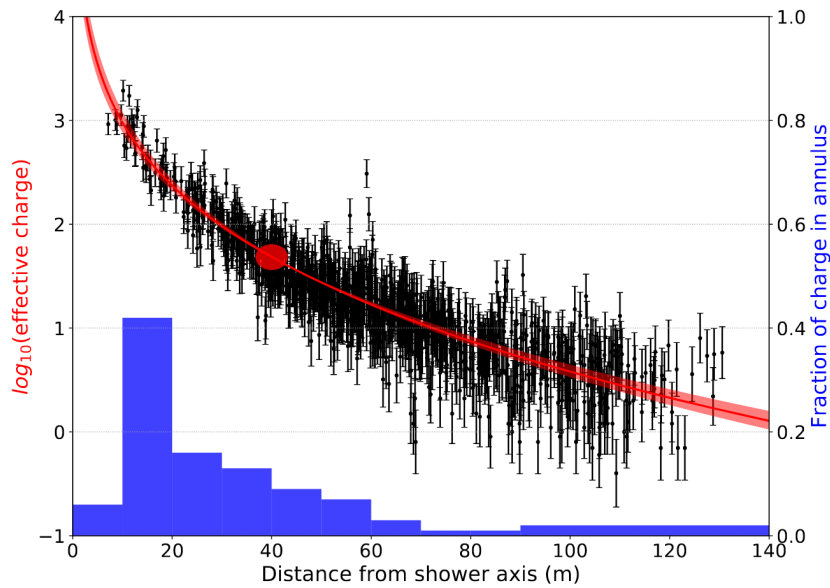
FIGURE 4.5: NKG fit (red) for the lateral distribution of charge (black) for a single event. The circle at 40 m portrays the location where the charge is measured for the GP method. The blue histogram is the fraction of charge, from several concentric rings, that is used as input for the NN method.

1. containment of the shower within the detector — percentage of triggered PMTs,

2. energy deposited in the detector — amplitude measurements and the lateral distribution of charge in concentric annuli from the shower core. This is shown as a histogram in Figure 4.5, and

3. atmospheric attenuation of the shower — obtained from the zenith angle.

The NN method enhances the energy resolution of the HAWC gamma-ray observatory likewise to the GP method (HAWC Collaboration et al., 2019).

4.1.4   Gamma/Hadron Separators

As outlined in Chapter 1, cosmic rays are the main background in the observation of gamma-rays. In order to reduce the influence of background for a study about any astrophysical source, we need to effectively discriminate between gamma-induced showers and hadron-induced showers. Two gamma/hadron separators currently used in HAWC are outlined below.

COMPACT

As described in Chapter 2, gamma-ray induced atmospheric showers have smooth lateral shower profiles, as they are almost purely EM, while hadronic showers generate, in general, larger signals further from the shower core by virtue of pion decay which provides
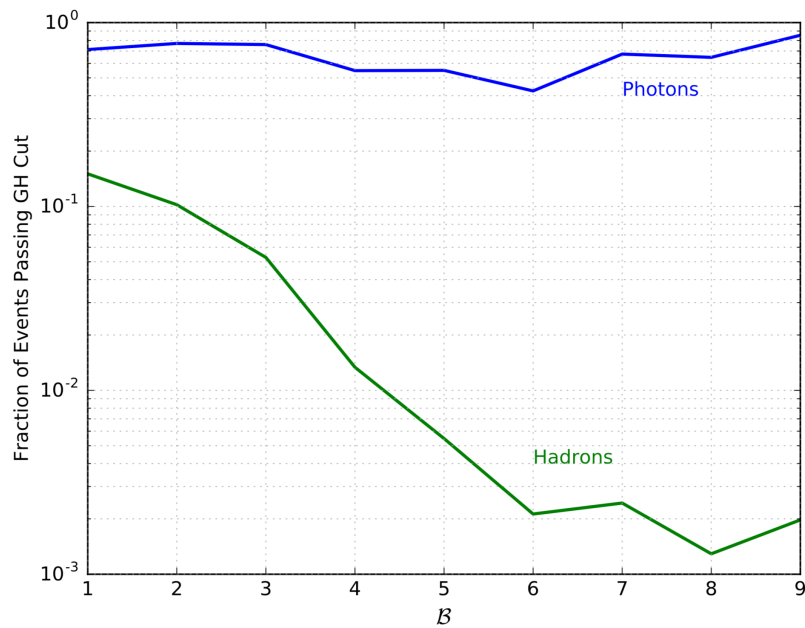
FIGURE 4.6: Fraction of gamma-rays and background hadron events passing gamma/hadron discrimination cuts as a function of the event size. Figure taken from HAWC Collaboration et al. (2017c).

greater transverse momentum to particles produced in the course of the shower. The COMPACT method of gamma/hadron separation exploits this difference by first getting the total number of triggered PMT in the shower in a 20 ns time window ($nHitSP20$), then identifying the largest PMT signal (in units of photoelectrons (PE)) beyond a radius of 40 m from the shower core ($CxPE40$). The gamma/hadron separator, $\mathcal{C}$, is the ratio of these two variables as given below (HAWC Collaboration et al., 2017c):

$$\mathcal{C} = \frac{nHitSP20}{CxPE40} \ . \tag{4.4}$$

COMPACT works well up to the point where gamma-ray induced shower sizes get close to 40 m in radius (Baughman, 2011). Beyond that point, the $\mathcal{C}$-separator increasingly rejects gamma-ray induced showers. An enhancement in the rejection power of the discriminator is obtained by applying an optimised $\mathcal{C}$ cut for the range of nHit values within $\mathcal{B}$. LiComp, $\log(\mathcal{C}^{-1})$, is often used instead of COMPACT as the latter has a long positive tail and the former is better for ease of handling.

PINC

Another discriminator for gamma/hadron separation in HAWC is called PINC, $\mathcal{P}$, and it quantifies how clustered the triggered PMTs are. The Parameter for Identifying Nuclear Cosmic-rays (PINC) method is basically a χ^2-distribution of PEs over lateral distance from the core. It can be summarised by the equation below as elaborated in HAWC Collaboration et al. (2017c):

$$\mathcal{P} = \frac{1}{N} \sum_{i=0}^{N} \frac{(\zeta_i - <\zeta_i>)^2}{\sigma_{\zeta_i}^2} \; . \tag{4.5}$$

In equation (4.5), $\sigma_{\zeta_i}^2$ represents standard deviation of the charge distribution from a sample of gamma-like events from the Crab nebula region, ζ_i is $\log_{10} q_i$, and $<\zeta_i>$ is the expectation value for triggered PMTs lying within an annulus of width 5 m from the shower core. This method is also sensitive to the spread of highly penetrating particles like muons to quantify the lateral spread as shown in Section 3.6, thereby making $\mathcal{P}$ a powerful gamma/hadron discriminator. Currently used cut values for $\mathcal{C}$ and $\mathcal{P}$ are given in Appendix C and Figure 4.6 depicts the predicted efficiency for gamma-rays and the measured efficiency for hadronic background under the aforementioned cuts (Figure 10 in HAWC Collaboration et al., 2017c).

4.2   Tank-Light-Distribution as Gamma/Hadron Discriminator

$\mathcal{C}$ and $\mathcal{P}$ discriminate better at higher nHit bins than lower ones. They are also dependent on a correct core reconstruction which, as discussed in Section 3.4, does not always happen. This motivates the need for another gamma/hadron separator that works independently of reconstruction and improves the background rejection at lower nHit bins. The light distribution in a tank for events triggered by gamma primaries and proton primaries are different, for instance, due to the presence of muons in hadronic showers, and this can be used to differentiate between them. In this method, we collect all differences from different tanks for an event and parameterise them. We then calculate a likelihood ratio, $R_{d/\gamma}$, which tests the hypothesis of an event to be gamma-like or background-like. We generate a gamma template (γ) using simulations and a background template is modelled using measurements from the detector (d) as it is the most accurate way of deriving a correct background. We further compare these measurements to simulation-based proton templates. To obtain $R_{d/\gamma}$, we must, in a first step, define the probability density distributions for all particles triggering the PMTs while accounting for the combination of 8″ and

10″ PMTs per tank. Then, in a second step, we will use these expected probability density distributions to compute the likelihood ratio, $R_{d/\gamma}$. Finally, we optimise the likelihood ratio to get an efficient gamma/hadron discriminator for different shower size ranges.

4.2.1 Deriving Probability Density Distributions

We hereby define the following symbols for the respective quantities: the charge (in units of PEs) on a PMT i, is Q_{PMT_i} where i is the PMT type, i.e. A, B, C or D. The total charge in a tank is $Q_{\text{Tank}_j} = \sum_i Q_{\text{PMT}_i}$, where Tank_j is a specific tank number in the main array, i.e. $1 \leq j \leq 300$. The fractional charge of PMT i in tank j is $Q_{\text{PMT}_i}/Q_{\text{Tank}_j}$. This is calculated for billions of showers (both simulated and observed) using `AERIE`. Using the statistics, a normalised 2-dimensional histogram is constructed as shown in Figure 4.7, with the x-axis depicting the total charge of tanks in log-scale ($\log_{10} Q_{\text{Tank}_j}$) and the y-axis indicating the fractional charge ($Q_{\text{PMT}_i}/Q_{\text{Tank}_j}$) on any given PMT for the whole array. The z-axis then represents the required probability density distribution, with $P_p\left(Q_{\text{Tank}_j}, \frac{Q_{\text{PMT}_i}}{Q_{\text{Tank}_j}}\right)$ for proton-induced simulated showers, $P_\gamma\left(Q_{\text{Tank}_j}, \frac{Q_{\text{PMT}_i}}{Q_{\text{Tank}_j}}\right)$ likewise for photon-induced simulated showers, and $P_d\left(Q_{\text{Tank}_j}, \frac{Q_{\text{PMT}_i}}{Q_{\text{Tank}_j}}\right)$ for measured events[3] used for calibrating the method.

The gamma and proton simulations used in this study are the most recent, nominal files developed for HAWC using (i) CORSIKA (Heck et al., 1998) to simulate incoming particles and associated air showers and (ii) GEANT4 (Agostinelli et al., 2003; Allison et al., 2006; Allison et al., 2016) to simulate the detector and its response to air showers. These were made at different energies, using different zenith and azimuth angles. In the case of simulations, noise was added to make a fair comparison to data. The added noise was derived from the HAWC data itself by extracting continuous, raw, and untriggered data in a time window of 1 500 ns from the data files and overlaying it to the simulations. The response of 1 200 PMTs over the HAWC main array were classified in 12 shower bins as there is a dependence of the light distributions with shower size. The shower bins are defined by percentage of the main array tanks triggered as detailed in Table 4.2, consistent with the concept of using shower size to define analysis bins as was done in PINC and COMPACT methods. This approach depends on the comparison of known gamma events to known hadron events to predict how gamma-like an observed event is. Proton-induced air shower simulations are not exactly known and different hadronic interaction models (`SIBYLL`, `EPOS-LHC`, `FLUKA`, amongst others) yield slightly different solutions (Parsons and Schoorlemmer, 2019). Additionally, since the HAWC data is background dominated, we

---

[3]The observed data set in use for this study is April 2016.
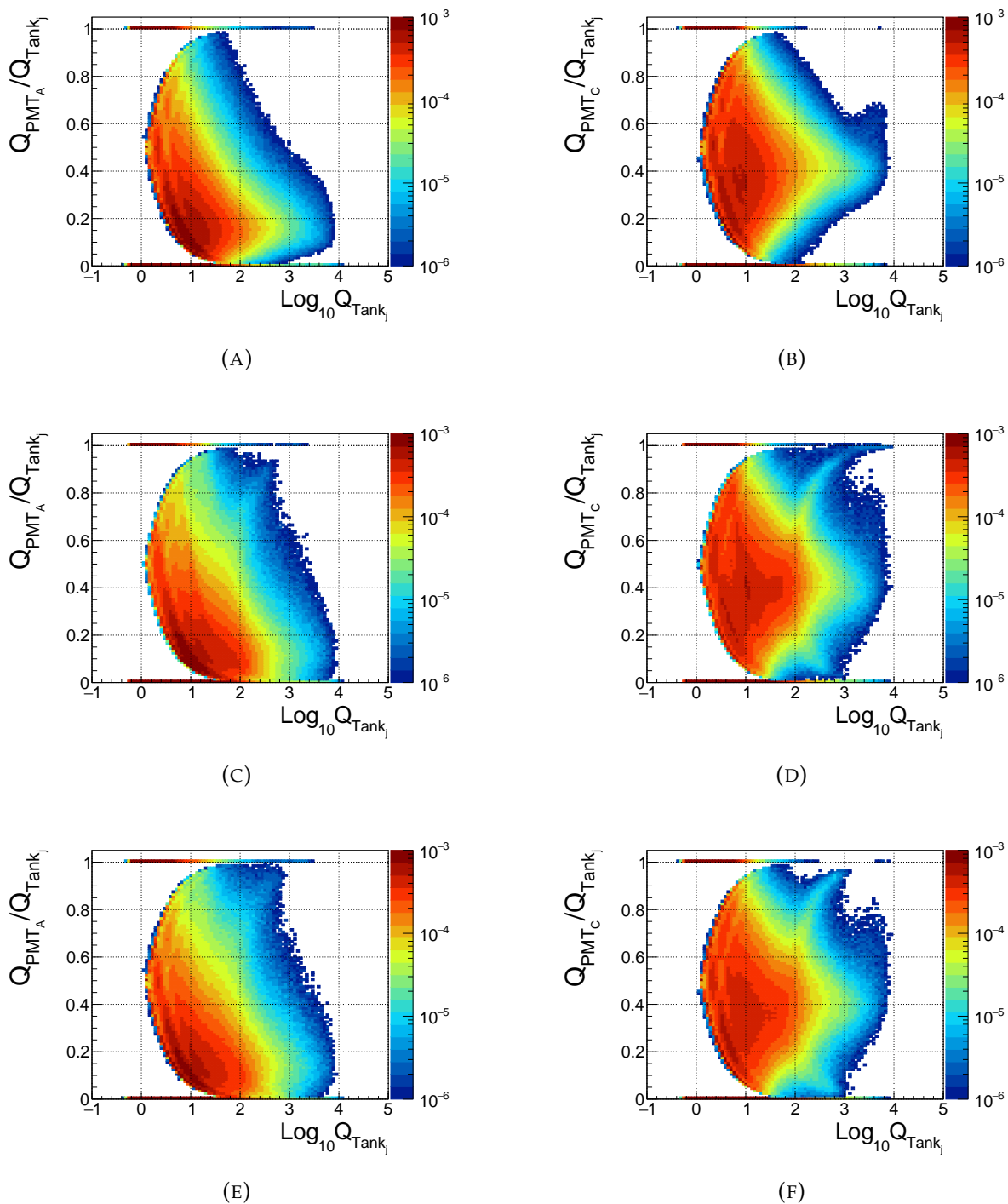
FIGURE 4.7: Probability density distribution of showers from simulated gammas (*top*), measured events (*middle*), and simulated protons (*bottom*) as seen by PMT A (*left*) and PMT C (*right*) for shower bin 5. An arm/fin-like structure is observed for measured events and proton-simulated showers which is a characteristic feature of the muonic component of hadronic showers. Significant differences from fractional charges of one and zero are also seen.

can use the probability density distribution of measured events (P_d) instead of simulation of showers induced by protons (P_p) and heavier atoms.

Figure 4.7 depicts the probability density distributions for PMTs A and C (8″ and 10″, respectively) for photon (gamma) simulation (top panel), measured events (middle panel) and proton simulation (bottom panel) for shower bin 5. The probability density distributions for PMTs B and D are similar to that of PMT A as shown in Figure C.7 in Appendix C. From these distributions, we observe similar features in the measured events and the simulated proton events which are not seen in the simulated gamma events, for instance an arm/fin-like structure. The 1D distribution for the fractional charge on PMTs A and C are shown in the top panel of Figure 4.8 to accentuate this arm-like structure. For gamma-ray induced showers, the light distribution is rather equally distributed among the PMTs. However, for proton-induced showers, the presence of a considerable number of muons, that produce more light in one of the PMTs, yields features like the arm. The bottom panel of Figure 4.8 displays the differences in light distribution for the same set of proton simulated showers recorded through PMT C for muonic and non-muonic components.

The probability density distribution is a function of PMT type because the fraction of light received by a PMT depends on the surface/collection area of the PMT. PMT C has a larger diameter such that it collects more light which results in different probability density distributions. The location of the PMT also affects the fraction of light it receives, for instance, PMT C is at the centre of the tank while PMTs A, B and D are peripherally situated as depicted in Figure 4.9. While in most of the cases (label 2 on Figure 4.9), the PMTs observe fractions of the same light pool, the arm/fin-like structure results from cases where one of the PMTs sees most of the Cherenkov emission (labels 1 and 3 on Figure 4.9). Gross differences in distribution of charges for PMTs A compared to C for photon, proton and observed showers are illustrated in Figure C.8 in Appendix C. Figure 4.10 is an illustration of the probability density distribution as a function of event size for PMT C. The probability density distributions, for all shower bins, for PMTs A and C, for gamma and proton simulations as well as measured events, are provided in Appendix C (cf. Figures C.1 to C.6).

While there is a difference in the general distribution as elaborated above, there is also a difference in the distribution of the zeros and ones of the fractional charge, i.e. in cases where the PMT received none or all of the light, respectively. This is illustrated further in Figure 4.11 for PMTs A and C for shower bin 5. Data in HAWC are recorded only if the signals obtained are above a certain trigger threshold, as discussed in Chapter 3. To effectively compare the MC simulations with data, we implement a PE cut on the total charge of a tank, i.e. a minimum number of PEs above which the likelihoods are calculated. This

(A)

(B)

(C)

(D)
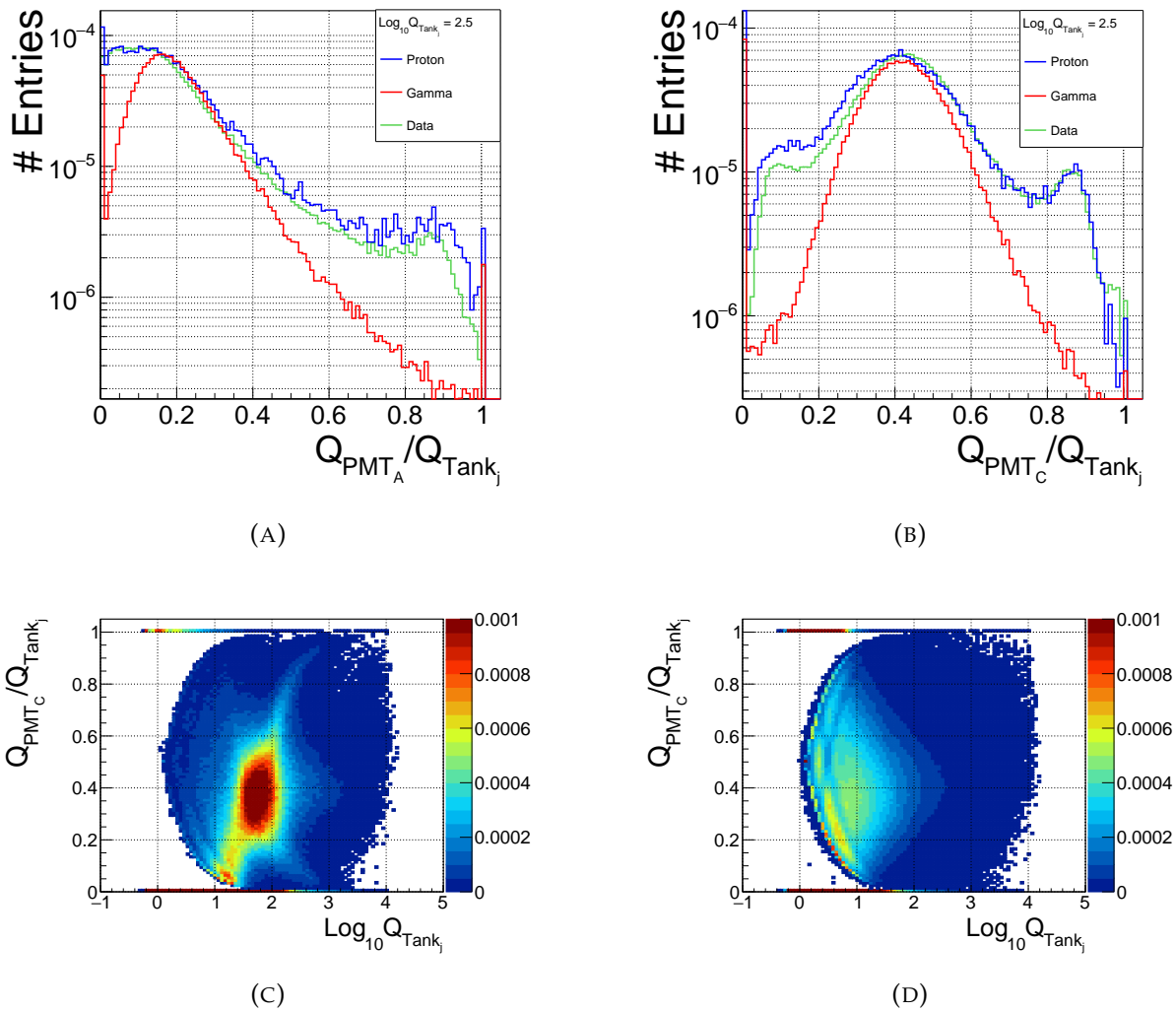
FIGURE 4.8: The *top panels* illustrate the probability density distribution at different fractional charges of PMT C (*right*) and PMT A (*left*) at a fixed (log) total tank charge of 2.5. *#Entries* on the y-axis is the sampling from the probability density for the chosen total tank charge. The *bottom panels* display the differences in simulated light distributions using proton showers for muonic component (*left*) and non-muonic component (*right*) both seen through PMT C.
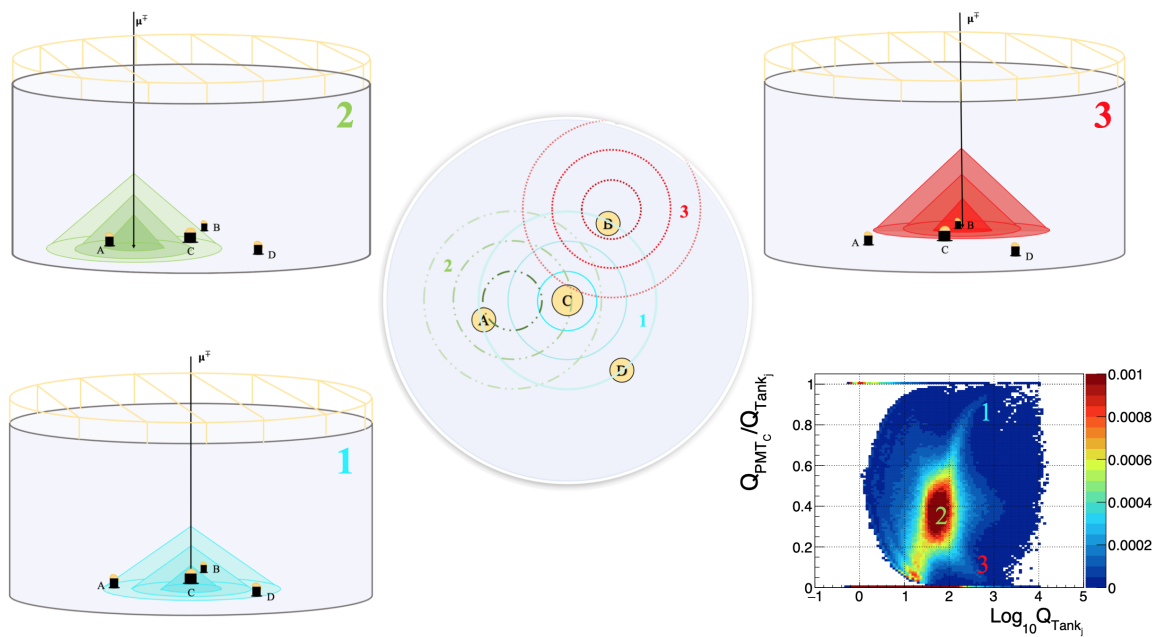
FIGURE 4.9: Figure depicting vertical muons in HAWC tanks. For illustration purposes, the Cherenkov emission was drawn only for the bottom part of the muon paths. Based on the location of the PMTs in the tank and the entry point of the vertical muons, the light signals seen by the PMTs are different and result in the different constituents of the probability density distribution shown.
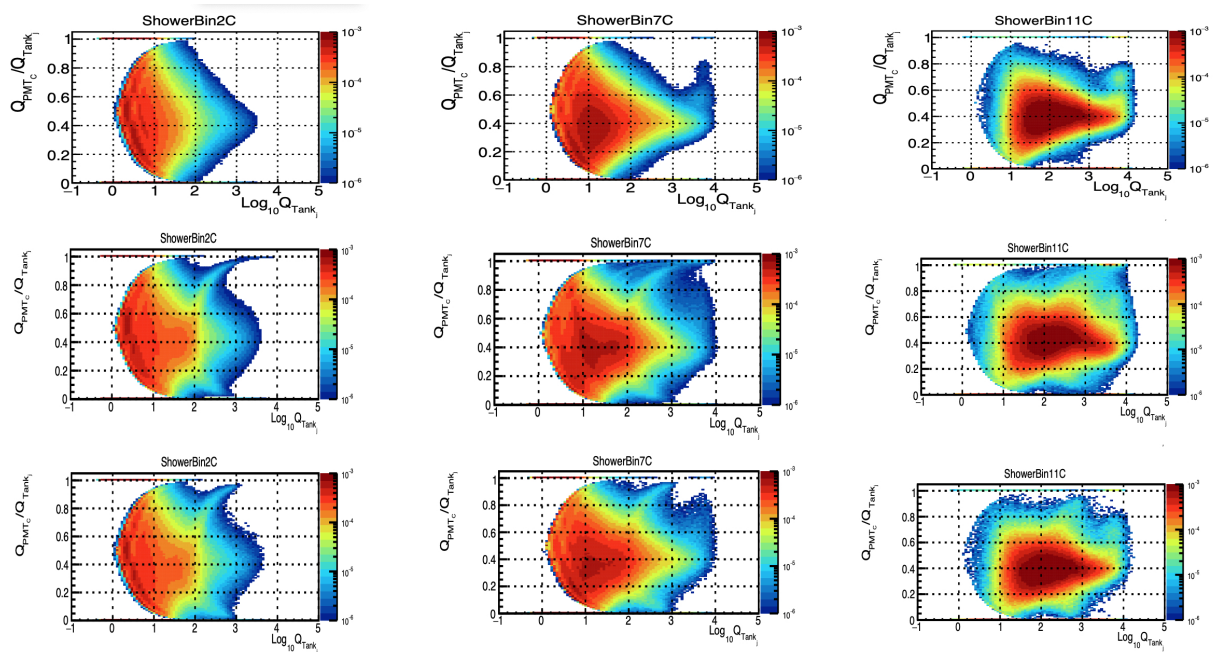
FIGURE 4.10: Probability density distributions of different event sizes. Vertically, the *left*, *middle* and *right panels* correspond to shower bins 2, 7 and 11, respectively. Horizontally, the *top*, *middle* and *bottom panels* are for gamma-simulated events, actual measurements and proton-simulated events, respectively.

is necessary because, as seen in Figure 4.11, there are cases where our MC simulations do not describe the observed data correctly. For instance, in the case of no light (top panels) or total light (bottom panels) in the PMT of interest, the distributions generated from simulated gamma-ray induced showers, simulated proton-induced showers and measured events look consistent above a PE of 1, i.e. $\log_{10} Q_{\text{Tank}_j} = 0$. In the case where all the light registered by a tank came from a single PMT (middle panels of Figure 4.11), there are significant discrepancies: For PMT C (right panel), for $\log_{10} Q_{\text{Tank}_j} \gtrsim 2.0$, proton-induced simulated showers are no longer reliable. For PMT A (left panel), the simulated proton-induced and observed showers are consistent with each other up to $\log_{10} Q_{\text{Tank}_j} \sim 1.2$ from where the measured events follow the simulated gamma-ray events. This implies that this method for gamma/hadron discrimination will not work in these regimes. These discrepancies also limit the PE cuts that can be applied to optimise the method.

Although we understand the charge distributions of individual PMTs, its relationship with other PMTs is more complex. While this approach for gamma/hadron separation depends on appropriate description of measurements by MC simulation, it has the advantage that it shows any discrepancy between simulations and measured data, which means that it can be used to improve the fidelity of the simulations to emulate actual observations. For the likelihood calculations, we do not consider cases that are not well described by MC. Further diagnostic plots regarding the charge recorded in a specific tank and participation fraction of tanks in an event are shown in Figures C.9 and C.10, respectively, in Appendix C.

An optimal analysis would involve combinations of the probability density distribution from the different PMT types as a function of the number and type of functioning PMTs in a tank. The best measurements are obtained when 4 PMTs contribute to describe the light distribution. However, this is not always the case as sometimes there are only 3, 2 or 1 working PMT(s). We ignore these cases in our computations and this work can be expanded non-trivially by considering the different permutations of working PMTs. This approach to calculate a likelihood ratio for a shower to be gamma-like, therefore, discards input from tanks that have one or more 'bad'[4] PMT. This simple approach is statistically sound as a randomly selected event still consists of a decent number of tanks contributing to the probability density distribution as shown by Figure 4.12.

4.2.2   Deriving Likelihood Ratio

For any shower, we test the hypothesis for it to be a gamma-like event or not, obtained from the probability density functions P_γ and P_d in a tank-wise integration method as

---

[4]'Bad' here is a term used for PMTs that are either broken or have been flagged as having unusually high/low event rates or unavailable.

(A)

(B)

(C)

(D)

(E)

(F)
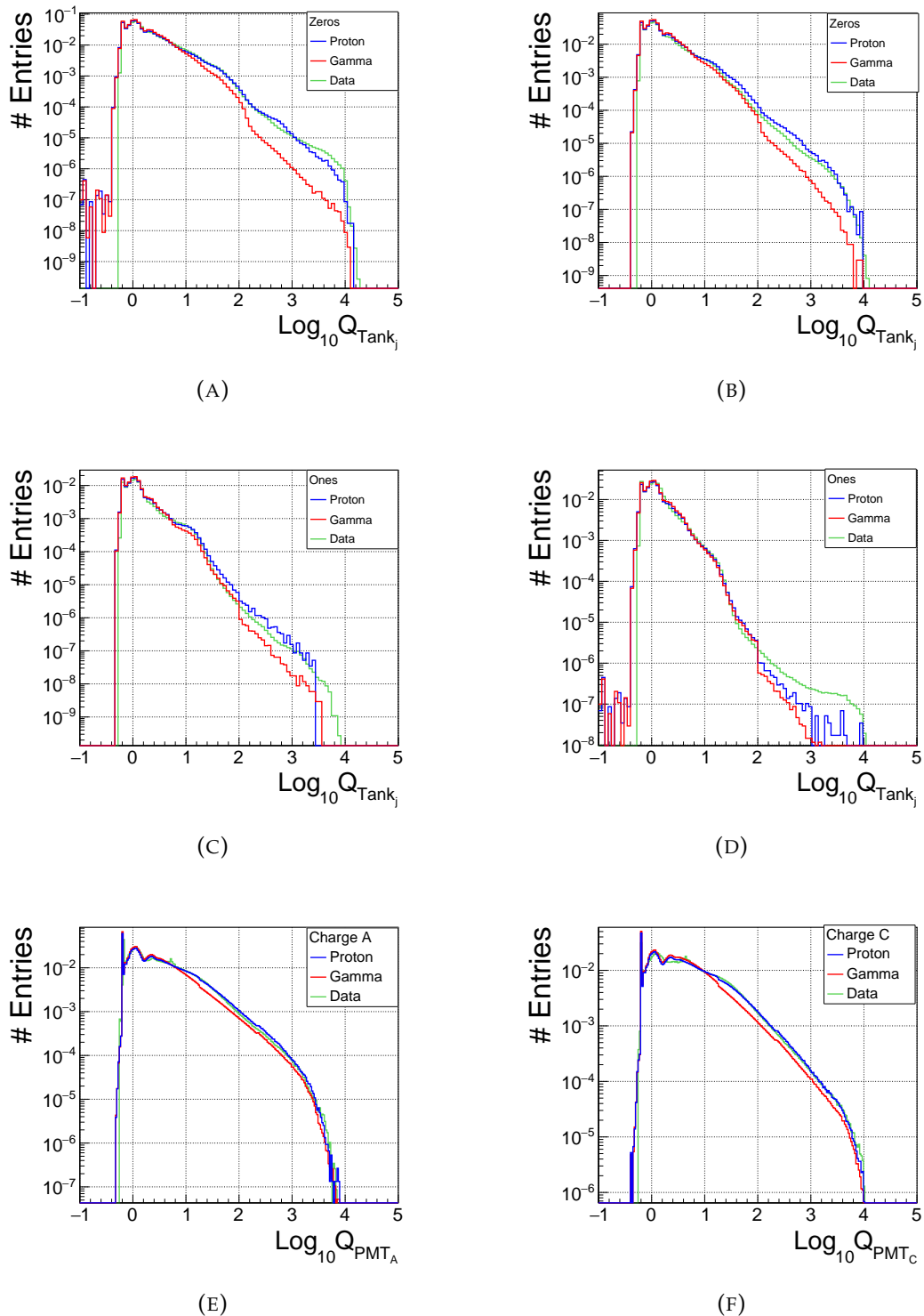
FIGURE 4.11: Comparison of the charges seen in PMT A (*left*) and PMT C (*right*) for shower bin 5. The *top* and *middle panels* are for when the PMT of interest received none or all of the light that was registered by the tank, respectively. The *bottom panel* displays the total charges by the respective PMTs. #*Entries* on the y-axis is the sampling from the probability density for the respective PMT.
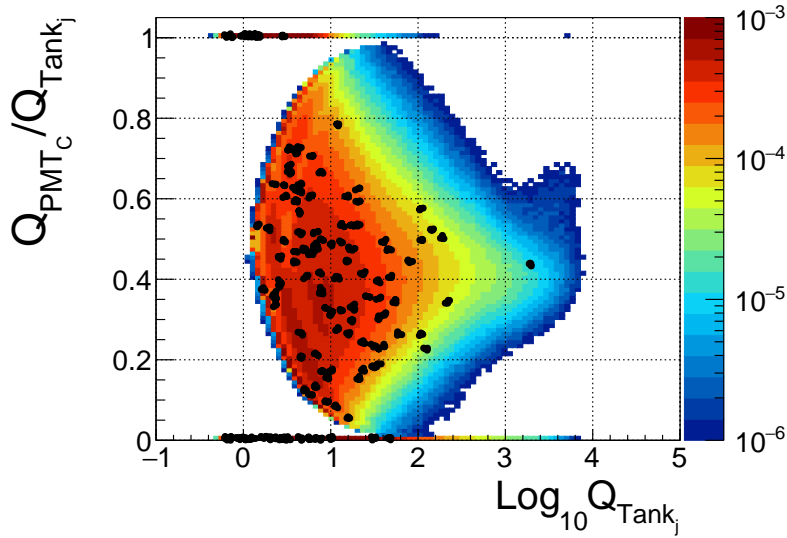
FIGURE 4.12: Number of tanks (black filled circles) in a randomly chosen gamma simulation event contributing to the derivation of the probability density distribution for PMT C for shower bin 5.

detailed by equations (4.6) and (4.7), respectively:

$$L_\gamma = \sum_j \sum_i \log_{10} P_\gamma \left(Q_{\text{Tank}_j}, \frac{Q_{\text{PMT}_i}}{Q_{\text{Tank}_j}} \right), \tag{4.6}$$

$$L_d = \sum_j \sum_i \log_{10} P_d \left(Q_{\text{Tank}_j}, \frac{Q_{\text{PMT}_i}}{Q_{\text{Tank}_j}} \right), \tag{4.7}$$

where L_γ and L_d are the log-likelihoods of simulated gamma-ray induced and measured showers. We then calculate the ratio of the two likelihoods ($R_{d/\gamma}$ or TankLHR) which translates as a difference of the log-likelihoods ($L_d - L_\gamma$). The more negative the value of $R_{d/\gamma}$, the more likely that the event is gamma-like as illustrated in Figure 4.13.[5] From the figure, it is seen that the method quantifies events as gamma-like when they are indeed gamma-ray simulated events and in the majority of cases classifies hadron-like events as not-gamma-like, as expected. Fundamentally, Figure 4.13 shows that the $R_{d/\gamma}$ value of an event can give an indication of the nature of the primary particle that caused the shower. Hence, for a given shower bin, a value of TankLHR can be defined such that showers with an $R_{d/\gamma}$ value lower than this threshold are classified as gamma events, whilst those above would correspond to hadron events. Figure 4.13 has entries from shower bins 8 - 11 as only big showers (nHits) were selected from the Crab nebula region.

---

[5]This figure displays the $R_{d/\gamma}$ distribution evaluated at a PE cut of 50, similar figures but with different PE cuts can be found in Figure C.11 in Appendix C.
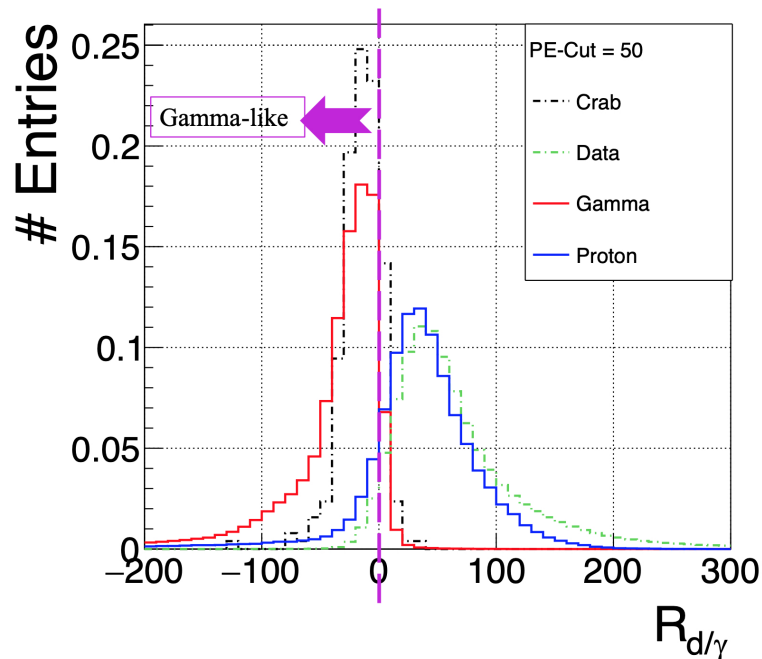
FIGURE 4.13: Normalised $R_{d/\gamma}$ distribution for simulated gammas in red, simulated protons in blue, data in green, and data specifically from the Crab nebula region in black dot-dashed lines. The more negative the distribution, the more gamma-like the events as seen in the case of pre-selected events from the Crab nebula.

From Figure 4.13, it is clear that there are still discrepancies present between measurements and MC simulations as the peak for measurements (green, labelled *Data*) does not align with that of MC proton simulations (blue, labelled *Proton*). This, however, only causes a shift in the selected value of TankLHR (cut on $R_{d/\gamma}$). Moreover, Figure 4.13 also shows that in the $R_{d/\gamma}$ parameter space, the gamma-like events are not completely separable from the hadron-like events and, therefore, need further tuning for it to provide optimal results as elaborated in the following Section 4.2.3. Lastly, given the definition of $R_{d/\gamma}$ as the difference between the logarithm of the likelihood values, $R_{d/\gamma} = L_d - L_\gamma$, the tails of the the respective distributions keep growing, with the display on Figure 4.13 truncated to illustrate the most significant parts of the $R_{d/\gamma}$ distribution.

4.2.3 Optimisation of TankLHR

Figure 4.14 illustrates the distribution of $R_{d/\gamma}$ for measurements and for gamma simulated events for two event sizes: shower bins 3 and 8. As seen in Figure 4.14, the tails of the gamma and hadron likelihood ratio distributions overlap. Because the overlap of the distributions is less for large event sizes, the discrimination power of the method gets better. It is, therefore, relevant to find a value of $R_{d/\gamma}$ for each shower bin that is gamma-ray efficient. The signal-to-noise ratio scales as the ratio of efficiencies of the gamma shower
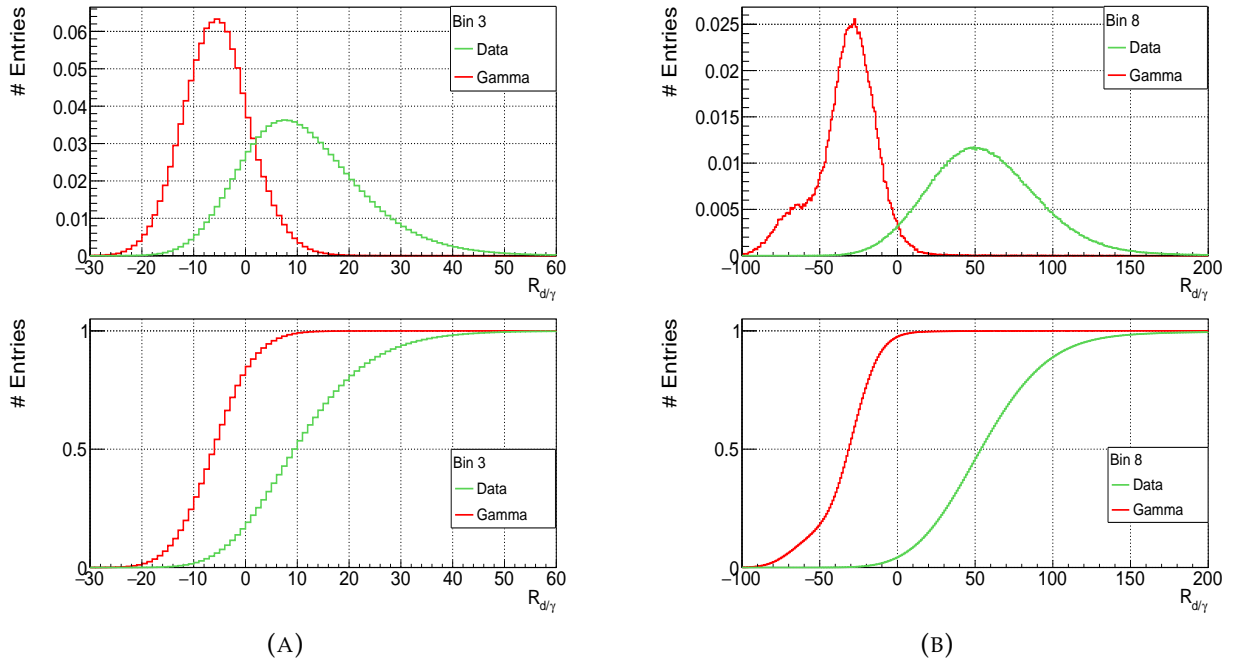
FIGURE 4.14: Normalised distributions of the likelihood ratio for shower bins 3 (*left*) and 8 (*right*). The *bottom panel* displays their corresponding cumulative forms.

accepted (ϵ_γ) to the square root of that of measured events (ϵ_d), for any chosen value of $R_{d/\gamma}$, as given by the following equation:

$$\frac{S}{N} \sim \frac{\text{Sig}}{\sqrt{\text{Bkg}}} \sim \frac{\epsilon_\gamma}{\sqrt{\epsilon_d}} \,. \tag{4.8}$$

We can extract an efficiency plot (distribution of signal-to-noise ratio) which shows the percentage of gammas accepted and protons rejected as a function of the cut we perform on the likelihood ratio as shown in Figure 4.15.[6] The trend obtained matches our expectations as a small cut would imply that we are discarding too many gamma events and a large cut would correspond to excessive contributions from hadrons. Hence, the signal-to-noise ratio pinpoints an optimal cut on the likelihood ratio that can be implemented for an efficient discrimination between gamma-like events and hadron-like events.

As mentioned earlier, the PE cut affects the optimal value of $R_{d/\gamma}$. We investigated different PE cuts of 0.1, 1, 5, 10, 20 and 50, i.e. calculating the likelihoods from the probability density distributions only if the total charge of the tank is equal to or above 0.1, 1, 5, 10, 20 and 50 PE in each case. Judging from Q_{Tank_j} and Figure 4.11, PE cuts of less than 1 and more than 100 are unreasonable choices: too low, for instance 0.1, is considered random hits and is also including a regime not correctly described by MC simulations, and

---

[6]Distribution of signal-to-noise was evaluated for $\epsilon_\gamma > 50\%$.
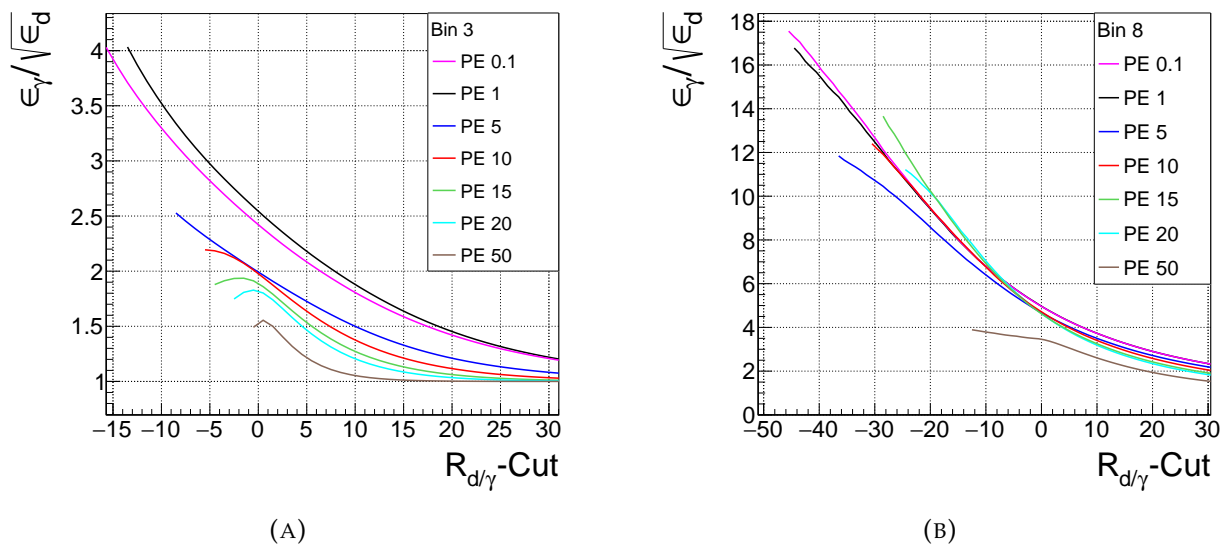
FIGURE 4.15: Distribution of the signal-to-noise ratio as a function of the likelihood ratio for different PE cuts implemented for shower bins 3 (*left*) and 8 (*right*).

too high implies discarding valuable information and reducing statistics. A PE cut of 0.1, for instance, in Figure 4.15, was evaluated to illustrate a comparison of the extent of the impact of applied PE cuts. Figure 4.16 illustrates the difference in the distribution of $R_{d/\gamma}$ for a PE cut of 1 and 50 for shower bins 3 and 8 for gamma-simulated events. The PE cuts with the highest signal-to-noise ratio for each shower bin are summarised in Table 4.2. The associated optimal $R_{d/\gamma}$ is also given, with harder cuts on bigger event sizes.

The $R_{d/\gamma}$ cuts were further tuned by optimising the significance of the Crab nebula region events. Since the discriminators currently in use in HAWC and TankLHR were found to have some underlying interdependency, as shown in Figure 4.17, the complementarity of TankLHR to PINC and COMPACT distributions were also assessed at a PE cut of 10, such that we revert to the conventional 10 nHit binning scheme. Events for a whole year (2016) of recorded HAWC data were reconstructed. Using a 2° box selection cut on reconstructed right ascension and declination, an 'on' region was defined to contain the Crab nebula. Similarly, six-non overlapping boxes with the same declination range but different right ascension ranges were defined. These were averaged to get an 'off' region.

The signal level (Excess$/\sqrt{\text{OFF}_{\text{CRAB}}}$) was computed as a function of TankLHR, PINC and LiComp, as illustrated in Figures C.12, C.13 and C.14, respectively, in Appendix C. Tuned $R_{d/\gamma}$, $\mathcal{P}$ and $\log(\mathcal{C}^{-1})$ cuts were extracted for odd-numbered event entries and assessed using even-numbered event entries for the 'on' region as shown in Figures C.15, C.16 and C.17 in Appendix C. The excess and TS (Test Statistic) functions for every pair

TABLE 4.2: Table detailing the percentage of tanks with triggered PMT(s) in the main array for each shower bin. The highest signal-to-noise ratio, the associated PE cut value and the optimal cut on $R_{d/\gamma}$ are also given.

Shower bin	Percentage of main array tanks triggered [%]	highest $\frac{\epsilon_\gamma}{\sqrt{\epsilon_d}}$	optimal $R_{d/\gamma}$	ϵ_γ [%]	PE cut
0	0.0 - 8.4	1.91	-4.5	51.8	1
1	8.4 - 16.7	2.97	-8.5	50.2	1
2	16.7 - 25.0	3.48	-10.5	52.0	1
3	25.0 - 33.4	4.03	-13.5	50.1	1
4	33.4 - 41.7	4.61	-16.5	50.8	1
5	41.7 - 50.0	5.86	-21.5	50.2	1
6	50.0 - 58.4	7.73	-27.5	50.4	1
7	58.4 - 66.7	11.08	-34.5	51.5	1
8	66.7 - 75.0	16.77	-44.5	51.4	1
9	75.0 - 83.4	28.44	-59.5	50.3	1
10	83.4 - 91.7	27.51	-56.5	72.5	10
11	91.7 - 100.0	172.61	-81.5	52.3	50

of discriminator are illustrated in Figures C.18 to C.23 in Appendix C. Using these functions, a combined set of cuts that results in the most significant signal was found and is summarised in Table 4.3. In that case, Figures 4.18 and 4.19 show the events passing separately the TankLHR, PINC and LiComp selection cuts.

4.3   Summary

A new method for gamma/hadron discrimination was described that is based on the light distribution in WCDs to define likelihood functions for showers to be gamma-induced or not. We made comparisons between measurements and MC simulations and optimised our results. While this approach does not have the best discrimination power, it separates gamma-induced showers from hadron-induced showers independent of core reconstruction. The TankLHR discriminator works complementary to the existing gamma/hadron separators and the efficiencies for different shower sizes were provided. As shown by Figure 4.11, while there is global agreement between our current MC simulations and
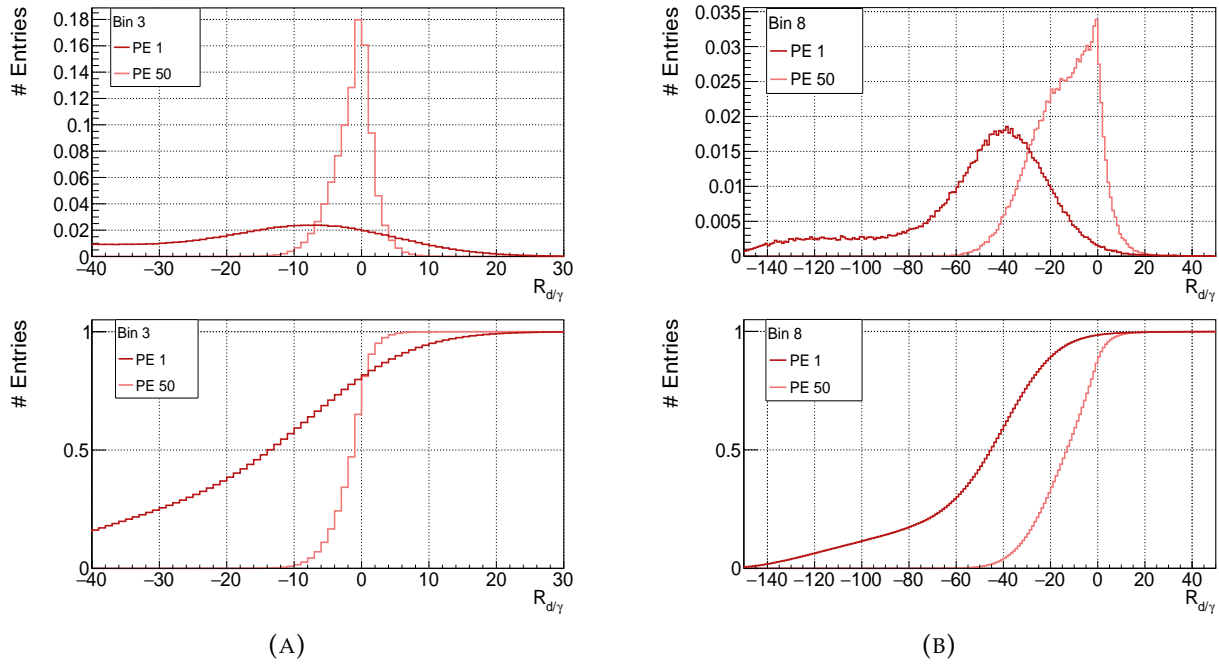
FIGURE 4.16: Normalised distributions of the likelihood ratio for gamma-simulated showers in shower bins 3 (*left*) and 8 (*right*) for implemented PE cuts of 1 and 50. The *bottom panel* displays the corresponding cumulative forms.

TABLE 4.3: Table detailing the optimal combined cuts on LiComp, PINC and TankLHR for the highest TS of the Crab nebula.

$\mathcal{B}$	Highest TS	Discriminator		
		LiComp	PINC	TankLHR
0	26.8	-4.36	2.36	-4.32
1	68.5	-1.40	2.36	3.06
2	255.5	-2.44	2.17	15.36
3	605.2	-2.68	2.08	12.90
4	563.4	-2.76	2.03	17.00
5	639.4	-2.84	1.90	17.00
6	426.8	-2.84	1.71	17.00
7	242.0	-2.92	1.85	3.88
8	170.4	-2.52	1.57	10.44
9	173.8	-2.04	1.30	-2.68

(A)

(B)

(C)
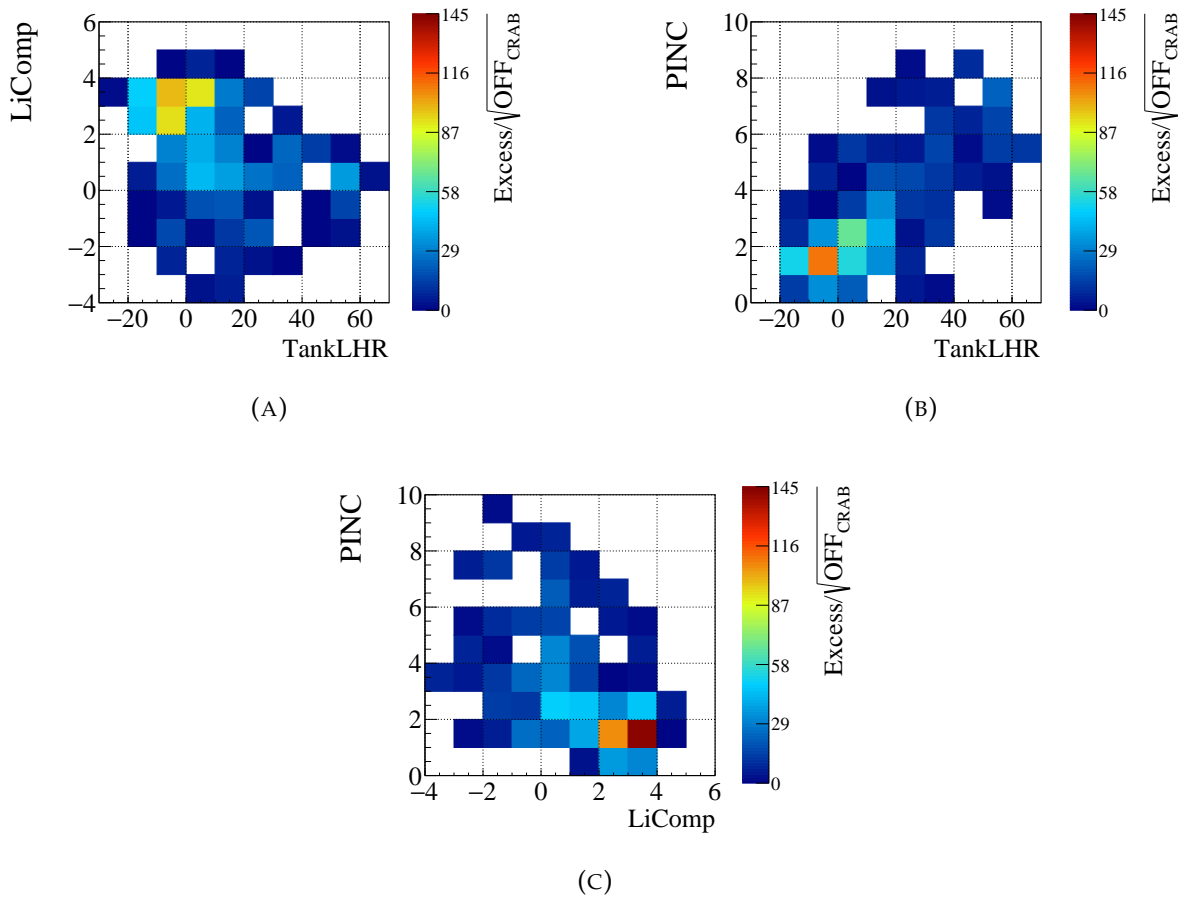
FIGURE 4.17: Discriminator interdependency for TankLHR, PINC and LiComp for nHit bin 3.

HAWC measured data, there are also instances where the MC simulations do not describe the measurements correctly. This approach has the advantage of showing any discrepancy between simulations and measured data, which means that, on top of being a gamma/hadron discriminator, it can additionally be used to improve the MC simulations to more accurately reflect actual observations.
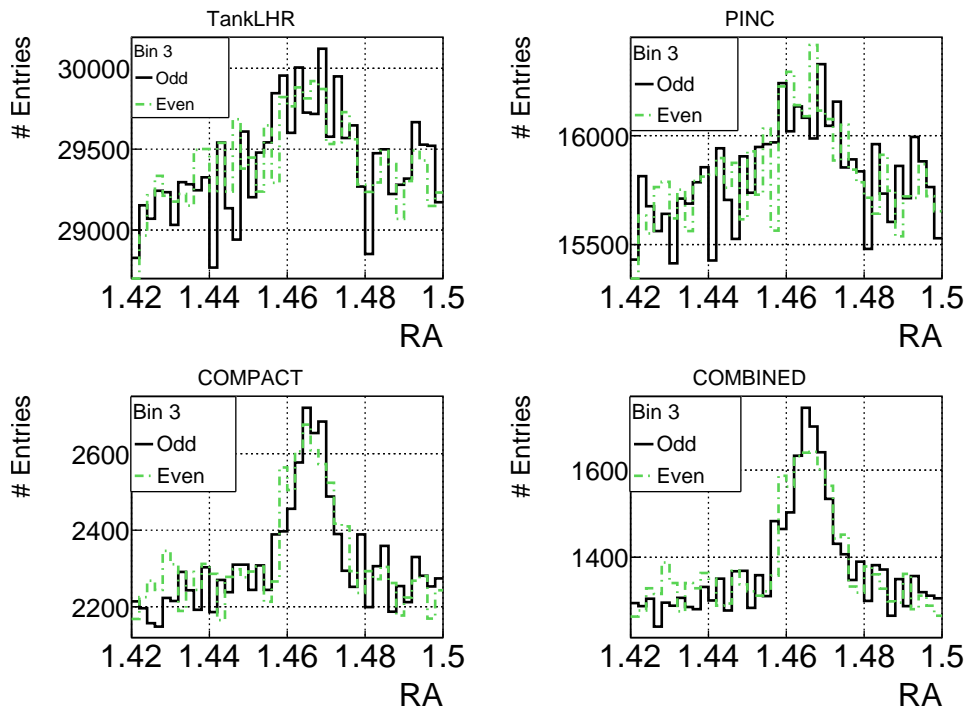
FIGURE 4.18: Events passing optimal TankLHR, PINC and LiComp cuts for nHit bin 3.
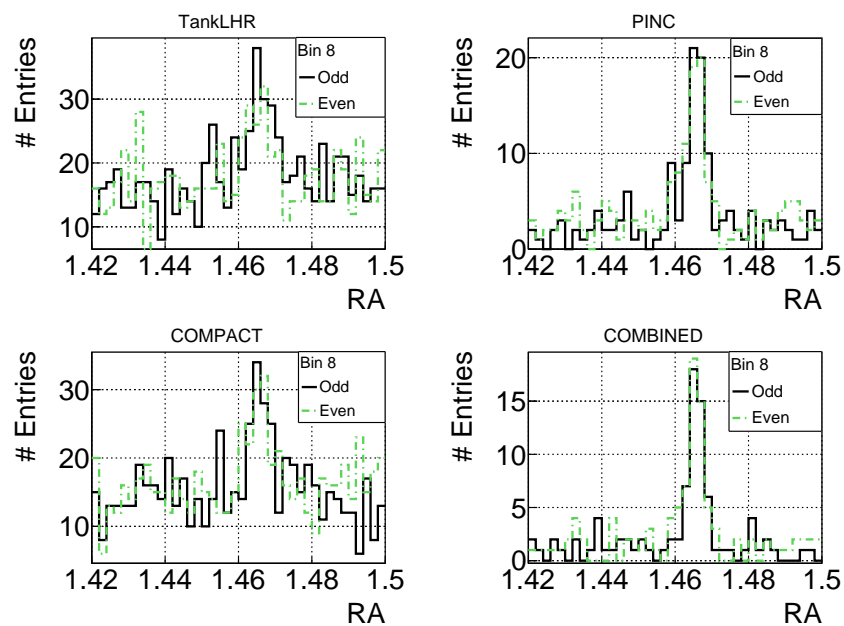
FIGURE 4.19: Events passing optimal TankLHR, PINC and LiComp cuts for nHit bin 8.

5

A New Approach to Background Modelling for HAWC

A major challenge in ground-based gamma-ray astronomy is the removal of the contribution from non-gamma-ray induced showers that pass gamma/hadron separation. It is important to correctly estimate this contribution as an over- or underestimate would lead to fake deficit or excess signal. In this chapter, we generate different maps from HAWC data, namely: maps that pass gamma selection of events, maps that pass hadron selection of events, the conventional HAWC background map, a new background map, excess maps and exposure maps. The exposure map provides the expected counts from different regions of the sky based on the amount of time that the region was in the field of view. It is very convenient as it allows the rapid extraction of spectral information for any region of the sky independent of spatial assumptions.

5.1 Building the Gamma-like Event Sky Map for HAWC

After the reconstruction process described in Chapter 4, there are parameters that describe the direction of the incoming particle (cf. Subsection 4.1.2) which can be used to project the reconstructed events onto the equatorial sky. The Hierarchical Equal Area isoLatitude Pixelation (HEALPix) scheme (Górski et al., 2005) is used in the mapping of HAWC reconstructed events onto a 12-piece tessellated sphere. Each tessellation is referred to as a base pixel. All base pixels cover the same area and can each be divided into 4 pixels which can be further subdivided into smaller area pixels to achieve higher

map resolution. The resulting grid has a resolution parameter denoted as N_{side}, where the number of pixels is $12 \times N_{\text{side}}^2$. The higher the number of pixels, the more computationally intensive the calculations are, hence we chose to work with an N_{side} of 256 for data taken from 27$^{\text{th}}$ November 2014 to 20$^{\text{th}}$ December 2017. In essence, a HAWC sky map is a display of the sum of reconstructed events that were projected in each pixel of size 0.228°.

The reconstructed event list is divided into groups (called `chunks`) of 2 hour period during which the detector was stable (Fiorino, 2017). In other words, random dead time and maintenance time are removed prior to the map-making procedure. Selection cuts on the different gamma/hadron separators (for this study, cuts were applied on PINC and COMPACT) can be applied to the reconstructed events to select gamma-like events and hadron-like events as shown in Figure 5.1. The cuts to select gamma-like events are given in Appendix C and are the same as in HAWC Collaboration et al. (2017c) while the cuts to select hadron-like events are given in Appendix D and were chosen, without loss of generality[1], to account for the very hadron-like events.

(A) PINC Distribution

(B) COMPACT Distribution
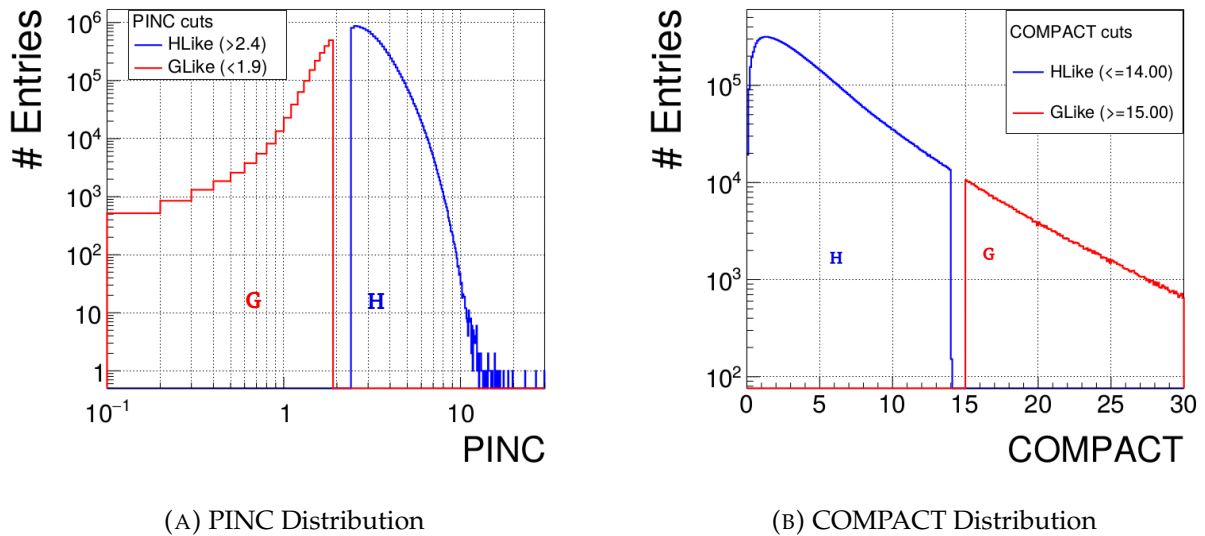
FIGURE 5.1: Selection of gamma-like events (red, $\mathcal{G}$ region) and hadron-like events (blue, $\mathcal{H}$ region) from the distribution of PINC (*left panel*) and COMPACT (*right panel*) for nHit bin 4.

A `map-maker` from HAWC (implemented in `AERIE`) performs the aforementioned HEALPix mapping using the `chunks` and returns, for each nHit bin, an all sky gamma-like event map ($\mathcal{G}$cut), an estimated background map, an on-time array describing the exposure of the sky to the instrument, amongst other output (Fiorino, 2016). The gamma-like event map (displayed in Figure 5.2) is generated from events that lie in the parameter space labelled $\mathcal{G}$ in Figure 5.1. Figure D.1 in Appendix D shows the gamma-like event map

---

[1]The choice of the extent of the hadron-like distribution is justified in Section 5.2.2.

for all nHit bins. The $\mathcal{G}$cut map is still dominated by background events (cosmic-ray induced air showers) even after applying gamma selection cuts. The contribution of the aforementioned background events can be thought of as the tail of the hadron-like event distribution (blue line in Figure 5.1) in the $\mathcal{G}$ region. The difference between the gamma-like event distribution and that tail is the excess signal of interest. To estimate this excess, one must first model the tail of the hadron-like event distribution, i.e. model the background seen through HAWC.
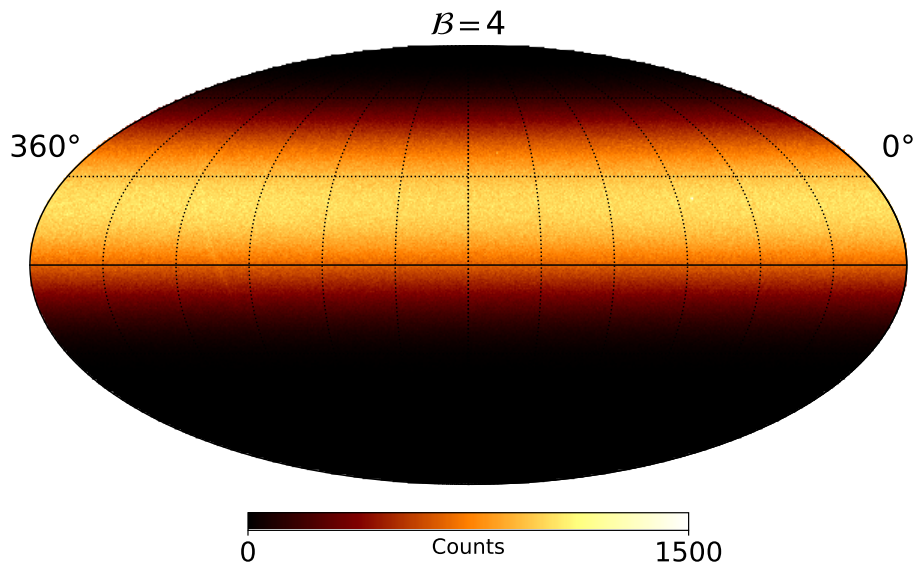
FIGURE 5.2: Gamma-like event map for $\mathcal{B} = 4$. The map was saturated at $1\,500$ for display purposes.

5.2 Background Modelling

5.2.1 Direct Integration

Currently, the standard background estimation method employed in HAWC is 'Direct Integration' (DI) which is a convolution of the event rate with the local arrival direction in a given time period, typically 2 hours. Within this time step, events rates are summed to form an integrated rate array, $\mathcal{R}(t)$, and a local arrival map is built by summing events from regions of the sky constituting a pixel. At the end of the time step, the arrival map is normalised to form an acceptance map, $\mathcal{A}(\mathrm{HA}, \mathrm{dec})$, which represents the local detector efficiency, i.e. how sensitive the detector is to different parts of the sky. This acceptance map is then convolved with the array of integrated rates as follows:

$$B_{\mathrm{DI}} = \int \mathcal{R}(t)\mathcal{A}(\mathrm{HA}, \mathrm{dec})\mathrm{d}t \,, \tag{5.1}$$

and the process is repeated over the next time steps until the end of the dataset to build the DI background model. Figure 5.3 depicts the counts estimate using DI for nHit bin 4 (Figure D.2 in Appendix D shows the same for all nHit bins).
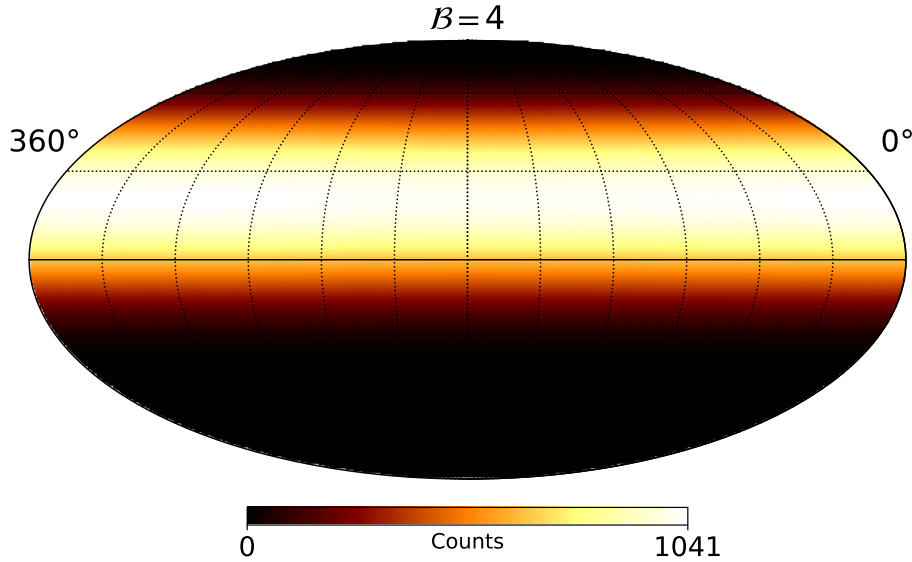
FIGURE 5.3: Counts estimate for $\mathcal{B} = 4$ using DI technique of background estimation.

Caveats of DI and motivation for a novel approach to background modelling

The DI method, as described above, suffer from the following limitations, thereby substantiating the need for an improved novel approach:

1. Disregards some events

   The mean local detector efficiency over the integration duration is taken as the normalised arrival map for that time step. As such, this method assumes that the acceptance of the detector is independent of the trigger rate for a period corresponding to the time step. The 2 hour period was chosen as a trade-off between collecting ample statistics for background estimation and minimising systematics stemming from variations in acceptance of the detector. For large-scale structures with faint emission, however, a larger integration time is required to provide sufficient statistics for the same accuracy (HAWC Collaboration et al., 2017c). One can generate chunks of 24 hours, but these will contain far less statistics as only the times when the detector was stable for 24 consecutive hours would contribute to building the DI background.

2. Cosmic-ray isotropy

   Another assumption made in DI is that the background produced from cosmic rays is isotropic (Atkins et al., 2003). But this is not consistent with actual observations,

in particular that of a local cosmic-ray anisotropy as shown in Figure 5.4 (HAWC Collaboration et al., 2018a). While working with point sources or sources of small angular extent, the local cosmic-ray anisotropy might not be relevant but in the study of large-scale structures, one has to account for anisotropy effects.
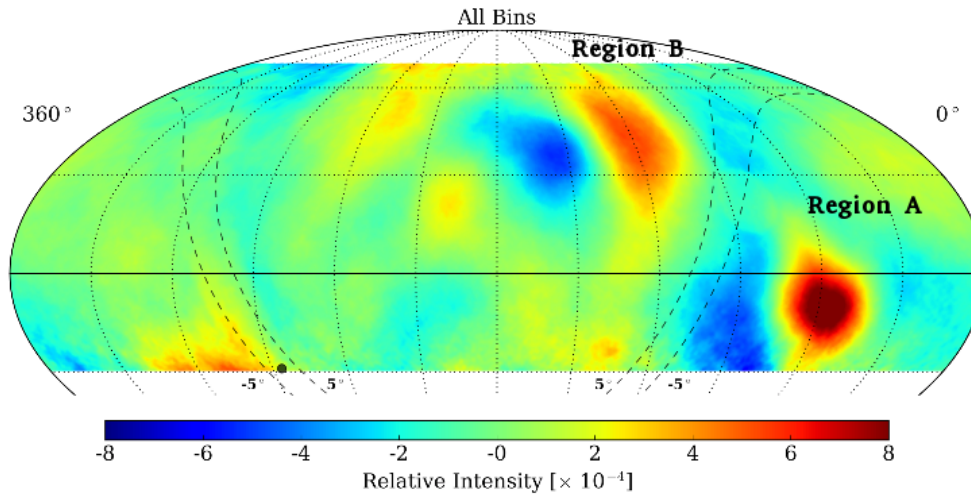
FIGURE 5.4: All sky cosmic-ray anisotropy in the HAWC field of view (HAWC Collaboration et al., 2018a).

3. Time consuming

   Given the way DI is computed, i.e. a normalisation after every time step involved in building the acceptance map, generating a DI background map is time intensive. Moreover, it must imperatively be computed at the same time as the event maps, slowing down the entire map-making process.

   Due to the limitations of DI listed above, it is crucial to have a different approach to model the background. In this novel background modelling scheme, all statistics can be used irrespective of detector stability, cosmic ray anisotropy is accounted for as the background model will be developed to have a right ascension (RA) dependency as well as a declination dependency, with the method staying computationally and user-time effective.

5.2.2 Model Background - Modelling Background using Hadron-like Events

Although events in the maps are from 27th November 2014 to 20th December 2017, they cover only 800 days because a 24 hour integration time was specified during the map-making process to generate reliable DI maps for comparison to new background maps generated through 'Model Background' (MB) which is a new approach to background estimation.

Input and Assumptions

The requirements of MB are:

1. Events maps — $\mathcal{G}$cut and $\mathcal{H}$cut
   We hereby define $\mathcal{H}$cut, an all sky map of hadron-like events (shown in Figure 5.5) which is produced in a similar way as the $\mathcal{G}$cut map (cf. Section 5.1) but using different gamma/hadron selection cuts as elaborated in Appendix D, i.e events in the parameter space labelled $\mathcal{H}$ in Figure 5.1. Henceforth, G_i denotes counts in a pixel (i) of a $\mathcal{G}$cut map and similarly H_i for an $\mathcal{H}$cut map.
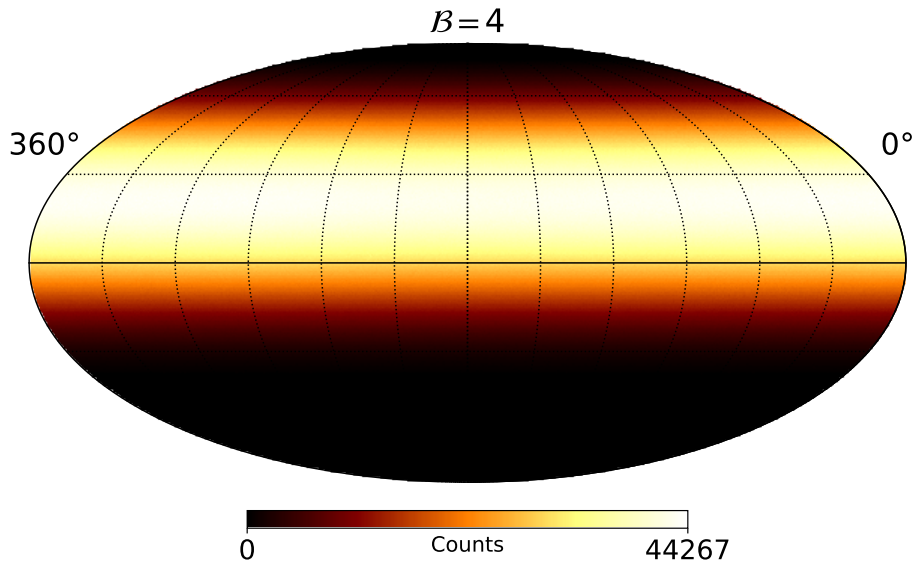
FIGURE 5.5: Hadron-like event map for $\mathcal{B} = 4$. Entries are events that pass the hadron selection cuts as elaborated in the text.

2. Masked regions
   To avoid any bias, MB requires computation from regions with probable gamma-ray emission masked out. This was done by building a map of the same N_{side} as the events maps, and masking out pixels within a certain angular extent from the position of known gamma-ray sources. This angular extent of the mask depends on the HAWC PSF and the extension of the source itself. For this purpose, circles of radii 2.6° for the Crab nebula, 2° for Markarian 421 (Mrk421), 2° for Markarian 501 (Mrk 501), 6° for Geminga, 6° for PSR B0656+14 were used. Moreover, a disk of 20°($\pm$10°) was used to mask out all the HAWC sources that lie about the Galactic plane. The northern *Fermi* bubble was also masked out, using a template[2] from `Fermi Tools`[3] as illustrated in Figure 5.6.

---

[2]gal2yearp7v6_v0.fits
[3]https://fermi.gsfc.nasa.gov/ssc/data/access/lat/BackgroundModels.html
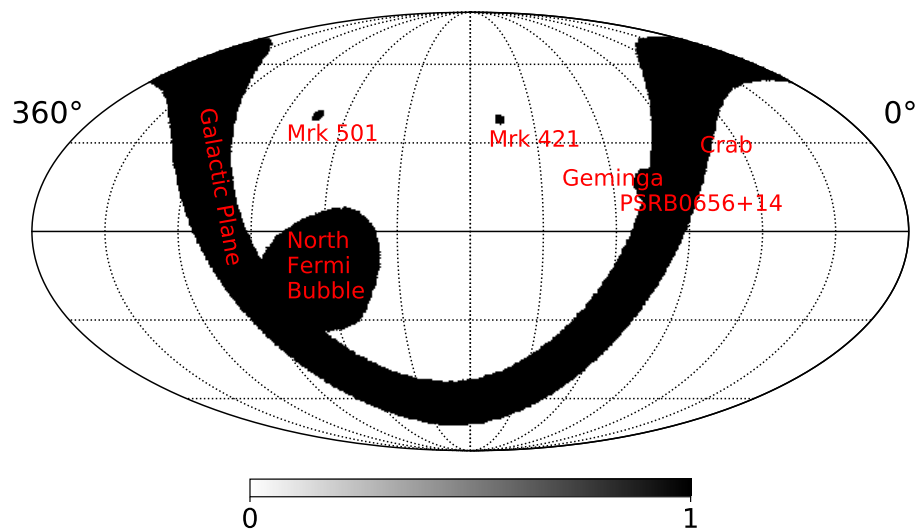
FIGURE 5.6: Map showing the mask used to avoid contamination from known gamma-ray emission regions: Crab Nebula, Mrk 421, Mrk 501, Geminga, PSR B0656+14, the Galactic plane and north *Fermi* bubble.

3. Livetime corresponding to the time for events used in the maps

   This is basically a count of the number of transits of different parts of the sky corresponding to the time during which the instrument was recording the data set in use, as shown in Figure 5.7. At this point, this is not a direct input to the method but is rather used to compare and understand the behaviour of the data set. It is an input for modelling the exposure maps and is therefore elaborated in Section 5.4.
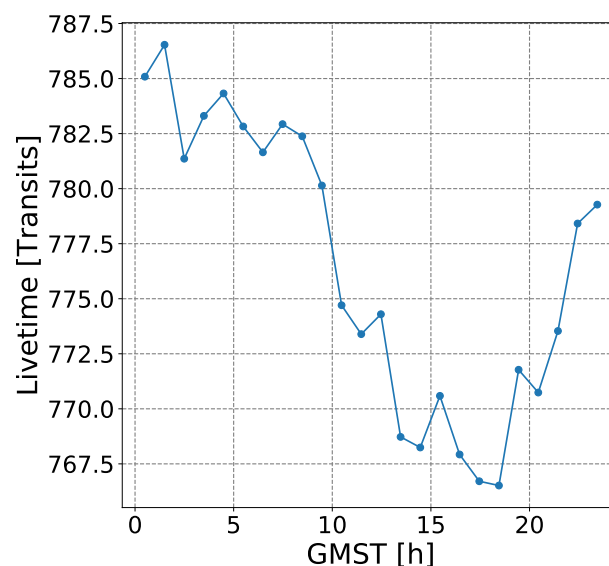
FIGURE 5.7: Number of recorded transits for different parts of the sky as a function of Greenwich Mean Sidereal Time. This is the on-time of the HAWC instrument corresponding to the data set in use.

In MB, we assume that there is no significant deviation in the behaviour of the tail of the distribution of hadron-like events (cf. Section 5.1), such that the selected very hadron-like events, as shown in Figure 5.1, can be used to parameterise this tail. The acceptance of an instrument is the probability of reconstructing a background event with a certain energy and direction after applying trigger, analysis and selection cuts (Berge, Funk, and Hinton, 2007). The instrument responds differently to gamma-like events than to hadron-like events. In a parameter phase space diagram like Figure 5.1, the further apart the $\mathcal{G}$ and $\mathcal{H}$ regions, the more significant is the difference in acceptance (Berge, Funk, and Hinton, 2007). While the extent of the $\mathcal{G}$ region is nominal for HAWC (as established in Chapter 4), the extent of the $\mathcal{H}$ region is a compromise between good separation from the $\mathcal{G}$ region and ample statistics to make a normalisation factor using events from those two regions small ($\ll 1$). Another (technical) assumption we employ in the tail-fitting procedure is that parameter variations in RA and declination are independent of each other. A third assumption is that the white region in Figure 5.6 is free of gamma-ray sources or consists of isotropic gamma-rays.

5.2.3 Generating an RA-Dec Dependent Background Model

We now proceed with a step-by-step derivation of MB which is a parameterisation of the distribution of hadron-like events in the $\mathcal{G}$ region. Basically, we scale the number of events in the $\mathcal{H}$ region to predict its behaviour in the $\mathcal{G}$ region. This scaling factor, $\mathcal{Y}$, is the acceptance-weighted relative exposure of the unmasked part of the sky (Berge, Funk, and Hinton, 2007) (cf. Figure 5.6). The acceptance, in turn, depends on zenith and azimuth angles, although the variation along zenith is expected to be the dominant effect. Figure 5.8 shows the instantaneous field of view of HAWC, in local and sky coordinates, which demonstrates this dominance. On the left map (local coordinates), the concentric rings represent different zenith angles while the radial lines correspond to different azimuth angles. Typically, at a specific zenith, there is only a small variation seen along azimuth but there is a significant gradient along zenith for a specific azimuth. Therefore, $\mathcal{Y}$ varies with RA and declination with the variation in declination being more assertive than that in RA.

Let the scaling with declination be a-factor. It is defined as the ratio of events in the $\mathcal{G}$ phase space region to that in the $\mathcal{H}$ phase space region (cf. Figure 5.1) as follows:

$$a(\delta) = \frac{G_\delta}{H_\delta},$$

(5.2)
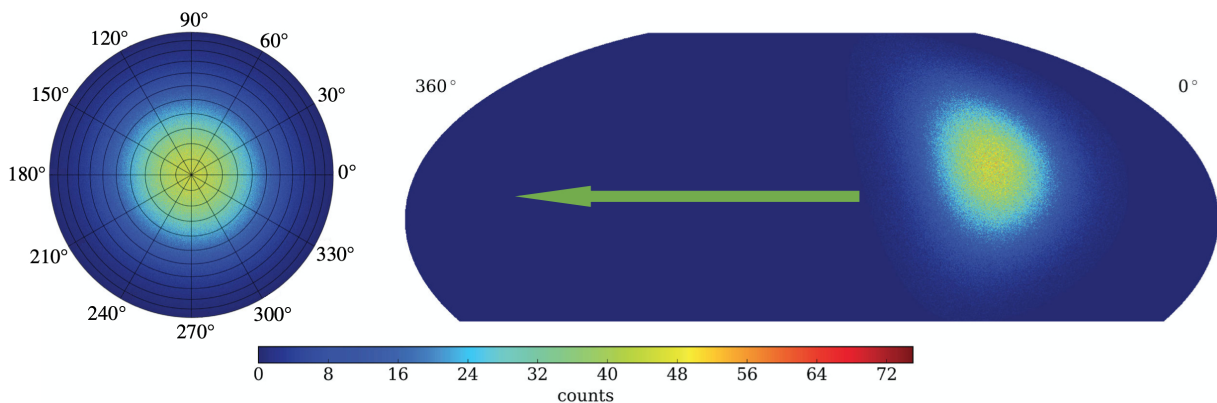
FIGURE 5.8: Instantaneous field of view of HAWC in local (*left panel*) and sky (*right panel*) coordinates (Martinez-Castellanos, 2016). The field of view moves as shown by the green arrow as the Earth rotates.

where G_δ and H_δ are counts from the respective maps, averaged over 2° declination window. A smooth form was obtained by using a moving average of 0.1° and a_i was determined by interpolating $a(\delta)$ linearly across declination rings of the HEALPix map. The top right panel of Figure 5.9 indicates the distribution of a-factor with declination for all nHit bins, while the top left panel illustrates only the distribution for nHit bin 4 ($\mathcal{B} = 4$). In both panels and following figures, only the variations within the field of view of HAWC, $-25° < \delta < +65°$, are shown. The events statistics in the $\mathcal{H}$ region are significantly larger than that in the $\mathcal{G}$ region, such that $a \ll 1$. Figure 5.9(A) shows that the variation in a-factor is over a factor of 2 only. The shape, whereby the a-factor decreases with increasing zenith or declination, matches our expectations as showers for larger zenith angles must encounter a thicker layer of medium before triggering the instrument. As the zenith angle increases, so does the shower absorption, such that the event rate decreases. Figure 5.9(B) shows that there is a systematic decrease overall in a-factor values across nHit bins, which might be a consequence of the decrease in statistics for higher nHit bins. An advantage of this approach is that it does not assume radial symmetry for the acceptance. Any asymmetry, resulting from the fact that HAWC is not a symmetric instrument or that γ/hadron selection cuts are azimuth angle dependent, is encoded naturally, as illustrated in the bottom left panel of Figure 5.9. Therein, δ_{HAWC} is the declination of the HAWC observatory and North/South are declinations that are bigger/smaller than δ_{HAWC}, respectively. Additionally, the bottom right panel of Figure 5.9 illustrates $\mathcal{D}_{\mathrm{NS}}$, the fractional deviation of North and South from an averaged behaviour of a-factor over $\delta - \delta_{\mathrm{HAWC}}$:

$$\mathcal{D}_{\mathrm{NS}} = 2 \times \left[\frac{a_N - a_S}{a_N + a_S} \right] \times 100\% \,. \tag{5.3}$$

The variations increase with bin size and a reason for this might be that we have far less statistics in $\mathcal{B} = 9$ than in $\mathcal{B} = 1$, thereby increasing the statistical uncertainty associated with higher nHit bins. We do not fully understand the behaviour shown, i.e., for instance for nHit bin 6, why there are more counts from the South and then a switch to a higher number of counts from North.

(A) $\mathcal{B} = 4$

(B) $\mathcal{B}$: 1 - 9

(C) $\mathcal{B} = 4$; Showing North/South asymmetry

(D) $\mathcal{B}$: 1 - 9; Showing north/south asymmetry
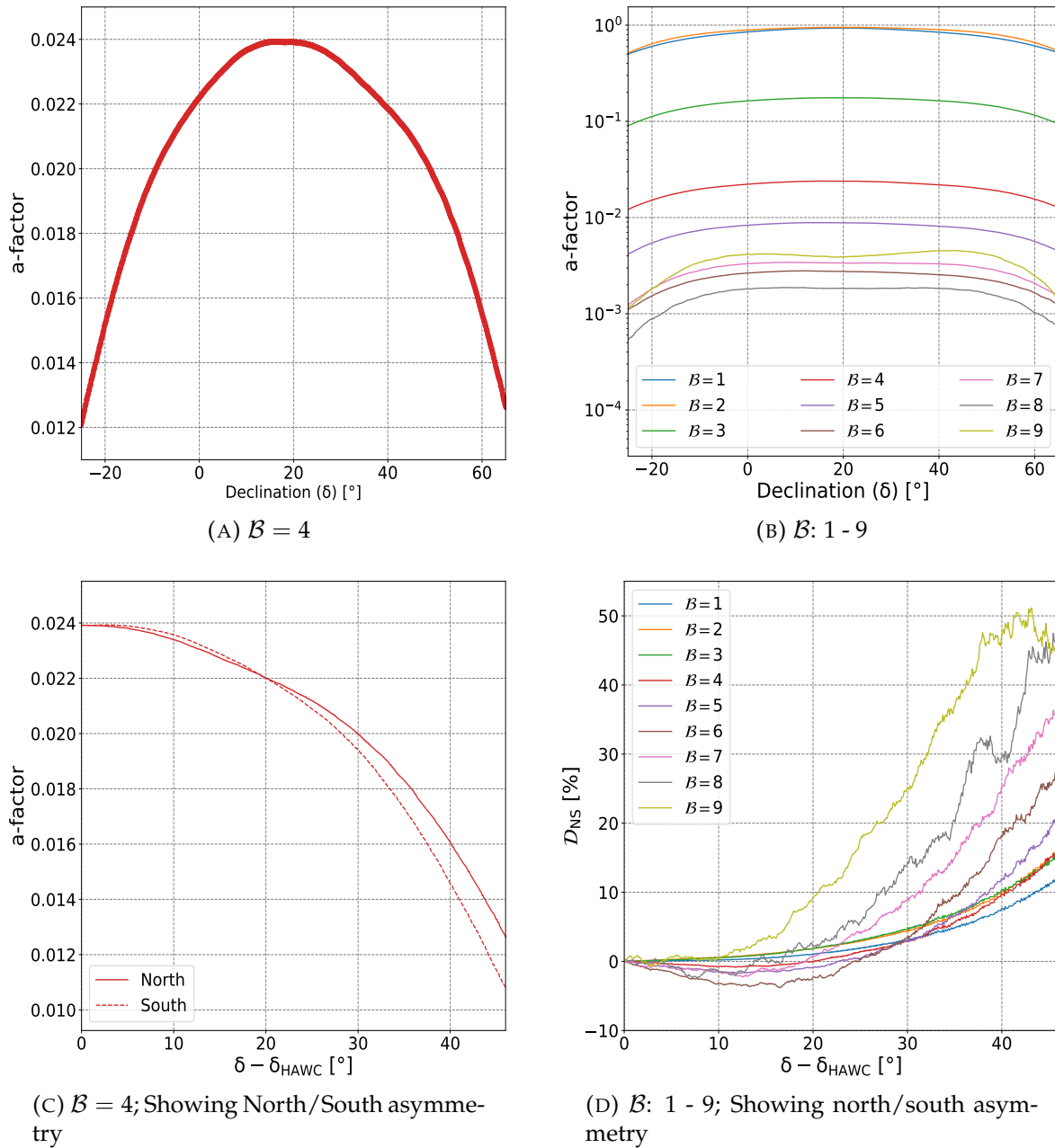
FIGURE 5.9: Distribution of *a*-factor as a function of declination for $\mathcal{B} = 4$ (*left panel*) and $\mathcal{B}$: 1 - 9 (*right panel*).

Since we want both a declination and RA dependent model, we take $\mathcal{Y}$ to be a product of *a*-factor as a function of declination (δ) and *b*-factor as a function of RA. Assuming an

independent behaviour in RA and in declination, we determined the distribution in RA
by factoring out the declination dependence from the pixel to pixel variation,

$$b'_i = \left(\frac{G_i}{H_i}\right) \div a_i \, . \tag{5.4}$$

b'_i was then averaged per $1°$ RA bin to extract $b'(\text{RA})$. The magnitude of the variations
in RA is small, such that statistical fluctuations dominate even after averaging over $1°$ as
depicted in the top left panel of Figure 5.10. Hence, a smoothing of the following type
was applied:

$$b(\text{RA}) = \mathcal{S}_G\left[b'(\text{RA})\right] \, . \tag{5.5}$$

$\mathcal{S}_G$ is a Gaussian smoothing function whose kernel (in degrees) depends on the nHit bin
as: *kernel* $= 2\mathcal{B} + 15$. This approach, using all data in deriving the background, provides
us with the flexibility of tuning the smoothing we apply across nHit bins. The smoothing
kernel was made to vary with $\mathcal{B}$ as we have a lot more statistics in smaller nHit bins
compared to higher ones. b_i was determined by interpolating $b(\text{RA})$ linearly through
neighbouring pixels.

The bottom left panel of Figure 5.10 illustrates the distribution of b-factor with RA for
nHit bins 1 to 5 and the right panel for nHit bins 6 to 9. The top panels are specifically for
nHit bin 4: the left panel shows the b-factor before and after smoothing (*kernel* $= 25°$),
while the right panel displays the comparison of the smoothed b-factor to the relative
livetime of HAWC corresponding to the time for events in the maps (see Section 5.4 for
more details). This shows that the main variation in RA results from a variation in live-
time, but there is also a contribution from the cosmic ray anisotropy at a level of 10^{-4}
(HAWC Collaboration et al., 2018a). The distribution along declination (in a-factor) is
the dominant contribution as expected. Once a- and b-factors have been calculated, they
can be multiplied together to extract the $\mathcal{Y}$-factor which can subsequently be convolved
with the $\mathcal{H}$cut map to acquire a new background estimate — MB ($B_{\mathcal{Y}_i}$) as given by the
following equations:

$$\mathcal{Y}_i(\text{RA}, \delta) = a_i(\delta) \times b_i(\text{RA}) \tag{5.6}$$

$$B_{\mathcal{Y}_i} = \mathcal{Y}_i H_i \, . \tag{5.7}$$

The resulting map for nHit bin 4 is shown in Figure 5.11 while for all nHit bins is given
in Figure D.3 in Appendix D.

(A) $\mathcal{B} = 4$: raw and smoothed (with a kernel of 25°) fluctuations in b-factor

(B) Relative livetime compared to smoothed b-factor for $\mathcal{B} = 4$

(C) Smoothed b-factor for $\mathcal{B}$: 1 - 5

(D) Smoothed b-factor for $\mathcal{B}$: 6 - 9
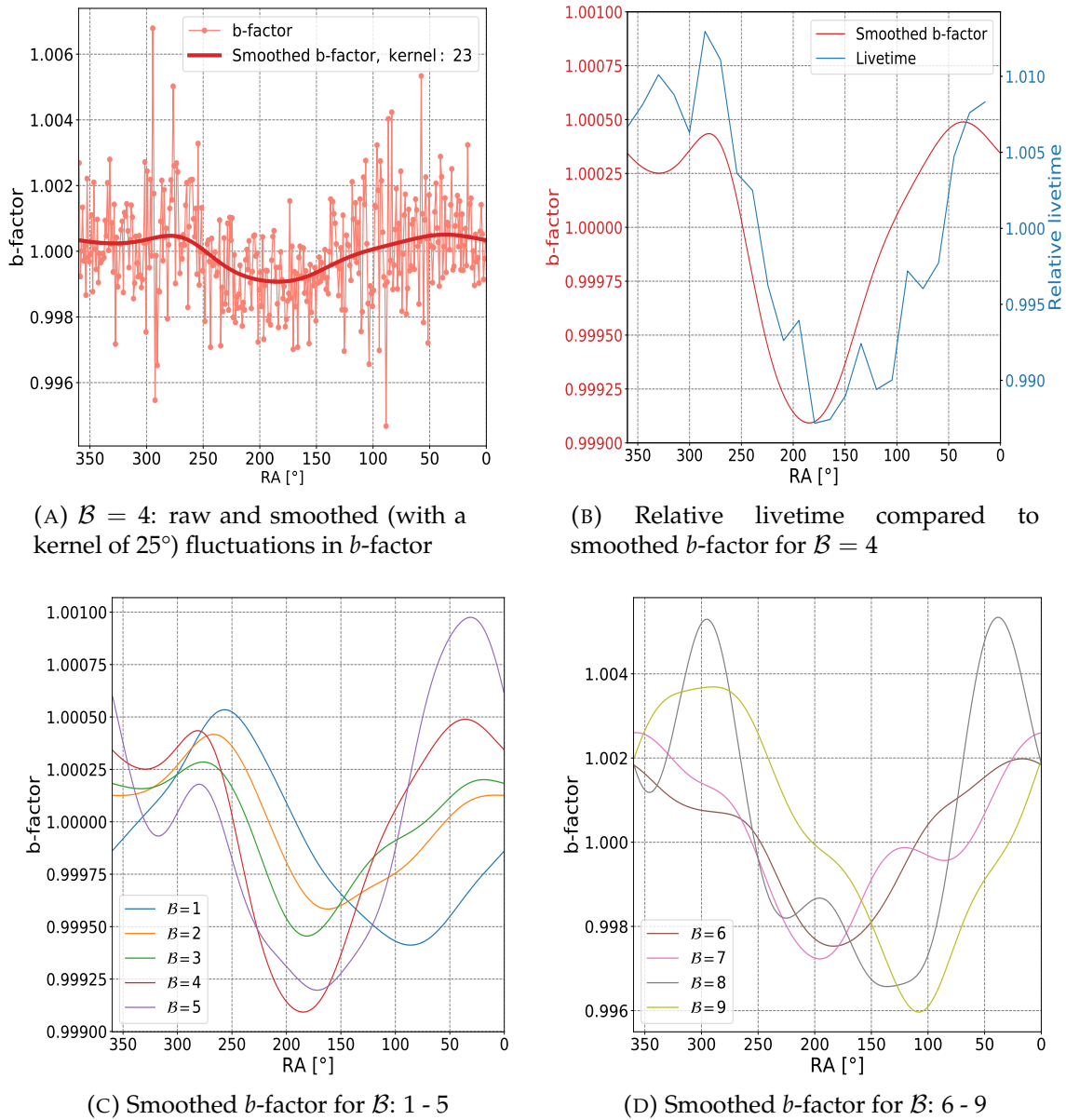
FIGURE 5.10: Distribution of b-factor as a function of right ascension.

5.3 Excess Maps

Now that we have a background model that incorporates the isotropic and anisotropic cosmic rays, we can subtract it from the data map to compute an excess map ($\mathcal{E}_i$):

$$\mathcal{E}_i \equiv G_i - B_{\mathcal{Y}_i} = G_i - \mathcal{Y}_i H_i \, . \tag{5.8}$$

This map indicates regions from which more events were recorded and consequently the regions of candidate sources as shown in Figure 5.12. The excess maps of all nHit bins derived from MB are provided in Figure D.4 in Appendix D.
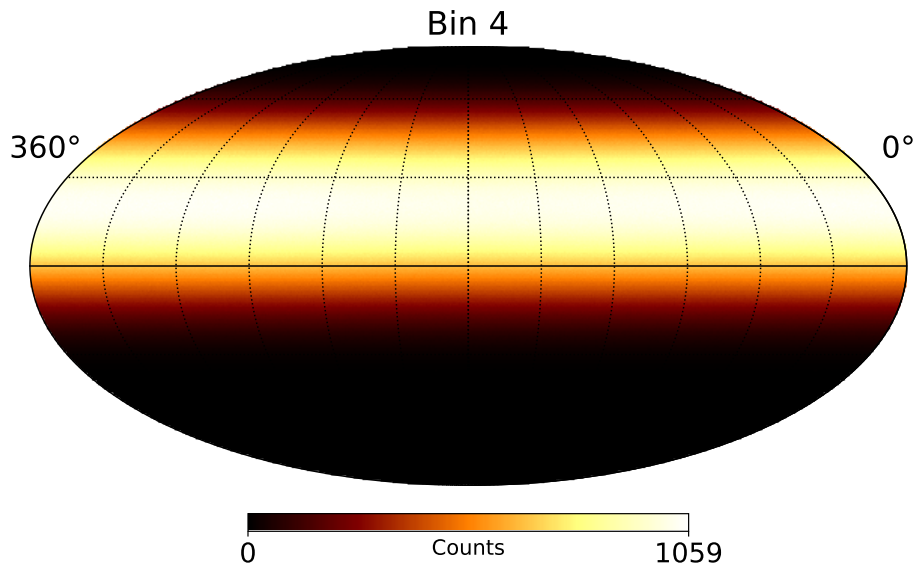
FIGURE 5.11: Counts estimate for $\mathcal{B} = 4$ using MB technique of background estimation.

5.3.1 Comparison with Direct Integration

To assess the credibility of the assumptions made, and how different the new background model is, we compare with the current model employed in HAWC, i.e. the DI method. Figure D.5 in Appendix D displays the excess maps of all nHit bins derived from DI. The top panel of Figure 5.13 shows the excess maps for $\mathcal{B} = 2$ as derived from DI. Therein, the contributions emanating from the cosmic-ray anisotropy are clearly incorporated as part of the excess. The bottom panel of Figure 5.13 depicts the excess maps for $\mathcal{B} = 2$ as derived from MB and it is evident that the method has effectively removed the contributions from the cosmic-ray anisotropy.

The left panel of Figure 5.14 shows a comparison between the relative livetime of HAWC and the average counts per pixel for the $\mathcal{G}$cut, MB and DI maps, as a function of right ascension for $\mathcal{B} = 4$. The counts per pixel in each case were obtained by summing, for the whole HAWC field of view, the counts in a right ascension bin of 12° wide and then dividing by the total number of pixels whose counts were summed. Without loss of generality, a bin of 12° was chosen to extract a global distribution with right ascension:

$$\text{counts per pixel} = \frac{\sum_i^{12°} G_i}{\sum_i^{12°} i} = \frac{G_I}{I} . \tag{5.9}$$

The right panel of Figure 5.14 illustrates, again for $\mathcal{B} = 4$, the relative excess seen as a function of right ascension. The relative excess was calculated using:

$$\mathcal{E}_{\text{rel}}(\text{RA}) = 2 \times \frac{G_I - B_I}{G_I + B_I} , \tag{5.10}$$
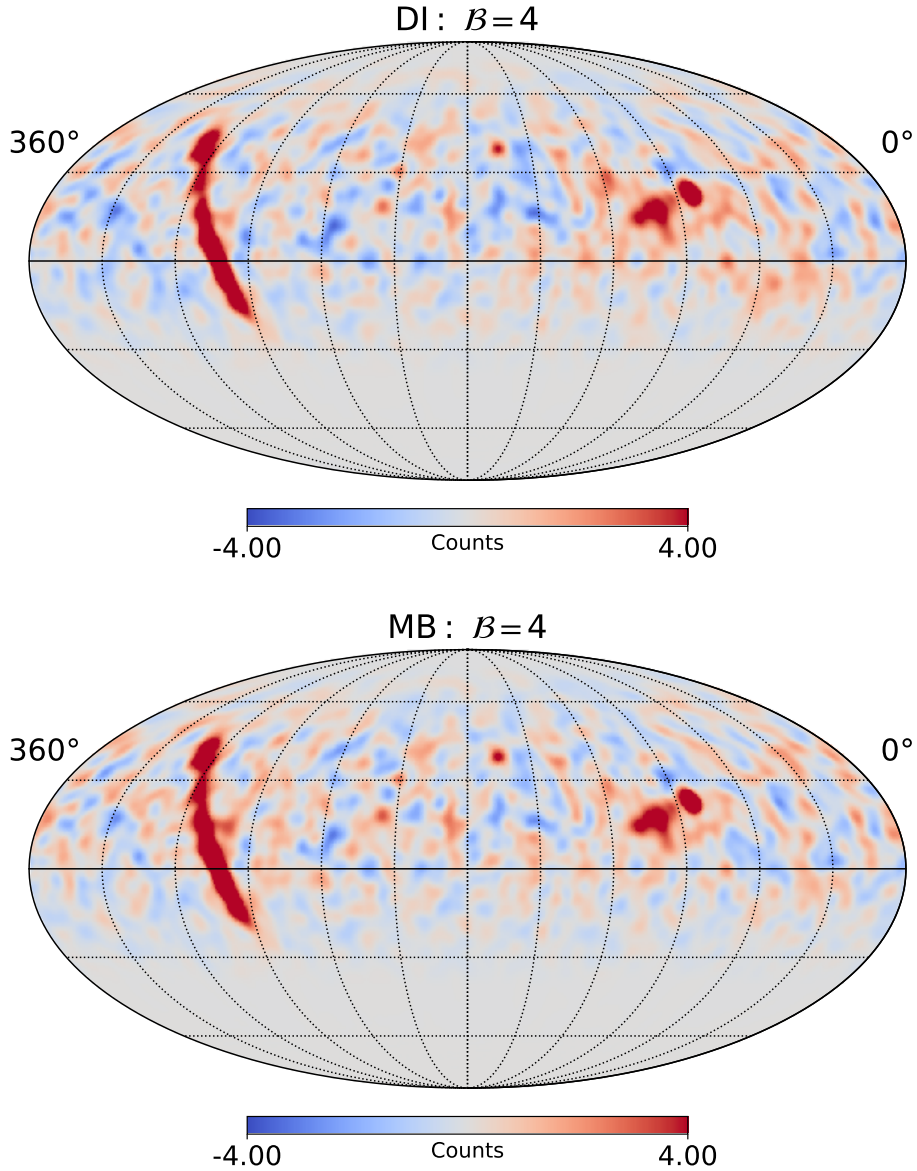
FIGURE 5.12: Excess counts map for $\mathcal{B} = 4$, using DI (*top*) and using MB (*bottom*). A 5° smoothing was applied and the map shown has a mean pixel size of approximately 0.229°.

where B_I is the background and can be B_{DI} or $B_{\mathcal{Y}}$. The error bars (and corresponding shaded region) shown were calculated by propagating statistical error using the following equation:

$$\Delta \mathcal{E}_{\text{rel}}(\text{RA}) = \mathcal{E}_{\text{rel}} \left[\frac{\Delta G_I}{G_I - B_I} + \frac{\Delta G_I}{G_I + B_I} \right] , \tag{5.11}$$

where we assumed that the background models are error-free (derived in Section 5.3.2) and that the error emanates solely from the $\mathcal{G}$cut map.
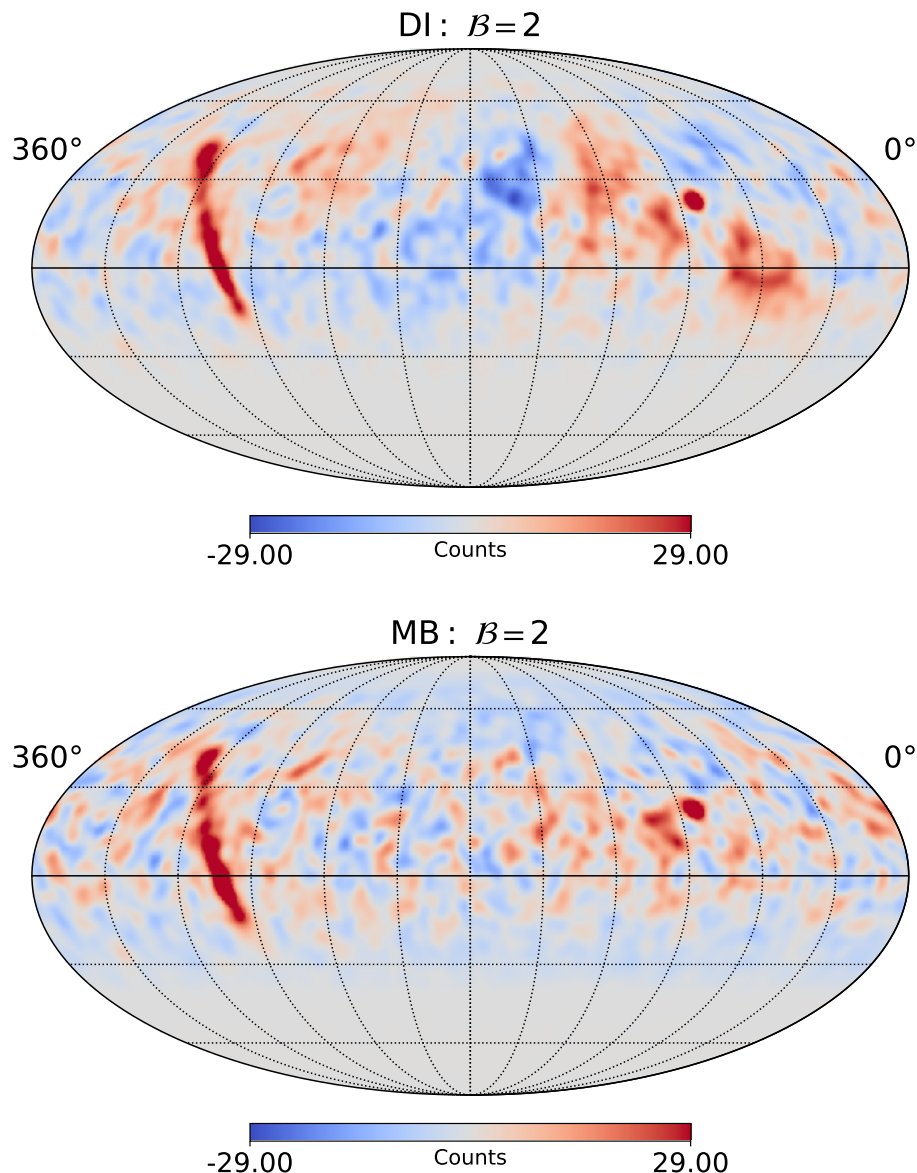
FIGURE 5.13: Excess maps derived using the DI (*top*) and MB (*bottom*) maps for nHit bin 2 with a 5° smoothing.

Having a Poissonian distribution, the error in $\mathcal{G}$cut map (ΔG_I) was taken to be (see Section 5.3.2 for justification):

$$\Delta G_I = \frac{\sqrt{G_I}}{I} .$$ (5.12)

Figure 5.14 shows that the MB model is comparable to DI. There are some differences that might indicate extended gamma-ray emission beyond what would have been obtained by using DI at 275° < RA < 300°. This RA band corresponds to part of the Galactic plane with known HAWC sources. Since the MB method does not depend on a 24 hour integration period, it takes into account data that might have been rejected by DI and hence contains more statistics than the latter. This is clearly seen in the right panel of

(A) Counts per pixel and relative livetime

(B) Relative excess
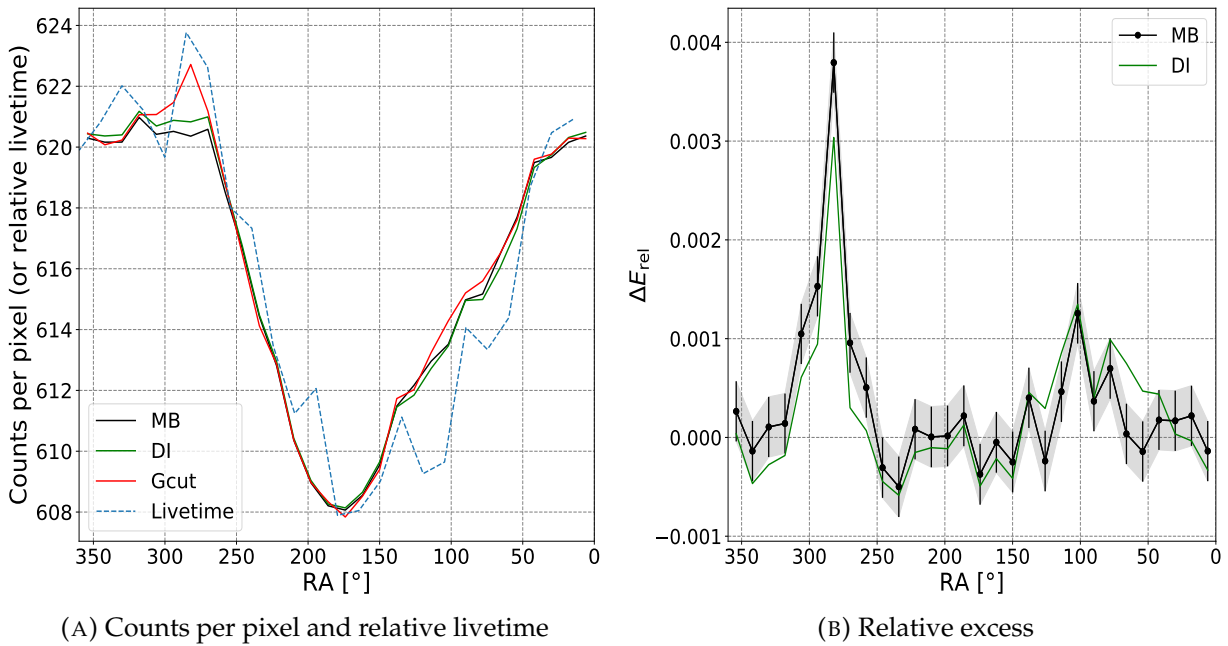
FIGURE 5.14: Comparison between DI and MB for $\mathcal{B} = 4$ as a function of right ascension. The *left panel* shows overall differences of counts per pixel between DI, MB and the $\mathcal{G}$cut map. It also shows that the trend is dictated by the livetime. The *right panel* shows the relative excess as a function of RA for both DI and MB.

Figure 5.14, where there is more relative excess in the MB map than in DI.

Figure 5.15 is a map showing the relative difference between DI and MB, i.e. $(B_{DI_i} - B_{\mathcal{Y}_i})/B_{DI_i}$ for $\mathcal{B} = 2$ in the top panel and $\mathcal{B} = 7$ in the bottom panel. The two dark bands at the extreme ends of the HAWC field of view ($-25° < \delta < +65°$), as labelled in the middle panel, are due to a significant decline in statistics with increasing zenith angles. Region A is evident in $\mathcal{B} = 2$ as it is present in the MB method but not in DI. A bright emission around part of the Galactic plane is also significantly discernible in higher nHit bins (for instance $\mathcal{B} = 7$), which is an indication that emission around the Galactic plane might have been underestimated with the DI method.

5.3.2 Error Propagation

With the large number of counts in each nHit bin, the error in every pixel of the excess map is given by:

$$\Delta \mathcal{E}_i = \sqrt{\Delta G_i^2 + \Delta B_{\mathcal{Y}_i}^2} \, . \tag{5.13}$$

As in equation (5.12), the error associated with the $\mathcal{G}$cut map is $\Delta G_i = \sqrt{G_i}$, which when evaluated for $\mathcal{B} = 4$ has an order of magnitude of 10, i.e. the fractional uncertainty on the $\mathcal{G}$cut map is 1%. Similarly, for $\mathcal{B} = 4$, the fractional error on the $\mathcal{H}$cut map is 0.1%. The
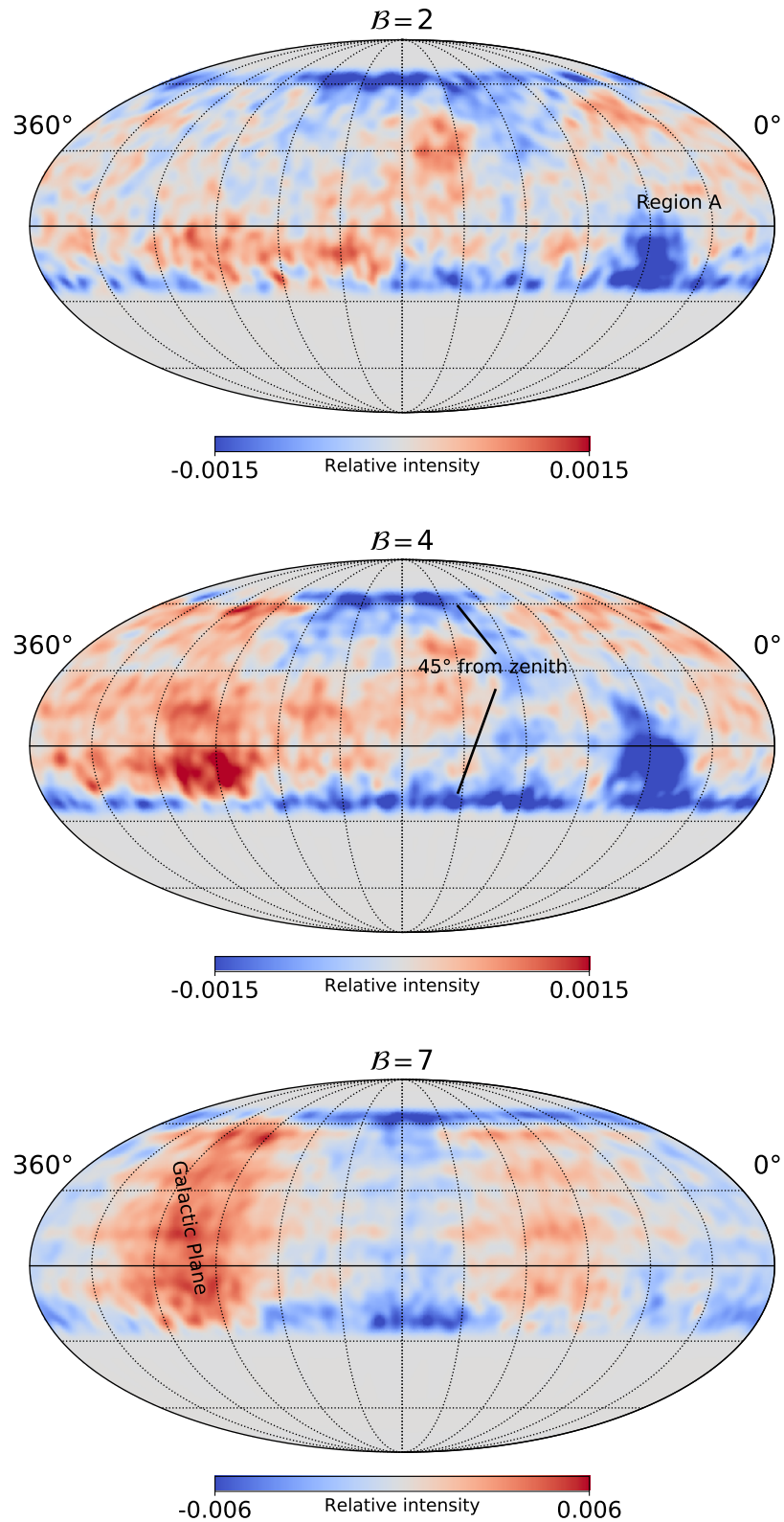
FIGURE 5.15: Relative difference in backgrounds: $\frac{B_{DI} - B_\mathcal{Y}}{B_{DI}}$ for nHit bins 2 (*top panel*), 4 (*middle panel*) and 7 (*bottom panel*).

error in the MB map is obtained by adding the errors in $\mathcal{Y}$ and H_i in quadrature:

$$\Delta B_{\mathcal{Y}_i} = \sqrt{H_i^2 \Delta \mathcal{Y}_i^2 + \mathcal{Y}_i^2 \Delta H_i^2} \, . \tag{5.14}$$

The error on $\mathcal{Y}$, $\Delta\mathcal{Y}_i = \sqrt{b_i^2\Delta a_i^2 + a_i^2\Delta b_i^2}$, has an order of magnitude of $\mathcal{O}(10^{-5})$ leading to a total statistical fractional uncertainty at the level of 0.1% for the MB map. Thence, the errors on the excess maps are completely dominated by the number of counts in the $\mathcal{G}$cut map.

For a specific region of interest (ROI), the error on every pixel making up the region should be added in quadrature:

$$\Delta\mathcal{E}_{ROI} = \sqrt{\sum_{i_{ROI}} \Delta\mathcal{E}_i^2} \, . \tag{5.15}$$

Since a and b factors vary over few degrees, for larger ROI (upto 10°), averaging $\mathcal{Y}$-factor is a very good approximation which also saves on computing time. An average $\mathcal{Y}$-factor can be defined as:

$$\overline{\mathcal{Y}} = \frac{\sum_{i_{ROI}} B\mathcal{Y}_i}{\sum_{i_{ROI}} H_i} \, , \tag{5.16}$$

such that the error in the excess is then:

$$\Delta\mathcal{E}_{ROI} = \sqrt{\Delta G_i^2 + \overline{\mathcal{Y}}^2\Delta H_i^2 + H_i^2\Delta\overline{\mathcal{Y}}^2} \tag{5.17}$$

$$\simeq \Delta G_i \, , \tag{5.18}$$

where $\Delta\overline{\mathcal{Y}}^2$ is $\overline{\mathcal{Y}}/\sum_{i_{ROI}}$.

5.3.3 Method Performance through Source Significance

We want to assess the performance of the MB method of background estimation. To obtain some quantitative diagnostics, we have to compute the statistical significance of a source in the sky. In HAWC, significance is computed using test statistic (TS) which measures the degree of agreement between a sample of data (*alternate hypothesis*) and the model background (*null hypothesis*) for each nHit bin. Conventionally, a spectrum is assumed and the nHit bins are assigned different weights before combining them to extract and maximise a likelihood ratio for the null hypothesis to the alternate hypothesis. We, however, calculated the significance of different nHit bins using the Li and Ma prescription as detailed by the equation below (comparable to equation (17) in Li and Ma, 1983):

$$\mathcal{S_B}^2 = 2\left\{N_{on}\ln\left[\left(\frac{1+\alpha}{\alpha}\right)\left(\frac{N_{on}}{N_{on}+N_{off}}\right)\right] + N_{off}\ln\left[(1+\alpha)\left(\frac{N_{off}}{N_{on}+N_{off}}\right)\right]\right\} \, . \tag{5.19}$$

The term "on" refers to a specific test region while "off" corresponds to a region or regions with no known gamma-ray emission, such that $N_{on} = \sum_{i_{on}} G_i$ and $N_{off} = \sum_{i_{off}} H_i$. The

significance is then calculated by taking $\sqrt{\mathcal{S_B}^2}$ and substituting α in equation (5.19) with $\overline{\mathcal{Y}}$ as defined in equation (5.16). We performed a test to compare the significance of a source, for instance, the Crab nebula, as computed using MB to that estimated using DI, as a function of nHit bins. The significance was computed for each nHit bin independently as displayed in Figure 5.16.
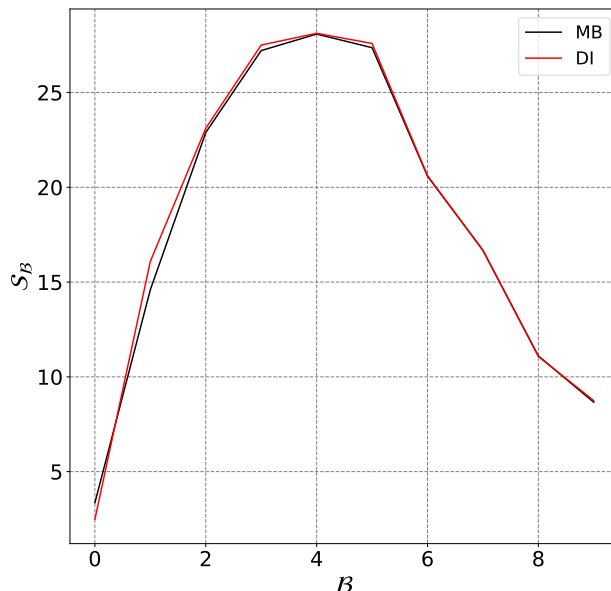
FIGURE 5.16: Significance of Crab nebula per nHit bin.

5.4 Exposure Maps

Given the location of HAWC, different celestial objects are seen for different lengths of time. This implies that that we collect more data from some regions than others. An exposure map is a spatial representation of the expected number of counts, given a source spectrum. To extract such a map, we require the livetime of HAWC which will give the variation in right ascension, and a HAWC detector response file for the variations in declination. The livetime of HAWC is stored as an array which can be obtained from the HAWC `map-maker`. The variations in the array are as a function of a sidereal day in Greenwich Mean Sidereal Time (GMST) and the content of array is the number of transits of the sky that were recorded corresponding to the data in use to derive the map as shown in Figure 5.7. Local mean sidereal time (LMST) is the sum of GMST and the longitude of HAWC ($\lambda_{\text{HAWC}} = 97.3°$ W). At zenith, the hour angle (HA) is zero, and therefore, LMST is equal to RA. Taking this into account, we can convert from GMST to RA.

By performing MC simulations of several parameters, such as instrument (PMT) response, the aforementioned detector response file is generated (Baughman and Smith,

2010). It comprises of the HAWC PSF, stored as histograms, at different declinations for each nHit bin, which defines the event rate for a source of given spectrum as a function of energy. Integrating these histograms and interpolating though all declinations, one can generate a map which depicts the expected counts per transit in different declination bands of the sky as illustrated for $\mathcal{B} = 4$ in the upper panel of Figure 5.17. A Crab nebula-like source spectrum, with spectral index -2.63 and normalisation 3.5×10^{-11} cm^{-2} s^{-1} at a reference energy of 1 TeV, was used. Figure D.6 in Appendix D similarly depicts for all nHit bins and the numbers are consistent with those published in Table 2 in HAWC Collaboration et al. (2017c).
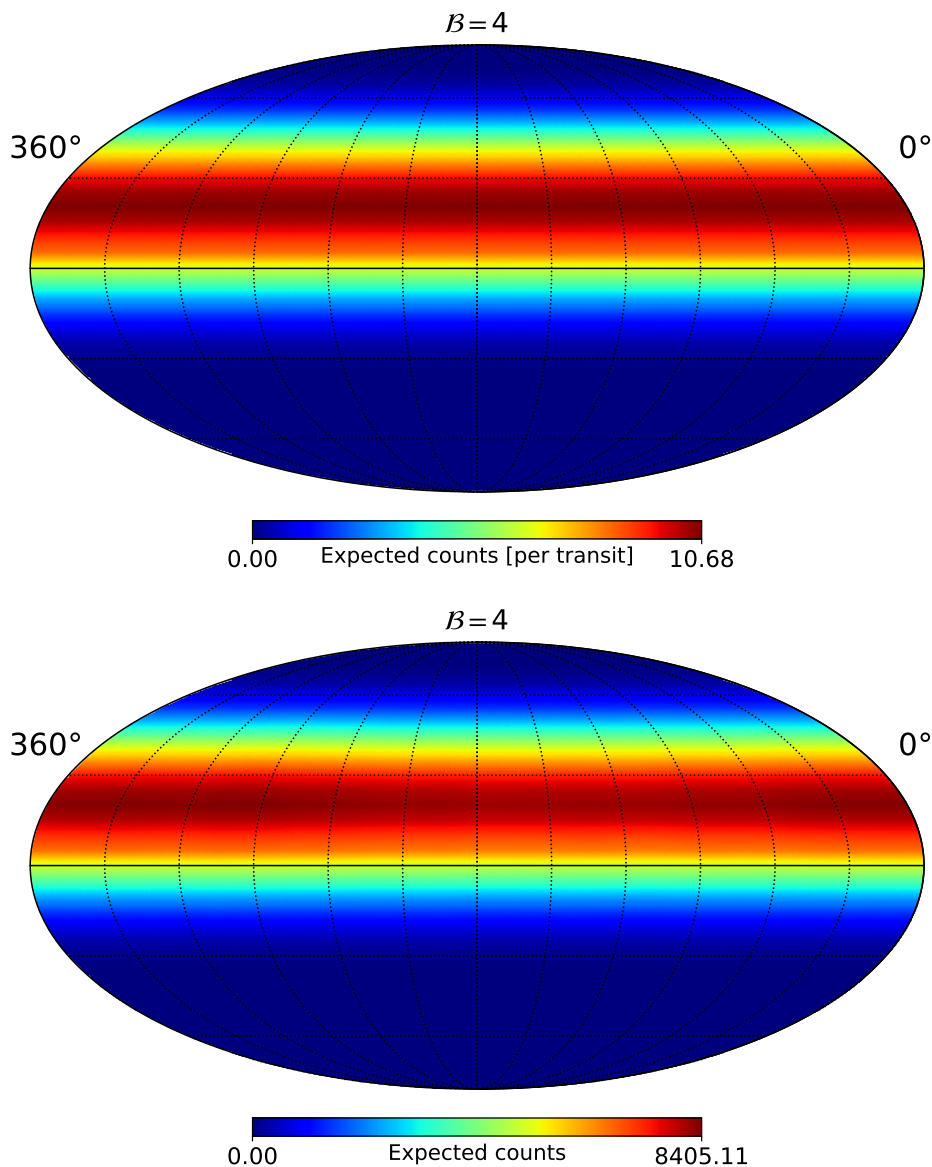
FIGURE 5.17: Map illustrating expected count per transit for $\mathcal{B} = 4$. A Crab nebula-like source spectrum, with spectral index -2.63 and normalisation 3.5×10^{-11} cm^{-2} s^{-1} at a reference energy of 1 TeV, was used. The *upper panel* depicts the expected counts per transit while the *lower panel* is the exposure map for the entire data set in use.

This map of expected counts per transit is further convolved with the livetime to incorporate the variations in RA, which yields the exposure map. The lower panel of Figure 5.17 depicts the exposure for $\mathcal{B} = 4$ for the entire data set used while Figure D.7, in Appendix D, illustrates the corresponding exposure maps for all nHit bins, both for a Crab nebula-like source with spectral index -2.63 and normalisation $3.5 \times 10^{-11}\,\mathrm{cm}^{-2}\,\mathrm{s}^{-1}$ at a reference energy of 1 TeV. As a validation of our exposure modelling, we compare the excess counts seen in a region, for instance the Crab nebula, to the expected number of counts based on the exposure. Figure 5.18 depicts a clear consistency between the two numbers across all nHit bins.
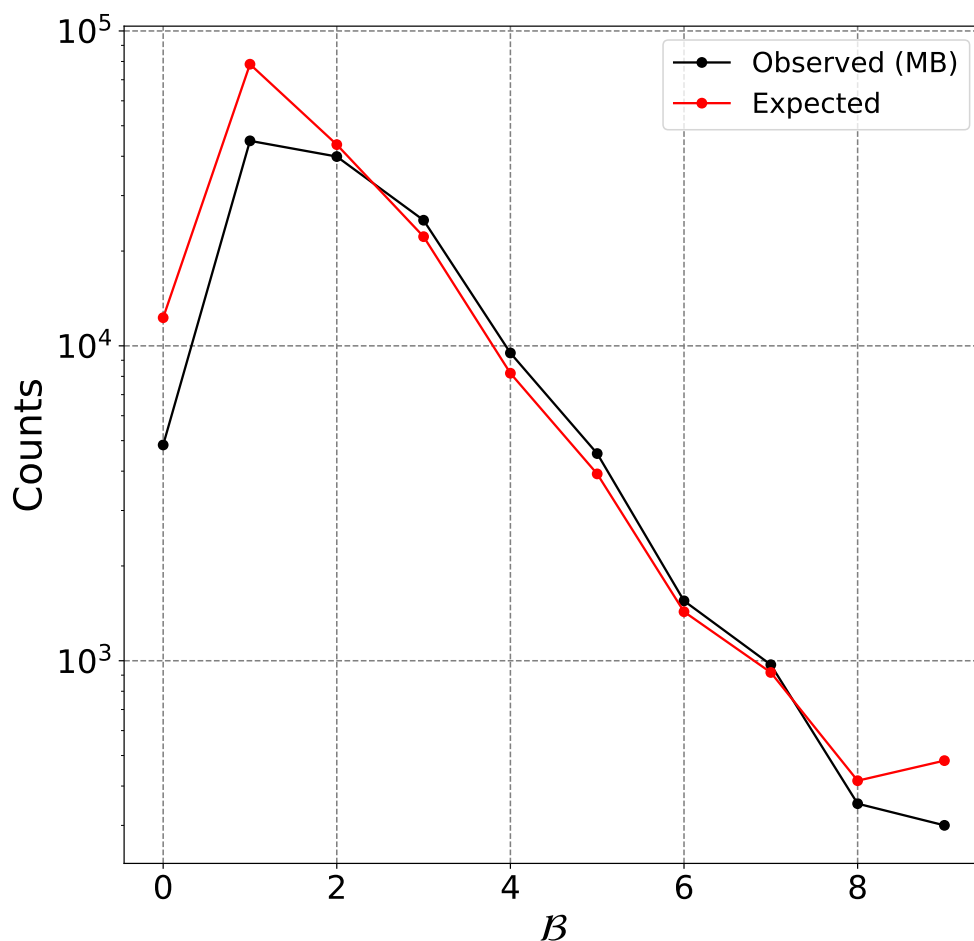
FIGURE 5.18: Distribution of flux as a function of spectral index assumed in computing the detector response.

5.5 Summary

A novel method for background estimation was described using events that pass either of a pair of selection criteria. A right ascension-declination dependent background was generated for each nHit bin by deriving a and b-factors. While it is still unclear how

much of the declination dependence of a-factor originates from a reduction of gamma-ray efficiency across declinations, some preliminary significance computations showed compatibility to the DI method of background estimation. Our approach for background estimation, results in faster computations, exploits all statistics available and accounts for the cosmic-ray anisotropy. Finally, we derived exposure maps, using the livetime and detector response of the instrument which will later be used for source significance and flux computations.

6

Search for Large-Scale Structures in HAWC Sky

In this chapter, we make a blind search for large-scale structures in the HAWC sky map. We describe the underlying formalism and conceptual foundations of our approach to combine the different nHit bins and present our results.

6.1 The Maximum Likelihood Method for Significance and Flux Computation

We will use the method of hypotheses test from mathematical statistics to estimate the significance of counts from different parts of the sky. Assuming Poissonian statistics, the likelihood function of N observed values with the probability of observing X given Θ, i.e. $\mathcal{L}(X|\Theta)$, which, as represented in Li and Ma (1983), is:

$$\mathcal{L}(X|\Theta) = \frac{\overline{N}_{\mathrm{on}}^{N_{\mathrm{on}}} e^{-\overline{N}_{\mathrm{on}}}}{N_{\mathrm{on}}!} \frac{\overline{N}_{\mathrm{off}}^{N_{\mathrm{off}}} e^{-\overline{N}_{\mathrm{off}}}}{N_{\mathrm{off}}!} \, , \tag{6.1}$$

and in logarithmic space is:

$$\ln \mathcal{L} = -\overline{N}_{\mathrm{on}} + N_{\mathrm{on}} \ln \overline{N}_{\mathrm{on}} - \ln \left(N_{\mathrm{on}}! \right) - \overline{N}_{\mathrm{off}} + N_{\mathrm{off}} \ln \overline{N}_{\mathrm{off}} - \ln \left(N_{\mathrm{off}}! \right) . \tag{6.2}$$

N_{on} is sampled from the measured gamma-like events map (G), N_{off} is sampled from the measured hadron-like events map (H), $\overline{N}_{\mathrm{off}}$ is the expected background, and $\overline{N}_{\mathrm{on}}$ is the

expected counts given by $\mathcal{E} + \overline{N}_{\text{off}}$, where $\mathcal{E}$ is an expected excess which is expressed as the product of flux $\mathcal{F}$, and exposure $\mathcal{E}$, i.e. $\mathcal{E} = \mathcal{F}\mathcal{E}$.

We initially treated the expected background as a known parameter ($B_\mathcal{Y}$), i.e. $\mathcal{Y}H$ as derived in Chapter 5, and maximised the flux. However, after running some diagnostic tests, we found that this is not the case for low nHit bins. For these nHit bins, $\mathcal{Y}$ (or equivalently the *a*-factor, as shown in Figure 5.9(B)) shows an increasingly larger deviation from zero. Thus, the expected background is a true unknown and is hereon treated as a *nuisance parameter*.

To search for structures at different angular scales, we set the sampling from the maps to different integration radii, namely 1°, 2°, 4°, 8° and 16°. Moreover, to avoid contamination of emission from known gamma-ray sources, the latter were masked with appropriate extensions. While a disk of 10°($\pm$5°) was used for the sources within the Galactic plane, the off Galactic plane sources were masked as detailed in Section 5.2.2. Additionally, few sources from the 2HWC catalogue were also masked with 1° circles, namely J0700+143, J0819+157, J1040+308, J1309-054 and J1829+070.

6.1.1   Background Optimisation - The Profile Likelihood Approach

Prior to maximising on the flux, in this profile likelihood approach, we will maximise the nuisance parameter:

$$\frac{\partial \ln \mathcal{L}}{\partial \overline{N}_{\text{off}}} = 0 \,, \tag{6.3}$$

such that the expected background is obtained using the model background (MB), with $\mathcal{E}$ or equivalently $\mathcal{F}$ as the only free parameter:

$$\overline{N}_{\text{off}} = \frac{1}{2\mathcal{Y}(\mathcal{Y}+1)} \left[\mathcal{Y}G + B_\mathcal{Y} - \mathcal{E}(\mathcal{Y}+1) + \sqrt{(\mathcal{Y}G + B_\mathcal{Y} - \mathcal{E}(\mathcal{Y}+1))^2 + 4\mathcal{E}B_\mathcal{Y}(\mathcal{Y}+1)} \right]. \tag{6.4}$$

The likelihood fit now maximises the Cash statistic with one degree of freedom (DoF) (Cash, 1979):

$$\mathcal{C} = 2 \sum_i \left[(\overline{N}_{\text{off}})_i - (N_{\text{on}})_i \ln (\overline{N}_{\text{off}})_i \right] . \tag{6.5}$$

We used an optimisation code which invokes the *Nelder-Mead* minimisation algorithm. For a given pixel of the sky map, the algorithm tests different flux values and outputs the global minimum flux, $\mathcal{F}_{\text{min}}$, and its corresponding Cash likelihood, $\mathcal{C}_{\text{min}}$. Figure 6.1 depicts the Cash minimisation for the Crab nebula centre position at different scales. A

likelihood ratio test is subsequently used to determine the statistical significance σ:

$$TS = \mathcal{C}_0 - \mathcal{C}_{\min} , \tag{6.6}$$

$$\sigma = sign(\mathcal{F}_{\min})\sqrt{|TS|} . \tag{6.7}$$
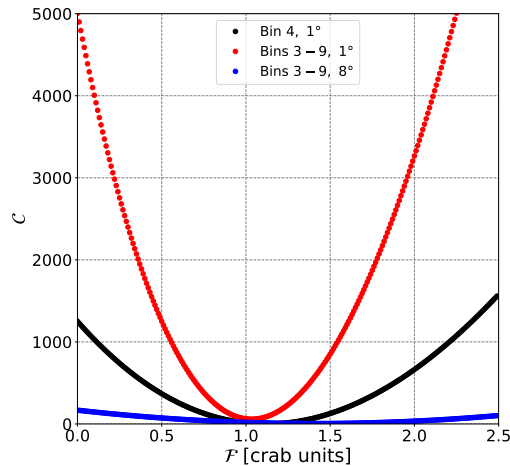
FIGURE 6.1: Minimising on the flux at the Crab nebula centre position for $\mathcal{B} = 4$ at $1°$, $\mathcal{B} : 3 - 9$ at $1°$ and $\mathcal{B} : 3 - 9$ at $8°$.

According to Wilks' theorem, for a large number of counts, the distribution of the TS asymptotically approaches a χ^2 distribution with a difference in DoF that corresponds to the difference of the DoF in each hypothesis. In this limit, although a negative flux has no physical interpretation, the $sign(\mathcal{F}_{\min})$ in equation (6.7) allows for negative significance values. This occurs in regions where the number of counts is smaller than the background estimate, for instance, a statistical downward fluctuation. Figure 6.2 displays the significance whole sky maps for $\mathcal{B} = 4, 7$ and 9 with a $4°$ and $16°$ integration radius. There are discernible regions of emission that form at larger integration scales, we need to combine the nHit bins to identify any conspicuous region that significantly stands out of the fluctuations.

6.1.2 Assessing the All-Sky Significance Map from Combined nHit Bins

In the context of our binned data, we combine the nHit bins by taking the product of the likelihoods (sum of $\ln \mathcal{L}_\mathcal{B}$) in each nHit bin. We use the computed significance and flux to first assess the distribution of off-source significance, then select and study regions of interest (ROI). The significance maps for all the integration radii are depicted the following section in Figures 6.6 through 6.10. The significance maps for $4°$ and $16°$ integration radii are illustrated in Figures 6.3 and 6.4 and will be used to assess the background.
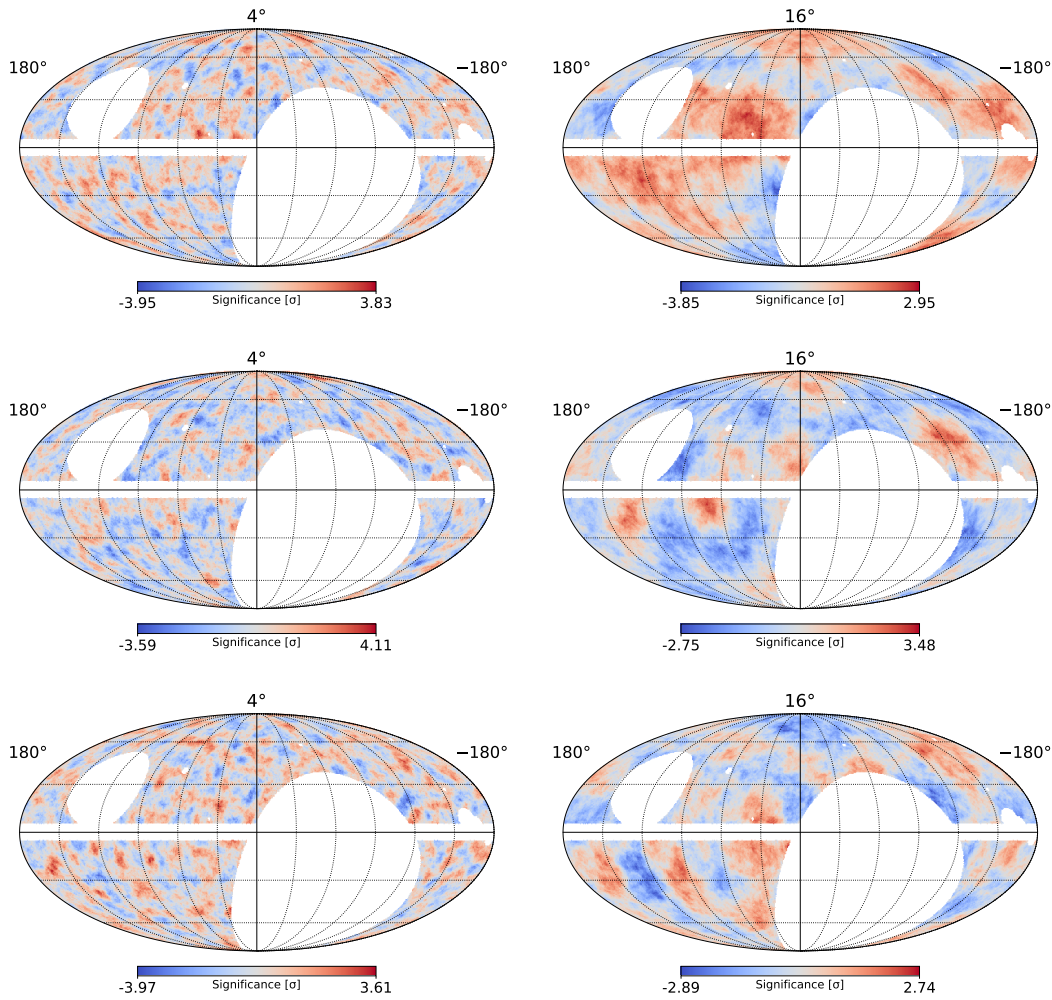
FIGURE 6.2: HAWC sky map for selected nHit bins at different scales. The *left column* is for an integration radius of 4°, while the *right column* is for a larger radius of 16°. The maps in the *upper panel* are for $\mathcal{B} = 4$, the *middle panel* for $\mathcal{B} = 7$ and the *lower panel* for $\mathcal{B} = 9$.

Figure 6.3 (and similarly Figure 6.4) illustrates three panels of significance maps and their corresponding histograms. The upper panel is the result of combining $\mathcal{B} : 1 - 9$, the middle and lower panels are for $\mathcal{B} : 3 - 9$. The middle panel presents the significance involving the alternate hypothesis, $\mathcal{L}(N_{\mathrm{on}}|\overline{N}_{\mathrm{off}})$, but the lower panel presents the significance generated from a fake counts map, which was taken to be a diced version of the background map, thereby testing $\mathcal{L}(\overline{N}_{\mathrm{off}}|\overline{N}_{\mathrm{off}})$). This fake counts map, devoid of any known source, allows us to verify whether we introduced a bias or not. In all cases, the histogram depicts the distribution of significance in off gamma-ray source regions, which in theory should have a normal distribution. This is because, in an off-source region, we expect as much upward fluctuation as downward, with the mode at zero, i.e. a mean of 0 and a standard deviation of 1. However, for $\mathcal{B}$ combination 1 to 9, there is a larger spread in the significance distribution, thereby deviating from the expected normal behaviour. This is indicative that the statistics of the lower nHit bins is biased which might

be because of potential sources/emission present in our off region and/or an incorrect background estimation. At the moment, we cannot remove the bias, hence, for the purpose of the blind search, we choose to work with $\mathcal{B}$ combination 3 to 9 which implies energies > 1 TeV. Lastly, we computed other combinations of nHit bins ($1 - 9$ and $4 - 9$) to allow comparison, wherever possible, to published values.

6.1.3   Computing the Differential Flux of Some Gamma-Ray Sources

Figure 6.5 illustrates $\mathcal{F}_{\min}$ at 7 TeV, equivalently F_7, as a function of spectral assumption made to model the exposure maps. The uncertainty on $\mathcal{F}_{\min}$ was estimated using parameter limits corresponding to a given difference, $\Delta(TS)$, in the log-likelihood function compared to the minimum value. $\Delta(TS)$ depends on the required confidence level (CL), and for this study was chosen to be 95% corresponding to $\Delta(TS) = 3.84$. Table 6.1 lists the calculated fluxes, at 7 TeV, of the Crab nebula, Geminga and the Galactic plane. By comparing to respective values from previous HAWC publications, we see a difference of up to 15% in the case of the Crab nebula and up to 54% for Geminga. This is plausible given that we are using a bigger dataset, a background model adapted for analysis of extended sources, as it incorporates the CR anisotropy, and altogether, a different approach to the flux computation.

TABLE 6.1: Table detailing the differential flux for the Crab nebula, Geminga, and the Galactic plane at a reference energy of 7 TeV. A comparison to published values was made where possible. The extension of the source used is given in parentheses next to the source name.

Source / Method	$\mathcal{F}_7$ [TeV^{-1} cm^{-2} s^{-1}]		
	Crab nebula (1.3°) $\times 10^{-13}$	Geminga (2°) $\times 10^{-14}$	Galactic plane ($\pm$5°) $\times 10^{-12}$
Likelihood approach ($\mathcal{B}$: 1 - 9)	2.12 ± 0.07	7.47 ± 1.03	7.16 ± 0.31
HAWC Collaboration et al. (2017e) ($\mathcal{B}$: 1 - 9)	1.85 ± 0.02	4.87 ± 0.69	-
Likelihood approach ($\mathcal{B}$: 4 - 9)	2.24 ± 0.09	9.56 ± 1.26	7.66 ± 0.37
HAWC Collaboration et al. (2017c) ($\mathcal{B}$: 4 - 9)	$2.51^{+1.47}_{-0.93}$	-	-
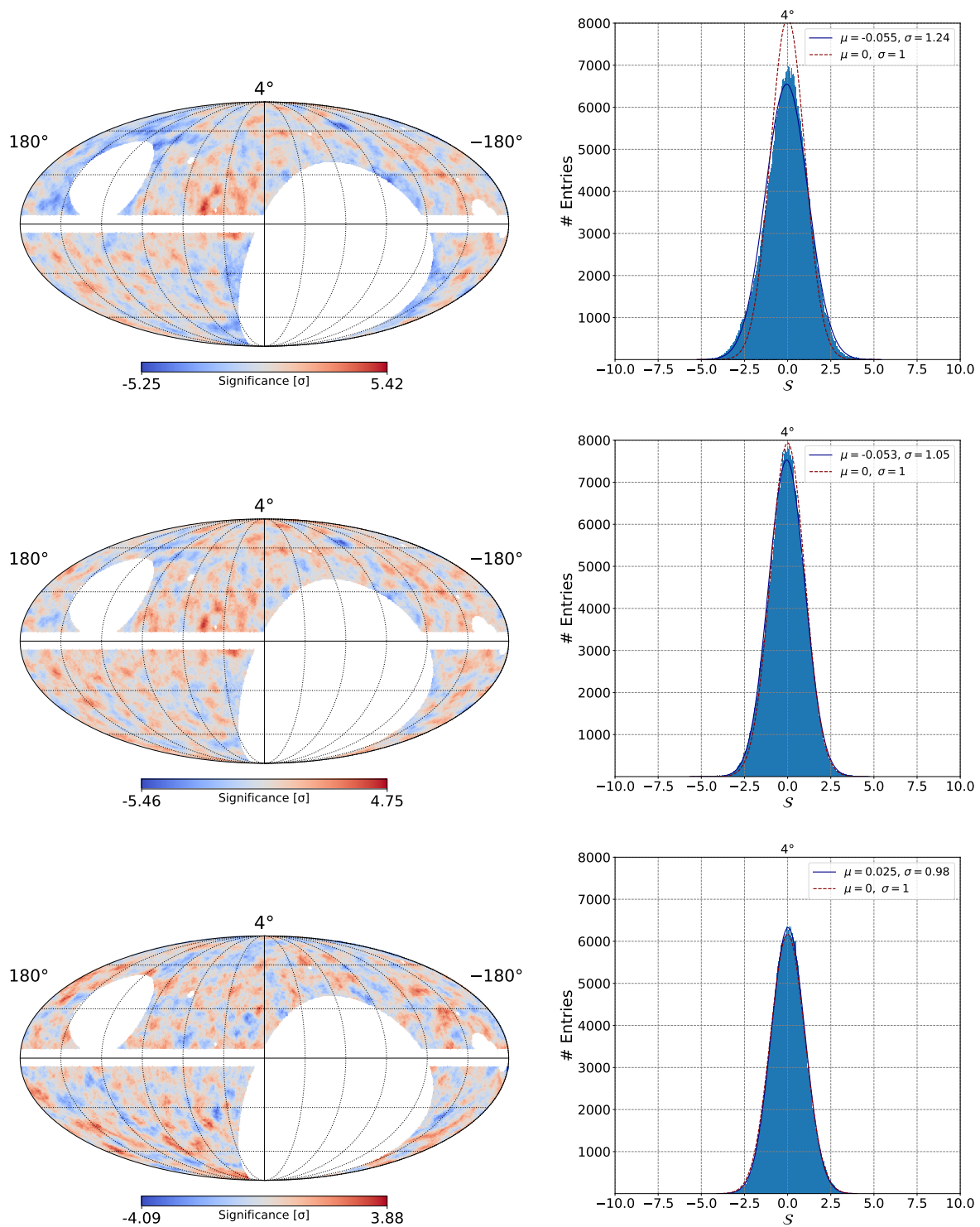
FIGURE 6.3: Combining different bins for integration radius 4°. The significance maps shown are in the *left column*, while the *right column* illustrates the 1D distribution of significance in the off-source region. The *upper panels* are for $\mathcal{B} : 1 - 9$, *middle panels* are for $\mathcal{B} : 3 - 9$ and the *lower panels* are also for $\mathcal{B} : 3 - 9$ but generated from fake counts map.

For part of the galactic plane in the field of view of HAWC, $10° < l < 95°$ and $b = \pm 5°$,
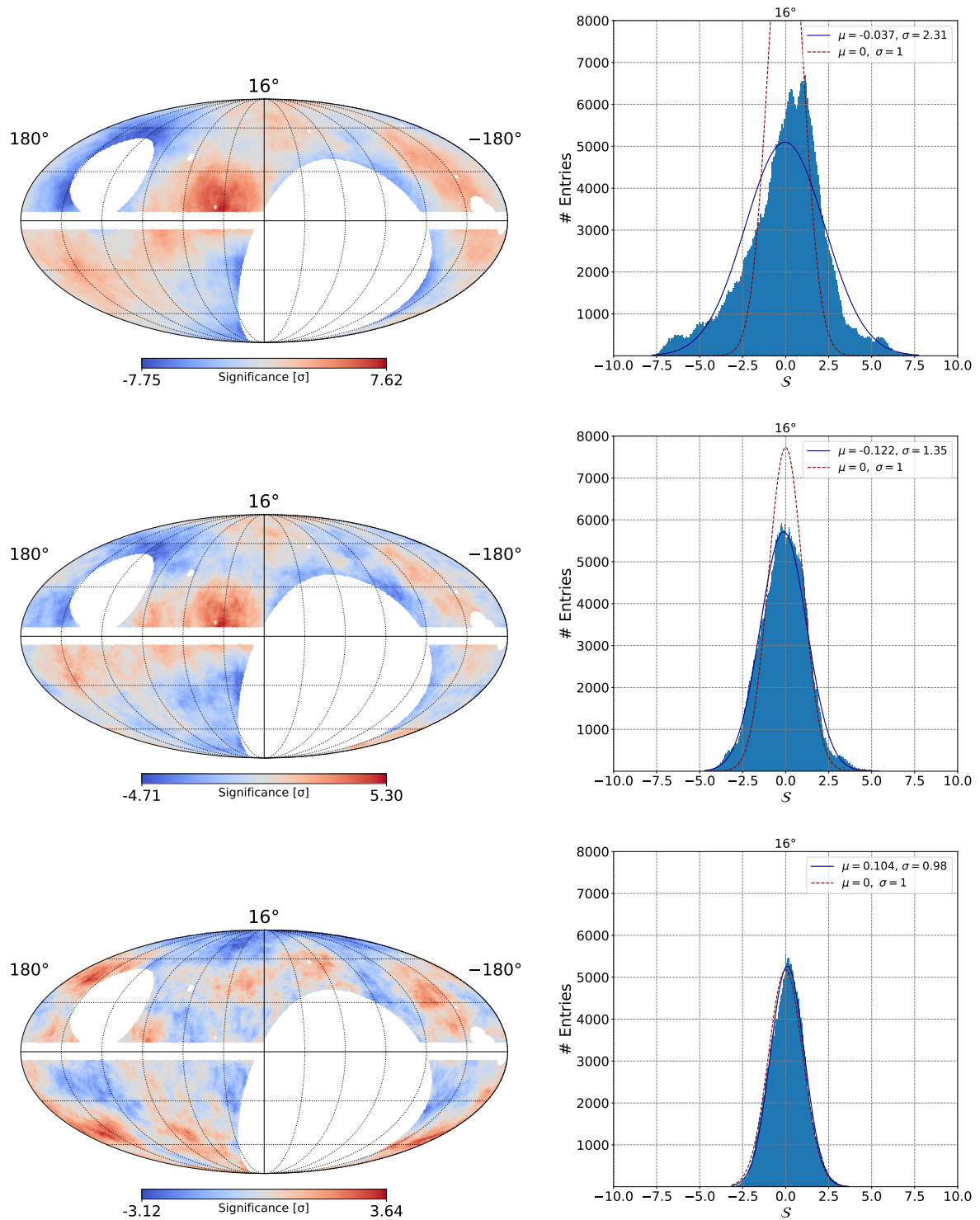
FIGURE 6.4: Combining different bins for integration radius 16°. The significance maps shown are in the *left column*, with the *right column* depicting the 1D distribution of significance in the off-source region. As in Figure 6.3, the *upper panels* correspond to $\mathcal{B} : 1 - 9$, the *middle panels* are for $\mathcal{B} : 3 - 9$ and the *lower panels* are also $\mathcal{B} : 3 - 9$ but generated from fake counts map.
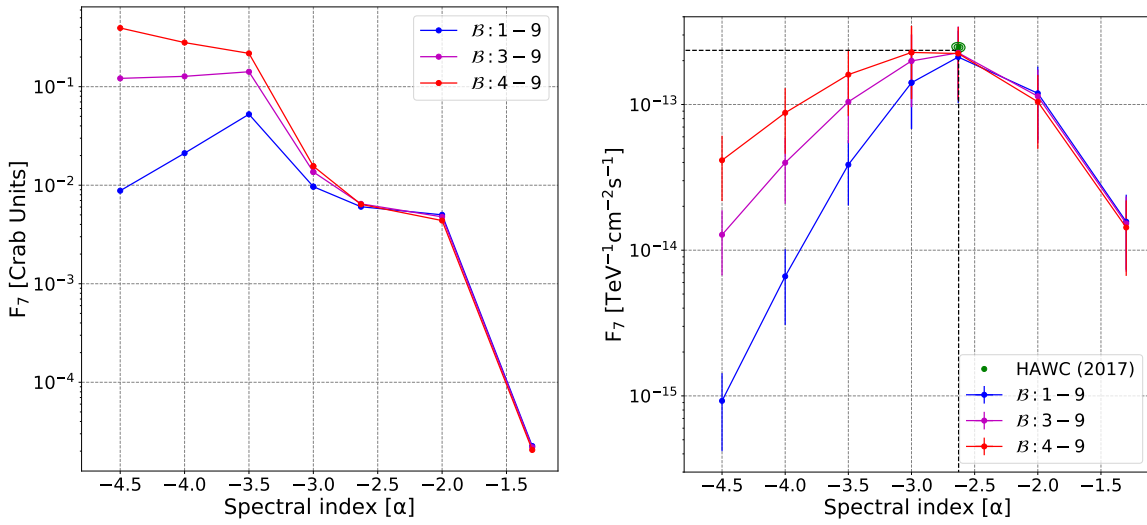
FIGURE 6.5: Distribution of flux for the Crab nebula region (extension radius = 1.3°) at 7 TeV as a function of spectral index assumed in computing the detector response. The distributions displayed are in the *left panel* in crab units while the *right panel* is in the converted differential flux units, with associated error bars and is further compared to the corresponding published value from HAWC Collaboration et al. (2017c).

for $\mathcal{B}$: 1 - 9, we found $\mathcal{F}_7 = (2.9 \pm 0.1) \times 10^{-12} \mathrm{TeV}^{-1}\mathrm{cm}^{-2}\mathrm{s}^{-1}$. By summing the differential fluxes at 7 TeV of individual sources previously reported in the 2HWC catalogue and from the same region, we found $\mathcal{F}_7 = 2.3 \times 10^{-12} \mathrm{TeV}^{-1}\mathrm{cm}^{-2}\mathrm{s}^{-1}$. Considering that we are comparing sources and diffuse emission in the selected region to the sum of resolved source fluxes, and that from the comparisons in Table 6.1, we expect $\sim 20\%$ differences between our values, the aforementioned $\mathcal{F}_7$ values appear to be consistent with each other.

6.2 Previously Unseen Large-Scale Emission Region in the HAWC Map towards $l \sim 30°$

From the middle panel of Figure 6.4, there is a region of extended emission just above the Galactic plane and centered around longitude $\sim 30°$ which exhibits a significance of up to 5.3σ. Figures 6.6 through 6.10 depict the significance and flux variations (in Crab units) in this ROI at different angular scales. In the maps shown for this ROI, the masked areas correspond to the Galactic plane ($< 5°$), 2HWC J1829+070 (centered at $l = 36.7°$, $b = 8.0°$) and partially MrK501 in the upper left corner.

Figures 6.6 and 6.7 display no discernible emission at integration radii of 1° and 2°, respectively, consistent with previous studies. Figure 6.8 (4° integration radius) displays few bright spots around $l = 45°$ and around J1846+0919 but these might still be construed as consistent with fluctuations in other regions of the sky. On the other hand, the ROI
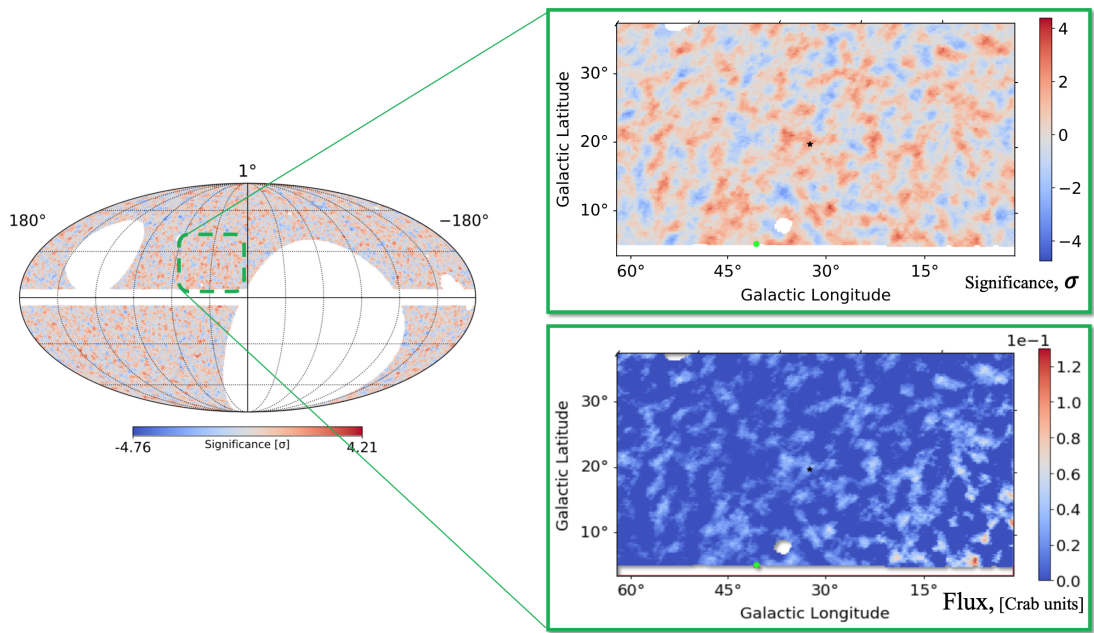
FIGURE 6.6: Zoom in on ROI at 1°. The *upper panel* displays the significance and the *lower panel* depicts the flux in the selected region. The black star is pulsar J1740+1000 and the green dot is pulsar J1846+0919.
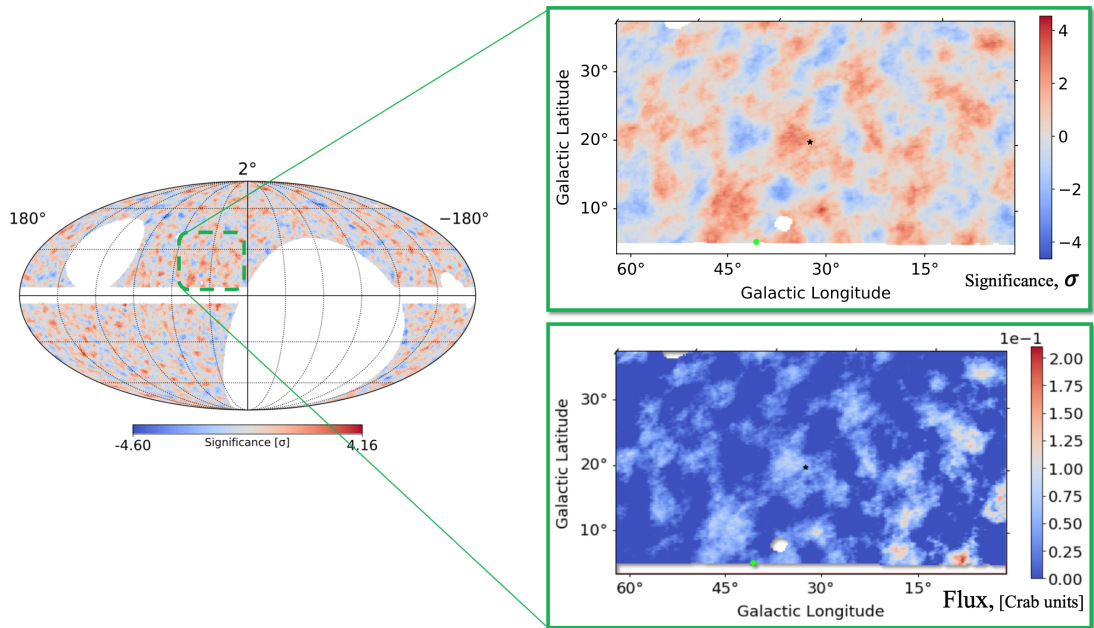
FIGURE 6.7: Zoom in on ROI, similar to Figure 6.6, except for an integration radius of 2°.

clearly demonstrates extended emission at integration radii 8° and 16° in Figures 6.9 and 6.10, respectively, which could be a TeV halo associated with a pulsar, molecular clouds or a galactic outflow.

As a preliminary investigation, we selected a circular region of radius 11° about the
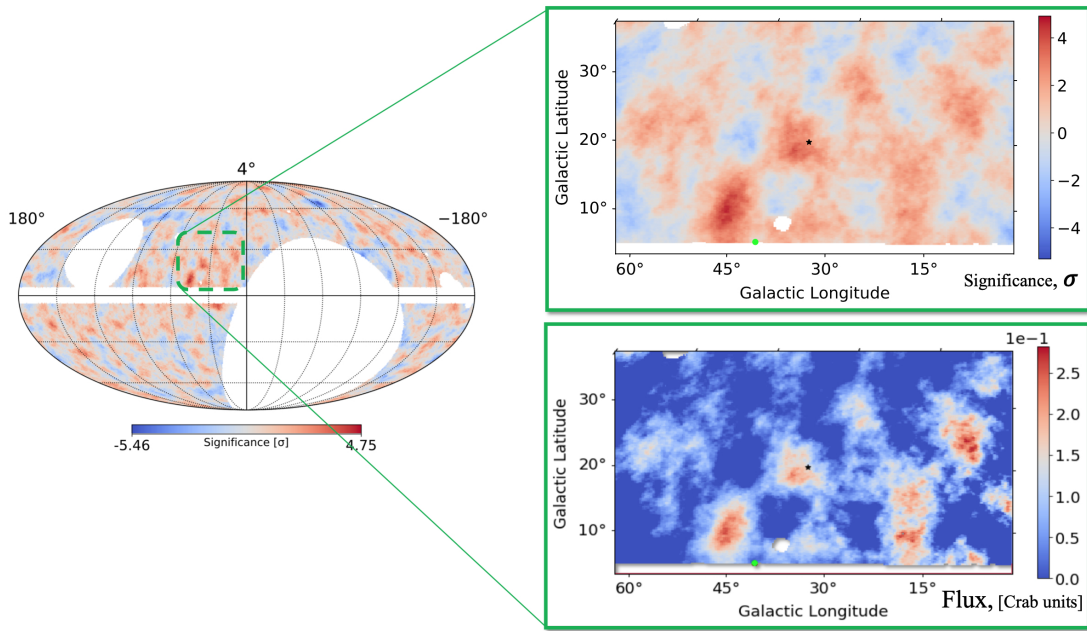
FIGURE 6.8: Zoom in on ROI, similar to Figure 6.6, except for an integration radius of 4°.
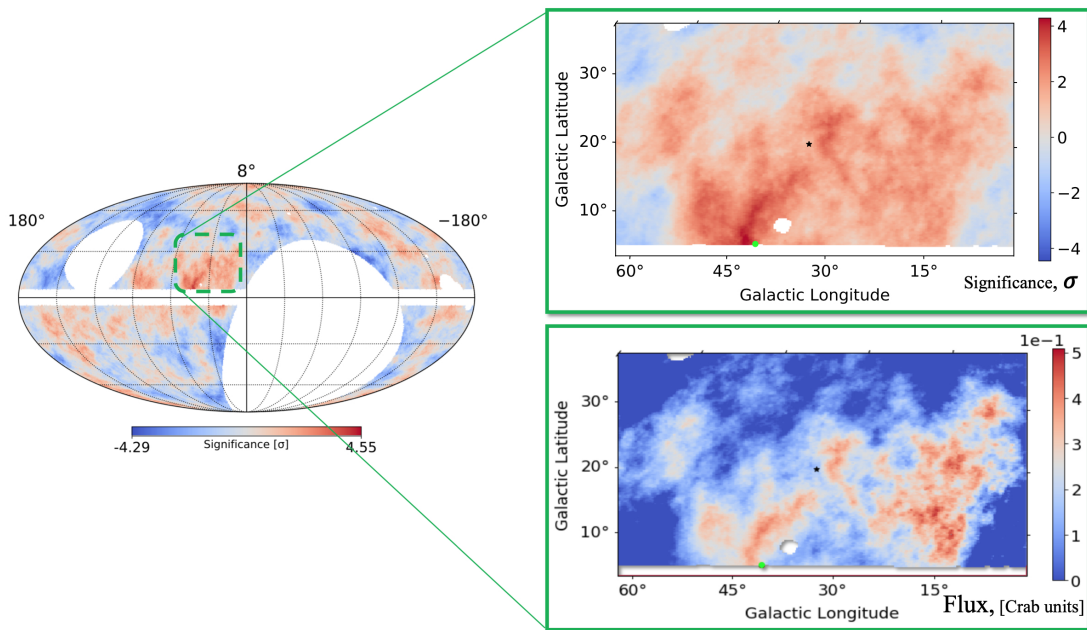
FIGURE 6.9: Zoom in on ROI, similar to Figure 6.6, except for an integration radius of 8°.

galactic coordinate (33°, 16°). Applying the profile likelihood approach, the differential flux at 7 TeV for that region was found to be $(8.05 \pm 6.86) \times 10^{-14}$ TeV^{-1}cm^{-2}s^{-1}. We repeat the computation with different spectral indices (cf. Section 5.5) and factor in the solid angle of the selected region. Figure 6.11 illustrates the upper flux limits obtained from different spectral indices tested and how the integral flux upper limit was found to
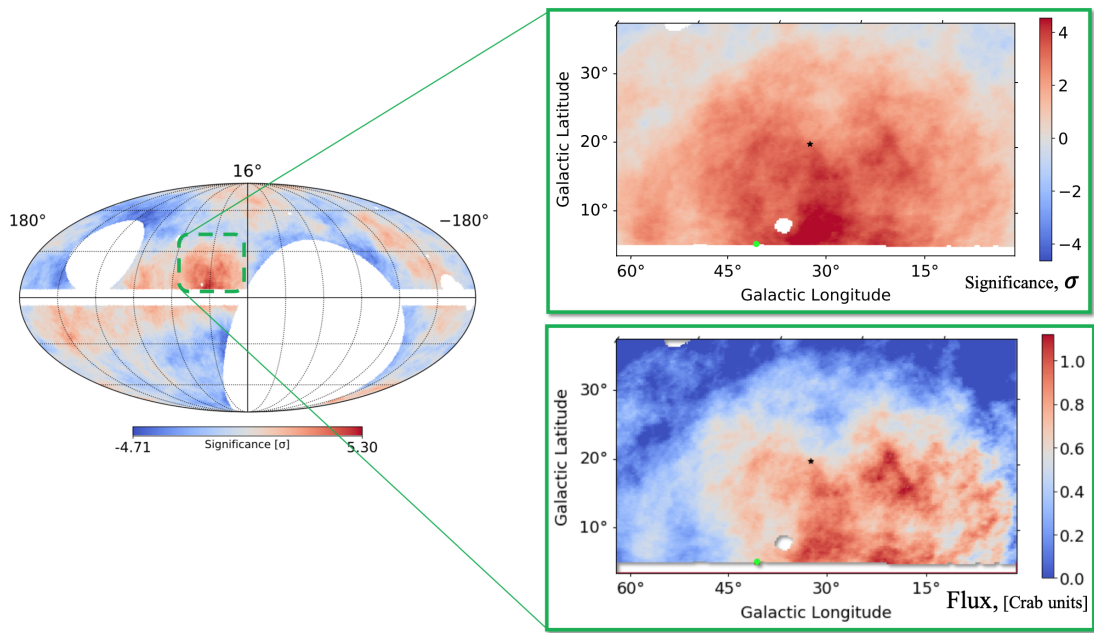
FIGURE 6.10: Zoom in on ROI, similar to Figure 6.6, except for an integration radius of 16°.

be $\sim 1 \times 10^{-6} - 3 \times 10^{-8}$ for energies between $1 - 100$ TeV. While no detailed source spectral or morphology analysis is done in this study, we provide the following description for the possible source(s) of this previously unseen large-scale emission.
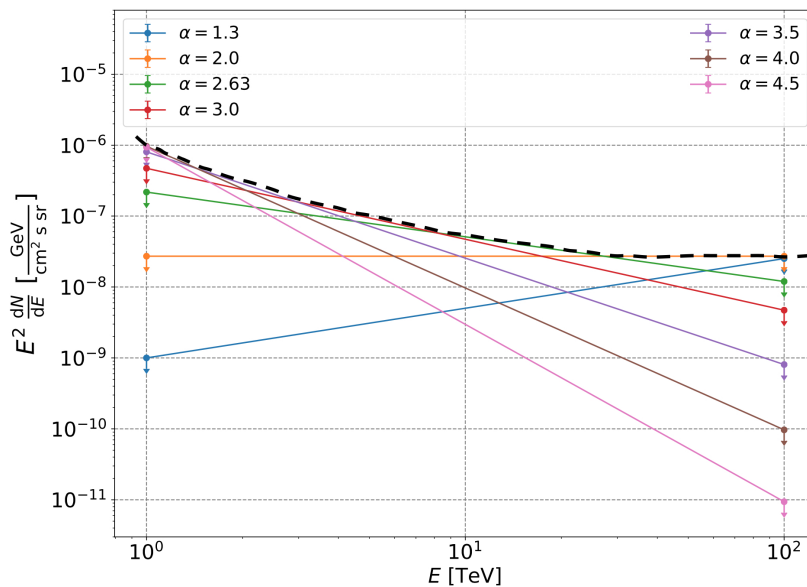
FIGURE 6.11: Extracting integral flux upper limits using 95% confidence level upper limits from different spectral indices.

6.2.1   Pulsar Related Emission?

The location of two nearby pulsars[1] are marked in Figures 6.6 - 6.10. The black star at $l = 34.0°$, $b = 20.3°$ is J1740+1000. It has a spin down power of 2.32×10^{35} erg/s, a characteristic age of 114 000 years and its distance, estimated via dispersion measurement, is 1.23 kpc from the Sun (McLaughlin, Cordes, and Arzoumanian, 2000; McLaughlin et al., 2002; Bilous et al., 2016). The green dot at $l = 40.7°$, $b = 5.3°$ is J1846+0919. It has a spin down power of 3.41×10^{34} erg/s, a characteristic age of 360 000 years and is at a (dispersion measure) distance of 1.53 kpc from the Sun (Saz Parkinson et al., 2010).

Building on equation (1.15), in the Thomson regime, the electron cooling timescale through IC scattering is:

$$\tau_{\text{IC}} \approx 3.1 \times 10^2 \text{kyr} \left(\frac{1}{U_{\text{rad}}} \right) \left(\frac{1}{E_e} \right). \tag{6.8}$$

The relation between E_e and E_γ produced through IC scattering is $E_e \approx 11\sqrt{E_\gamma}$ TeV. Assuming a CMB photon field, $U_{\text{rad}} = 0.26$ eV/cm^3, and given the characteristic age of PSR J1740+1000, the electrons can cool down to 10 TeV which corresponds to 1 TeV photon. Assuming a power-law spectrum for $\mathcal{F}(E)$, with index -2.1 and normalisation 8.05×10^{-14} TeV^{-1}cm^{-2}s^{-1}, as calculated above for the ROI, we compute $\mathcal{F}_{>1\text{TeV}}$, the power required in gamma-ray as $\int E\mathcal{F}(E)\mathrm{d}E$ from 1 to 100 TeV. The gamma-ray luminosity, $\mathcal{L}_\gamma$, is then $4\pi d_{\text{PSR}}^2 \mathcal{F}_{>1\text{TeV}}$. Using these values, we estimated $\mathcal{L}_\gamma$ to be approximately 5.0×10^{33} erg/s for PSR J1740+1000 or 2% of its spin down power and 3.4×10^{34} erg/s for PSR J1846+0919 or 23% of its spin down power. Thus, both pulsars have the minimum power to drive the emission seen at TeV energies.

PSR J1846+0919 was detected through *Fermi*-LAT (Saz Parkinson et al., 2010) and given its location at the edge of the ROI, it is unlikely that the large-scale emission originates solely from PSR J1846+0919. On the other hand, PSR J1740+1000, detected through an Arecibo survey, is close to the centre of the ROI (McLaughlin, Cordes, and Arzoumanian, 2000; McLaughlin et al., 2002). It is a relatively young pulsar and has higher energetics than PSR J1846+0919. PSR J1740+1000 is located at a large distance from the Galactic plane and was originally thought to be representative of a class of high velocity pulsars ejected from the Galactic plane. It was also suggested that the pulsar was actually born out of the Galactic plane, likely from a halo-star progenitor. Kargaltsev et al. (2008) used data from *Chandra* and XMM-*Newton* to study the PWN properties of the pulsar in X-rays, i.e. in the $(0.4 - 10)$ keV energy band. This study revealed a tail associated with PSR J1740+1000, the orientation of which suggests that the pulsar is moving

---

[1]The properties of the pulsars were taken from ATNF (Australia National Telescope Facility) pulsar catalogue at https://www.atnf.csiro.au/research/pulsar/psrcat/.

at a small angle (7°) towards the Galactic plane. The occurrence of a tail associated with PSR J1740+1000 is regarded as an extreme case of ram pressure-confined outflow from the pulsar moving supersonically. As mentionned above, the pulsar reveals relativistic electrons that can produce TeV emission via the IC scattering of IR and CMB photons. However, interestingly, no extended radio emission has been reported around this pulsar which could be due to a lack of observation with sufficiently deep exposures.

6.2.2 North Polar Spur or Galactic Outflow?
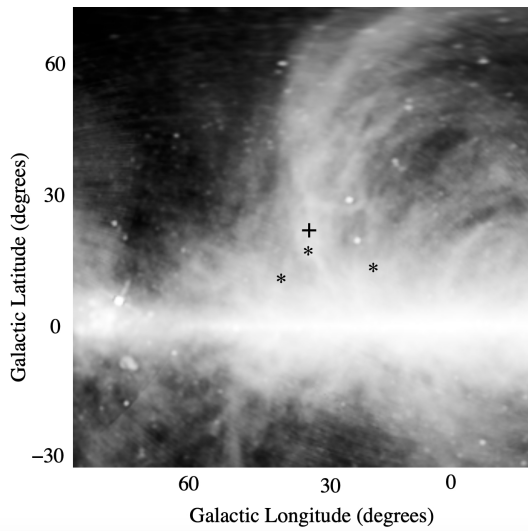
(A) ROI at 408 MHz (Haslam et al., 1982). PSR J1740+1000 is denoted with a plus (McLaughlin et al., 2002).
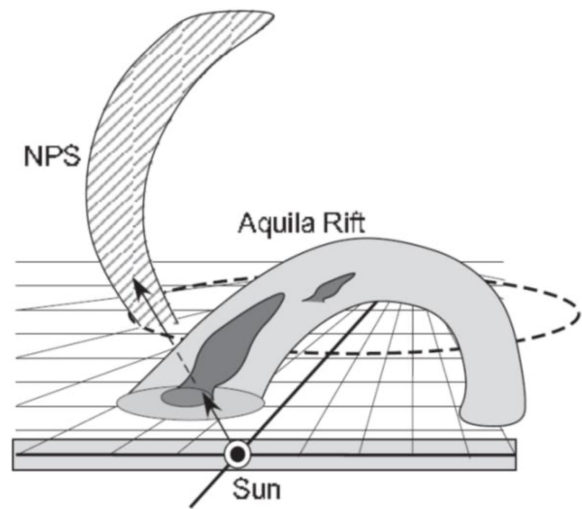
(B) Proposed 3D view of NPS and Aquila Rift from the sun (Kataoka et al., 2018).
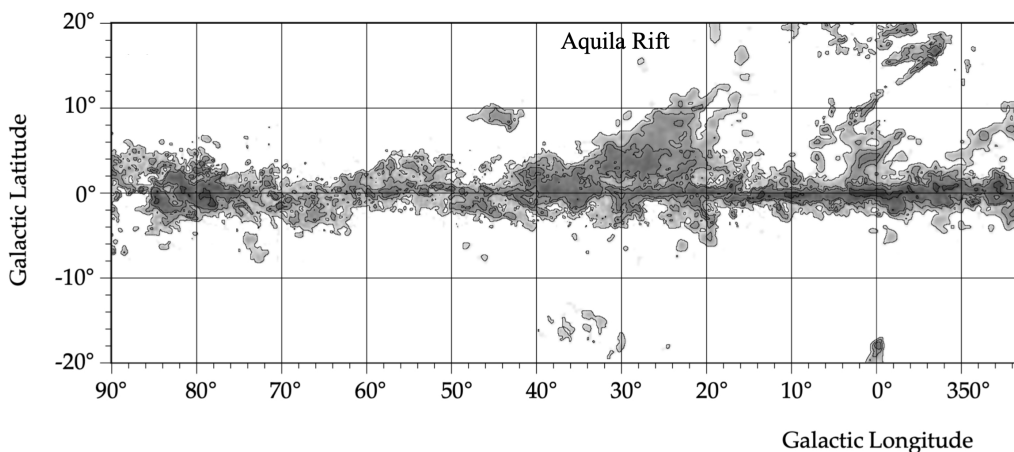
(C) ROI in velocity-integrated CO map (Dame, Hartmann, and Thaddeus, 2001). The Aquila Rift region is labelled.

FIGURE 6.12: ROI in different light and perspective.

Figure 6.12(A) depicts the ROI at 408 MHz. It is the desourced and destriped[2] radio continuum survey (Haslam et al., 1982). It reveals that the ROI comprises of the North Polar Spur (NPS) which is part of a hot interstellar bubble created by winds of young, hot stars and several supernova explosions. It is a coherent structure of the soft X-ray sky, however, in radio maps, it forms a bright ridge of emission emanating perpendicularly from the Galactic plane at $l \sim 30°$ (Dickinson, 2018), then joins the Loop I.[3]

NPS is usually assumed to be the remnant of a local supernova (Heiles et al., 1980; Salter, 1983; Egger and Aschenbach, 1995) which leads to distance estimates ranging from 50 pc to 200 pc (Berkhuijsen, 1973; Bingham, 1967). The age of NPS is not known; It should be fairly young as it it observed in X-rays and it should be sufficiently old for expanding into such shells via the release of energy into the ISM. McLaughlin et al. (2002) quotes age estimates between 2×10^5 years to 2×10^6 years old. Location-wise, the NPS seems to match the large-scale emission seen in our ROI. It is noteworthy that SAS-II, COSB and EGRET searched for HE gamma-rays associated to accelerated electrons or protons from NPS which did not come to fruition (Casandjian and Grenier, 2009). None of the detectors had enough statistics to distinguish the faint signal of the NPS from broad galactic emission, such as IC emission from CR electrons scattering with interstellar radiation field or bremsstrahlung associated to hydrogen gas or emission from pion production and subsequent decay. However, Casandjian and Grenier (2009) modelled the galactic diffuse emission and compared it to *Fermi*-LAT photons detected above 300 MeV to find an excess whose structure is similar to that seen in synchrotron emission maps.

6.2.3   Giant Molecular Cloud-Associated Emission?

As introduced in Section 1.6, molecular clouds are sources of particularly intense and localised gamma-ray emission as well as diffuse emission in the presence of CRs. The ROI overlaps with the Gould Belt, an expanding disk of gas and young stars (Stothers and Frogel, 1974), which major local molecular clouds appear to follow (Dame, Hartmann, and Thaddeus, 2001). These molecular clouds are part of the Serpens-Aquila Rift (or simply Aquila Rift) which lies on the line of sight to NPS as illustrated in Figure 6.12(B). The molecular clouds do not have ionised gas as most of ISM. Instead, they have molecular hydrogen which is difficult to detect directly, but can be traced using CO survey.[4]

---

[2]Because of variations in the thermal and electronic stability of telescope systems, residual offsets are observed from one detector to another which results in strips in the reconstructed maps. Destriping is a Fast Fourier Transform (FFT) algorithm that models and removes this noise.

[3]Loop I is a circular feature on the sky, centered on Scorpius-Centaurus OB Association, at longitude 330°, latitude 18°, and with a diameter of 116°.

[4]Far infrared emission is used as a total gas tracer to calibrate the ratio of molecular hydrogen column density to velocity-integrated CO distribution. Dame, Hartmann, and Thaddeus (2001) cites the conversion factor as approximately constant at $X \equiv \frac{N_\mathrm{H}}{W_\mathrm{CO}} = 1.8 \times 10^{20}$ cm^{-2}K^{-1}km^{-1}s

Figure 6.12(C) depicts the velocity-integrated CO map from Dame, Hartmann, and Thaddeus (2001), showing the Aquila Rift within our ROI. At this point, knowing that the line of sight to PSR J1740+1000 passes through the NPS and the Gould Belt (McLaughlin et al., 2002), it is not possible to single out a single source for the large-scale emission without further detailed study.

6.3 Galactic Plane Flux using Independent Integration Boxes
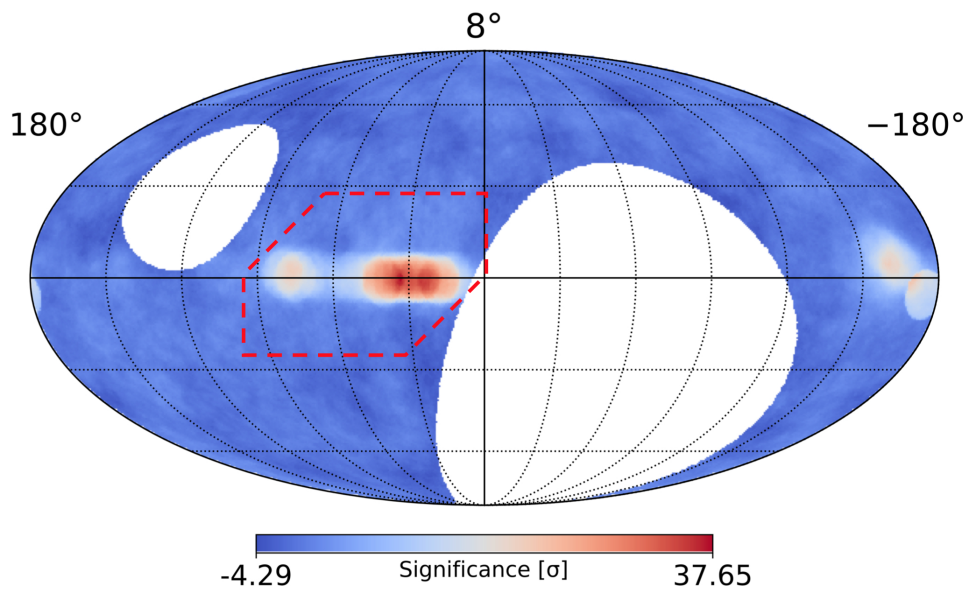
FIGURE 6.13: HAWC significance sky map with 8° integration radius without mask over Galactic plane. The significance and flux of selected region will be computed again using independent boxes.

The method described above correlates any given pixel on the sky to its neighbouring pixels within the integration radius. Figure 6.13 illustrates the sky significance map with 8° integration radius including the Galactic plane. We now compute the significance and flux of the selected region shown using $5° \times 5°$ non-overlapping boxes to get insight on its distribution as a function of longitude, $10° < l < 95°$ and latitude, $-25° < b < 25°$, in the HAWC field of view. Figure 6.14 displays the resulting significance, flux and error in flux calculated, using the same profile likelihood approach for $\mathcal{B} : 3 - 9$, within the selected region.

As expected, the latitude profile peaks in the Galactic plane for all longitudes considered and the longitudinal profiles off plane are more or less flat for the latitudes considered. The longitudinal profile within the Galactic plane is displayed in Figure 6.15 which illustrates a comparison to a scaled velocity-integrated CO intensity profile of the same
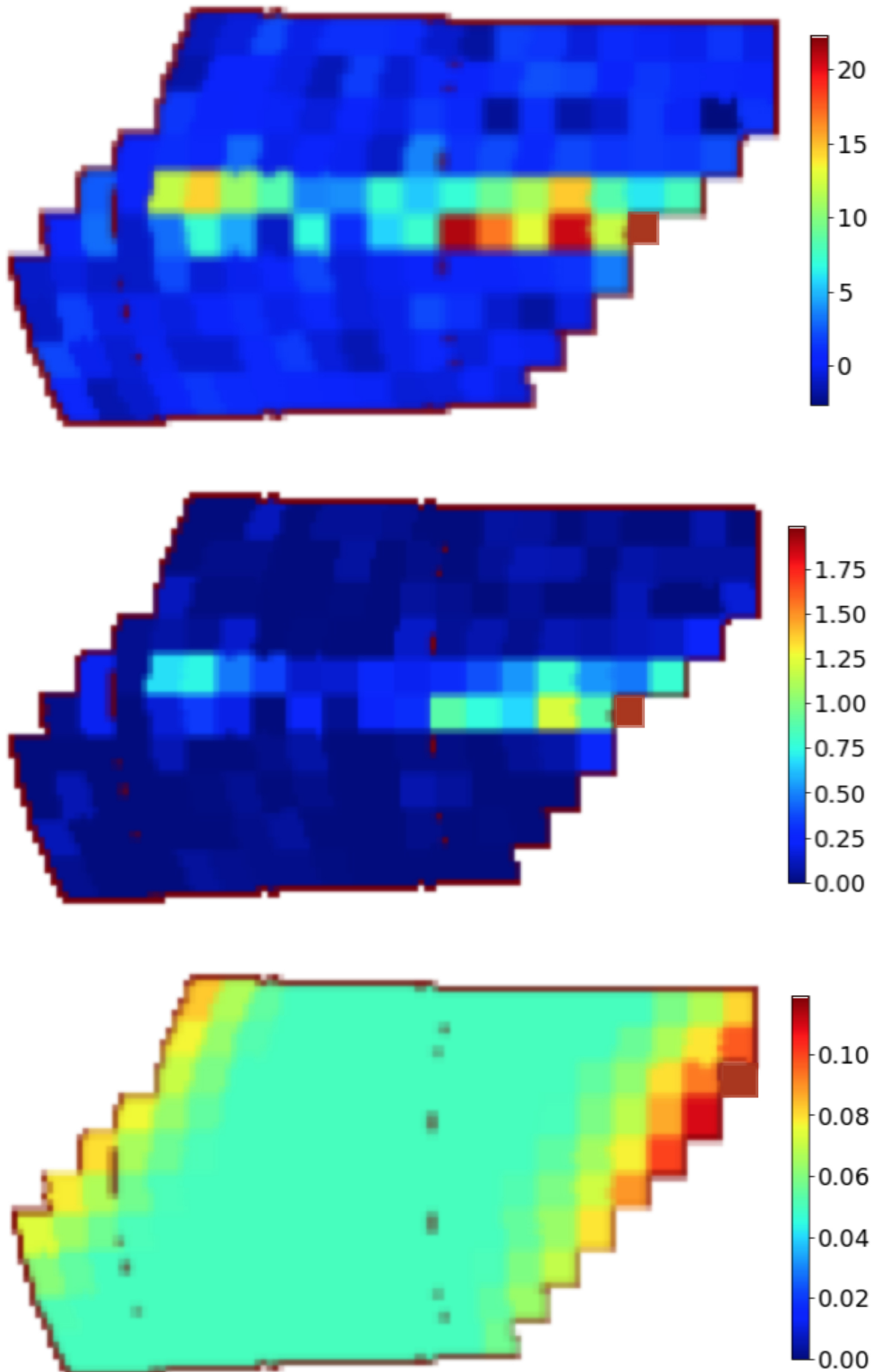
FIGURE 6.14: Significance (*upper panel*), flux (*middle panel*) and error on flux (*lower panel*) of Galactic plane through independent box integration. The flux (and error on the flux) is given in Crab units.

region extracted from Dame, Hartmann, and Thaddeus (2001). It is noted that the gamma-ray flux, from both sources and diffuse emission from the Galactic plane, correlates with the distribution of molecules.
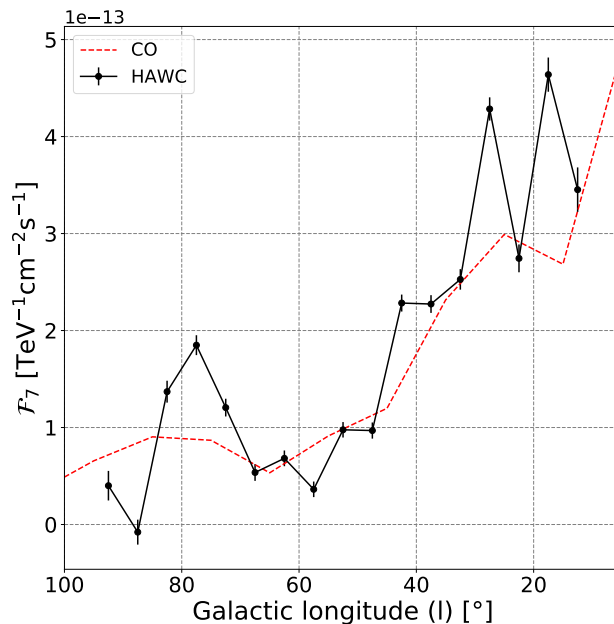
FIGURE 6.15: Comparison of the distribution of flux at 7 TeV along longitude to a scaled velocity-integrated CO intensity profile of the same region extracted from Dame, Hartmann, and Thaddeus (2001).

We can now make the following 'back-of-the-envelope' calculations for the CR energy density, assuming that the extra $\sim 20\%$ of our computed value for differential flux (cf. Section 6.1.3) is due to diffuse emission. The energy density of CRs, $\mathcal{W}_{CR}$, assuming it consists of relativistic protons is $\mathcal{W}_{CR} = \mathcal{L}_\gamma \tau_p$, where $\mathcal{L}_\gamma$ is the gamma-ray luminosity and τ_p is the characteristic cooling timescale from *pp*-interactions. $\mathcal{L}_\gamma$ is calculated through $\int E\mathcal{F}(E)dE$ from 1 to 100 TeV, which, broadly, defines the functioning range of HAWC. We assume a power-law spectrum for $\mathcal{F}(E)$, with index -2.5 and normalisation of 20% of the integrated value from Figure 6.15. $\tau_p = 1/f\sigma_{pp}cn_p$, where n_p is the density of ambient protons which is obtained by converting the CO integrated value from Figure 6.15 into hydrogen column density using the constant ratio X. c is the speed of light, σ_{pp} is the inelastic *pp*-interaction cross-section and f is the coefficient of inelasticity. On average, a proton loses about half of its energy per interaction such that $f = 0.5$ (Aharonian, 2004). σ_{pp} is almost energy-independent for energies above 1 GeV and is taken to be 40 mb (Aharonian, 2004). These values evaluate to a CR energy density of about 3×10^{-3} eV/cm^3 as being responsible for diffuse emission which is of the same order of magnitude ($\sim 1.10^{-3}$ eV/cm^3) as the sea of galactic cosmic rays above 10 TeV (Gabici, Aharonian, and Casanova, 2009).

6.4   Summary

We presented the mathematical formalism for significance and flux computation through the profile likelihood approach. After assessing the credibility of the resulting maps, we performed a blind search for large-scale structures in the HAWC sky map. A ROI, centered about galactic longitude $\sim 33°$, with significance up to 5.30σ was observed in the $16°$ significance map, for which candidate sources were discussed by comparing to data from CO survey, radio and X-ray maps. The differential flux of some gamma-ray sources were computed through the aforementioned approach and compared to previously published literature.

7

Modelling and Search of the *Fermi* Bubbles

In this chapter, we first provide a literature review of the *Fermi* bubbles, briefly introduced in Section 1.6, covering a brief summary of the different physical quantities that have been measured, inferred or remain unknown, and the potential source(s) 'blowing' the bubbles. We compare the structures seen in multiwavelength sky maps that might be associated with the *Fermi* bubbles, contrast against multimessenger searches and what is observed in other galaxies to constrain the gamma-ray emission mechanism(s). Thereon, we derive templates that describe the northern *Fermi* bubble (and its base), which are subsequently used to search for an emission signal at very high energies with HAWC.

7.1 Introduction to the *Fermi* Bubbles

The quest for the *Fermi* bubbles is fairly recent and was instantiated as a search for counterpart gamma-ray signals to what has previously been observed at other wavelengths, more specifically, at radio, X-ray, IR and microwave energies. As depicted in Figure 7.1(B), the ROSAT all-sky survey, at 1.5 keV, revealed a biconical structure over the inner region of $b = \pm 10°$ about the Galactic centre (Snowden et al., 1997). Moreover, the map displays the NPS and Loop I (Haslam et al., 1982) which are features, believed to originate from the same source as the *Fermi* bubbles, also observed in the 408 MHz radio continuum map, shown in Figure 7.1(A), since the early 1980's. Observations from the *Midcourse Space Experiment*, at 8 microns, together with data from Infrared Astronomical
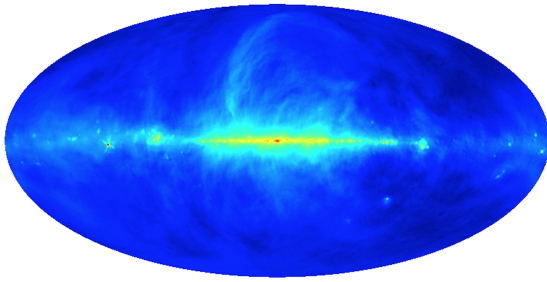
(A) Radio continuum survey using Jodrell Bank MkI, Bonn, Parkes, Jodrell Bank MkIA: 408 MHz (Haslam et al., 1982; Remazeilles et al., 2015)
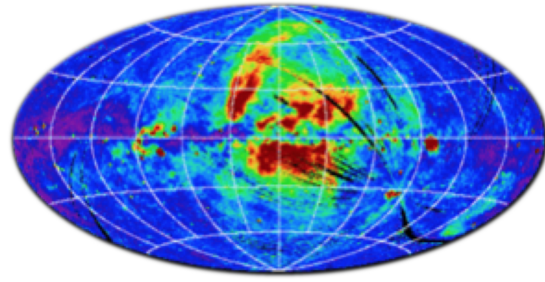
(B) Diffuse X-ray background map from ROSAT 1.5 keV (Snowden et al., 1997)
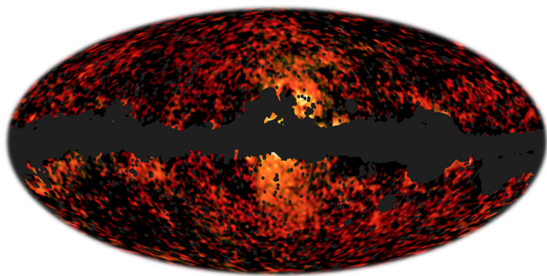
(C) Microwave emission seen with Planck (30 - 857) GHz after known contributions were subtracted. Image copyright: ESA, Planck Collaboration (Planck Collaboration et al., 2014; Finkbeiner, Langston, and Minter, 2004)
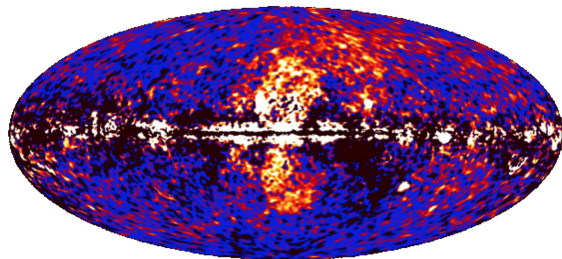
(D) *Fermi*-LAT (1 - 10) GeV residual map showing the *Fermi* bubbles (Su, Slatyer, and Finkbeiner, 2010). Image from NASA/DOE.
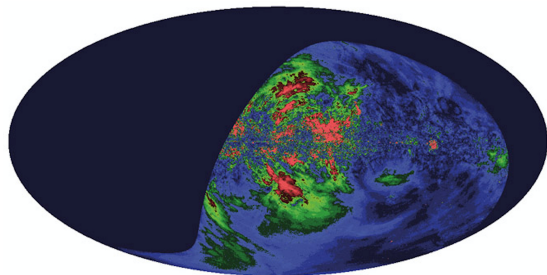
(E) S-PASS polarisation by Parkes dish: 2.3 GHz (Carretti et al., 2013)
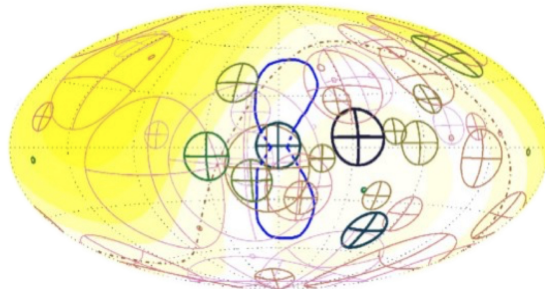
(F) Neutrino search with ICECUBE showing 1σ shower events and outline of *Fermi* bubbles region on the sky (Sherf, Keshet, and Gurwich, 2017)

FIGURE 7.1: Multimessenger and multiwavelength whole sky maps of or searches for the *Fermi* bubbles and potential associated structures.

Satellite (IRAS), at $(12 - 100)$ microns, corroborated the existence of a bipolar structure (Law, 2010) on smaller scales of $b = \pm 2°$. Finkbeiner (2004) found the *microwave haze* by removing signals originating from various known emission mechanisms such as soft synchrotron (Haslam et al., 1982), Galactic Hα (Finkbeiner, 2003), and thermal dust emission (Finkbeiner, Langston, and Minter, 2004). Figure 7.1(C) depicts the microwave haze, from

Planck at (30 - 857) GHz, reaching up to at least $b = \pm 30°$. While it is hypothesised that the haze originates from synchrotron emission, the 7-year WMAP results did not detect the predicted haze polarisation. This might be indicative of either a different emission mechanism or the presence of densely tangled magnetic fields.

Figure 7.1(D) displays the *Fermi*-LAT (1 - 10) GeV map (Su, Slatyer, and Finkbeiner, 2010; Dobler et al., 2010) which exhibits the gamma-ray lobes of interest. Fermi-LAT Collaboration et al. (2014b) performed a detailed spectral and morphological study of the bilobular structure for $|b| > 10°$, the conclusion of which was that the surface brightness is roughly uniform, the total luminosity is $4.4^{+2.4}_{-0.9} \times 10^{37}$ erg/s and the spectrum is well-described by an exponential cut-off power-law with index 1.9 ± 0.2 and a cut-off energy of 110 ± 50 GeV. Other observed features and their implications are discussed in the following sections. Interestingly, both leptonic and hadronic gamma-ray emission models fit the *Fermi*-LAT data, which sparked the search for counterpart signals though multi-messenger astronomy. Figure 7.1(E) depicts the S-PASS polarisation by Parkes dish at 2.3 GHz (Carretti et al., 2013), where the authors claim the detection of two linearly polarised radio lobes that bear close correspondence to the *Fermi* bubbles. Neutrinos can assist in recognising the dominant gamma-ray emission mechanism, as introduced in Section 1.5, with neutrinos expected in the hadronic scenario and but not in the leptonic scenario. Therefore, ICECUBE performed neutrino searches over the *Fermi* bubble region, as illustrated in Figure 7.1(F). However, the results are inconclusive as neutrino signals are difficult to detect with high accuracy (Sherf, Keshet, and Gurwich, 2017).

In the past decade, the *Fermi* bubbles have been the subject of several studies. We now describe some physical quantities associated with the *Fermi* bubbles that have, since its discovery in 2010, been measured, inferred or remain unknown.

7.1.1 Observed Features

The *Fermi* bubbles are gamma-ray structures that appear to be emanating from the central part of the Milky Way galaxy. They are gigantic in size, extending up to 55° ($\equiv$ 8 kpc) above and below the Galactic plane, with a width of about 40°, as illustrated in Figure 7.2. The bubbles have relatively sharp edges that match the features seen in the ROSAT X-ray maps (Su, Slatyer, and Finkbeiner, 2010; Casandjian, 2015). A study by Ponti et al. (2019) revealed two X-ray emitting features, which they called *chimneys*, that extend north and south of the Galactic plane for hundreds of parsecs. Lastly, the *Fermi* bubbles demonstrate asymmetry through a slight bend westward (Crocker et al., 2015) and also with the southern bubble being $\sim 5°$ bigger than the northern one (Sarkar, 2019).

There are additional measurements that can may provide some insights in deciphering the properties of the *Fermi* bubbles:
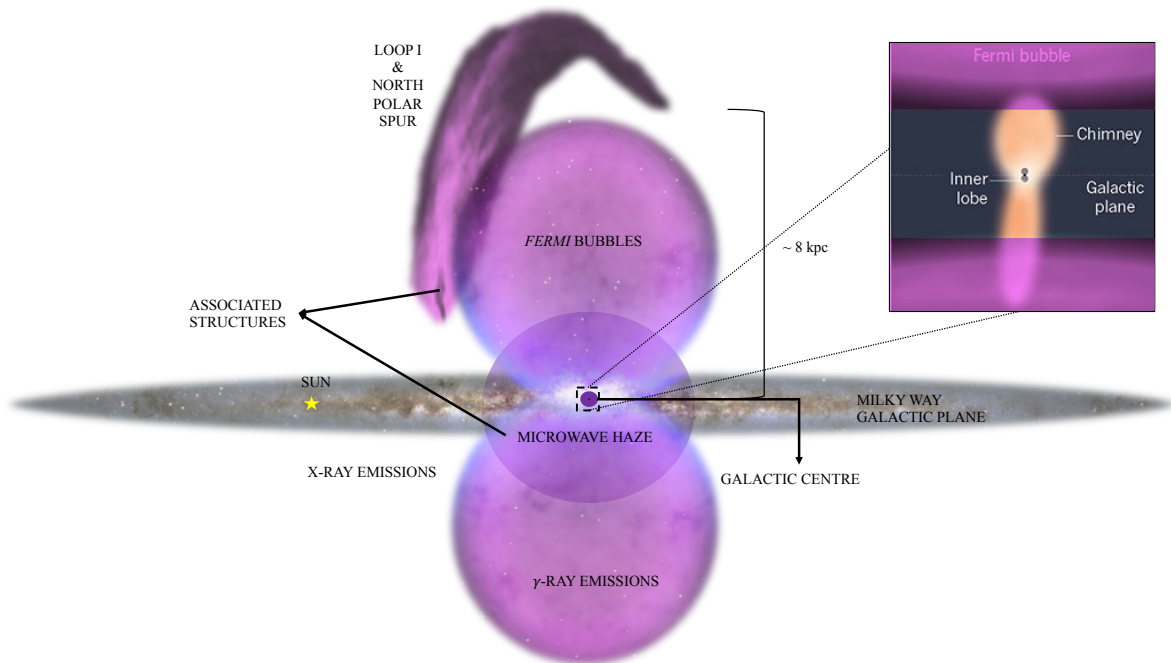
FIGURE 7.2: Schematic of *Fermi* bubbles depicting location, size and potential associated structures: North polar spur, Loop I, X-ray chimney (zoom-in view over the inner 200 pc), and microwave haze.

1. Velocity: Karim et al. (2018) used UV absorption line spectra from the Cosmic Origins Spectrograph (COS) on the Hubble Space Telescope to measure velocities of clouds within the southern bubble which provide the Galactic baryonic flow rate.

2. Magnetic field: a measure of the Zeeman splitting of radio/maser lines in the interstellar gas enables the study of galactic magnetic fields which, in turn, allows us to understand or predict particle motion and certain associated processes Kronberg (1994).

3. Lobes in other galaxies: Observation of lobes from other galaxies can assist in understanding what is happening in our own galaxy. X-ray and radio lobes have been detected in NGC 3079, M82, M31 and Hydra-a through data from Chandra, Spitzer, Herschel, XMM-Newton and the Hubble Space Telescope (cf. Figure E.1 in Appendix E).

7.1.2   Derived Properties

Based on the observed features, further quantities can be constrained, for instance, since the bubbles emit high energy gamma-ray photons, it implies non-thermal processes are at work. The striking resemblance in morphology of several features displayed in Figure 7.1 indicates the possibility of a common physical origin. The *cavity* in ROSAT X-ray

measurements suggest that the bubbles are hot ($\sim 10^7$ K) and underdense regions, i.e. have lower gas density than the ambient ISM. This further implies that the bubbles might experience a buoyant force that drives their contents away from the GC (Su, Slatyer, and Finkbeiner, 2010). The sharp edges indicate that the *Fermi* bubbles were initiated from substantial energy and mass input either through episodic events or a quasi-continuous injection (Ponti et al., 2019). However, since the bubbles are neither limb brightened nor centrally brightened, a non-trivial emissivity distribution is required to produce the observed projected flat intensity distribution. We discuss the energetics which are dependent on the gamma-ray emission mechanism in the following paragraphs. The east-west asymmetry seen in the *Fermi* bubbles is also seen in the NPS and Loop I which is an indication of an enhanced density towards the east (Sarkar, 2019). Finally, the bubbles are likely shaped by the galactic magnetic fields (Kronberg, 1994; Aharonian et al., 2008; Crocker and Aharonian, 2011).

7.1.3 Unknown Parameters

In the past decade, the *Fermi* bubbles have been the subject of several studies and yet, the source, age and dominant gamma-ray emission mechanism remain unknown. These three physical characteristics are interconnected through the energetics driving the enigmatic, gigantic structure. The age cannot be measured and its estimate strongly depends on the processes occurring within. Moreover, the bubbles range over hundreds of parsecs close to the Galactic plane making it impossible to single out a source. Therefore, for any further perception, we rely on understanding the gamma-ray emission mechanism at work. The hadronic and leptonic channels are the most popular gamma-ray emission mechanisms considered for the *Fermi* bubbles, either of which can partially account for the observed features but none of them can singly justify all of the observed features. We summarise below the features that the two gamma-ray emission mechanisms can justify, the associated energetics, age and most likely candidate source for the *Fermi* bubbles.

Leptonic Driven Scenario

Candidate source: Past AGN activity injecting a population of CR electrons into the *Fermi* bubbles with a power comparable to the Eddington luminosity $\sim 5 \times 10^{44}$ erg/s (Fermi-LAT Collaboration et al., 2014b; Crocker et al., 2015).

The observed gamma-rays result from the IC scattering of interstellar radiation field (ISRF) photons by the CR electrons. The same population of electrons, in a magnetic field approaching 10 μG, can produce synchrotron radiation which is then seen as the microwave haze. Synchrotron and IC cooling of the electrons would explain a cut-off in

the observed spectrum (Mertsch and Sarkar, 2011; Yang and Ruszkowski, 2017, cf. Sections 1.5.2 and 1.5.3).

Age: $\sim 10^6 - 10^7$ years (Guo and Mathews, 2012; Crocker et al., 2015).

Caveats:

1. Electron cooling timescales are short implying that they will not reach to the top part of the bubbles even with convection velocity as high as $1\,000$ km/s. Mertsch and Sarkar (2011) proposed stochastic acceleration of the electrons in magnetised medium (cf. Section 1.4). This, however, lowers the energy input requirements associated with this scenario;

2. ISRF constitutes predominantly of star light at low latitudes, CMB at high latitudes and IR at intermediate latitudes (Yang and Ruszkowski, 2017). Thus, a spatially uniform spectrum is not plausible;

3. This scenario does not account for radio lobes observed with S-PASS (Carretti et al., 2013).

Hadronic Driven Scenario

Candidate source: Sustained star formation activity from CMZ which generates galactic winds that transport a population of CR protons (and heavier nuclei) into the *Fermi* bubbles with a power $\sim 5 \times 10^{40}$ erg/s (Fermi-LAT Collaboration et al., 2014b; Crocker et al., 2015).

The observed gamma-rays are due to neutral pion decay which are themselves produced via *pp*-interaction, i.e. interaction between CR protons and ambient gas (cf. Section 1.5.4). The power from nuclear star formation matches the gamma-ray luminosity of the steady state bubbles. *pp*-interactions also release a secondary population of electrons which would explain the observed radio plumes (Carretti et al., 2013).

Age: $> 10^{10}$ years (Crocker and Aharonian, 2011; Crocker et al., 2015).

Caveats:

1. The observed gamma-ray emission depends on the product of the two proton population densities. Since the *Fermi* bubbles are underdense regions, the emission can only be bright if the CR proton density compensates for the reduced gas density. In other words, protons need to be trapped for sufficient timescales $\sim 10^8$ years (Crocker et al., 2015);

2. Given that the population of secondary electrons undergoes IC and synchrotron cooling, they cannot account for the microwave haze. There is an inherent need for

a population of primary electrons to produce the emission seen from the microwave haze;

3. The hadronic model per se cannot account for the sharp edges of the *Fermi* bubbles. These might be originating from trapped electrons and protons behind shock fronts.

7.2 Characterising the *Fermi* Bubbles at GeV Energies

A search of VHE gamma-ray signal from the north *Fermi* bubble with HAWC was presented by HAWC Collaboration et al. (2017d). With just 290 days of data, no significant excess was observed from the region corresponding to the north *Fermi* bubble and differential upper limits above 1 TeV were computed. We perform another search in a similar region, with 800 days of HAWC data, new sets of gamma/hadron cuts, a more appropriate background model, and a different approach for computing the signal likelihood of the nHit bins towards significance calculation.

Although initial reports have claimed a sharp cut-off in the spectrum of the *Fermi* bubbles and a flat projected brightness distribution (Su, Slatyer, and Finkbeiner, 2010; Fermi-LAT Collaboration et al., 2014b), we show that there is a gradient in the surface brightness profile of the bubbles. A recent study by Herold and Malyshev (2019) provides evidence of harder and brighter gamma-ray emission coming from the base of the bubble which fits a power-law spectrum without cut-off. Whether this emission originates from the *Fermi* bubbles or contributions unaccounted for in the diffuse emission model they use, or the GC excess, is debatable (Goodenough and Hooper, 2009; Vitale and Morselli, 2009; Fermi LAT Collaboration et al., 2017). Nevertheless, we use the profile likelihood approach introduced in Chapter 6 to search for VHE gamma-ray signals from the low-latitude north *Fermi* bubble region ($b < 10°$).

The *Fermi* bubble excess is expected to be faint and distributed over a fairly extended region. Therefore, we implement a uniform and a weighted spatial template for the two aforementioned search regions. The uniform template for the north *Fermi* bubble is the same one used for masking in Chapter 5, obtained from `Fermi Tools` and truncated at latitude 10°, as illustrated in Figure 7.3. In the following sections, we describe how we derive the uniform template for the base for the north *Fermi* bubble and the weighted spatial template for both regions.

7.2.1   Deriving Uniform Spatial Template for the Base of the Northern *Fermi* Bubble

As mentioned in Section 1.2.3, the sensitivity of HAWC is dependent on declination and, unfortunately, the base of the north *Fermi* bubble is at the edge of the HAWC field of view, where sensitivity is minimal. We therefore select a region which most likely contains the signal for the prominent part of the emission. We define a four-sided search region, henceforth referred to as the *wedge*, as illustrated in Figure 7.3 through the following functions:

1. $b = 10°$: The region below this line is typically referred to as the base of the *Fermi* bubble.

2. $b = 3°$: A study by Jardin-Blicq (2019) showed that most of Galactic plane emission in HAWC data are contained within a galactic latitude of $\pm 3°$.

3. $\delta = -25°$: Declination limit for HAWC field of view.

4. $b = 10.5(\cosh(\frac{l-1}{10.5}) - 1)$: This function was put forward by Casandjian (2015) as they compared the *Fermi*-LAT data to the X-ray edges.
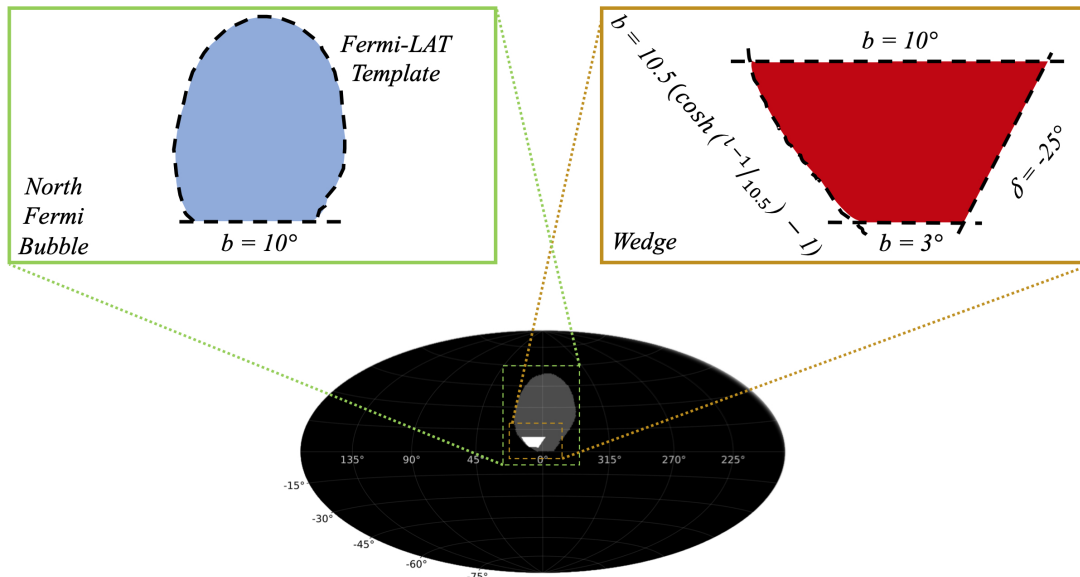
FIGURE 7.3: Description of search regions, illustrating the north *Fermi* bubble and wedge, and the base of the northern *Fermi* bubble.

7.2.2 Modelling Weighted Spatial Template through Lon-Lat Surface Brightness Profiles

Since the *Fermi* bubbles are highly extended structures, we want to define a template that surrounds the edge of the *Fermi* bubbles that also accounts for the expected number of counts from different parts within the said region. We make use of the publicly available data[1] associated with the paper "*The Fermi Galactic Center GeV Excess and Implications for Dark Matter*" by Fermi LAT Collaboration et al. ([2017](#)), which includes a residual counts map and its corresponding exposure map. The residual map has counts from the central part of the sky map with point sources masked out and consists primarily of the *Fermi* bubbles, IC emission, isotropic background and Loop I. The exposure map consists of the expected counts from a source with respect to the amount of time that the source spent in the field of view of the LAT instrument (cf. Section [1.2.2](#)).
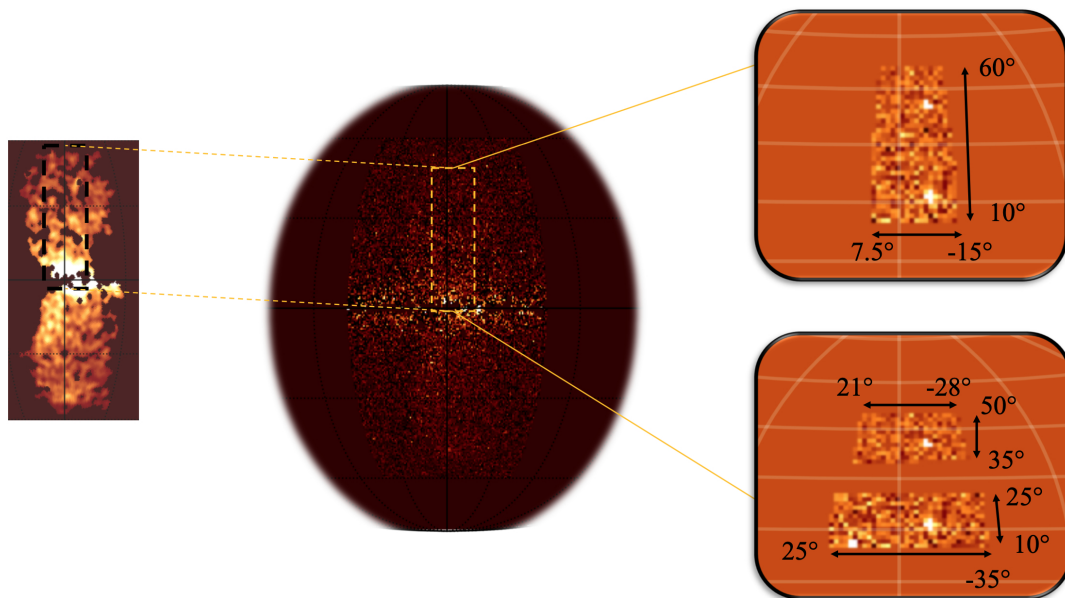
FIGURE 7.4: The leftmost component is part of a significance map, depicting the *Fermi* bubbles. The map at the centre is the residual counts map from Fermi-LAT, while the components on the right illustrate the regions for profile extraction (top for latitude and bottom for longitude).

We select longitude and latitude regions, as illustrated in Figure [7.4](#), on the exposure corrected residual map to extract corresponding surface brightness profiles. For latitude profile where $b > 10°$, displayed in the right panel of Figure [7.5](#), we essentially sum the exposure corrected counts every 2° and divide it by the solid angle that it occupies. Contrary to the Fermi-LAT Collaboration et al. ([2014b](#)) result where it was concluded that the brightness is constant over the entire bubble volume, we find that there is a latitude

---

[1]https://www-glast.stanford.edu/pub_data/1220/GCexcess_Pass8_1704.03910_data/

dependence in the surface brightness profile. Since we do not have the original counts map but a modified residual one, we compute the standard error, i.e. root-mean-square of fluctuations about the average value, which we associate to each value extracted from the 2° strip. We choose to apply a simple linear fit, $f = -8.7 \times 10^{-10}b + 6.6 \times 10^{-8}$, to the distribution, which can be eventually improved upon if required.

We repeat the profile extraction and error computation for the two longitude strips illustrated in Figure 7.4. However, since the latitude dependence is expected to be the dominant one, we average the longitude strips and fit with a top hat function as depicted in the left panel of Figure 7.5. The top hat fit was achieved using `rectangle` function in `LMFit` which involves the combination of two Heaviside step functions of same amplitude 4.3×10^{-8} but distinct centres $l = -21°$ and $l = 17°$. From the data points, we perceive the asymmetry in the bubble with a bend to the west. Here, once more, the fit is not physically motivated but constitutes a simplified starting point which can be improved upon if required.
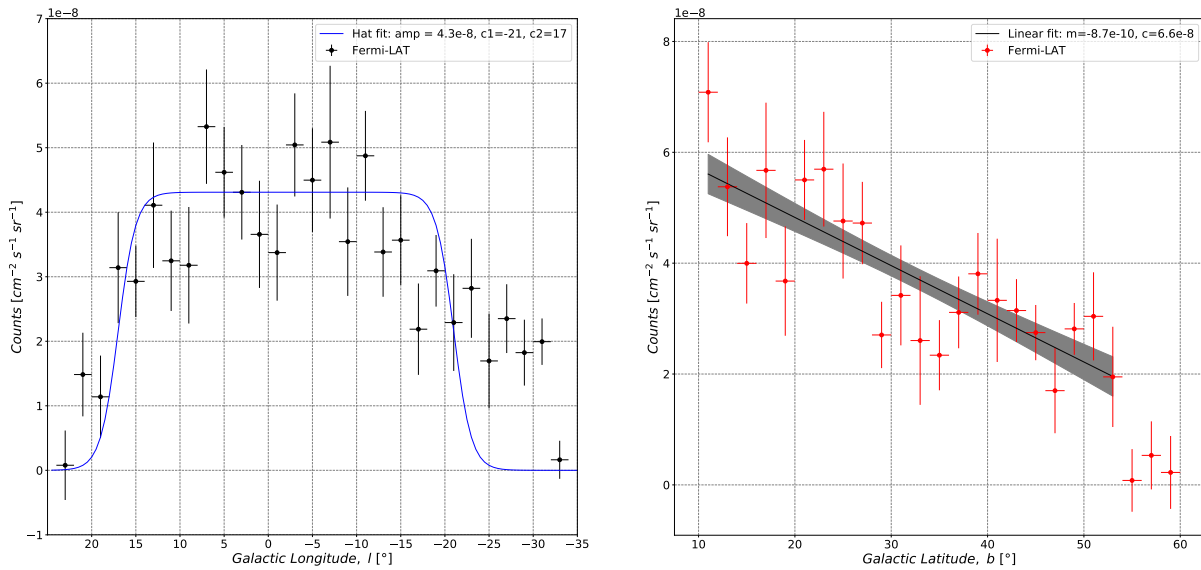
(A) Longitude profile with the fit parameters (amplitude and centres) of the two Heaviside step functions used.

(B) Latitude profile with the linear fit (gradient, m and y-intercept, c) used.

FIGURE 7.5: Longitude and latitude surface brightness profiles for the north *Fermi* bubble.

We proceed by convolving the longitude and latitude surface brightness profiles and projecting it back to the *Fermi* bubble region so as to retrieve a *counts* map analogous to the residual map with which we started. We can verify the validity of the simplistic fits we made on the profiles by generating a difference map. This map is created by subtracting the *counts* map from the residual *Fermi*-LAT map. For visualisation purposes, we apply a 10° smoothing, i.e. we integrate the counts in a 10° radius for every pixel of

both the residual *Fermi*-LAT map and the difference map as depicted in Figure 7.6. From the difference map, it is evident that our simplistic fits are adequate as they conveniently describe the north *Fermi* bubble which could be excised. Now that we have a valid model for expected counts from different parts of the north *Fermi* bubble, we normalise the sum of counts in the bubble to create a weighted spatial template of it.
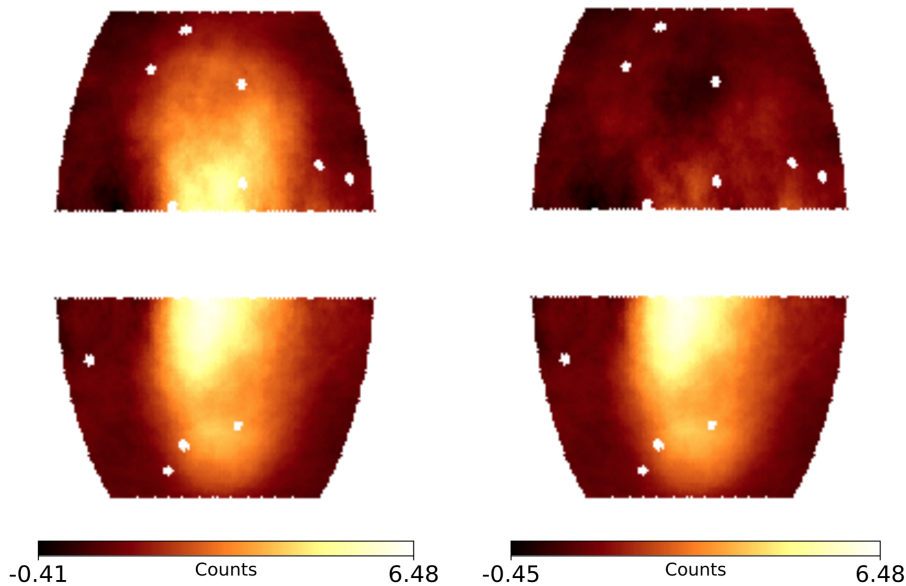
FIGURE 7.6: Spatial template evaluation. The *left panel* shows the residual counts map from *Fermi*-LAT smoothed with a 10° integration radius and the *right panel* shows a map with same smoothing after subtraction of the modelled counts from the north *Fermi* bubble region.

We wish to have a weighted spatial template for the wedge as well, so we, once again, apply the latitude profile extraction procedure for $b < 10°$ using 1° strips. We apply a linear fit and the result is plotted in Figure 7.7. From the data, it is evident that there is brighter emission from the base of the bubble. In principle, there should be a continuous function to describe the surface brightness profile over the entire *Fermi* bubble, however, we choose to work with two distinct fits. The blue points, $b > 10°$, indicate the north *Fermi* bubble and the red points, $b < 10°$, correspond to the wedge which is representative of emission expected from the base of the north *Fermi* bubble, i.e. including contributions other than the bubble, for instance, diffuse emission. Using the fit $f = -1.6 \times 10^{-8} b + 2.2 \times 10^{-7}$ in latitude and the same top hat fit in longitude as for $b > 10°$, we create a weighted spatial template for the wedge.
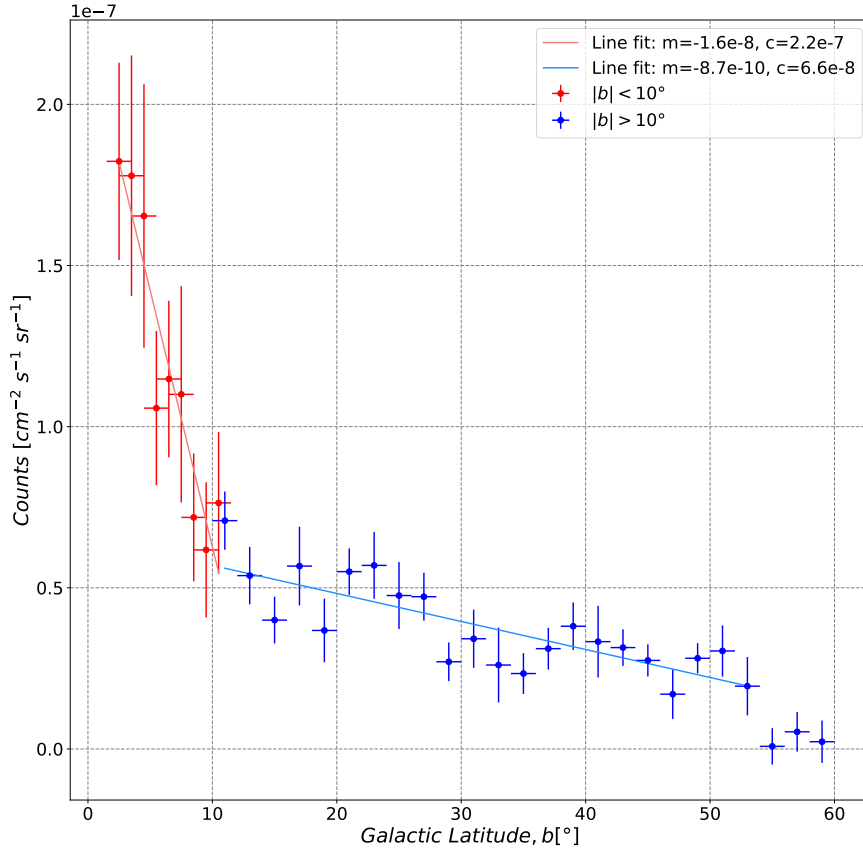
FIGURE 7.7: Latitude surface brightness profile comparison between the wedge and the north *Fermi* bubble. The linear fits with the corresponding gradients (m) and y-intercepts (c) used for the two regions are shown.

7.3   Model Independent Flux Limits

Using the profile likelihood approach described in Chapter 6, we search for an excess signal within the four aforementioned spatial templates. However, instead of integrating in a circle of set radius for each pixel, we integrate over the entire search region. We compare our results for the base of the *Fermi* bubbles to those from Herold and Malyshev (2019) which are also for the base of the *Fermi* bubbles but not exactly the same as the wedge. Figure 7.8 illustrates the different regions, to scale, whose fluxes are compared.

No significant excess seen in any of the four cases. We therefore compute upper limits with 95% confidence level as detailed in Section 6.1.3. Figure E.2 in Appendix E depicts the difference in flux upper limits between 68% and 95% confidence levels. In our approach of flux calculation, the latter depends on the exposure which, in turn, depends on the assumed source spectral index α. We compute integral flux limits, as was implemented in Section 6.2. Figure E.3, in Appendix E, illustrates the different spectral indices used to derive the integral flux limit.

Figure 7.9 displays the computed upper limit for the wedge as compared to regions
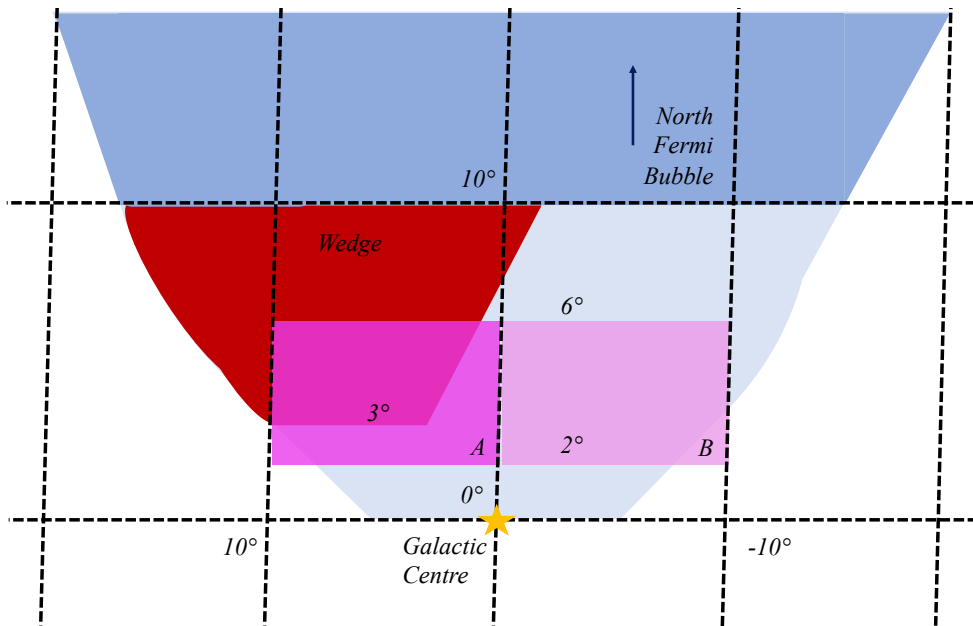
FIGURE 7.8: Description of regions at the base of the *Fermi* bubble.
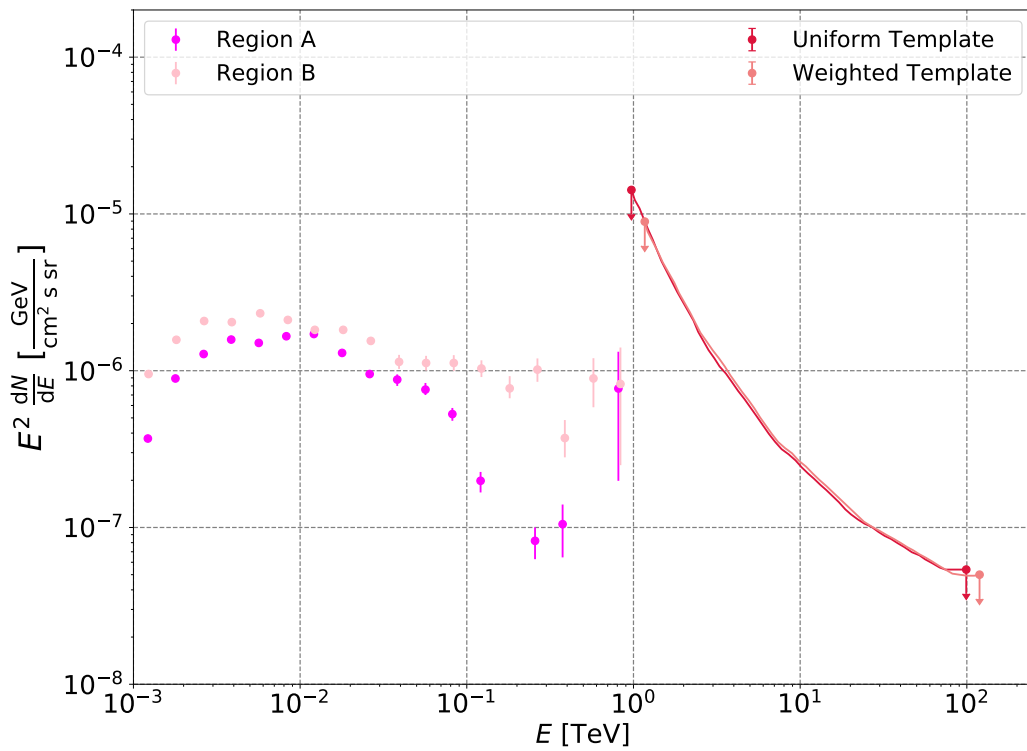
FIGURE 7.9: Integral flux upper limit on the wedge as compared to regions A and B.

A and B from Herold and Malyshev (2019). Between $1 - 100$ TeV, the flux is expected to be below $1.42 \times 10^{-5} - 5.00 \times 10^{-8}$ GeV cm^{-2} s^{-1} sr^{-1}. Figure 7.10 depicts the integral flux upper limits for the ($b > 10°$) north *Fermi* bubble as compared to a previous study from HAWC (HAWC Collaboration et al., 2017d) and the *Fermi*-LAT data (Fermi-LAT Collaboration et al., 2014b). Between $1 - 100$ TeV, the flux is expected to be below $6.31 \times 10^{-7} - 8.64 \times 10^{-9}$ GeV cm^{-2} s^{-1} sr^{-1}. These integral flux upper limits are, by construction, more constraining than the previous limits reported by HAWC. In both cases, i.e. the entire bubble and wedge regions, both the uniform and weighted templates provide almost the same integral flux upper limits.
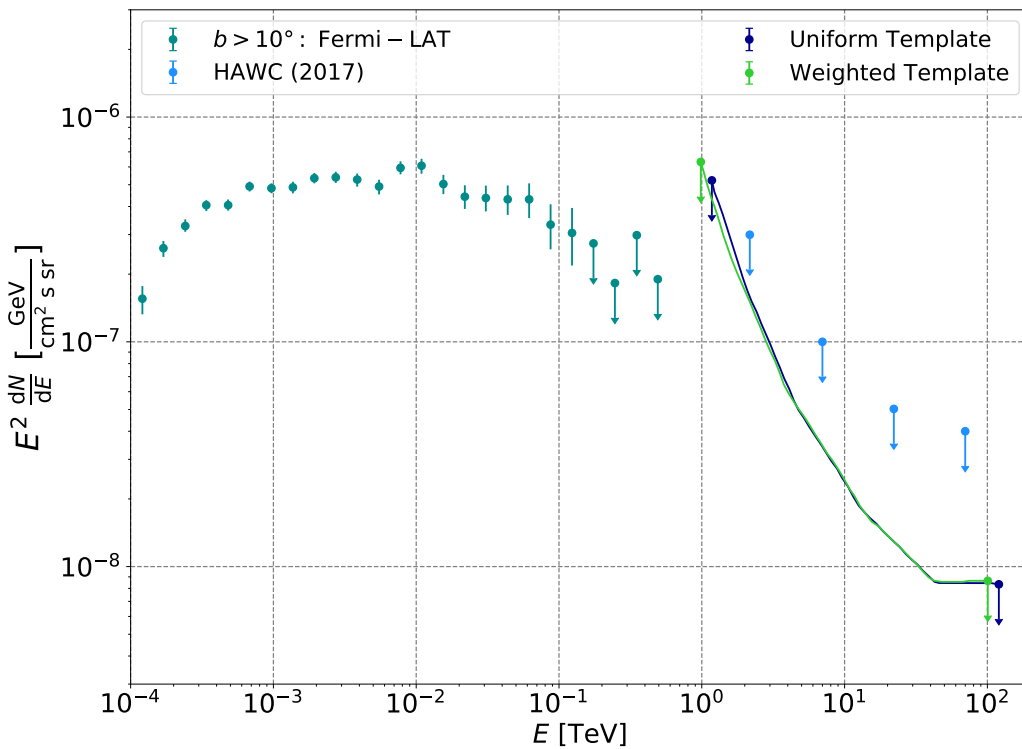
FIGURE 7.10: Integral flux upper limit on the north *Fermi* bubble compared to a previous HAWC study.

Figure 7.11 illustrates the observed spectrum and integral flux upper limits of the north *Fermi* bubble and wedge. Although we expected more emission from the wedge, we have higher flux limit than for the $b > 10°$ north *Fermi* bubble. This is due to the substantial decline in HAWC sensitivity at low declinations. We fit an exponential cut-off power-law such that it would satisfy both the *Fermi*-LAT observations (Fermi-LAT Collaboration et al., 2014b) and (barely) our integral flux upper limit. From this fit, the slope Γ is -2.25 and the cut-off energy occurs at 3.6 TeV. Hence, in a leptonic scenario for gamma-ray emission, we expect electrons with cut-off energy ~ 21 TeV from the north *Fermi* bubble. From Kappes et al. (2007), where the spectrum of neutrinos was considered:

$$\frac{\mathrm{d}N_{\gamma/\nu}}{\mathrm{d}E_{\gamma/\nu}} \approx \mathcal{F}_{\gamma/\nu} \left(\frac{E_{\gamma/\nu}}{1\mathrm{TeV}} \right)^{\Gamma_{\gamma/\nu}} \exp\left(-\sqrt{\frac{E_{\gamma/\nu}}{\epsilon_{\gamma/\nu}}} \right), \tag{7.1}$$

where $\epsilon_\nu \approx 0.59\epsilon_\gamma \approx \epsilon_p/40$. Therefore, in a hadronic scenario, we expect a proton cut-off at energy ~ 85 TeV.
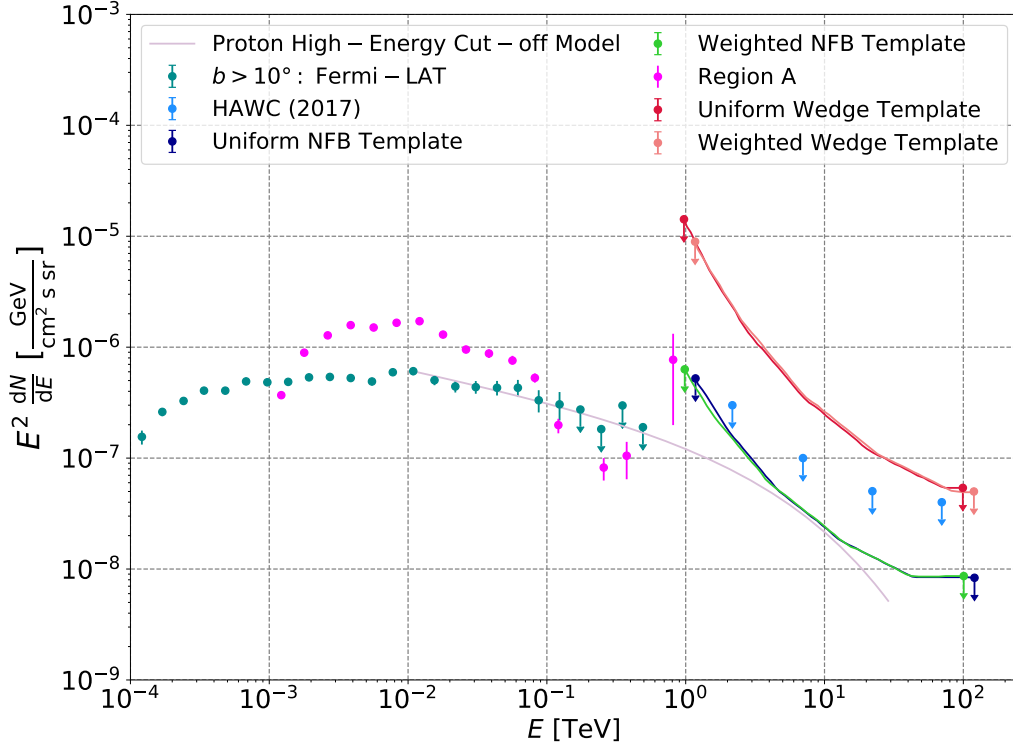
FIGURE 7.11: Flux Upper limit comparison between north *Fermi* bubble and wedge. Probable proton high-energy cut-off model, extending to TeV energies, is shown.

To grasp the implications of this high-energy proton cut-off, we plot, in Figure 7.12, the acceleration timescale for second order Fermi acceleration of interacting magnetohydrodynamic (MHD) turbulence with Alfvén waves and the escape timescale through diffusion in the Kolmogorov limit. The rate $(1/\tau)$ of these processes are energy dependent:

$$\frac{\mathrm{dln}E}{\mathrm{d}\tau_{\mathrm{acc}}} = \beta_A^2 \eta \left(\frac{r_g}{\lambda_{\mathrm{max}}} \right)^{q-2} \left(\frac{c}{\lambda_{\mathrm{max}}} \right), \tag{7.2}$$

$$\frac{\mathrm{dln}E}{\mathrm{d}\tau_{\mathrm{esc}}} = \eta \left(\frac{r_g}{\lambda_{\mathrm{max}}} \right)^{2-q} \left(\frac{\lambda_{\mathrm{max}}\beta c}{L} \right), \tag{7.3}$$

where β_A is the Alfvén wave velocity relative to c, η is the ratio of turbulent to mean magnetic field (assumed here to be 0.1) and λ_{max} is the maximum Alfvén wavelength,

typically taken to be $(1 - 10)\%$ of the system size L. A more detailed description of these timescales can be found in Schlickeiser (2002). q is the index of MHD turbulence and is $5/3$ in the Kolmogorov regime. r_g is the gyration radius, which is obtained by equating the centripetal force experienced by a charged particle undergoing circular motion in a magnetic field to its Lorentz force:

$$r_g = 33.36 \text{ km} \left(\frac{p}{\text{GeV/c}} \right) \left(\frac{1}{Z} \right) \left(\frac{G}{B} \right). \tag{7.4}$$

For this phase-space plot, we varied two parameters: density and magnetic field. We find that a maximum density of 10^{-2} cm^{-3} and a minimum magnetic field of 7 μG satisfy the hadronic upper limit where protons accelerated up to $\sim$ 85 TeV are confined and undergo pp-interaction while those accelerated above $\sim$ 85 TeV escape the bubble. Densities above 10^{-2} cm^{-3} would conflict with pp losses. This density and magnetic field are also in agreement with other studies, for instance, Fujita, Ohira, and Yamazaki (2014) and Fermi-LAT Collaboration et al. (2014a).
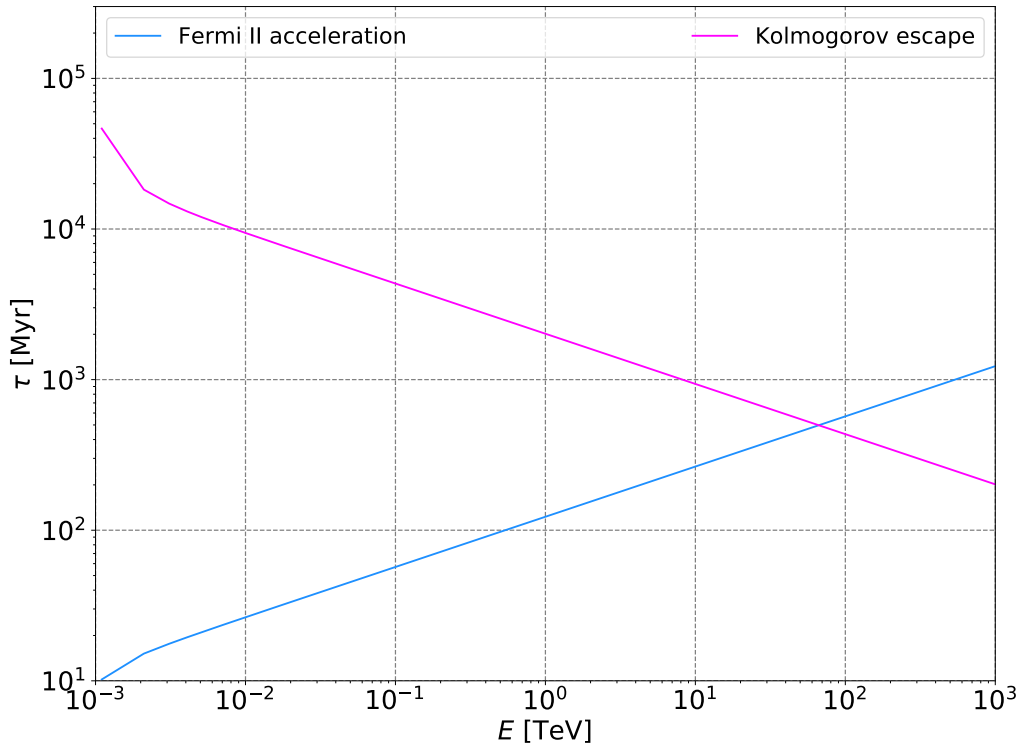
FIGURE 7.12: Interaction timescales of Fermi second order acceleration and escape through Kolmogorov diffusion.

Substituting a magnetic field of 7μG and the aforementioned proton cut-off energy, we estimate a gyration radius of $\sim 2 \times 10^{10}$ km. Moreover, using equation (1.19), we estimate the size of the source region for the VHE particle to be $\sim$ 85 pc. The magnetic

energy density, as introduced in Section 1.5.2, is estimated to be ~ 1.2 eV/cm^3. The mean Alfvén wave velocity is ~ 153 km/s, which lies in the range of values for high velocity clouds observed in the southern *Fermi* bubble in Karim et al. (2018).

7.4 Summary

The *Fermi* bubbles are few kpc-scale structures emanating from the central region of our galaxy. The physical mechanisms that source the bubbles and produce the observed spectrum are still unknown. Two of the leading gamma-ray production mechanisms involve leptonic or hadronic scenarios, both of which fit the hard gamma-ray spectrum observed and energetics involved but none of them alone can explain all of the observed features and the associated substructures. We perform a template-based search for TeV signals from the northern *Fermi* bubble and just from the base of it. A template search is better suited for such an extended but faint source as different parts of the search region are weighted according to their contribution to the overall signal, thereby integrating over less noise. Yet, no significant excess was observed and integral upper limits at 95% confidence level were computed. This is due to the substantial decline in HAWC sensitivity at low declinations. With the advent of the Southern Wide-Field Gamma-Ray Observatory (SWGO), both *Fermi* bubbles would be in its field of view. Moreover, with a novel detector design that optimises gamma/hadron discrimination and higher sensitivity, SWGO is better suited to elucidate the mysteries surrounding the *Fermi* bubbles.

Our integral flux upper limits for the north *Fermi* bubble are more constraining than the previous limits reported by HAWC while those for the wedge provide a more fair comparison to *Fermi*-LAT data points from the base of the bubble. Between $1 - 100$ TeV, the flux is expected to be below $6.31 \times 10^{-7} - 8.64 \times 10^{-9}$ GeV cm^{-2} s^{-1} sr^{-1} for the north *Fermi* bubble and $1.42 \times 10^{-5} - 5.00 \times 10^{-8}$ GeV cm^{-2} s^{-1} sr^{-1} for the wedge region. For the north *Fermi* bubble, we present a hadronic model with proton cut-off energy at 85 TeV that fits the *Fermi*-LAT data and conforms to our flux limits. This fit is a power-law with index -2.25 and cut-off at 3.6 TeV. Using the high-energy proton cut-off, we further constrain the density and magnetic field of the bubble to be $\sim 10^{-2}$ cm^{-3} and ~ 7 μG.

8

Summary, Conclusions and Outlook

Key aspects of doctoral work

The essence of this doctoral thesis constitutes cutting edge research in the development and application of sophisticated data analysis and simulation tools to optimise the scientific returns from the HAWC gamma-ray observatory. The latter has produced some interesting results using its first year of data. With its wide field of view, it is currently a unique detector to study extended sources ($> 2°$) at energies above a few TeV. One of the largest structures in the gamma-ray sky are the *Fermi* bubbles, extending to the North and South about the milky way centre. At energies around 1 TeV and above, the HAWC observatory is in a unique and privileged position to observe and constrain the flux of such large-scale structures. This inevitably entails an adequate modelling of the bubbles, improving the gamma/hadron separation of the HAWC observatory with a focus on the low energies and further improving on the background estimation of HAWC.

The salient aspects of my research are summarised as follows:

- Development of reconstruction tools to improve gamma/hadron separation for HAWC or HAWC-like detectors;

- Modelling of an exposure map for the HAWC observatory;

- Development of a novel background estimation method for wide field of view survey instruments;

- Search for large-scale structures at very high (TeV) energies, in particular the *Fermi* bubbles.

Improving Gamma/Hadron Separation

When a high-energy photon enters a medium, it pair produces in the vicinity of nuclei of the medium, with the resulting particles emitting bremsstrahlung radiation which is still of sufficiently high energy to pair produce. This process develops a cascade of particles that emit Cherenkov radiation, which subsequently triggers our instrument. However, our instrument also responds to the cascade of particles produced when a cosmic ray particle enters the medium. While the gamma-ray primary is indicative of its source region, the cosmic ray primary comes from every direction as they are charged particles that have undergone some deflection in space magnetic fields. Identification and rejection of such background events is paramount. We developed a method which uses the relevant observables, such as the charge at the PMTs and the lateral spread of the triggered PMTs, to define a discriminator between gamma and hadronic primaries. Our novel discriminator separates gamma-induced showers from hadron-induced showers, and is complementary to the existing gamma/hadron separators, while being independent of core reconstruction. The approach requires a gamma-likelihood table drawn from PMT responses which may also be employed to improve the MC simulations to more accurately emulate actual observations.

Background Modelling

Despite applying multiple discrimination parameters, gamma-like events are still overwhelmed by hadron-induced events, which can be thought of as the tail of a hadron-like event distribution. Therefore, it is essential to quantify this tail and remove it by estimating the background. We model the background through a new approach whereby we use the prime ratio of gamma-like to hadron-like event distributions to parameterise the background in right ascension and declination. Our new improved approach for background estimation, in contrast to the current background estimation technique employed in HAWC, results in faster computations, exploits all statistics available and accounts for the cosmic-ray anisotropy. By exploiting the detector response of HAWC and its livetime for the period during which the data is being recorded, we further modelled the exposure of the instrument so that we can compute the expected counts from any region of the sky within the HAWC field of view.

Unbiased Search for Large-Scale Structures

We obtained a map of excess counts by computing the difference between the gamma-like event map and the modelled background. Those excesses are potential gamma-ray source regions in the gamma-ray sky. The significance of excess counts from each region

and the corresponding flux are computed by maximising the likelihood ratio of having background counts only to that with the presence of a source. Using the new background model, we performed a blind search for large-scale structures in the HAWC sky map at different angular scales and observed several exciting and intriguing regions. This is the first application of the profile likelihood approach to HAWC data analysis, which allows the combination of data from different shower sizes while consistently accounting for their relative contributions. Within this framework, we also model the background as a nuisance parameter, such that the optimisation routine first computes the correct background, based on statistics available, and subsequently performs the likelihood maximisation. A particular region of interest, with significance up to 5.30σ was seen in $16°$ significance maps. We discussed potential candidate sources, which could be a TeV halo associated with a pulsar, molecular clouds or a galactic outflow, by comparing our results to data from CO survey, radio and X-ray maps.

Modelling and Search of the *Fermi* Bubbles at TeV Energies

The *Fermi* bubbles are kpc-scale structures emanating from the central region of our galaxy, which have been detected with *Fermi*-LAT gamma-ray instrument in the GeV energy range so far. The physical mechanisms that source the bubbles and produce the observed spectrum are still unknown. Two of the leading gamma-ray production mechanisms involve leptonic or hadronic scenarios, both of which fit the hard gamma-ray spectrum observed and energetics involved but none of them alone can explain all of the observed features and the associated structures.

A template search is better suited for such an extended but faint source as different parts of the search region are weighted according to their contribution to the overall signal, thereby integrating over less noise. We create the template based on surface brightness profiling from *Fermi*-LAT data. We make use of the optimised set of gamma/hadron separators available together with the new background and exposure maps in a profile likelihood approach for parameter estimation, which is consequently used for significance computation, to search for signals from the northern *Fermi* bubble at TeV energies. We compare our results from the weighted template to ones we calculate using a uniform template. Moreover, since we expect more signals from the base of the bubble, we also compute flux calculations for a wedge region at low latitudes.

Our searches did not yield significant detections, and hence, we provide integral flux upper limits, at 95% confidence level, for the north *Fermi* bubble and wedge regions. Between $1 - 100$ TeV, the flux is expected to be below $6.31 \times 10^{-7} - 8.64 \times 10^{-9}$ GeV cm^{-2} s^{-1} sr^{-1} for the north *Fermi* bubble and $1.42 \times 10^{-5} - 5.00 \times 10^{-8}$ GeV cm^{-2} s^{-1} sr^{-1} for the wedge region. These upper limits are the best constraints available for the
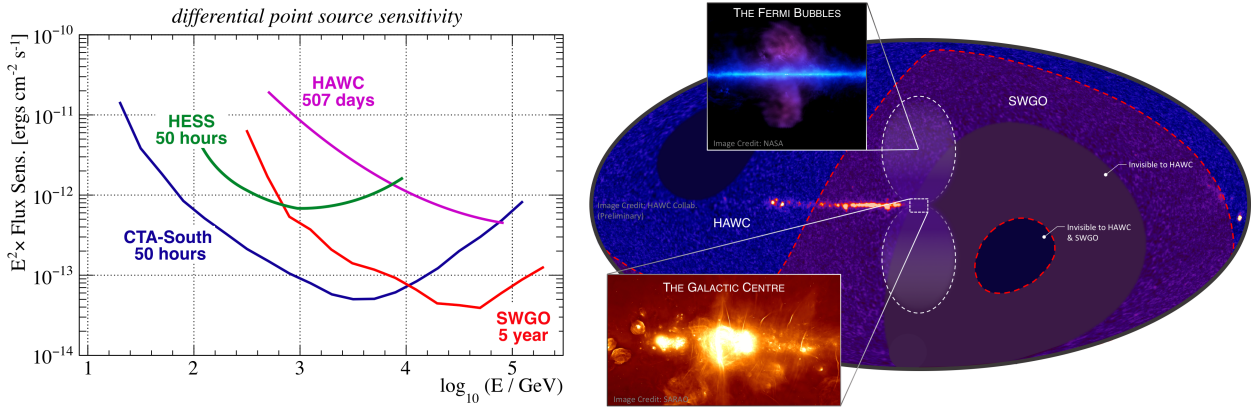
FIGURE 8.1: Sensitivity and sky coverage of SWGO. *Left panel:* Variation of differential point-source sensitivity with energy for the SWGO detector compared to other current or future instruments. *Right panel:* Sky coverage of SWGO, depicted in Galactic coordinates, overlaid on a significance map from HAWC that contains several sources. Figure from SWGO Collaboration et al. (2019).

integral flux at TeV energies. For the north *Fermi* bubble, we present a hadronic model with proton cut-off energy at 85 TeV that fits the *Fermi*-LAT data and conforms to our flux limits. This fit is a power-law with index -2.25 and cut-off at 3.6 TeV. The wedge region is at the edge of the HAWC field of view, such that the decline in sensitivity would justify the absence of the expected bright signals. However, the upper limits for the wedge region provide a more fair constraint of the flux expected from the base of the *Fermi* bubbles.

Outlook

With more data of higher quality from upcoming gamma-ray observatories, as outlined below, we can attempt another search for signals from both *Fermi* bubbles using our improved gamma/hadron separation technique and the novel background estimation algorithm. A proper understanding of the mechanisms driving the emission seen from the *Fermi* bubbles will constrain the source of the emission, thereby providing information on the activities in the GC region, i.e. the central molecular zone or Sagittarius A*.

Southern Wide-Field Gamma-Ray Observatory

As an instrument of wide field of view, HAWC is well-suited to make a survey of gamma-ray emission. A similar instrument is desirable for the southern sky as the GC and inner Galaxy is fully visible only from the southern hemisphere. The southern sky detector, driven by adequate detector design and optimisation, together with accurate modelling, will be in a prime position to survey the gamma-ray sky with high sensitivity.

The Southern Wide-Field Gamma-Ray Observatory (SWGO, SGSO Collaboration et al., 2019; SWGO Collaboration et al., 2019) is a next-generation project for the Southern Hemisphere, with unprecedented sensitivity to the VHE band (from below 1 TeV to beyond 100 TeV) and wide-field of view coverage of a significant fraction of the southern sky. It is anticipated to be fully operating in 2026, with large ($\sim$100%) duty cycle, and will subsequently provide a complementary view to both current and future gamma-ray observatories, such as HAWC (HAWC Collaboration et al., 2013) and CTA (Cherenkov Telescope Array Consortium et al., 2019), respectively.

The overall key science goals of SWGO are centered around unveiling the nature, dynamics and physical mechanisms of extreme astrophysical phenomena and sources, and investigating the possibility of new physics beyond the Standard Model, and are, therefore, similar to those of HAWC. In comparison to the latter, SWGO will possess a higher sensitivity and will potentially observe both the North and South *Fermi* bubbles, as illustrated in Figure 8.1. As such, the work presented in this thesis, in particular the gamma/hadron separation, background and exposure modelling, profile likelihood approach and template weighting for the *Fermi* bubbles, will be extremely relevant to SWGO and will undoubtedly contribute in exploiting the immense potential of such an observatory.

A

Supplementary to Non-thermal Astrophysics and Ground-based Particle Detection Techniques

As supplementary material, we provide a review of the Crab nebula as it is often used to calibrate both computations and measurements. We also summarise some other gamma-ray sources such as Geminga, Markarian 421 and Markarian 501.

Gamma-ray Sources

The Crab Nebula

The Crab nebula is the remnant of the SN explosion that occurred in 1054 AD and reported by Chinese, Japanese, Middle Eastern, and Native American astronomers. The light show from the explosion was seen even in daylight for weeks and at night for almost two years before fading away. In 1731, an English astronomer, John Bevis, located the remnant in the constellation of Taurus and so, the Crab nebula became the first object in the Messier catalog of nebulae and star clusters. Historically, William Parsons, in 1850, named the Crab nebula and Lundmark (1921) and Hubble (1928) proposed that it was associated with the SN explosion of 1054. However, it was not until 1941, that the Crab nebula was unambiguously established as the remnant of the SN 1054.

The Crab nebula is located at a distance of approximately 2 kpc from Earth or ~ 6500 light-years at an equatorial right ascension of 83.64° and declination of 22.01°. Figure A.1 illustrates the Crab nebula as seen at different wavelengths, which shows that the nebula consists of a pulsar and a pulsar wind nebula. It was first seen at TeV energies by Whipple (Weekes et al., 1989) and for a recent study by HAWC for observations above 100 TeV, we suggest the reader to HAWC Collaboration et al. (2019). While the Crab nebula occasionally flares in the gamma-ray energy regime, over the course of months, it is regarded as quiescent and consequently is often used to cross-calibrate TeV instruments. The nebula is approximately 11 light-years in diameter. This is much smaller than the point spread function (PSF) of most ground-based TeV instruments, further justifying its use in the calibration of the angular resolution of a detector. Until now, the morphology of the Crab Nebula has only been resolved in radio, optical, and X-ray telescopes, up to photon energies of around 80 keV (Hester, 2008; Madsen et al., 2015). The H.E.S.S. collaboration recently improved the telescope's PSF description which enables resolving gamma-ray source sizes below 1 arcminute (H.E.S.S. Collaboration et al., 2019b). The *Crab unit* is sometimes used as unit for flux within this thesis and it corresponds to a spectrum with spectral index 2.63 and normalisation factor $3.5e^{-11} \mathrm{TeVcm}^{-2}\mathrm{s}^{-1}$.
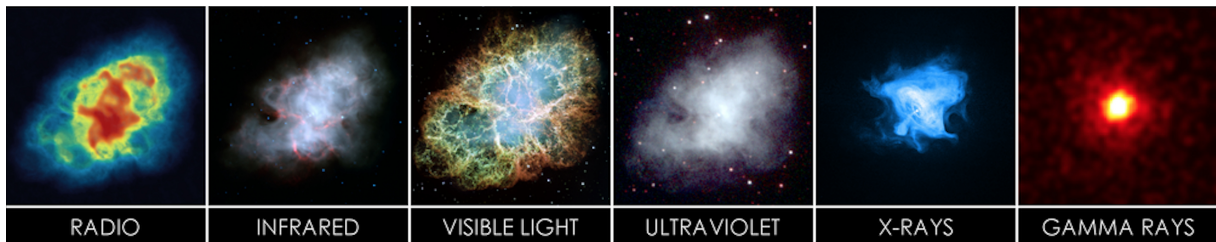
FIGURE A.1: The Crab nebula in different wavelengths. Image accessed and adapted from https://www.cta-observatory.org/science/gamma-rays-cosmic-sources/.

The associated pulsar (PSR J0534+2200) has the following properties:[1]

1. The pulsar has a period of 33 ms;

2. The spin-down power is approximately 4.5×10^{38} erg s^{-1};

3. The age, $\tau \sim 1$ kyr.

The emission from the Crab nebula is sourced from the interactions of relativistic electrons in the pulsar wind with the magnetic field present and the material ejecta from the SN explosion. The energetic flow of electrons scatters lower energy synchrotron photons up

---

[1]Properties were taken from the gamma-ray catalog, TeVCat at http://tevcat.uchicago.edu/?mode=1&showsrc=74 and the ATNF (Australia National Telescope Facility) pulsar catalogue at https://www.atnf.csiro.au/research/pulsar/psrcat/ (Manchester et al., 2005).

to TeV energies. The size of the synchrotron nebula varies as a function of energy, being smaller when observed at higher frequencies. This is interpreted as an effect of cooling of high-energy electrons.

Geminga

Geminga is a pulsar wind nebula, or TeV halo, located in the Gemini constellation, approximately 250 parsecs from Earth. Unlike the Crab nebula, Geminga is highly extended with TeV emission up to 6° from its centre. We refer the interested reader to HAWC Collaboration et al. (2017b) for further details.

Markarian 421 and Markarian 501

First studied and described by Benjamin Markarian in 1963, the Markarian galaxies are characterised by the presence of intense UV radiation. Markarian 421 is a blazar located in the constellation of Ursa Major, between 122 Mpc and 133 Mpc from Earth. The spectrum of Mrk 421 extends well into the TeV range and is highly variable with intense and intermittent flaring. Markarian 501 is also a blazar located in the constellation of Hercules. It is highly variable in the TeV range and is prone to flaring. For more details, we refer the reader to the HAWC publication (HAWC Collaboration et al., 2017a).

Fermi-LAT

The *Fermi*-LAT telescope has four main subsystems, namely tracker, calorimeter, anticoincidence detector (ACD), and data acquisition system (DAQ), which are reviewed below.

The tracker contains an array of tower modules, with each module consisting of alternate layers of (silicon-strip) particle tracking detectors and (tungsten) converter foils. The latter are capable of making precise measurements of the trajectories of the electron-positron pair produced from the initial gamma-ray photon. The resulting pair conversion signature is also used as indicator in rejecting the CR background.

Once a particle is absorbed, its energy is then measured by the calorimeter. The calorimeter is built using cesium iodide since this material emits a flash of light with intensity that is indicative of the particle's energy. The calorimeter also contributes to CR background rejection because the pattern of energy deposition of a CR particle differs from that of a gamma-ray.

The role of the ACD, which encloses the tracker, is to identify the high-energy charged CR particles which constitutes the dominant noise background. The ACD is constructed

using specially formulated plastic scintillation tiles, where the light from every tile is collected by wavelength shifting fibers connected to two PMTs. The motion of a charged CR particle through the tiles produces a flash of light, whilst a gamma-ray photon being electrically neutral proceeds through without any interaction and does not yield any signal. This is the key feature employed to distinguish CR events from gamma-rays.

The DAQ system, consisting of a series of specialised electronics and microprocessors, lies at the core of the LAT, collecting information from the other three sub-systems. It makes the initial decision whether a signal should be relayed to the ground, which requires the distinction between undesired CR signals and the real gamma-ray signals, and is also involved in the search for GRBs.

Acceleration by Unipolar Inductors

Rapidly rotating and highly magnetised astrophysical systems, such as pulsars and neutron stars, induce high electric fields which can accelerate particles to ultra-high energies (Blasi, Epstein, and Olinto, 2000; Arons, 2003). Conceptually, the rationale lies in the extraction of electrons from the astrophysical object's surface due to the electric field. Assuming a dipolar magnetic field, as in the case of neutron stars, the electrons will trace the field lines and emit radiation as a result of the curvilinear motion. As such, the photons emitted may interact with the magnetic field of the surrounding environment to generate electron-positron pairs, yielding feedback for this recurring process. The increasingly larger number of pairs fills the magnetosphere with an abundance of electrons and positions, with the difference in potential subsequently inducing acceleration.

Other Acceleration Mechanisms

In addition to the above processes, magnetic reconnection (de Gouveia Dal Pino and Lazarian, 2000), wake-field acceleration and reacceleration in sheared jets are some other possible acceleration mechanisms. An in-depth review of such processes is provided in Blasi (2013).

Lateral Distribution Function

The NKG Function

The following is adapted from the lecture notes of Bernlöhr (2018): the NKG function for the lateral distribution of secondary particles in electromagnetic showers is :

$$\rho_e = \frac{N_e}{r_M^2} c(s) \left(\frac{r}{r_M} \right)^{s-2} \left(1 + \frac{r}{r_M} \right)^{s-4.5},$$ (A.1)

where N_e is the shower size, $c(s)$ is such that $N_e = \int_0^\infty 2\pi r \rho_e dr$ and s is the shower age. The shower age, $s = 3t/t + 2t_{max}$ with $t = x/X_0$, and $t_{max} = \ln\left(\frac{E_0}{E_c}\right) - \frac{1}{2}$ such that $s = 1$ at X_{max}.

Figure A.2 displays a schematic of the Cherenkov flash cone with the eventual detection by WCDs, as in the case of HAWC.
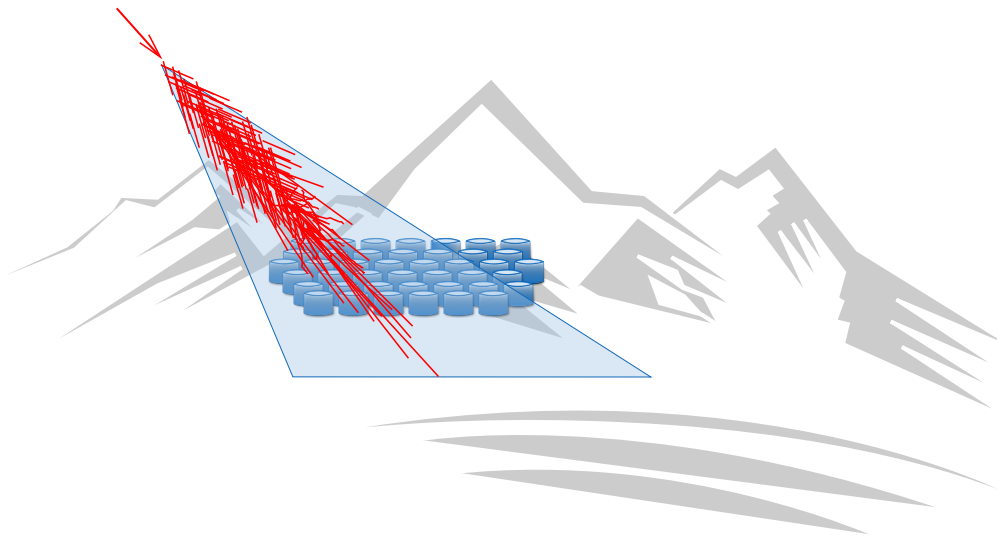
FIGURE A.2: Schematic depicting the Cherenkov flash cone with the detection in a HAWC-like scenario. A charged particle or gamma-ray entering the atmosphere generates a shower of secondary particles which are detected by water Cherenkov detectors via the production of Cherenkov light in the water. Image credit: A. Jardin-Blicq.

Geomagnetic Field

CRs, being charged particles, interact with the Earth's magnetic field which deflect their trajectories, with this deviation depending on both the particle charge and energy. This

bending effect is more substantial for low-energy showers. This geomagnetic field influences the development of EAS, causing the collected photons to be spread out, thereby reducing the sensitivity of the Cherenkov telescope. Hence, the geomagnetic field strength (rigidity[2]), as illustrated in Figure A.3, is one of the key factors to consider when planning the location of a Cherenkov particle detector. This is the rationale underlying the choice of location of the HAWC observatory in Mexico.
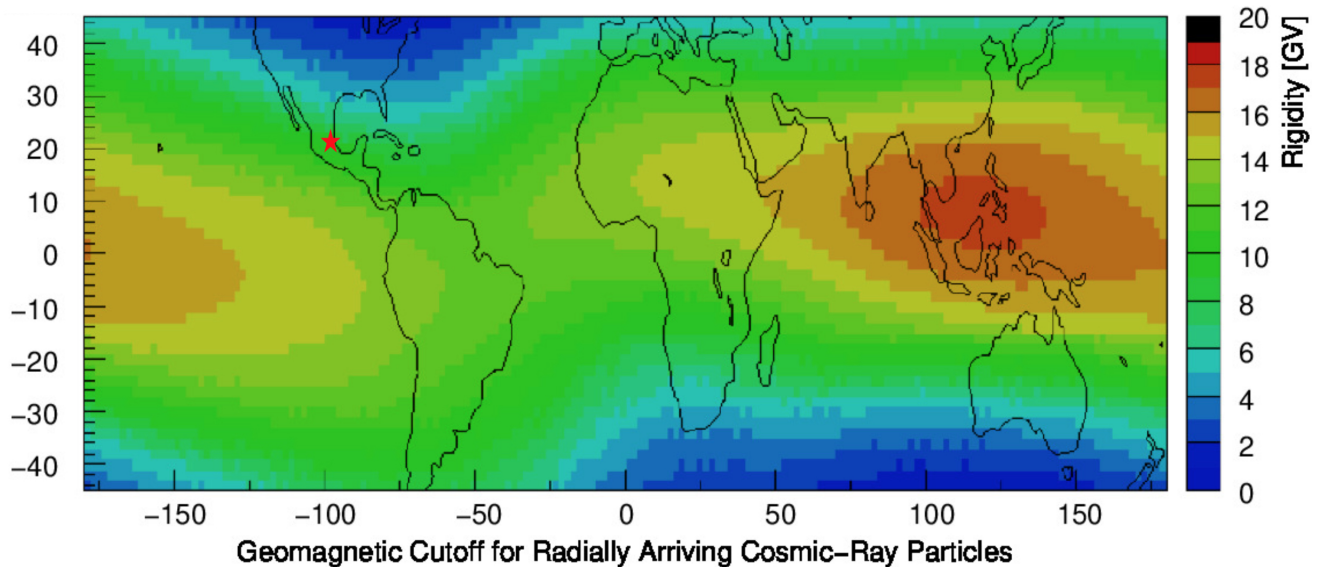
FIGURE A.3: Rigidity or equivalently magnetic field strength at different locations on Earth, with the red star indicative of the location of HAWC. Figure adapted from Biland (2018) which was computed using https://www.ngdc.noaa.gov/geomag/data.shtml.

---

[2]Rigidity is the product of magnetic field strength and gyroradius of a charged particle moving in the field. Equivalently, it is the particle momentum divided by its charge, $R = pc/Ze$, and thus implies that a higher momentum particle has a higher resistance to deflection by a magnetic field.

B

Supplementary to HAWC Gamma-ray Observatory

As supplementary material, we provide a brief review of water cherenkov detectors and their use of photomultiplier tubes (PMTs). We then define the photoelectric effect, the work function and gain of a PMT, and finally outline the different types of noises in a PMT. Moreover, we study the lateral distribution of muons with zenith angles binned equally in degrees and the behaviour of the same distribution with slant depth.

Water Cherenkov Detectors

The top of the bladder has an access hatch and four light tight instrumentation ports which feed the necessary cabling for depth monitoring, temperature monitoring, calibration fiber optics diffuser, and PMT cabling. The top of the tanks have a protective canvas dome supported by a steel frame to prevent rain or snow accumulation. Each tank is optically isolated to facilitate detection of variations in energy reaching ground, which can be used for distinguishing between gamma-ray and hadronic initiated showers.

The altitude of HAWC places it at an atmospheric depth of approximately 638 gcm^{-2} and considering pair production and bremsstrahlung interactions in air, this altitude corresponds to roughly 17.2 radiation lengths (COESA, 1976). Thus, the dimensions of the WCDs were chosen to optimise both the sensitivity of HAWC to TeV showers and to minimise the dependence of the number of detected photoelectrons (PE) on the location of the PMTs at the bottom of the WCDs. For shallow water depths, low energy secondary

particles penetrate all the way to the bottom of the WCD. This causes a large number of PEs to be detected by the PMTs, such that every detection would appear to be an EAS secondary. The depth was therefore chosen based on the penetration depth of vertical, median energy muons produced by TeV showers which is about 10.5 radiation lengths.

Photomultiplier Tubes

PMTs are a class of light-sensing devices that operate on the principle of the photoelectric effect.[1] They are sensitive enough to detect single photons and have extremely fast response speeds on the order of tens of nanoseconds. Moreover, they are designed with large collection areas, thereby reducing the total number of devices required to instrument an area the size of the HAWC observatory. The read-out signal from a PMT is amplified by applying a high voltage (HV) across it. PMTs typically consist of an evacuated glass casing whose inner surface is lined with a vapour-deposited semiconductor with a low work function.[2] This is known as the *photocathode*.

When a Cherenkov photon strikes the the photocathode, it liberates an electron which is then accelerated towards a series of metal plates, called a *dynode*, located behind the photocathode and held at a significantly higher voltage. This primary electron, upon collision with the first dynode, liberates a new group of electrons which are accelerated towards the next dynode. This process is repeated through 10 dynodes, such that the number of electrons flowing through the dynode chain continues to grow until they reach the final dynode. Thereon, all secondary electrons are transferred to the anode where they are collected and delivered to the PMT output for measurement. The ratio of the mean output charge for a single photon (producing a single primary electron) to the fundamental electron charge yields the *gain*, or amplification factor, of the PMT. This factor depends on the HV at which the PMT is operated, the total number of dynodes, and location where the incoming photon was absorbed as elaborated in Section B. Both populations of PMTs are operated with a positive HV of approximately 1 700 V, with the exact value tuned to gain-match all PMTs, thereby producing uniform electronics response.

Issues with PMTs

Although PMTs are highly sensitive, not every photon incident on the photocathode produces a free electron as the photoelectric effect is determined by a probabilistic quantum process quantified by the quantum efficiency (QE). It is the per-photon probability for creating a free electron and it depends on the photocathode material, the incident angle

---

[1] The photoelectric effect is explained in Section B.
[2] The work function is defined in Section B.

and the incident photon frequency. The collection efficiency, i.e the probability for a free electron to land on the first dynode is another factor that influences PMT read-out signals. Manufacturers like Hamamatsu report QE numbers which are interpreted as the product of quantum and collection efficiencies. For Cherenkov light spectrum, the manufacturer-quoted peak QE for the 10″ PMT is almost double that of the 8″ PMT. However, there is no distinction between photons that fail to produce free electrons at the photocathode and photons that produces an electron which subsequently fails to reach the first dynode. Thus, there is a direct relationship between the number of the incident photons and the integrated charge of the final current, implying that if a PMT is properly characterised, it can be used to count PEs by making measurements on the resulting current pulse.

PMTs are subject to different types of noise, but since we have multiple PMTs in a tank, the effects of some noise can be reduced by comparing the signals between these PMTs. Nonetheless, they introduce crosstalk which are undesired signals produced by high pulses on a neighbouring channel. The most prominent sources of noise in PMTs are dark currents, prepulsing, and afterpulsing. These are described in Section B.

The Photoelectric Effect

In the photoelectric process, the innermost electron within some material absorbs the energy of one photon and acquires more energy than the electron binding energy of the material, and is ejected. A rise in intensity increases the number of similar energy photons sent over a given time interval, but it does not affect the energy of the emitted electrons. Only the energy of the individual photons affects the photoemission of a material.

Work function of a PMT

The maximum kinetic energy of PEs produced at the photocathode is given by:

$$K_{\text{max}} = h\nu - \mathcal{W}, \tag{B.1}$$

where h is the Planck constant, ν is the frequency of the incident photon, and $\mathcal{W}$ is the work function of the photocathode. The work function describes the minimum energy required to remove a single electron from the surface of the photocathode. The work function depends on both the electrostatic potential of the cathode and the intrinsic physical properties of the cathode material.

PMT Gain

PMT gain also depends on where the initial photon was absorbed as asymmetries in the geometry of the PMT, particularly for locations far from the photocathode centre, produce different final electron velocities at the first dynode and therefore different numbers of secondary electrons (Matsubara et al., 2012). This results in the broad spread of output charge for single photon measurements, which acts as an uncertainty of about 35% to any calibration relating total charge to photon number.

Noises in PMT Signals

Dark Current

Dark current corresponds to noise that originates from current flow when the PMT is not exposed to light. The PMT functioning requires the use of materials that have low work functions for both the photocathode and dynode. These materials are also prone to the thermionic emission[3] of electrons. The current density of these emissions within a PMT is therefore dependent on the temperature.

Prepulse

Sometimes, a photon passes through the photocathode and interacts to produce a PE at the first dynode which is then accelerated through the remaining dynode chain to yield a lower signal compared to when PEs are initiated at the photocathode. This is because, in the former case, the amplification obtained from collision with the first dynode is lost. This effect produces a signal that precedes the arrival of the main pulse in multi-PE signals and is hence termed prepulse. It artificially changes the calibrated pulse timing.

Afterpulse

While an ideal PMT would contain vacuum, real PMTs contain low quantities of air. This enables electrons travelling the distance between the photocathode and first dynode to strike neutral atoms and ionise them. Although the electron continues its path to the first dynode and triggers the subsequent processes, the resulting ion drifts back to the photocathode. There, the ion collides to liberate another electron which accelerates towards the first dynode and initiates a second electronic signal, known as an afterpulse.

---

[3]Thermionic emission is the liberation of electrons from an electrode by virtue of its temperature.

Since the vacuum inside a PMT slowly degrades over time, afterpulsing is especially prevalent in older populations of PMTs, like the $8''$ PMTs re-used from Milagro. Afterpulses affect the total charge and timing of calibrated pulses because their correlation to the original pulse yields a much higher noise rate immediately following real signals, thereby increasing the chance for waveform overlap. Such waveforms are flagged and are excluded from both the air shower triggering and reconstruction algorithms.

Cable Propagation

The PMT read-out is transmitted back to a centrally located electronics building using three RG-59 coaxial cables. The total cable run for each PMT is identical and has a length of 1.85 m. The coaxial cable provides both the high voltage to the PMT, and carries the signal back to the data acquisition (DAQ) system. The propagation delay and signal dispersion within a cable depend on both the cable length[4] and the temperature. Hence, identical cable lengths were used and the cables were buried underground to minimise temperature variations, thus maintaining a similar temperature for all PMTs and ensuring uniform signal propagation throughout the array.

Digital Front-End-Boards

The digital FEB receives the low and high threshold outputs from the analog FEB and applies additional digital ECL logic to combine the low and high threshold signals into a single waveform. The DAQ records the PMT location, the charge (after charge calibration) and the time of this detection (a stream of digital pulses colloquially known as "hits").

Investigating Lateral Distribution of Muons

The distribution of the cumulative number of muons as a function of lateral distance from the simulated shower core for different incoming zenith angles binned equally in degrees is illustrated in Figure B.1.

Slant depth is given by:

$$X(z, \theta) = \int_{\infty}^{z} \rho_{\text{atm}}(z', \theta) \cos \theta \mathrm{d}z' , \tag{B.2}$$

---

[4]Signal attenuation due to the finite resistance per unit length of the conductor becomes important over long cable runs. Additionally, the structure of the coaxial cable introduces inductance, capacitance, and conductance per unit length behaviour that are considered to be on the short timescales of typical PMT signals.

(A)

(B)
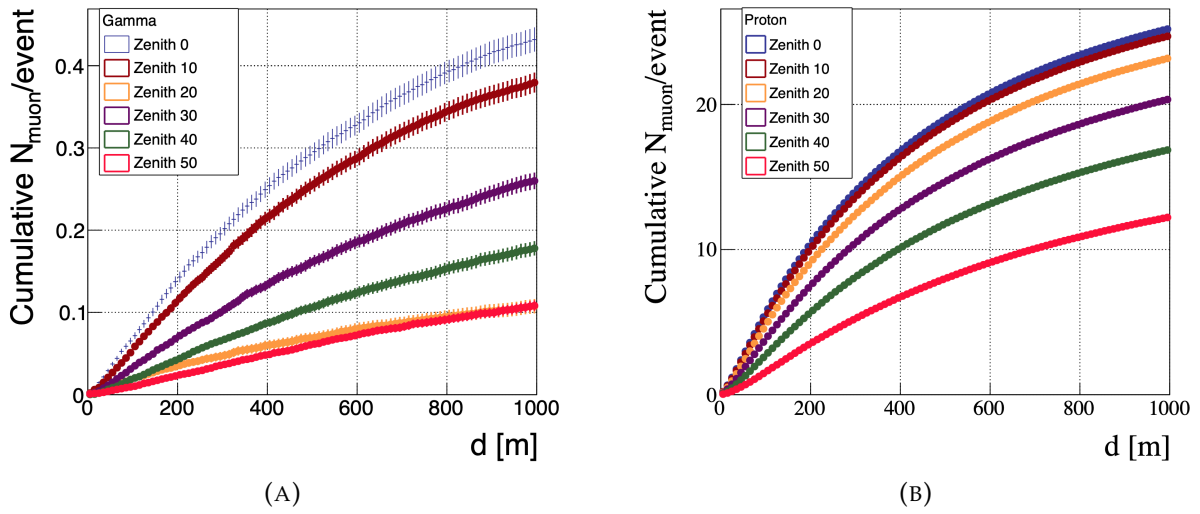
FIGURE B.1: Distribution of the cumulative number of muons per event as a function of lateral distance for a gamma-ray induced shower (*left panel*) and proton-induced shower (*right panel*) for showers with an initial energy of 1 TeV and detection was set at an altitude of 4 100 m while the incoming zenith angles were binned equally in degrees.

where z is the altitude, θ is the incoming zenith angle of the primary particle and ρ_{atm} is the density of the atmosphere. The behaviour of the lateral distribution of muons with slant depth is given in Figure B.2.

(A)

(B)
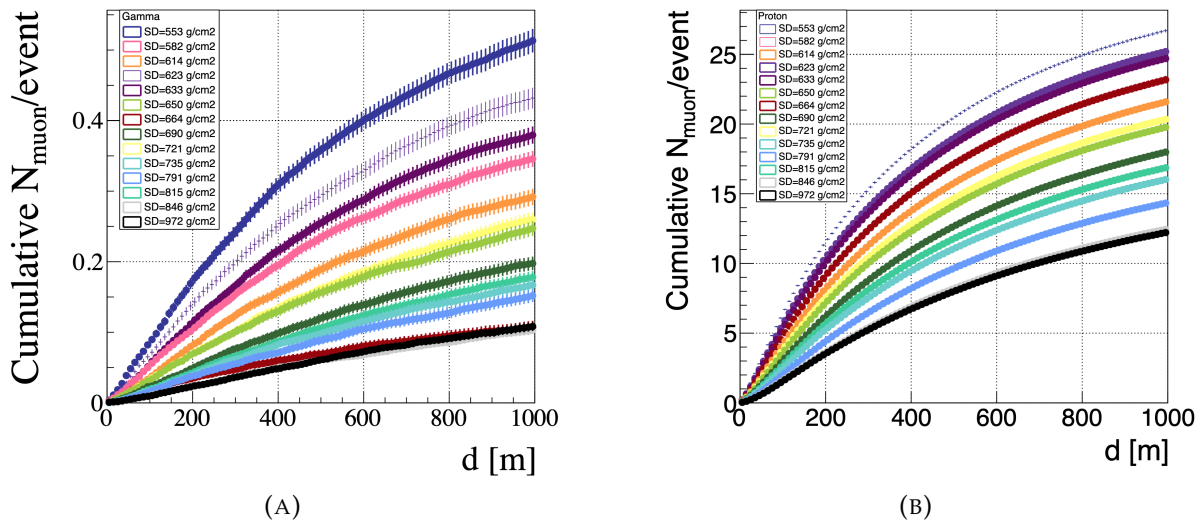
FIGURE B.2: Distribution of the cumulative number of muons per event as a function of lateral distance for a gamma-ray induced shower (*left panel*) and proton-induced shower (*right panel*) for different slant depths. The above showers had an initial energy of 1 TeV.

C

Supplementary to Air Shower Reconstruction & Gamma/Hadron Discrimination in HAWC

As supplementary material, for all shower bins for PMTs A and C, the probability density distribution of fractional charge in main array tanks as a function of the total charge collected for the tank is illustrated in Figures C.1 to C.6 for gamma and proton simulations as well as observed data as discussed in Chapter 4. The probability density distributions for shower bin 5 are shown, for PMTs A and C, in Figure 4.7 in Chapter 4 and for PMTs B and D, here in Figure C.7. The differences in light seen from PMT A compared to PMT C is shown in Figure C.8. Some diagnostic plots regarding the charge recorded in a specific tank and participation fraction of tanks in an event are displayed in Figures C.9 and C.10. We show the likelihood ratio distribution for gamma simulation, Crab sample events, a set of observed data and proton simulations for different PE cuts implemented in Figures C.11 to C.17. Lastly, optimal TankLHR, PINC and LiComp cuts and combined TS plots are illustrated in Figures C.18 to C.23 and in Table C.1.

$$\mathcal{COMPACT} - \text{\&\&} \ \mathcal{PINC} - cuts$$

```
0 "(rec.nHitSP20/rec.CxPE40>= 21.00) && (rec.PINC<1.50)"
1 "(rec.nHitSP20/rec.CxPE40>= 7.00) && (rec.PINC<2.20)"
2 "(rec.nHitSP20/rec.CxPE40>= 9.00) && (rec.PINC<3.00)"
3 "(rec.nHitSP20/rec.CxPE40>=11.00) && (rec.PINC<2.30)"
4 "(rec.nHitSP20/rec.CxPE40>=15.00) && (rec.PINC<1.90)"
```

```
5 "(rec.nHitSP20/rec.CxPE40>=18.00) && (rec.PINC<1.90)"

6 "(rec.nHitSP20/rec.CxPE40>=17.00) && (rec.PINC<1.70)"

7 "(rec.nHitSP20/rec.CxPE40>=15.00) && (rec.PINC<1.80)"

8 "(rec.nHitSP20/rec.CxPE40>=15.00) && (rec.PINC<1.80)"

9 "(rec.nHitSP20/rec.CxPE40>= 3.00) && (rec.PINC<1.60)"
```
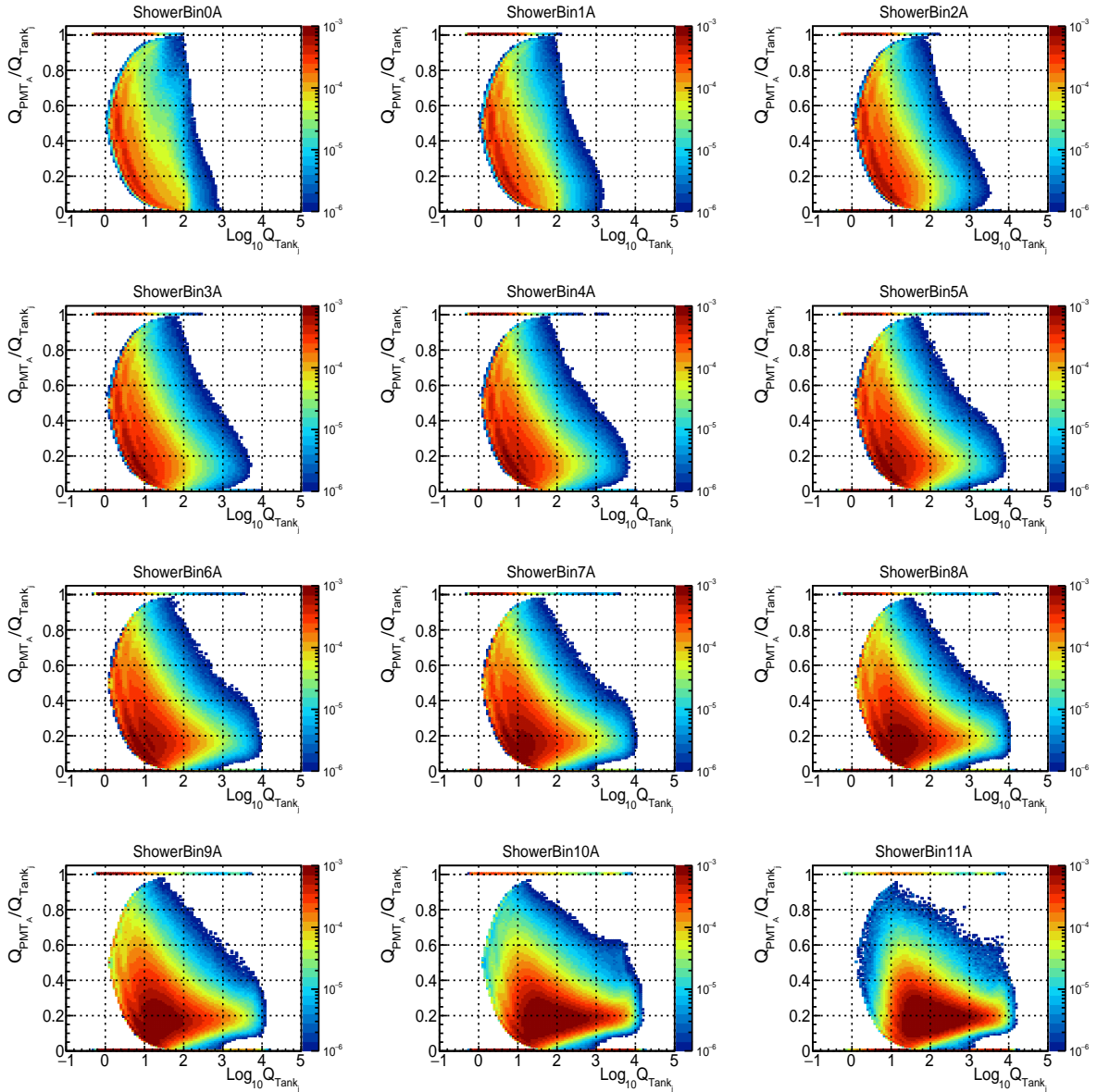

FIGURE C.1: Fractional charge of PMT A as a function of total charge in a tank for a simulated gamma particle.
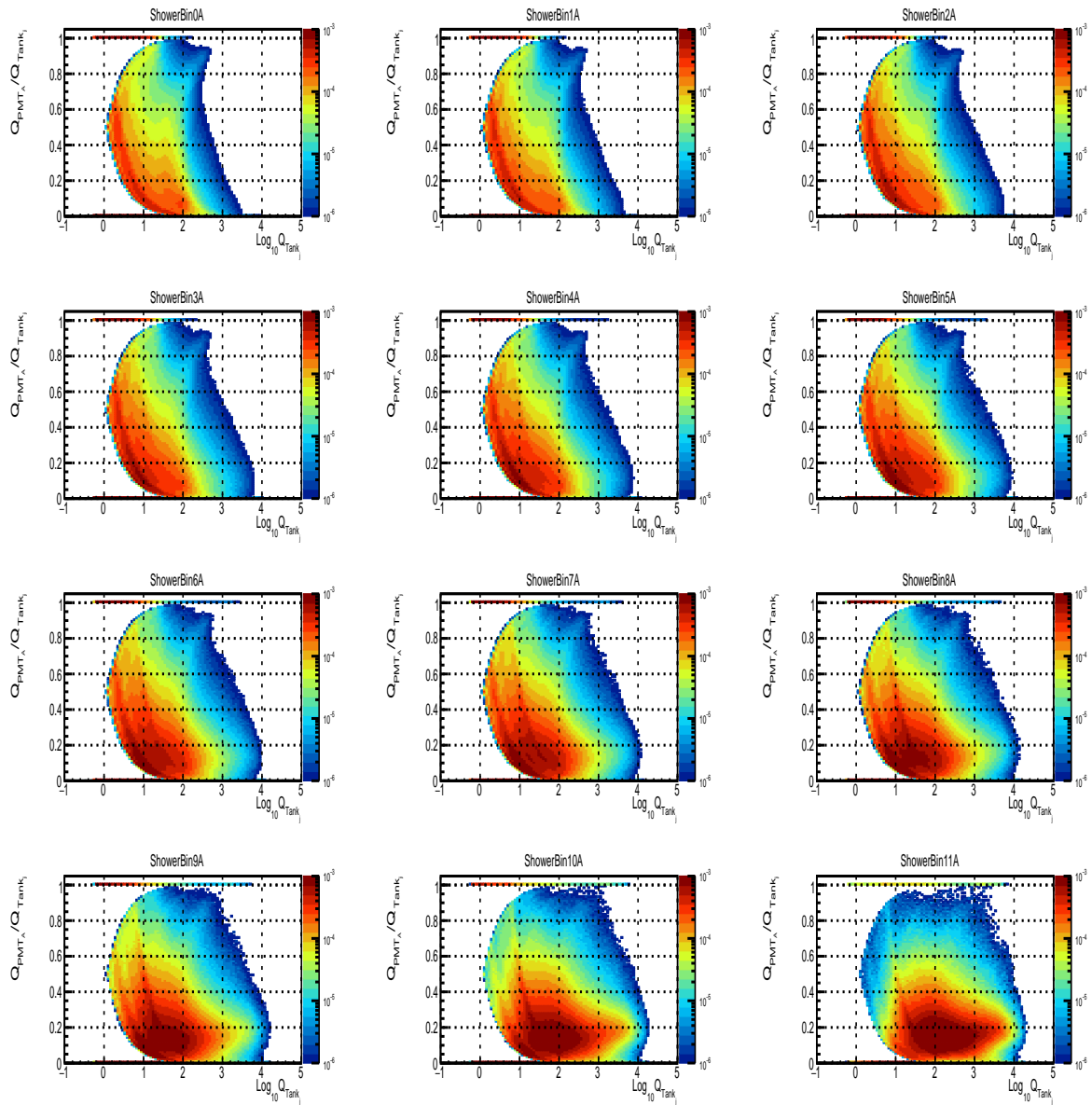
FIGURE C.2: Fractional charge of PMT A as a function of total charge in a tank for observed events at HAWC.
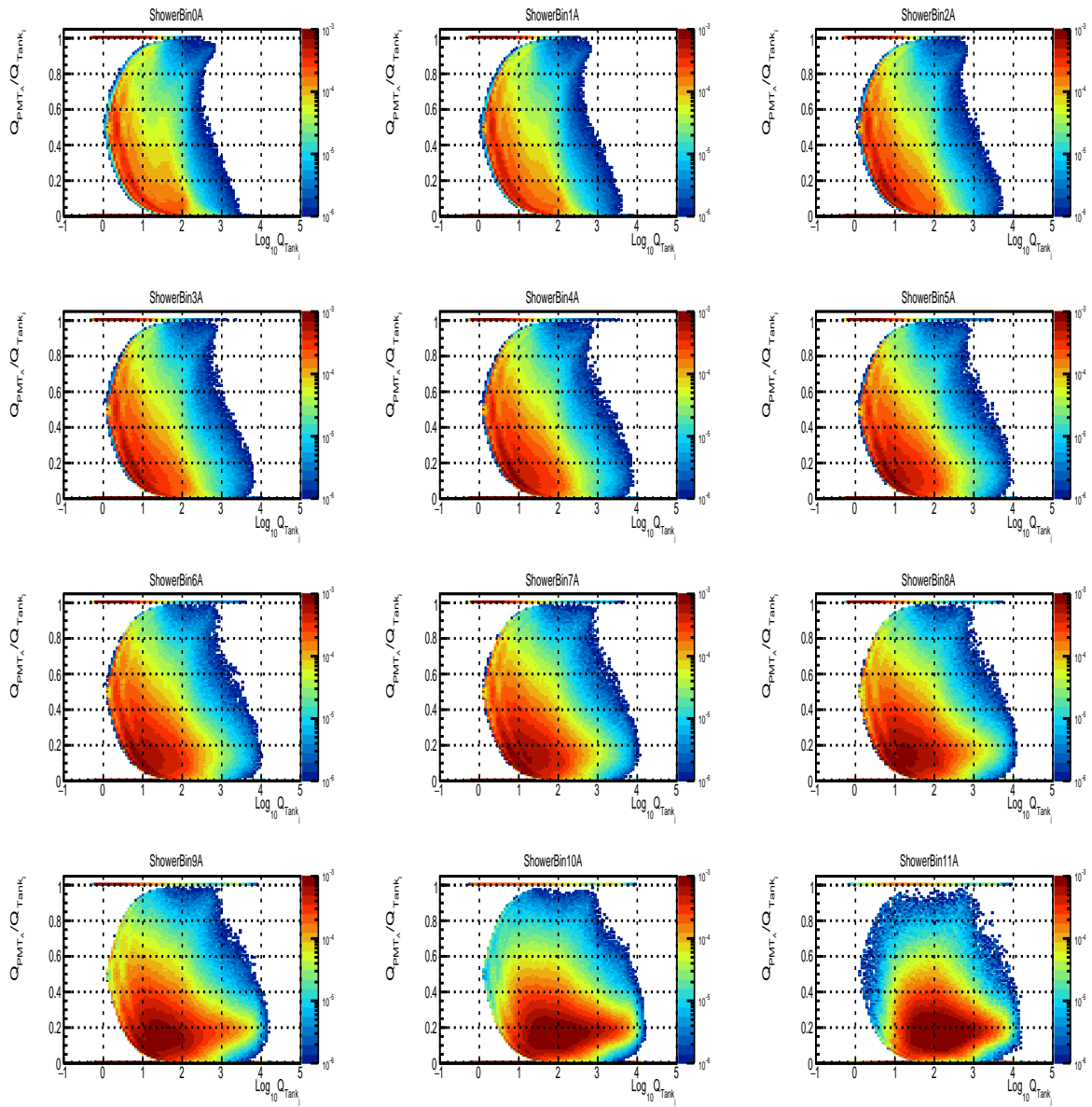
FIGURE C.3: Fractional charge of PMT A as a function of total charge in a tank for a simulated proton.
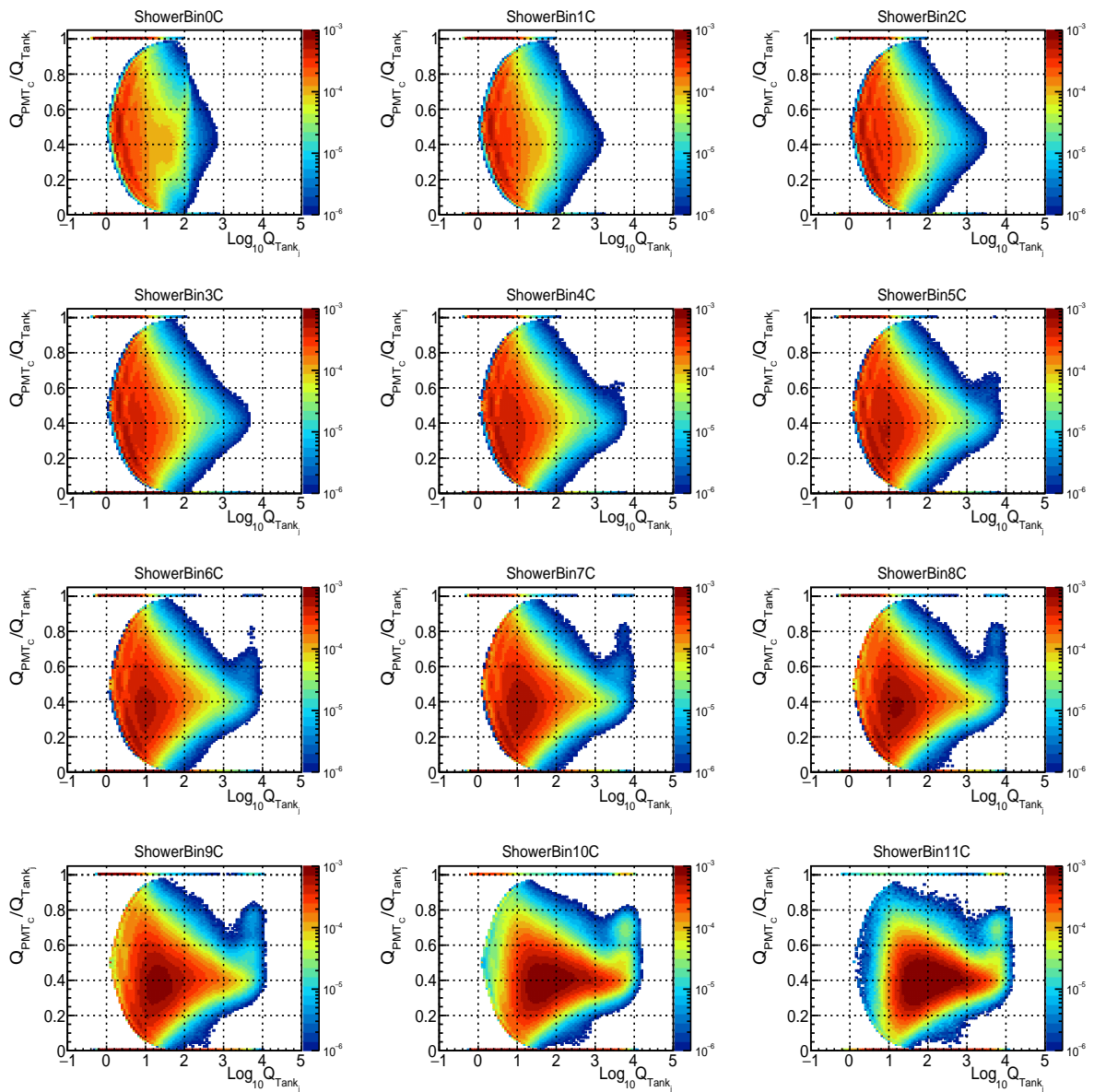
FIGURE C.4: Fractional charge of PMT C as a function of total charge in a tank for a simulated gamma particle.
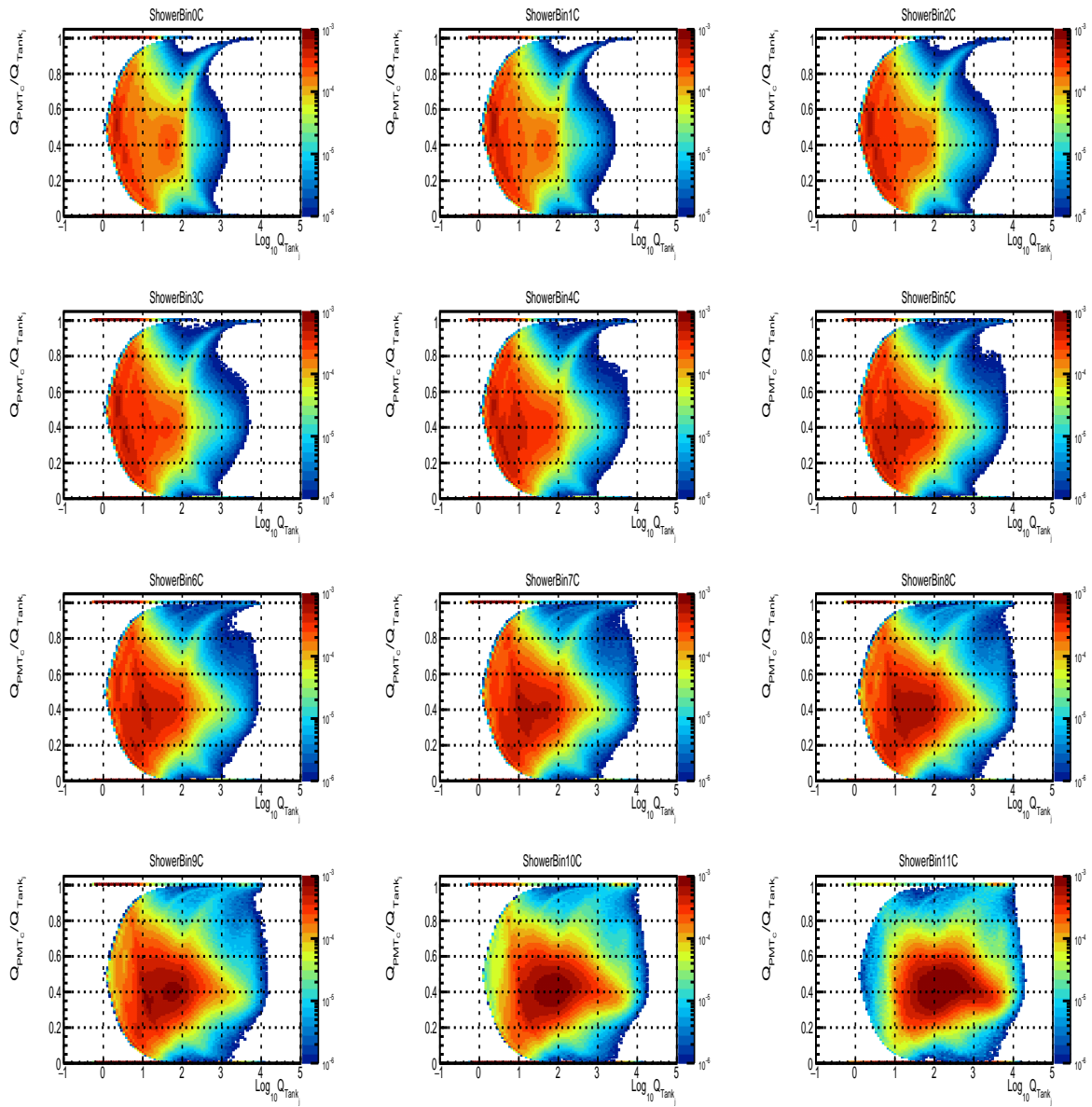
FIGURE C.5: Fractional charge of PMT C as a function of total charge in a tank for observed events at HAWC.
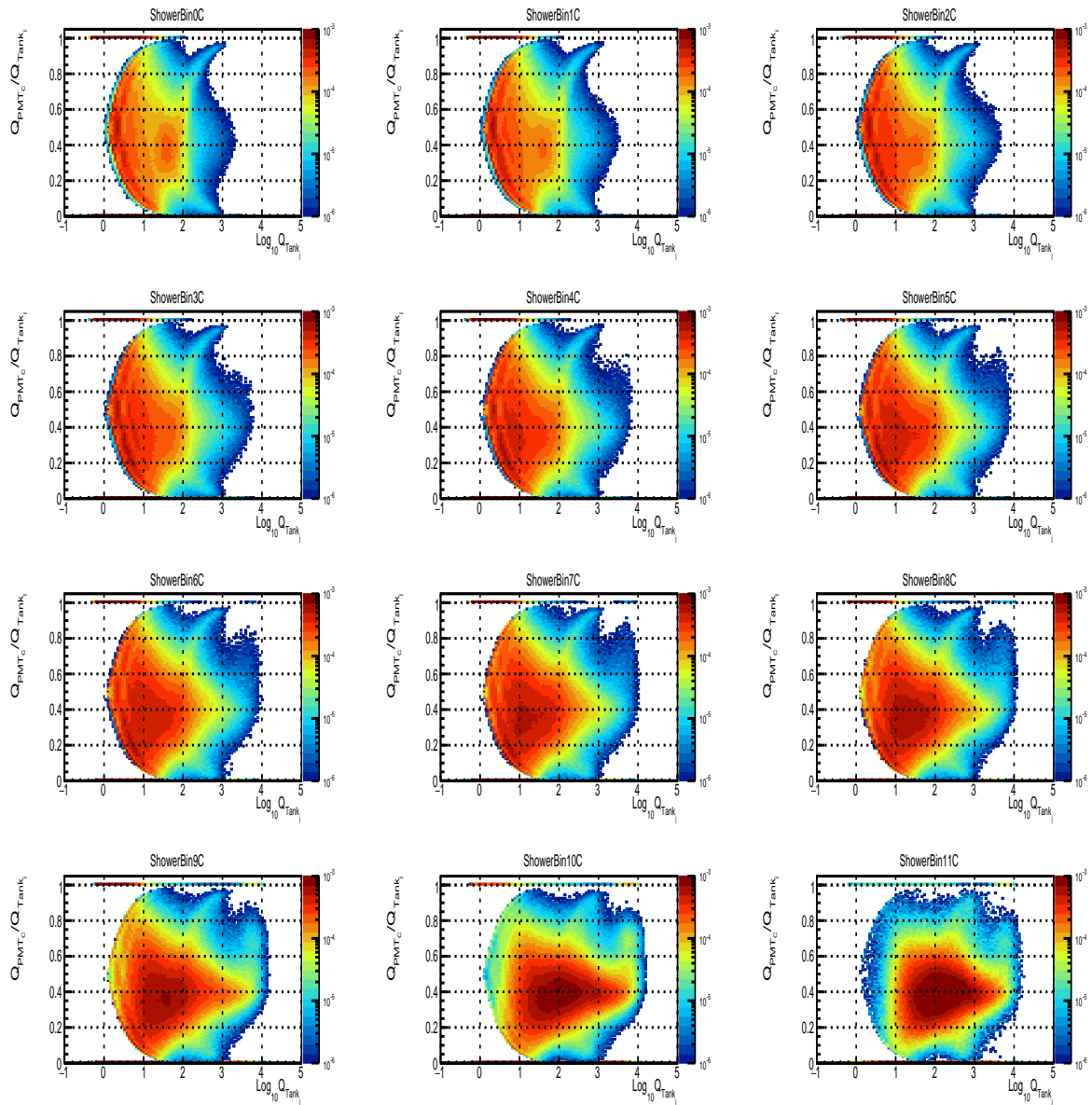
FIGURE C.6: Fractional charge of PMT C as a function of total charge in a tank for a simulated proton.

(A)

(B)

(C)

(D)

(E)

(F)
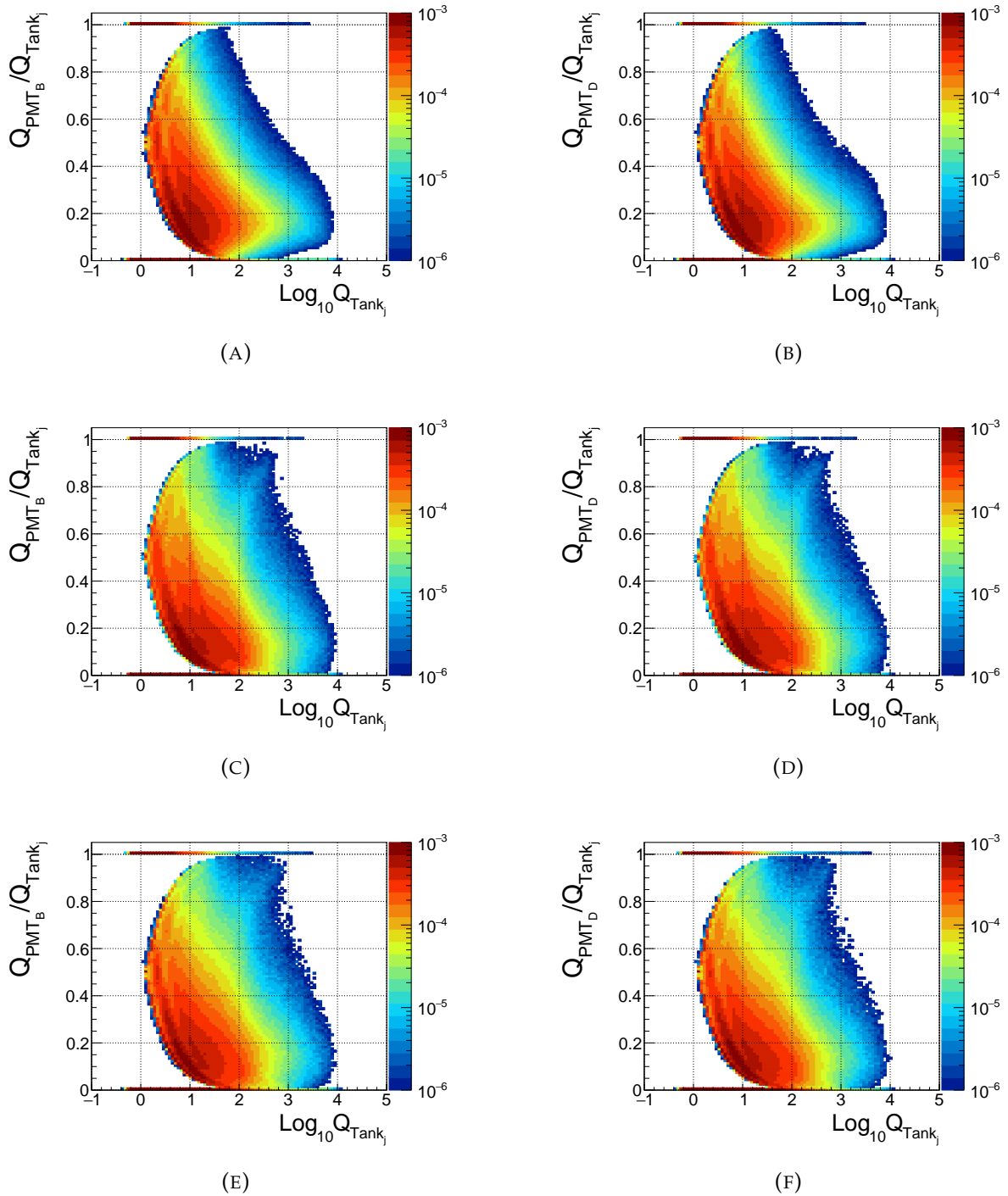
FIGURE C.7: Probability density distribution of showers from simulated gammas (*top*), data (*middle*), and simulated protons (*bottom*) as seen by PMT B (*left*) and PMT D (*right*) for shower bin 5.
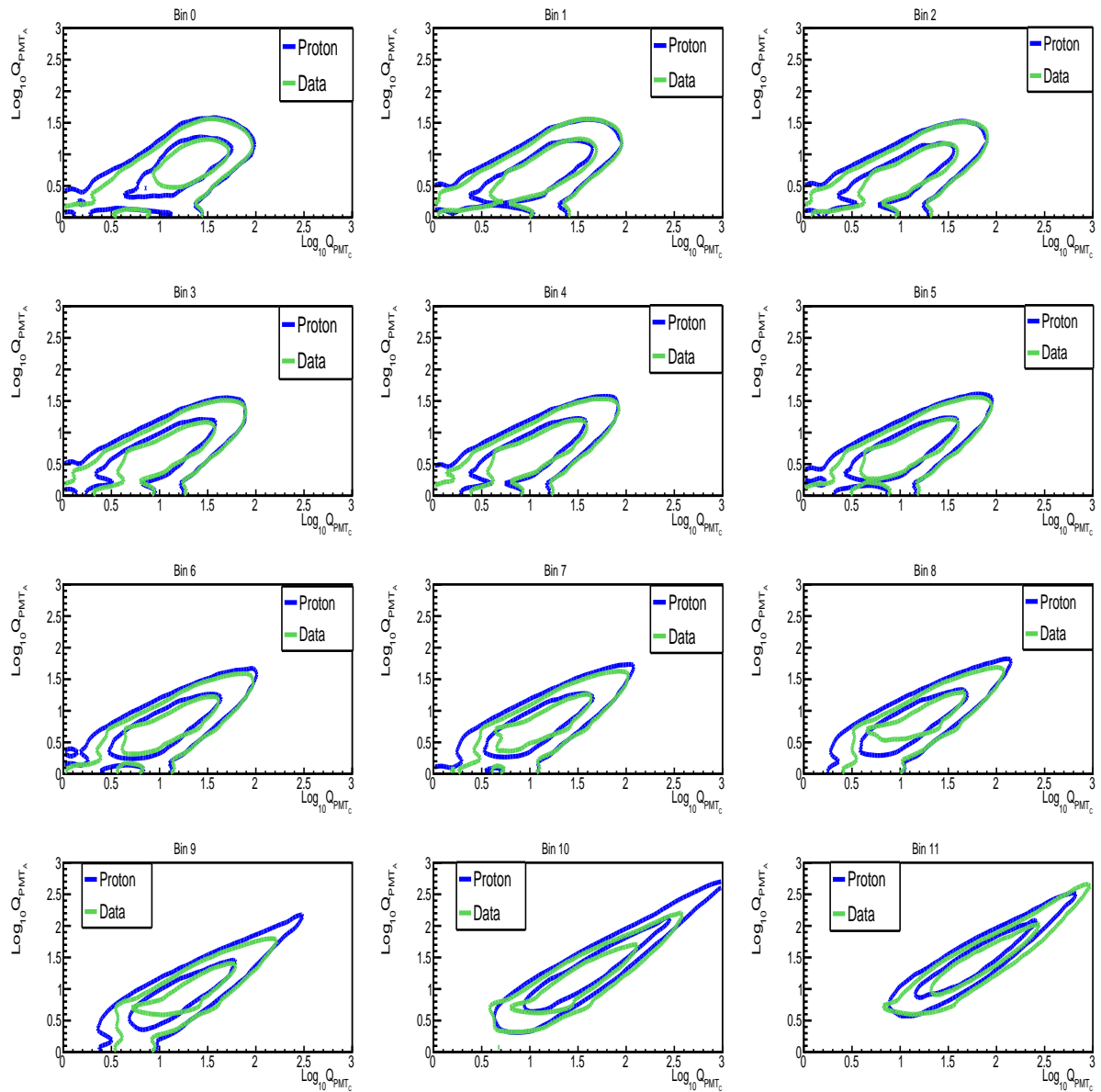
FIGURE C.8: Gross differences between PMT A and PMT C for proton simulations (blue) and measured events (green).

(A)

(B)

(C)
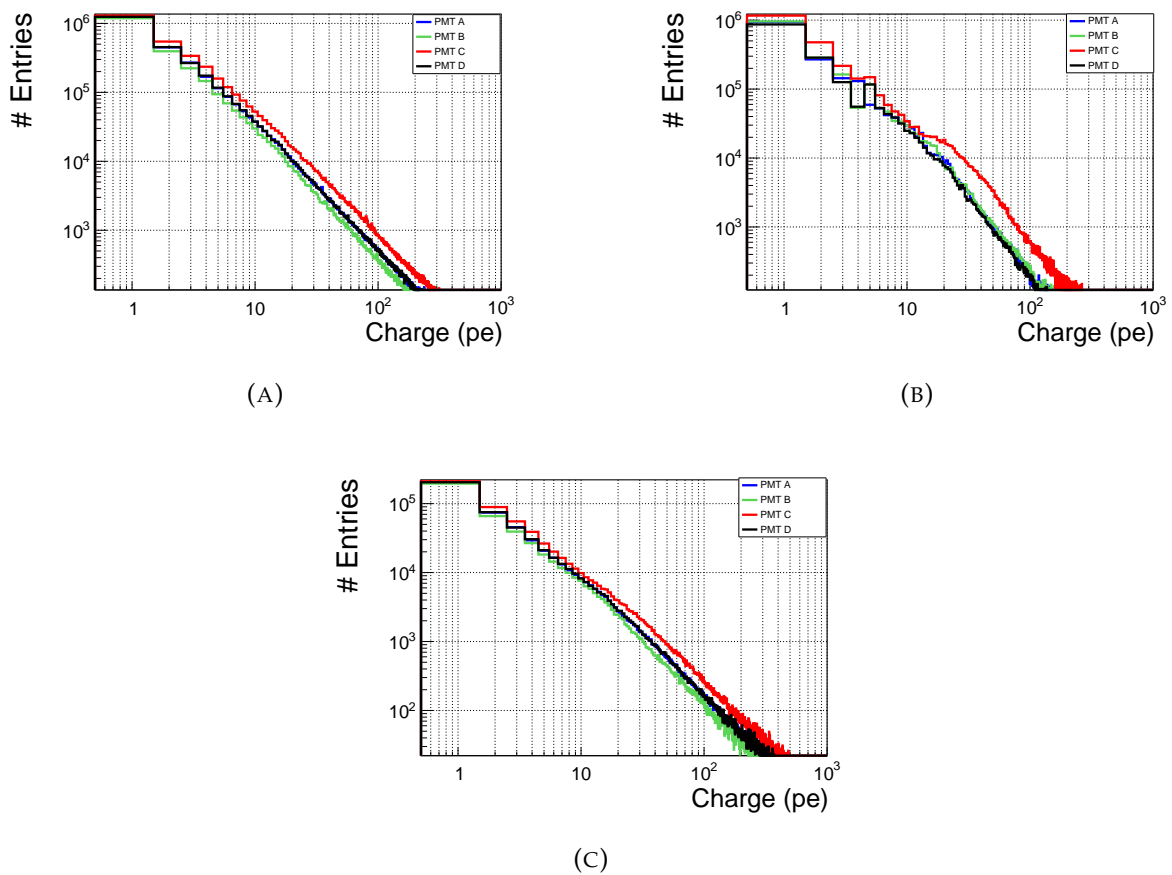
FIGURE C.9: Charges registered in a specific tank for all PMTs for gamma simulations (*top left*), observed data (*top right*), and proton simulations (*bottom*).

(A)

(B)

(C)
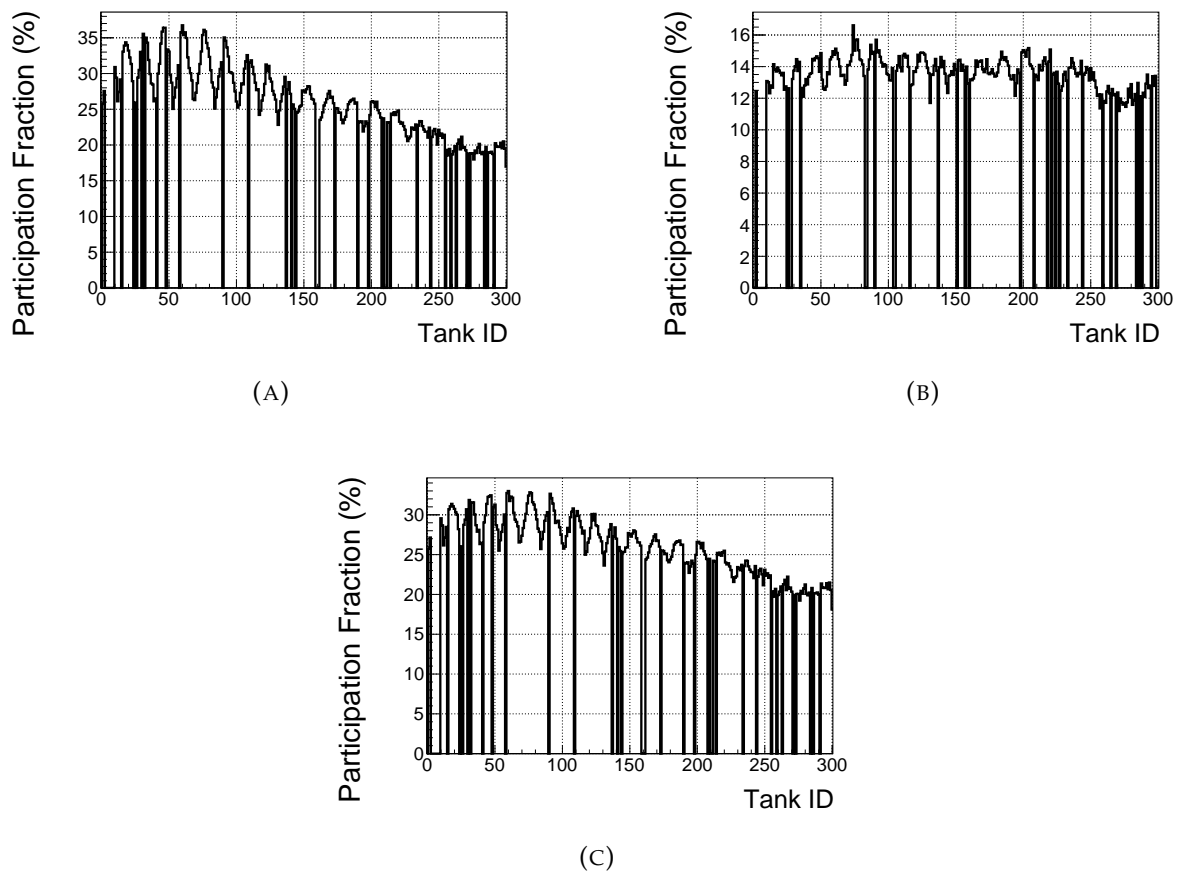
FIGURE C.10: Percentage of main array tanks that participate in an event for gamma simulations (*top left*), observed data (*top right*), and proton simulations (*bottom*).
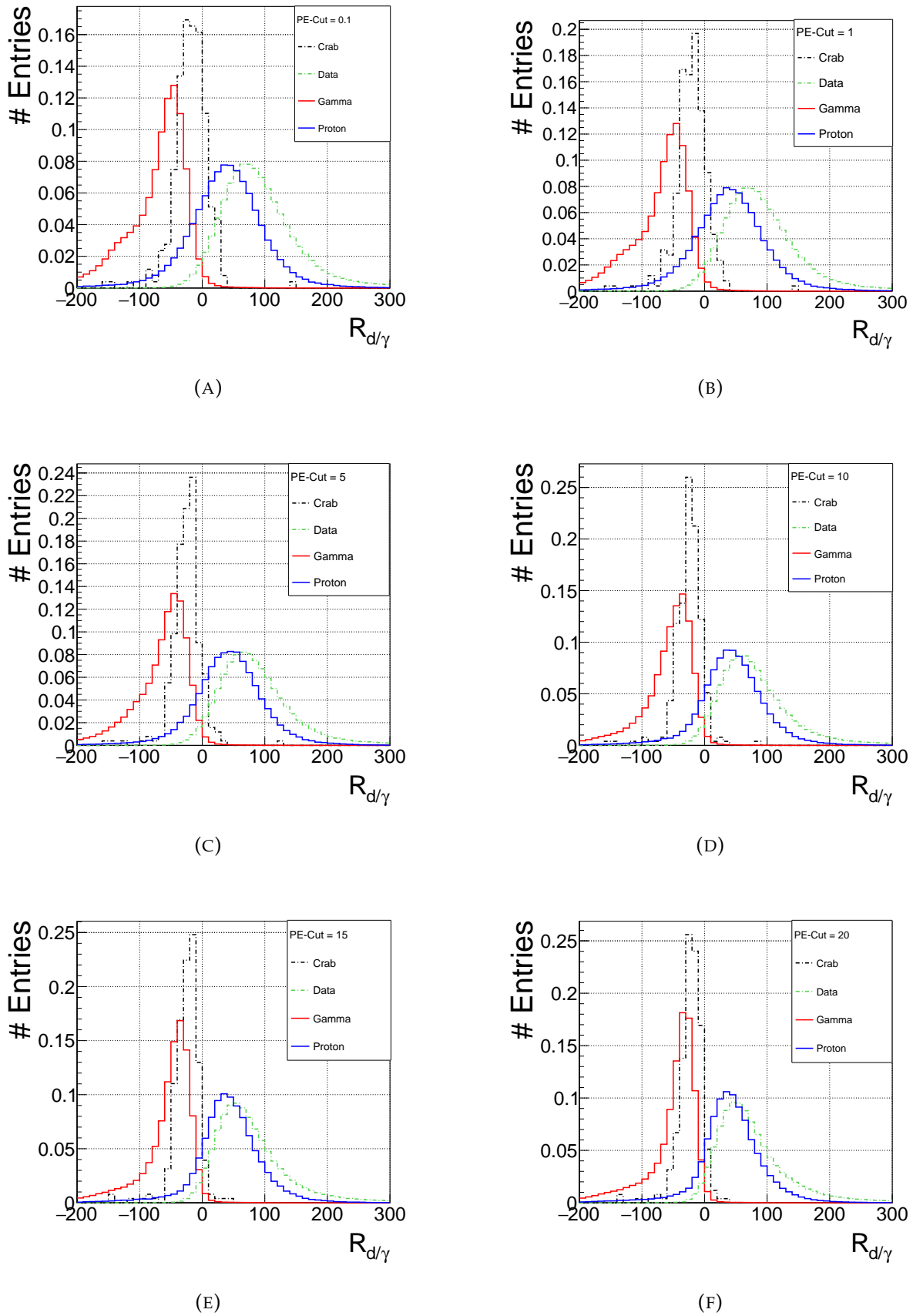
FIGURE C.11: $R_{d/\gamma}$ distribution for simulated gammas in red, simulated protons in blue, data in green, and data specifically from the Crab nebula region in black, dot-dashed lines. The different panels are for the different PE cuts applied, (A) is 0.1, (B) is 1, (C) is 5, (D) is 10, (E) is 15, and (F) is 20.
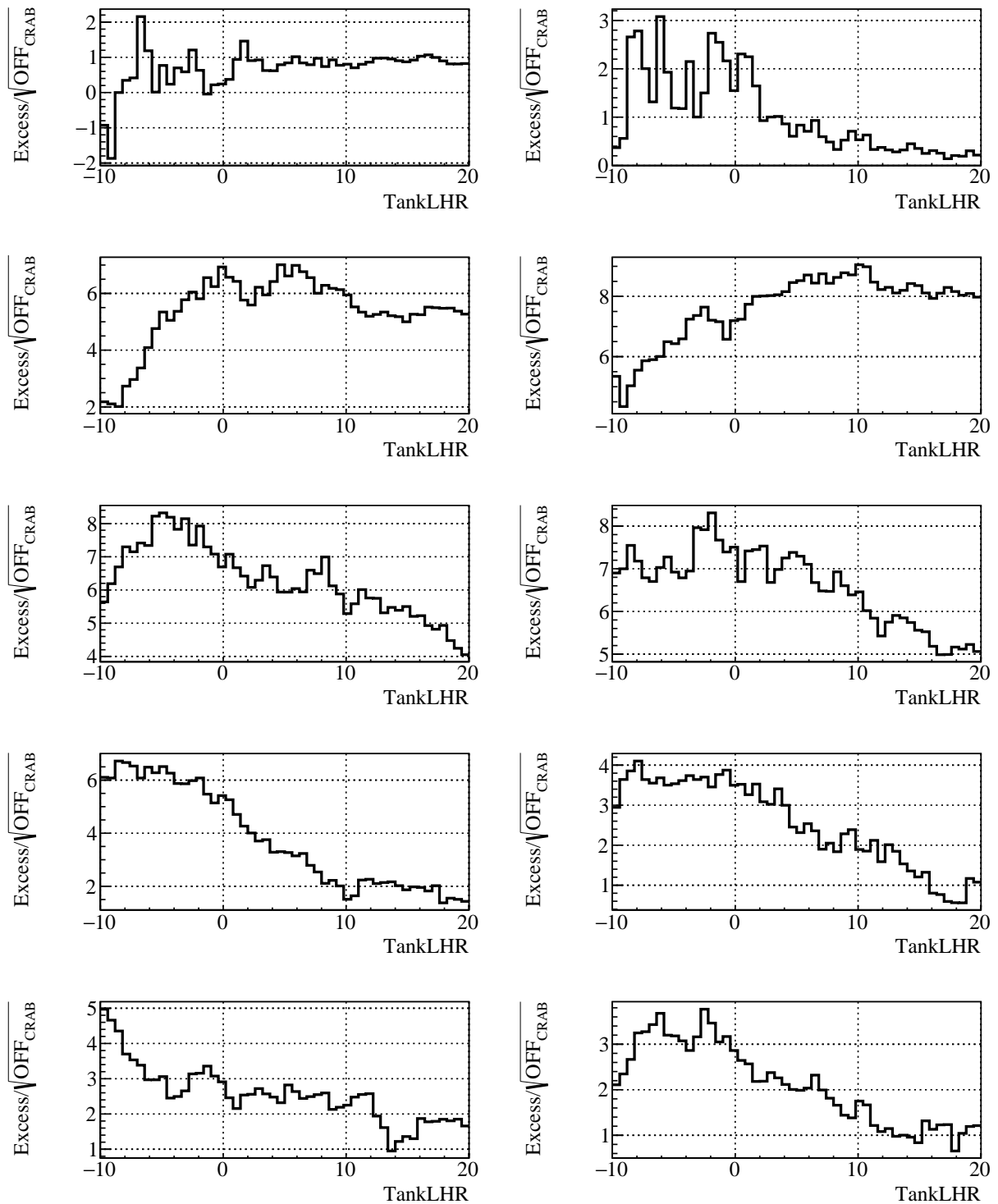
FIGURE C.12: Probable excess signal from the Crab nebula region using TankLHR.
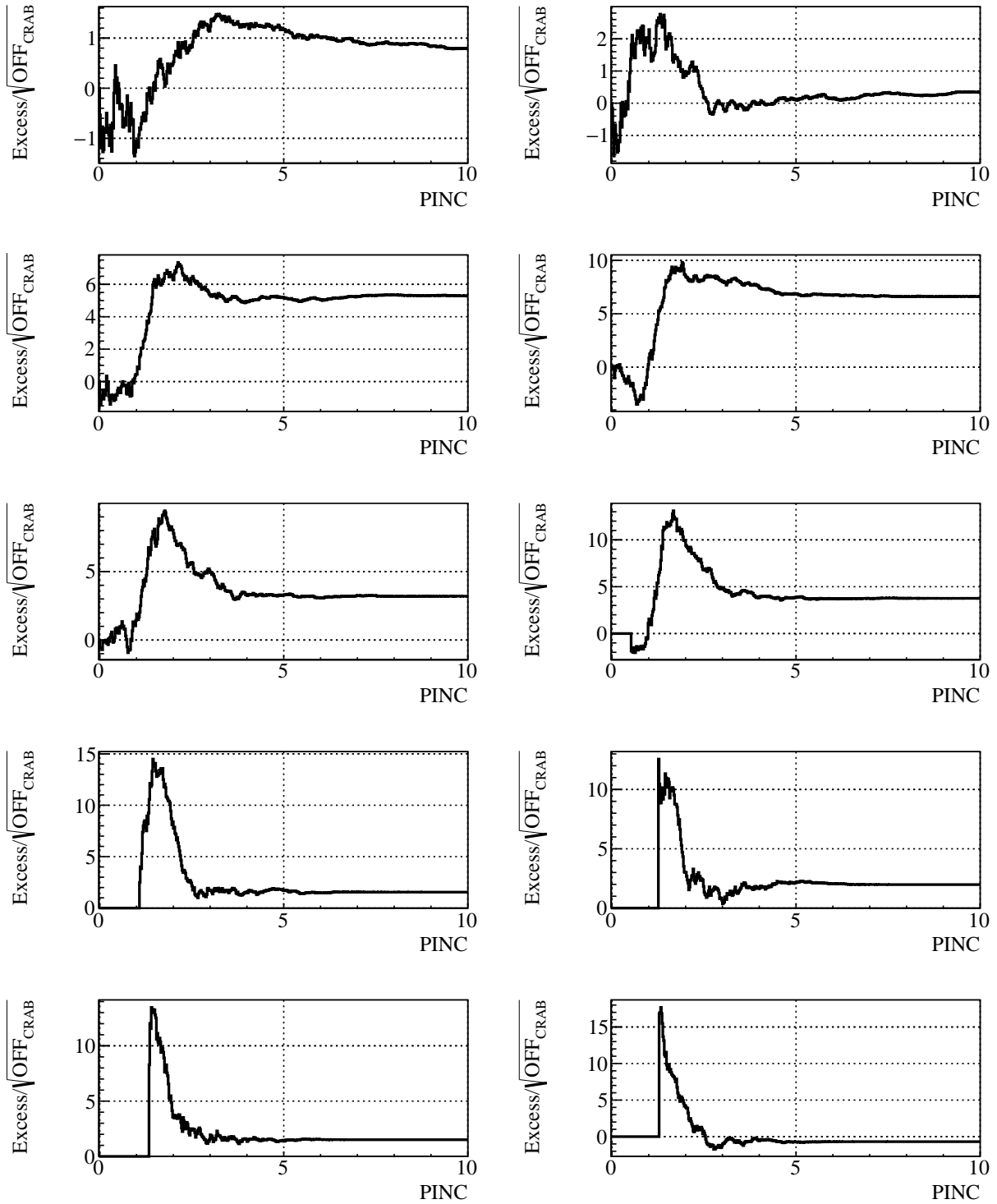
FIGURE C.13: Probable excess signal from the Crab nebula region using PINC.
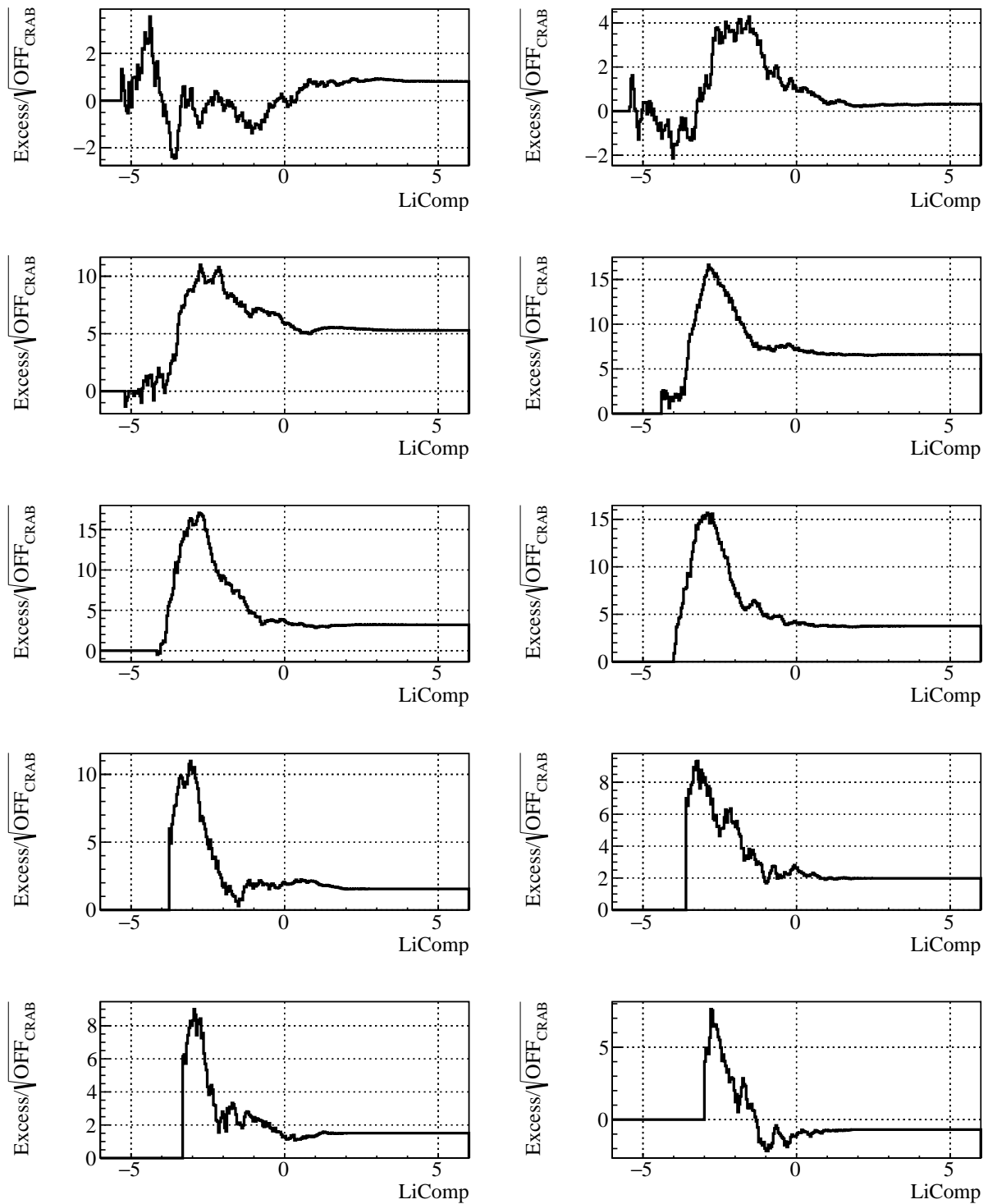
FIGURE C.14: Probable excess signal from the Crab nebula region using LiComp.
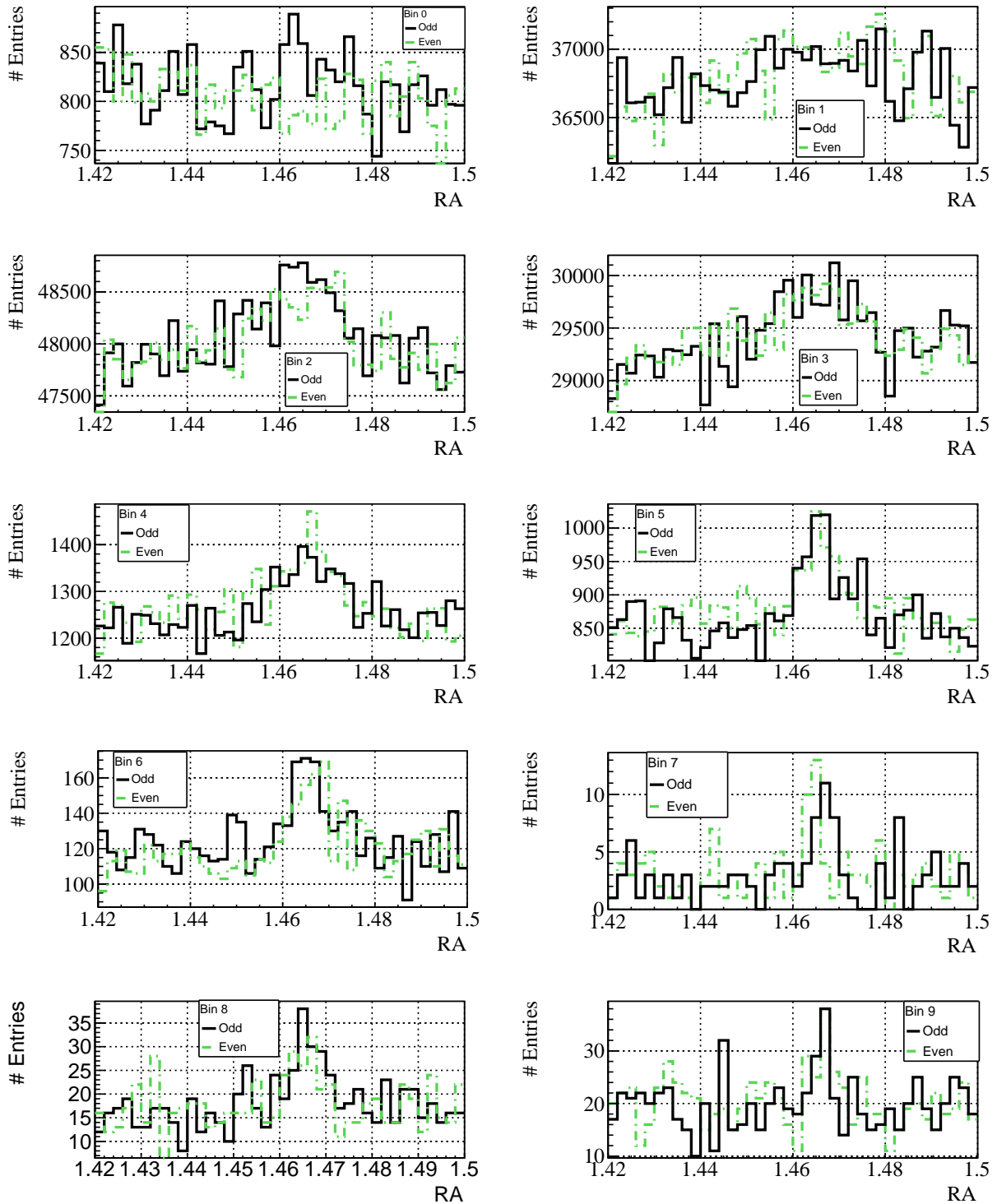
FIGURE C.15: Events passing the TankLHR selection cut in the Crab nebula region.
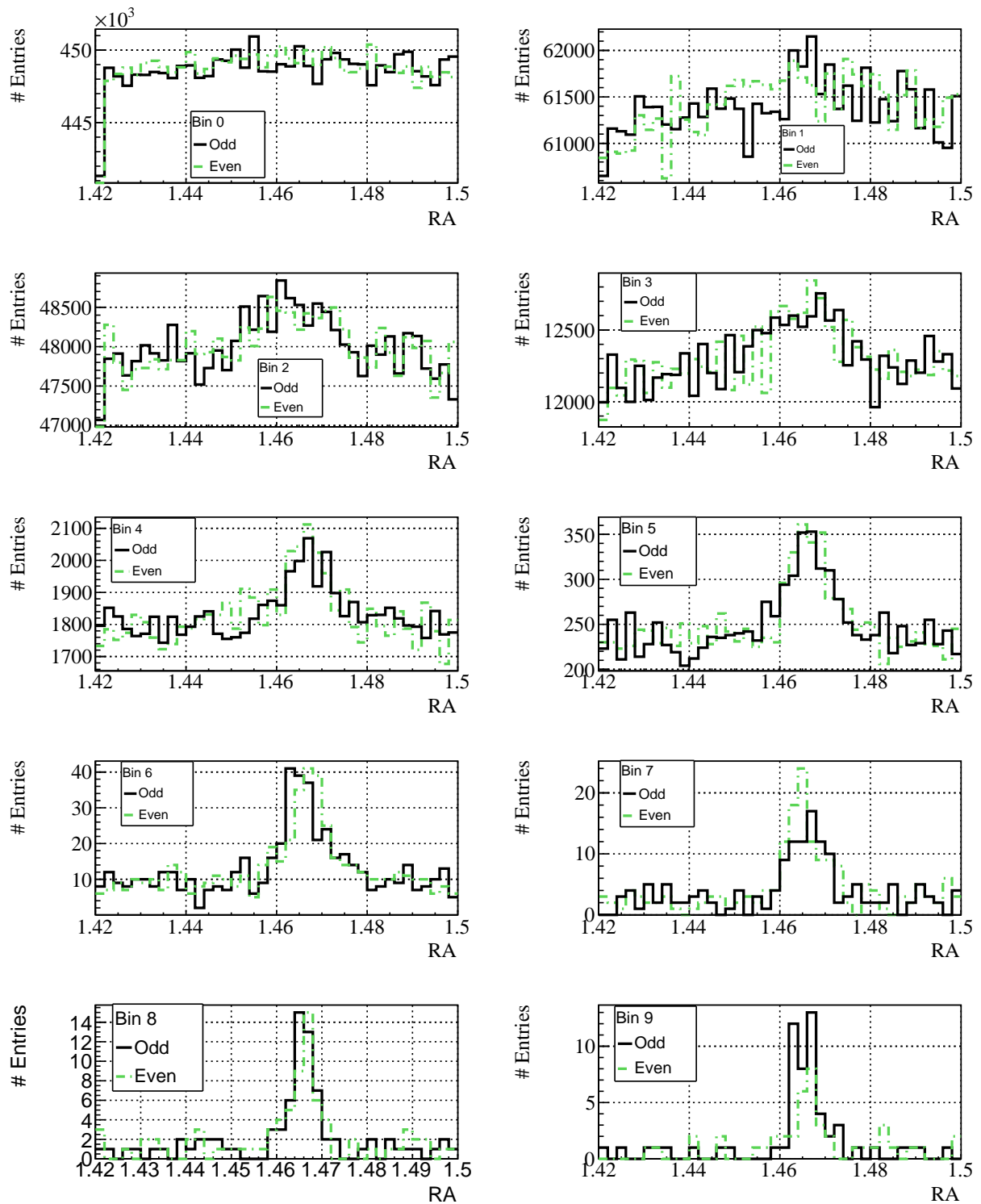
FIGURE C.16: Events passing the PINC selection cut in the Crab nebula region.
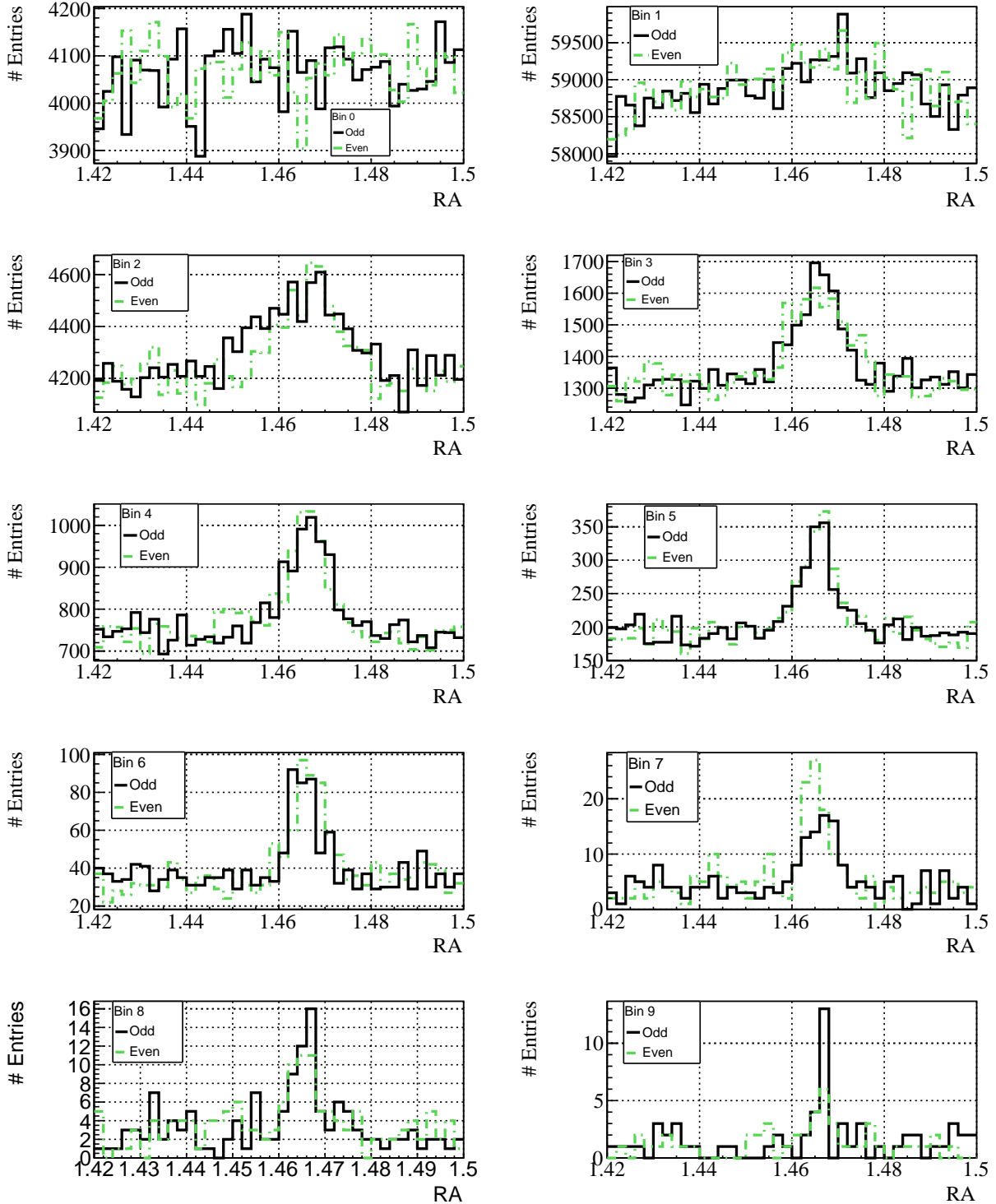
FIGURE C.17: Events passing the LiComp selection cut in the Crab nebula region.
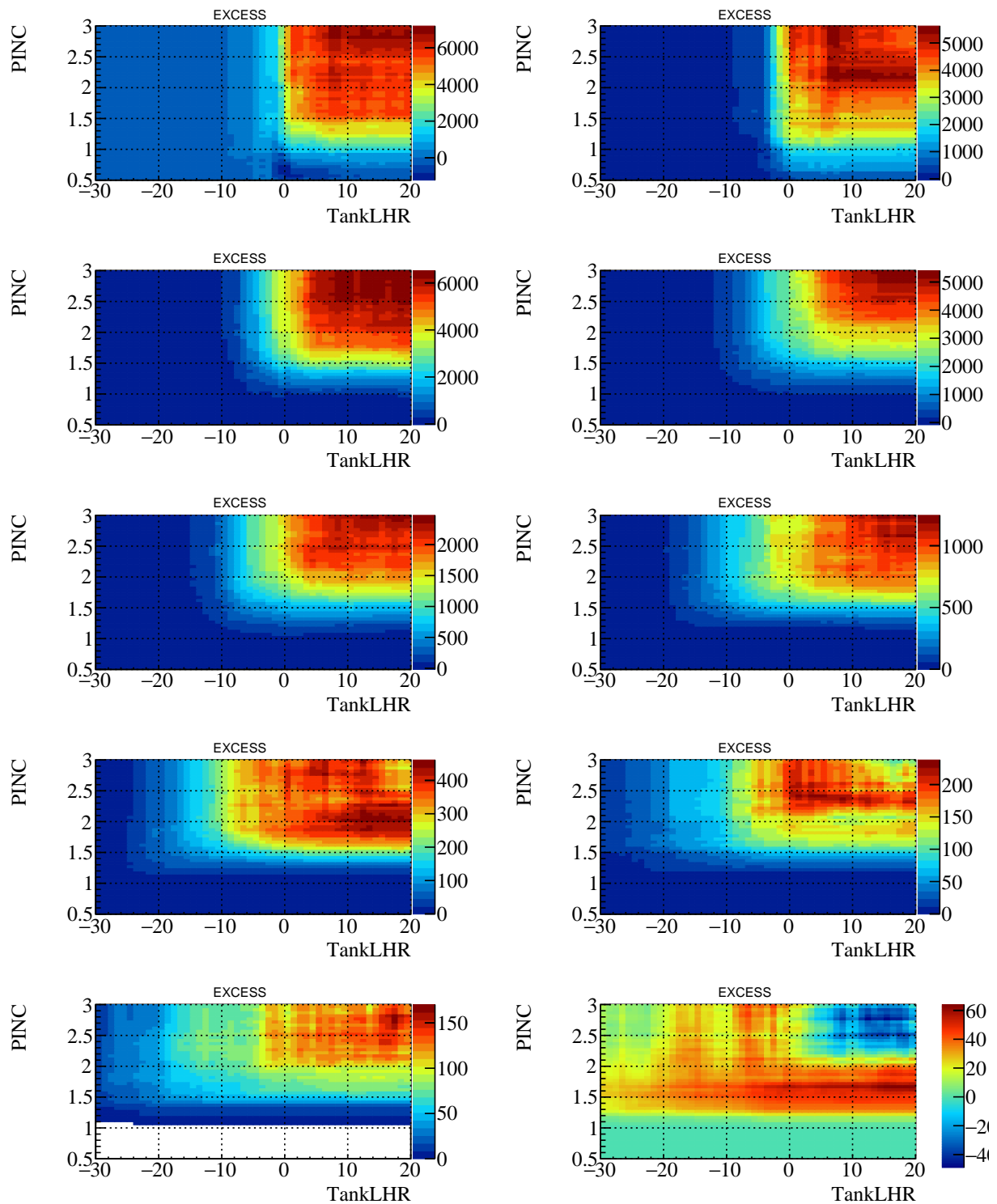
FIGURE C.18: Excess signal as a function of TankLHR and PINC
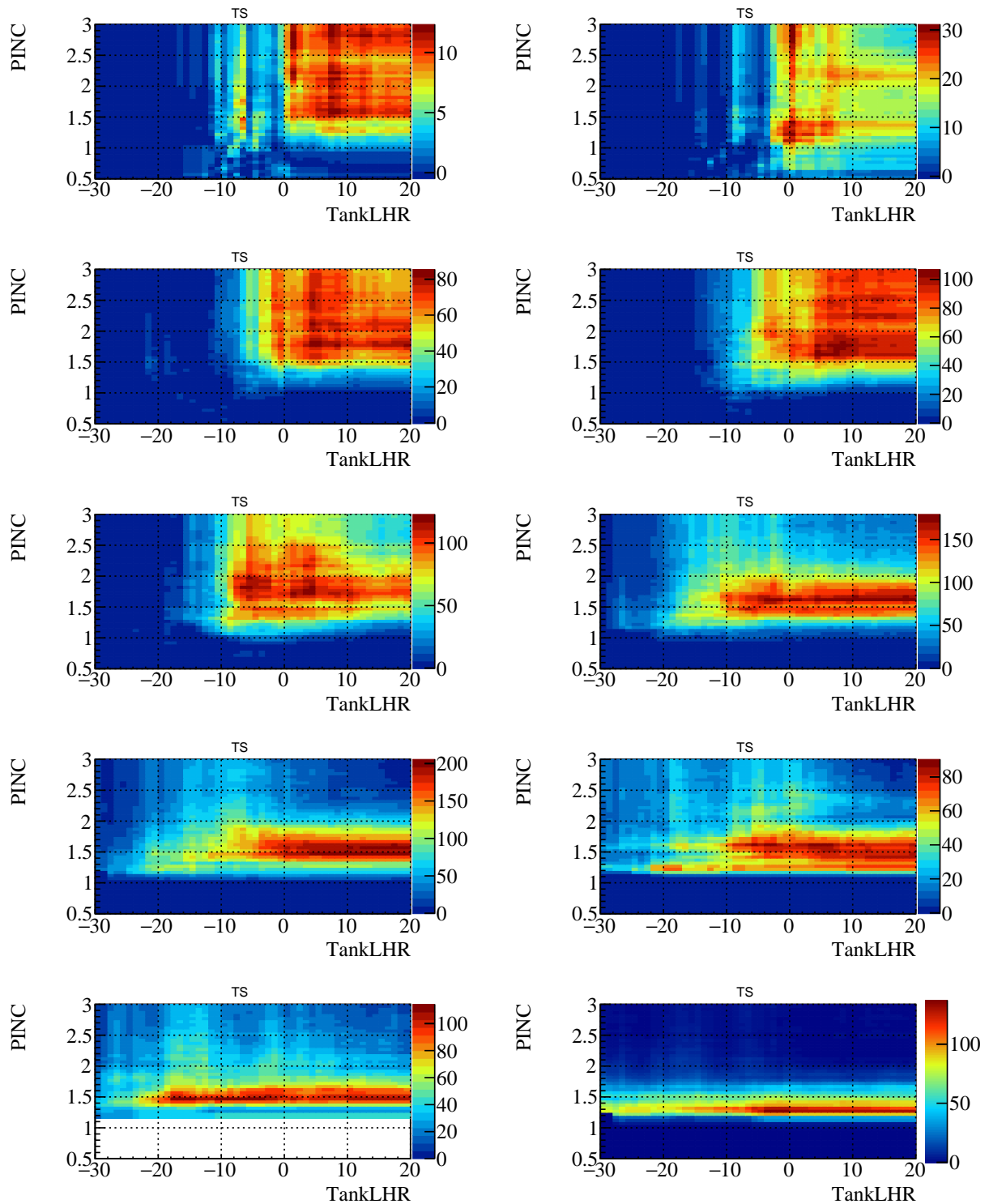
FIGURE C.19: TS of signal as a function of TankLHR and PINC
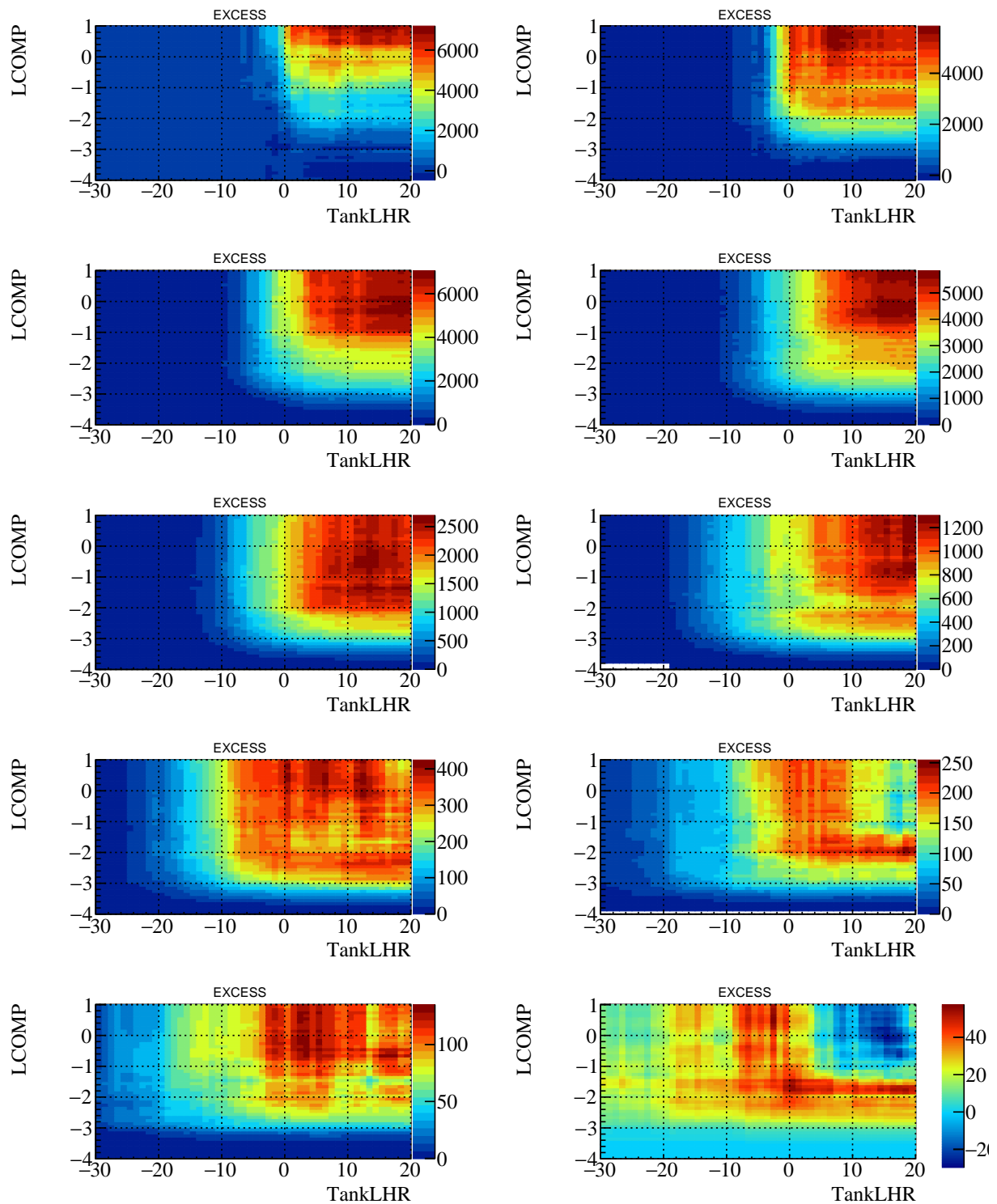
FIGURE C.20: Excess signal as a function of TankLHR and LiComp
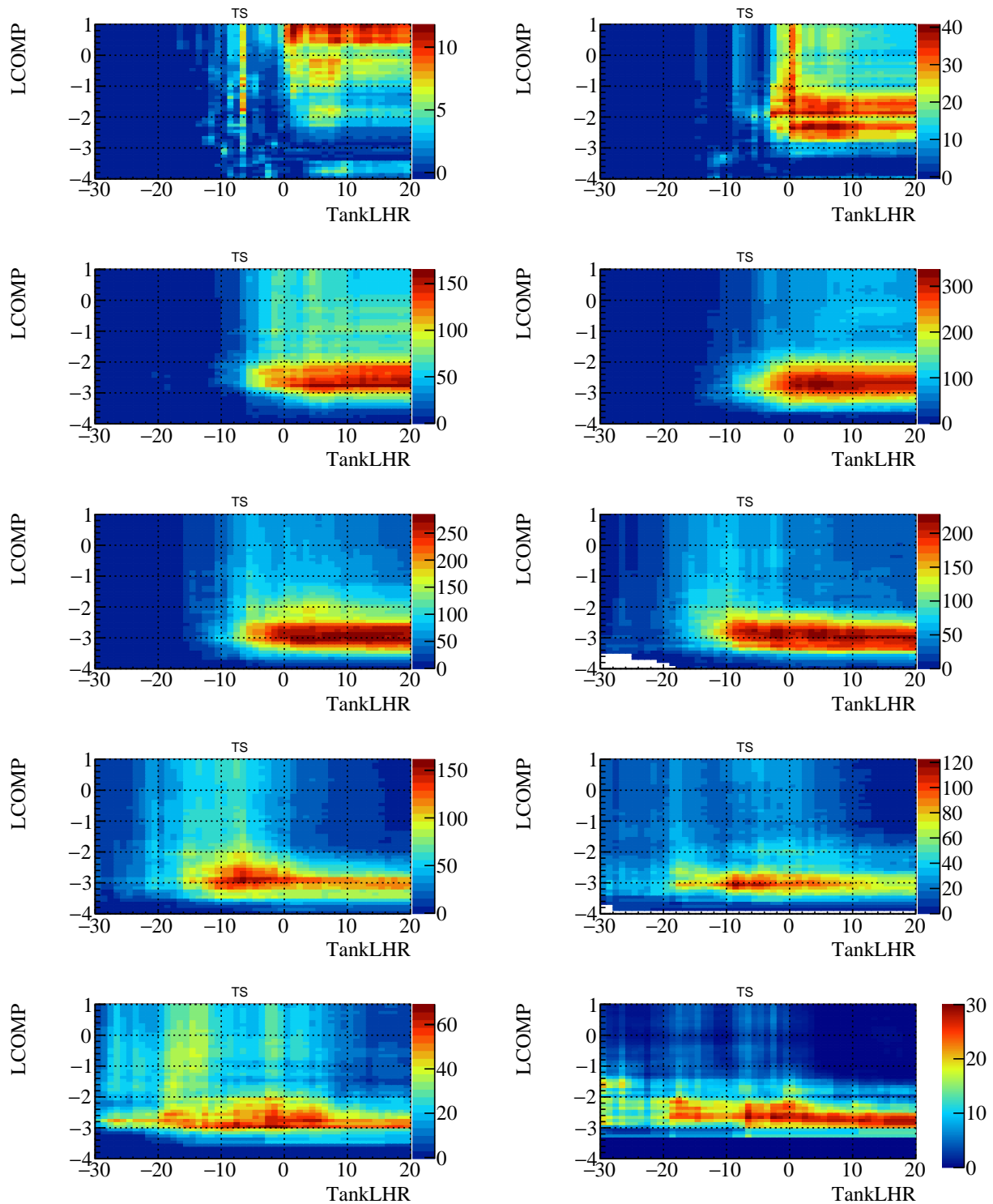
FIGURE C.21: TS of signal as a function of TankLHR and LiComp
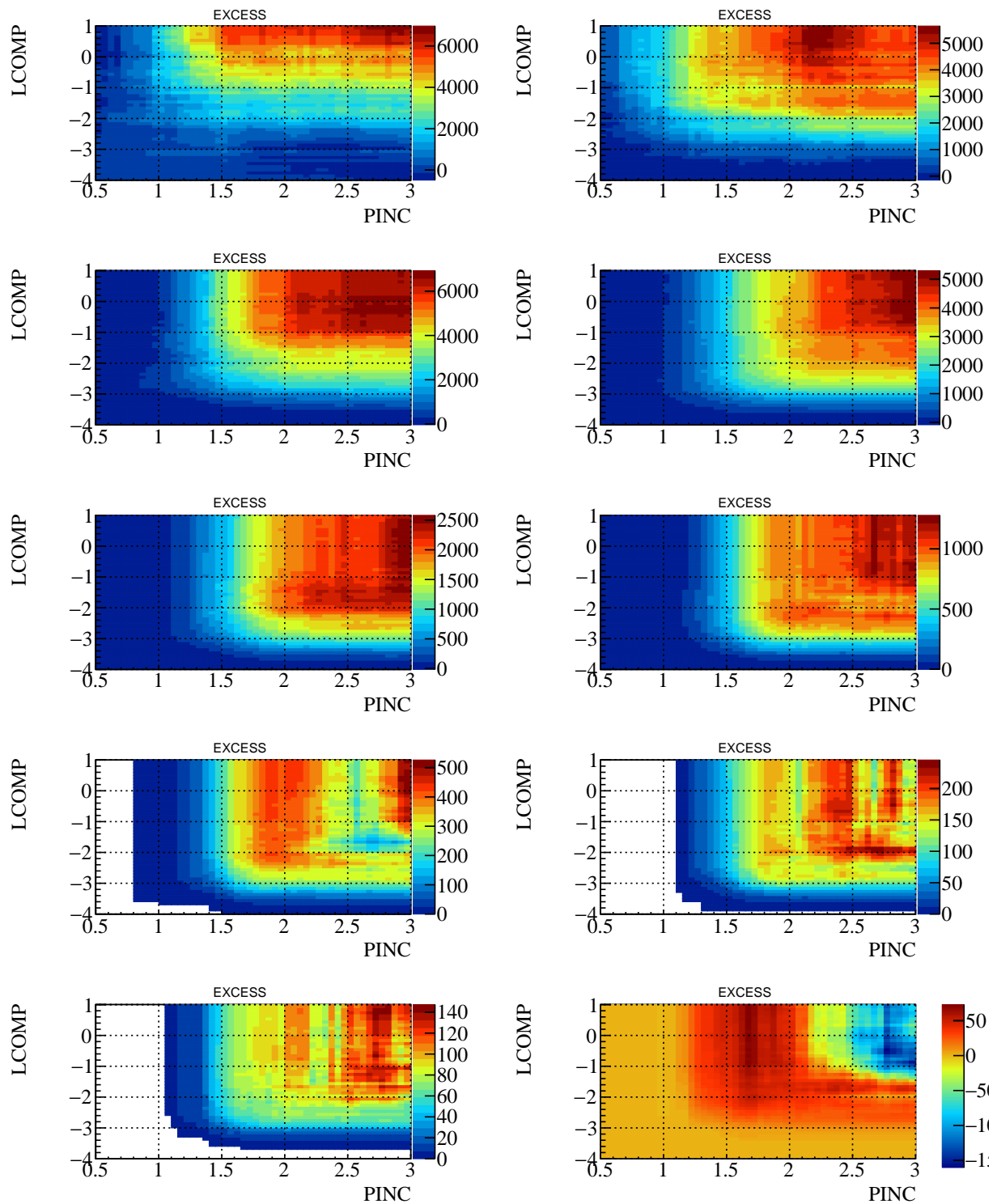
FIGURE C.22: Excess signal as a function of PINC and LiComp
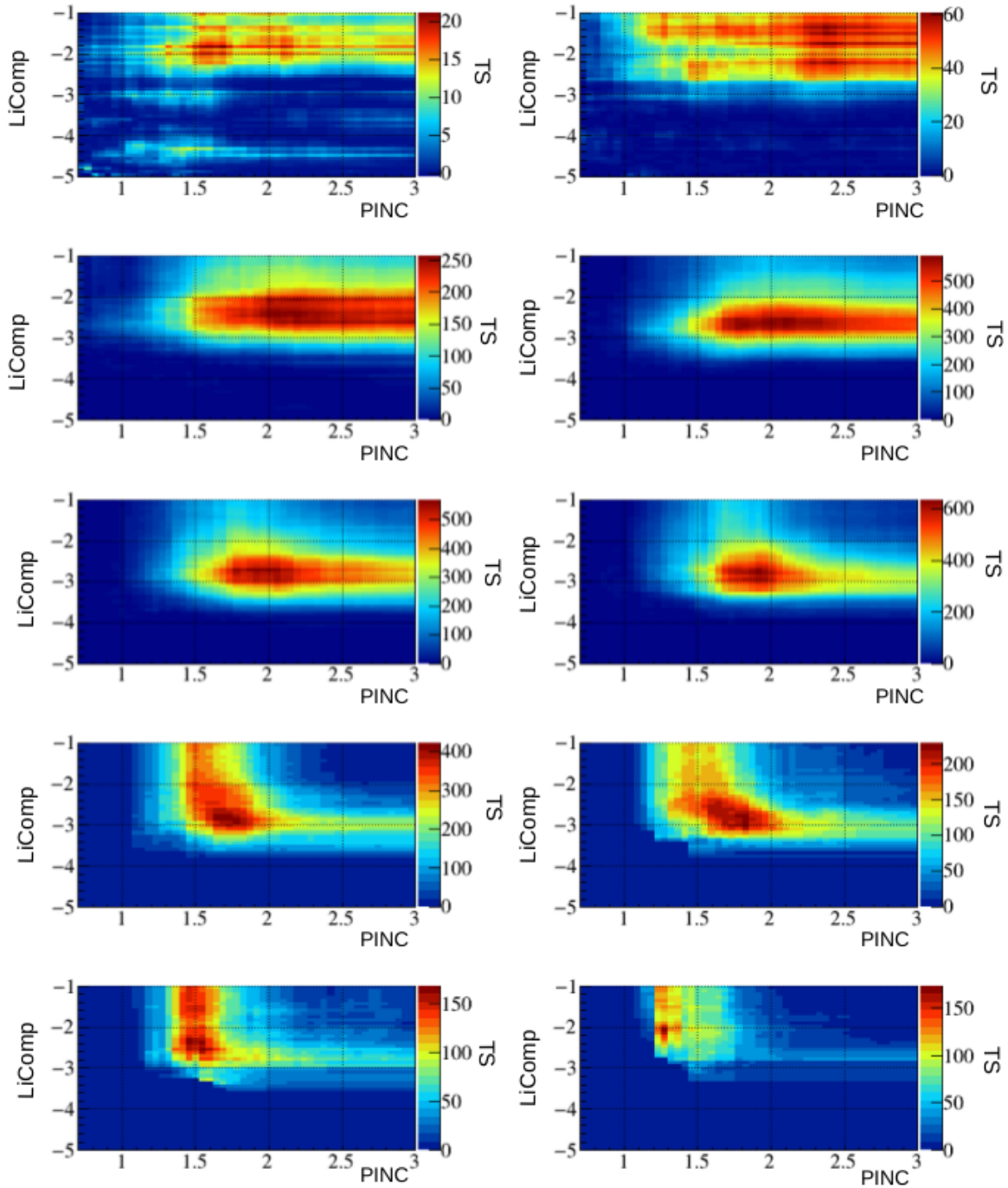
FIGURE C.23: TS of signal as a function of PINC and LiComp

TABLE C.1: Table detailing the optimal combined cuts on LiComp and PINC for the highest TS of the Crab nebula.

$\mathcal{B}$	Highest TS	Discriminator	
		LiComp	PINC
0	21.2	-1.84	1.69
1	60.7	-1.76	2.38
2	257.3	-2.40	2.19
3	592.5	-2.64	2.10
4	569.7	-2.72	2.06
5	636.5	-2.80	1.92
6	423.2	-2.88	1.69
7	229.7	-2.88	1.83
8	168.0	-2.56	1.55
9	173.8	-2.08	1.27

Other Gamma/Hadron Separators

A method based on neural network is being developed for gamma/hadron separation. It is the predictive modelling of few parameters that distinguish between gammas and protons via training of a dataset. Yet another method of discriminating gamma-ray induced showers from cosmic-ray induced showers is through the implementation of convolutional neural network (CNN). An image of the shower which contains information of the detected charge in each PMT is mapped onto a square array and the CNN is trained using MC simulations. This trained model then takes as input a given data set and outputs the probability of a given shower to be gamma-like or hadron-like.

D

Supplementary to A New Approach to Background Modelling for HAWC

As supplementary material, we first provide the gamma/hadrons cuts used to make the $\mathcal{H}$cut maps. Then, we illustrate, for all nHit bins, the gamma-like event maps, the DI maps, the MB maps, and the excess maps for both MB and DI in Figures D.1, D.2, D.3, D.4 and D.5, respectively, as discussed in Chapter 5. Furthermore, we provide the expected counts per transit and the exposure maps for a Crab nebula-like source in Figures D.6 and D.7.

```
┌─ HCuts ─┐
0 "(rec.nHitSP20/rec.CxPE40<= 20.00) && (rec.PINC>2.00)"
1 "(rec.nHitSP20/rec.CxPE40<= 6.00) && (rec.PINC>2.80)"
2 "(rec.nHitSP20/rec.CxPE40<= 8.00) && (rec.PINC>3.50)"
3 "(rec.nHitSP20/rec.CxPE40<=10.00) && (rec.PINC>2.80)"
4 "(rec.nHitSP20/rec.CxPE40<=14.00) && (rec.PINC>2.40)"
5 "(rec.nHitSP20/rec.CxPE40<=17.00) && (rec.PINC>2.40)"
6 "(rec.nHitSP20/rec.CxPE40<=16.00) && (rec.PINC>2.20)"
7 "(rec.nHitSP20/rec.CxPE40<=14.00) && (rec.PINC>2.30)"
8 "(rec.nHitSP20/rec.CxPE40<=14.00) && (rec.PINC>2.30)"
9 "(rec.nHitSP20/rec.CxPE40<= 2.00) && (rec.PINC>2.10)"
```
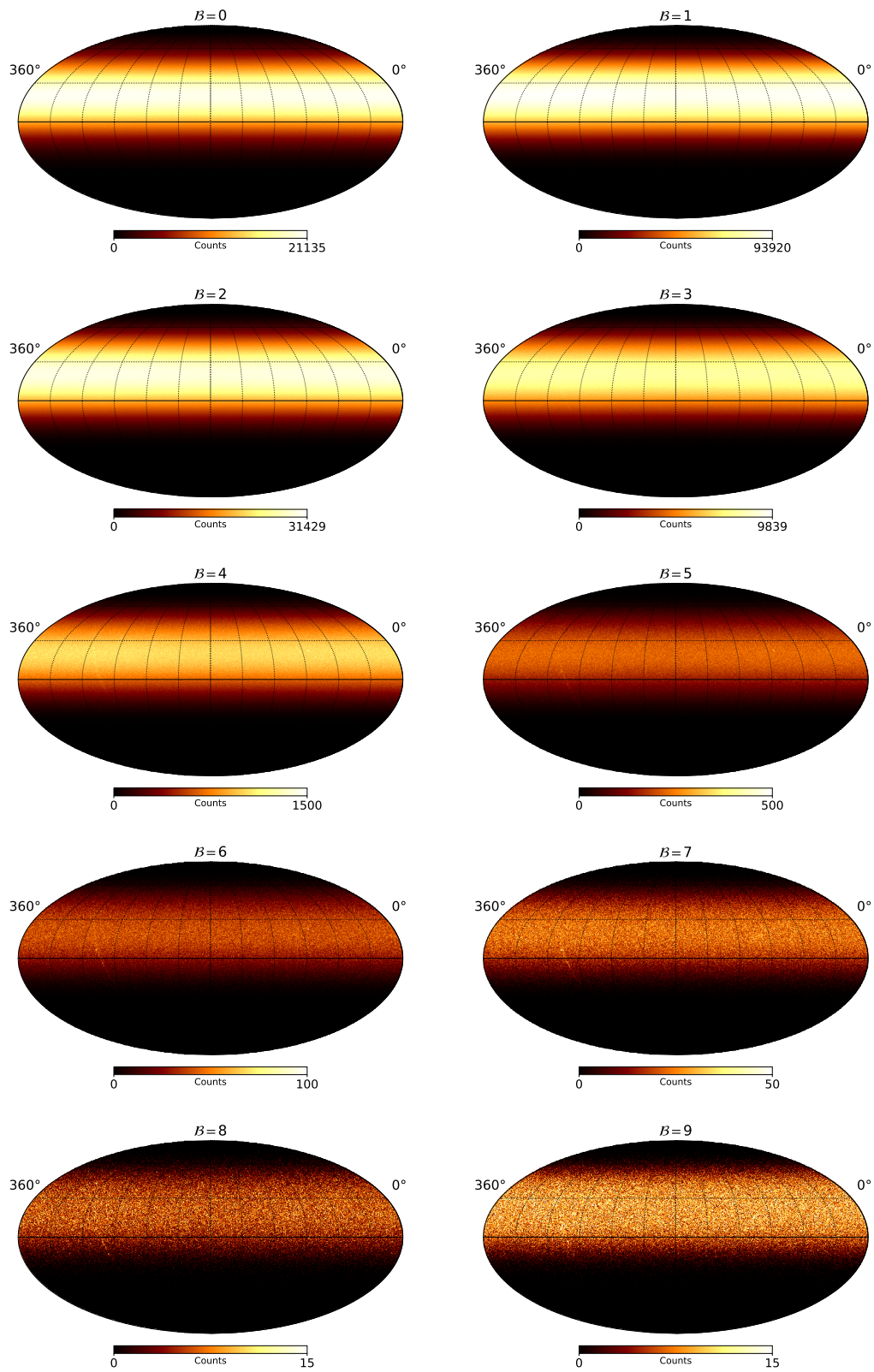
FIGURE D.1: Gamma-like event maps for nHit bins 0-9.
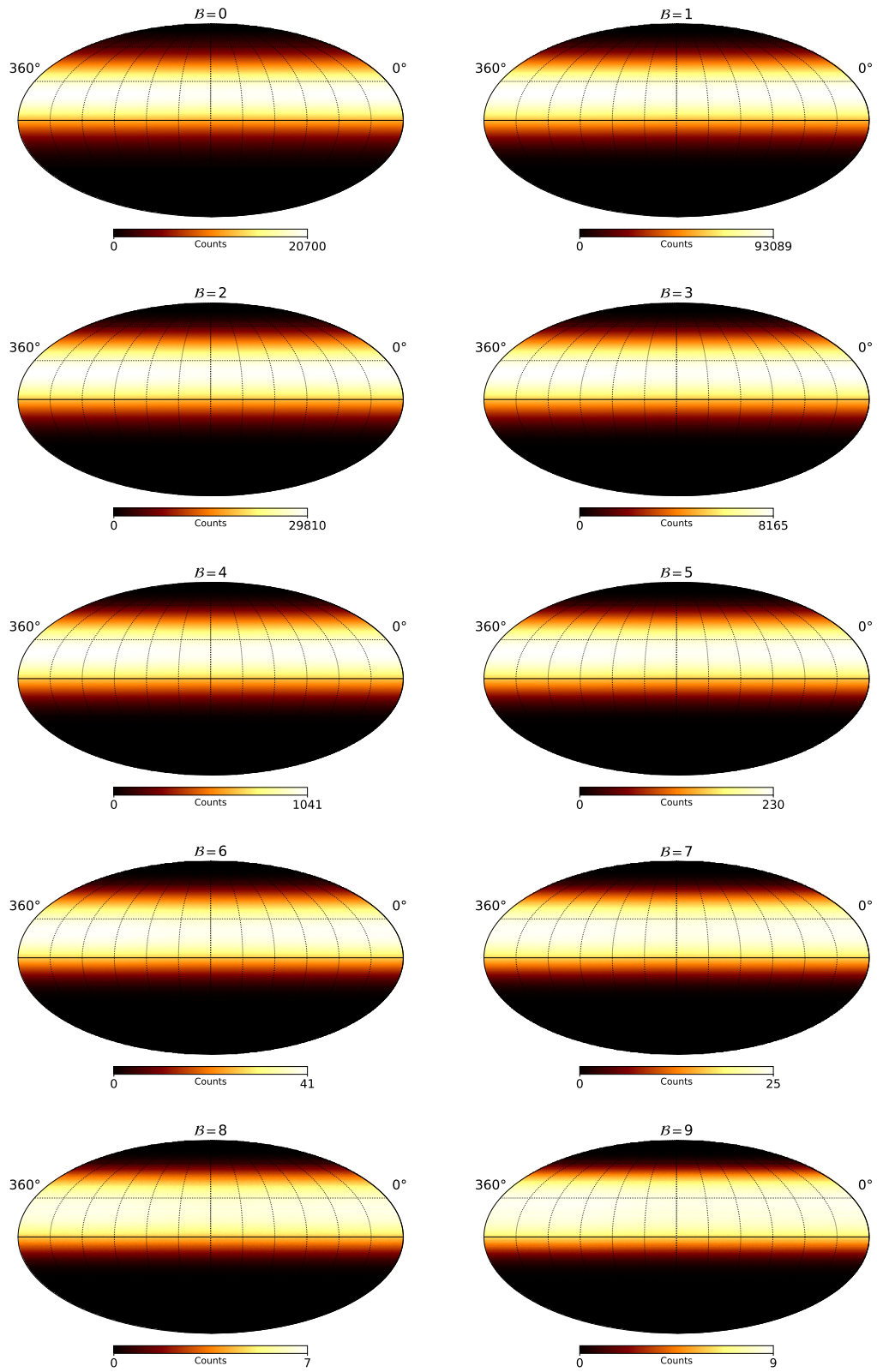
FIGURE D.2: DI maps for nHit bins 0-9.
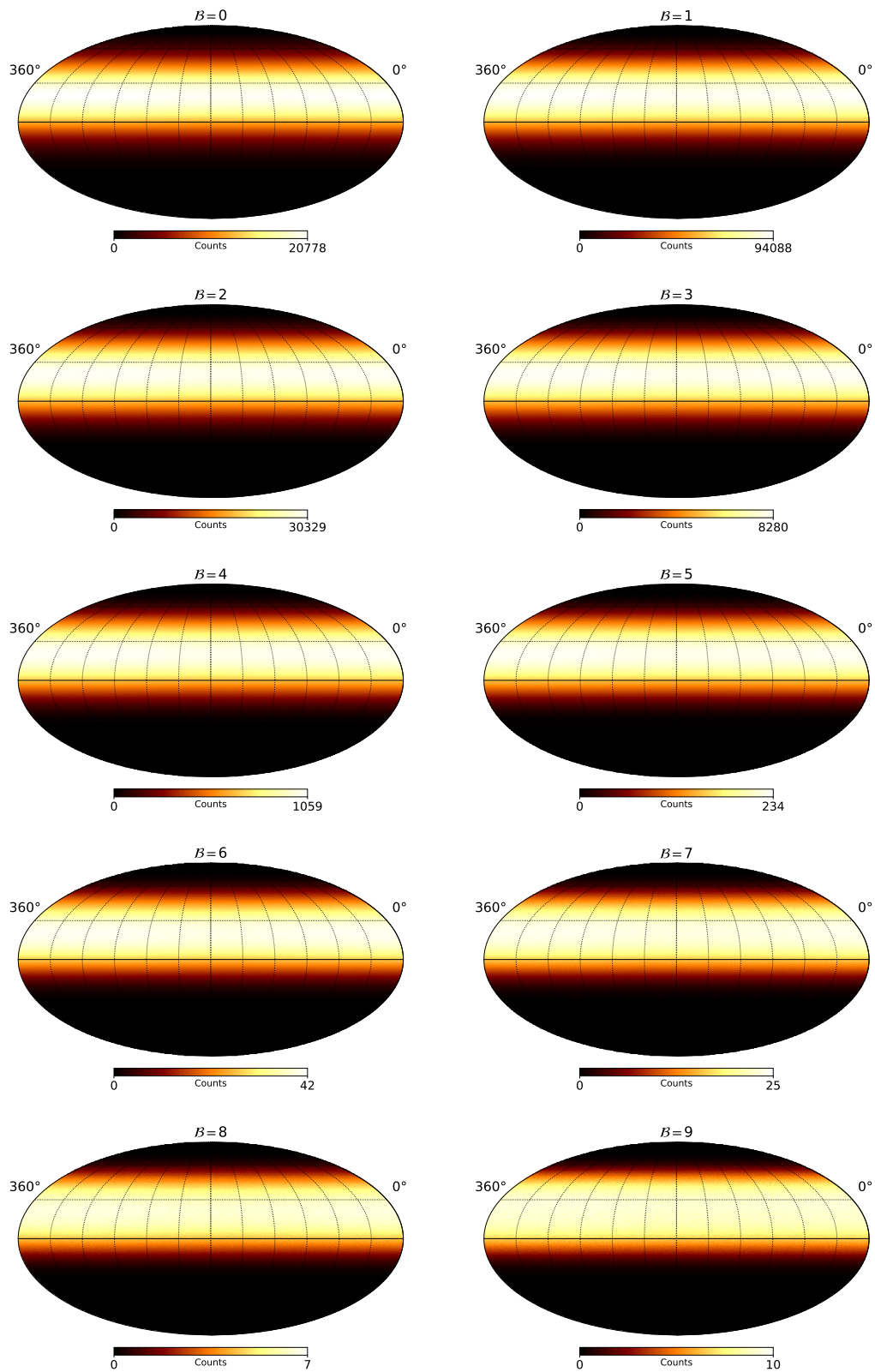
FIGURE D.3: MB maps for nHit bins 0-9.
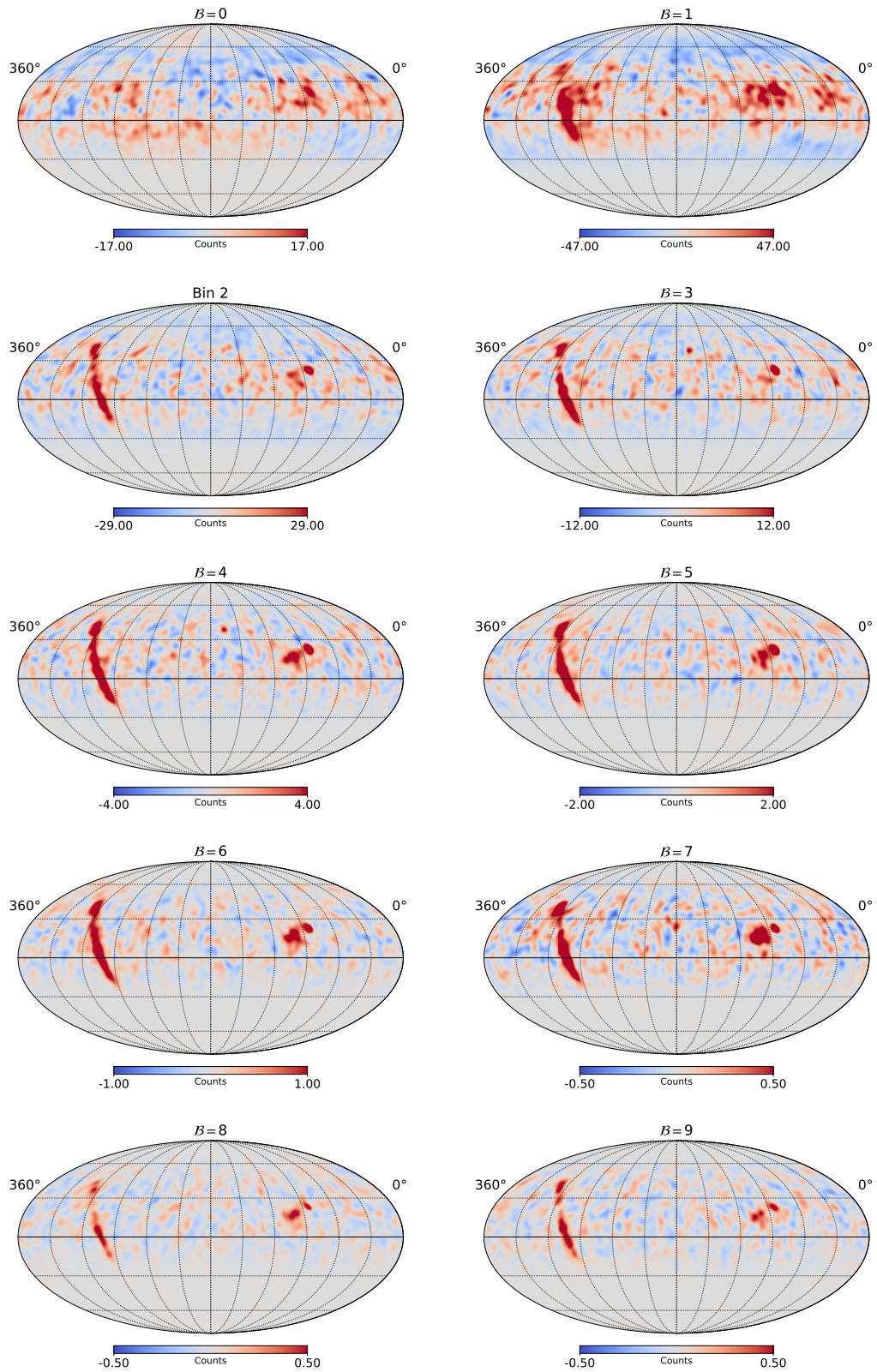
FIGURE D.4: Excess maps derived using the MB map for nHit bins 0-9 with a 5° smoothing.
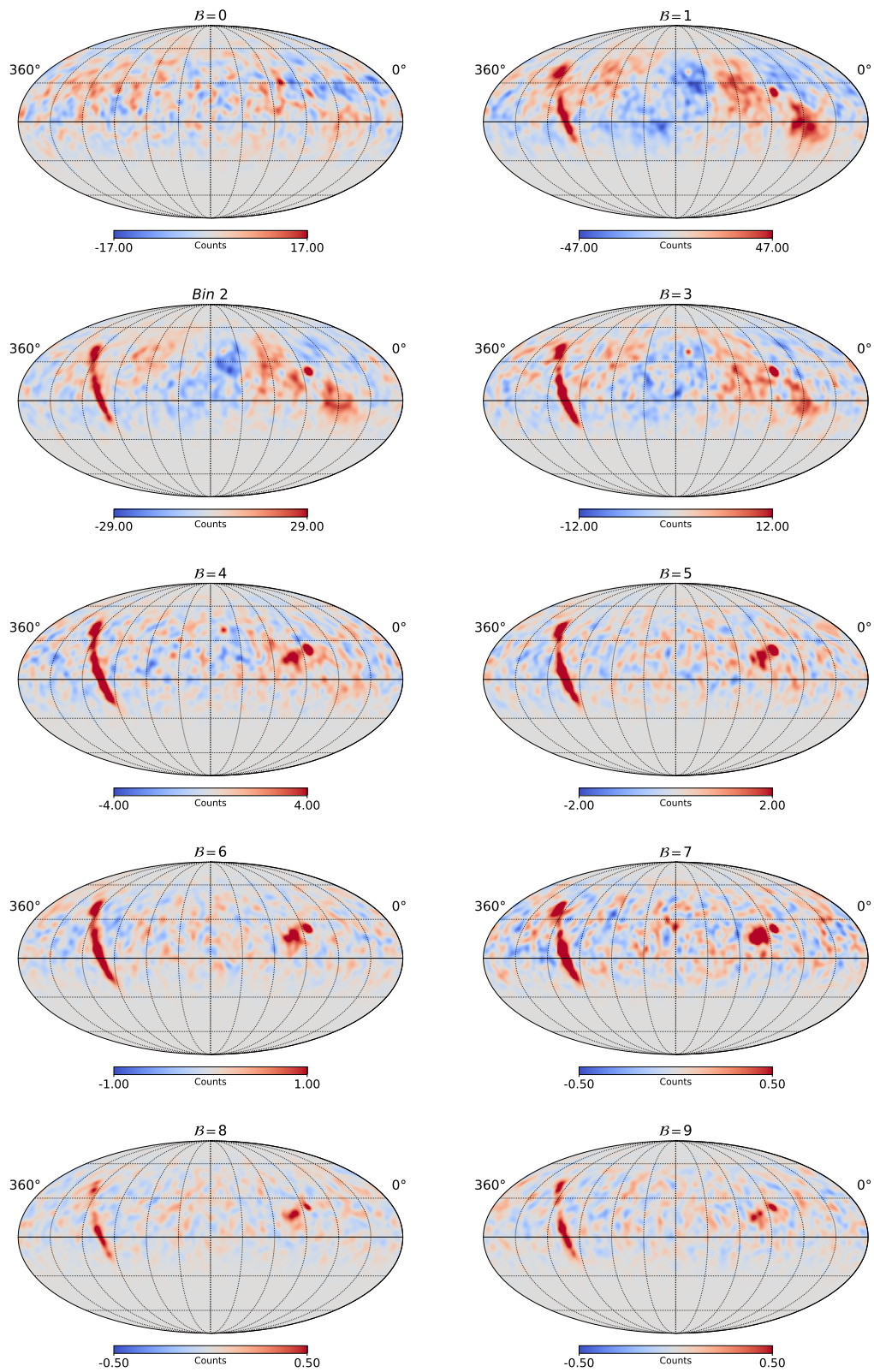
FIGURE D.5: Excess maps obtained using DI as background for nHit bins 0-9 with a 5°
smoothing.
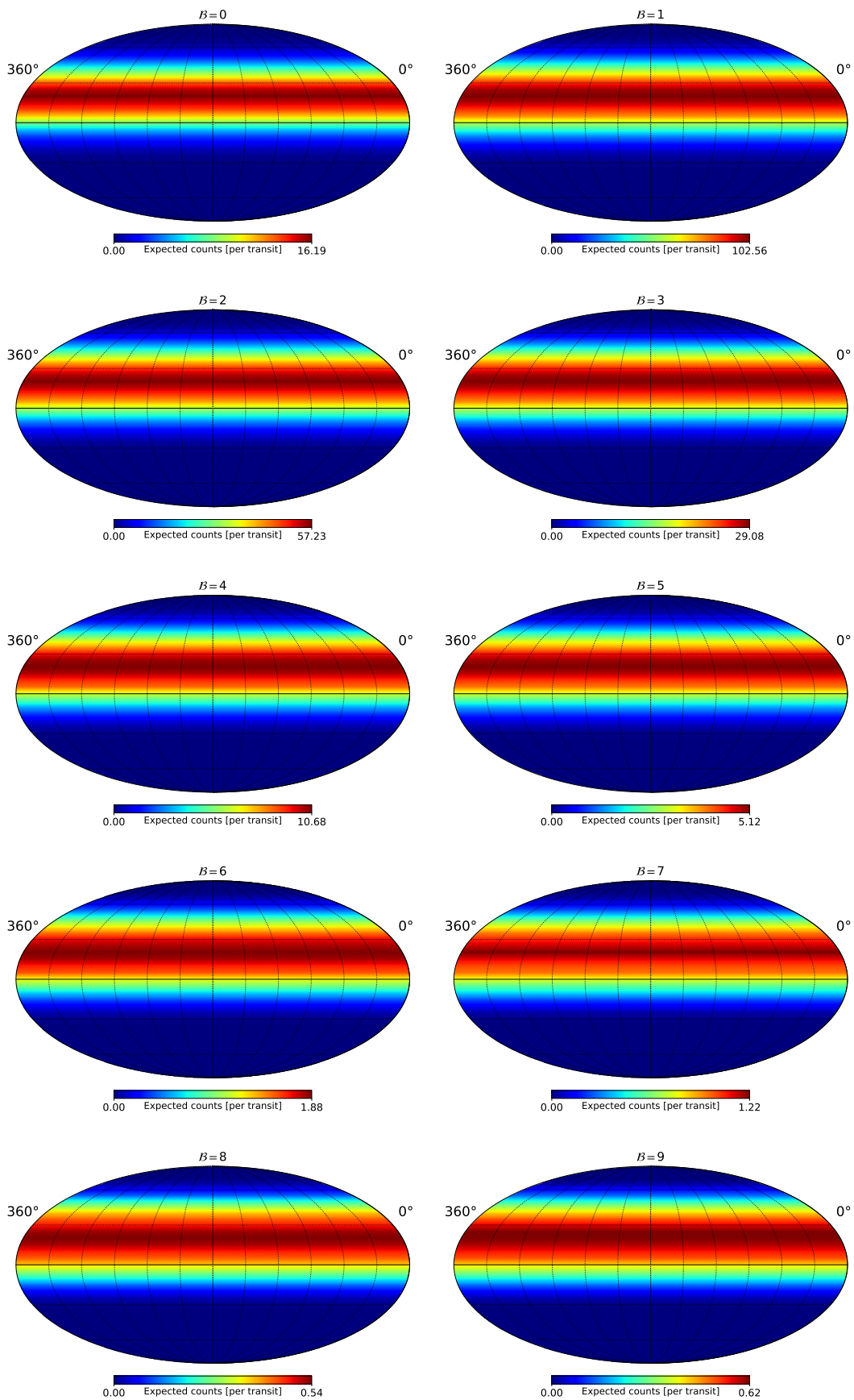
FIGURE D.6: Maps showing expected counts per transit for nHit bins 0-9. A Crab nebula-like source spectrum, with spectral index -2.63 and normalisation 3.5×10^{-11} cm^{-2} s^{-1} at a reference energy of 1 TeV, was used.
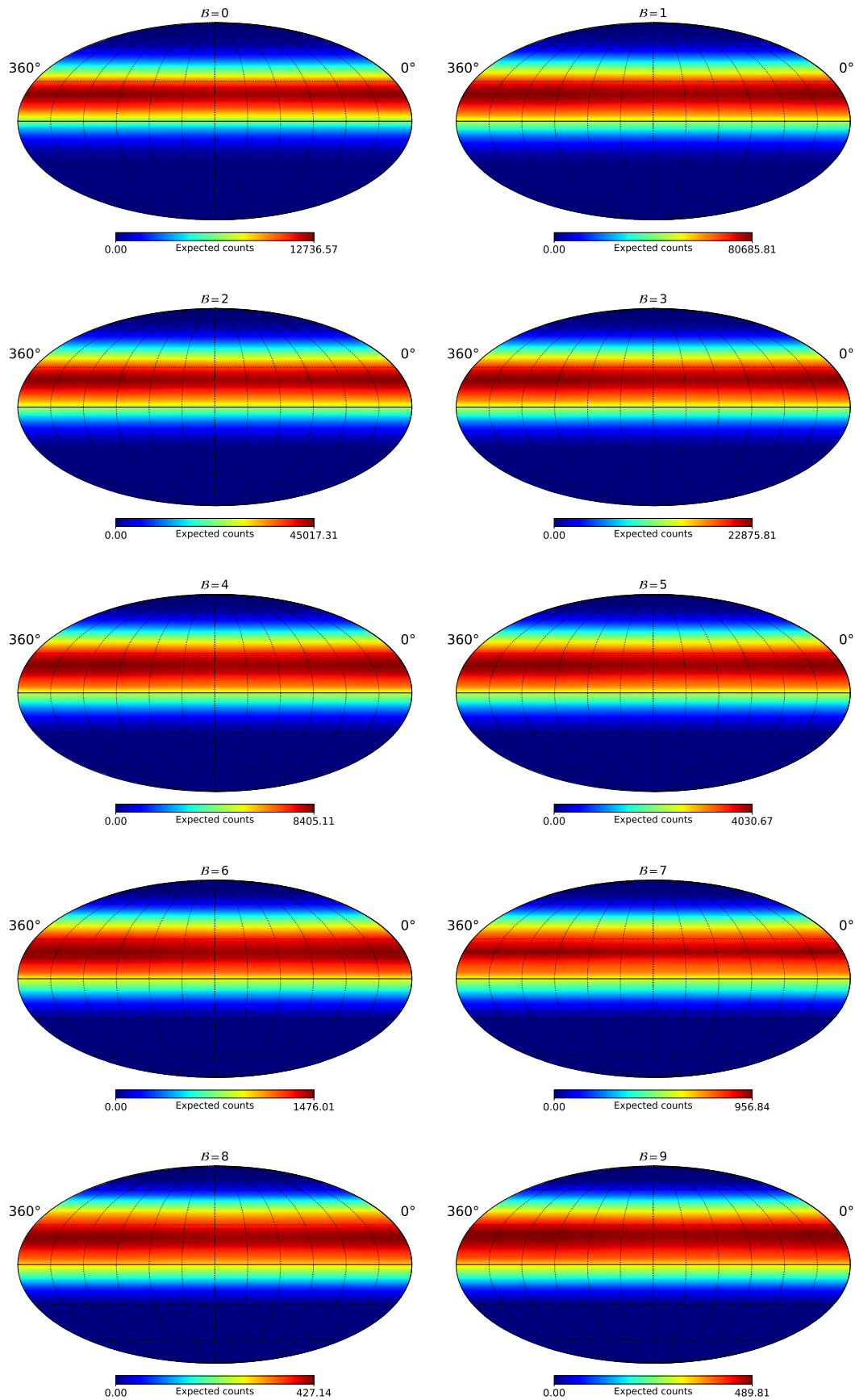
FIGURE D.7: Exposure maps showing expected counts for nHit bins 0-9. A Crab nebula-like source spectrum, with spectral index -2.63 and normalisation 3.5×10^{-11} cm^{-2} s^{-1} at a reference energy of 1 TeV, was used.

E

Supplementary to Search for Large-Scale Structures such as *Fermi* Bubbles in HAWC Sky

As supplementary material, we display, in Figure E.1, *bubbles* in other galaxies, and the flux upper limit comparison for confidence levels 68% and 95% in Figure E.2. Finally, in Figure E.3, we illustrate the extraction of integral flux upper limits using different spectral indices.

(A) NGC3079. Image credit: NASA/CXC/U, Michigan, https://chandra.harvard.edu/photo/2019/ngc3079/more.html

(B) Galaxy cluster Hydra-a
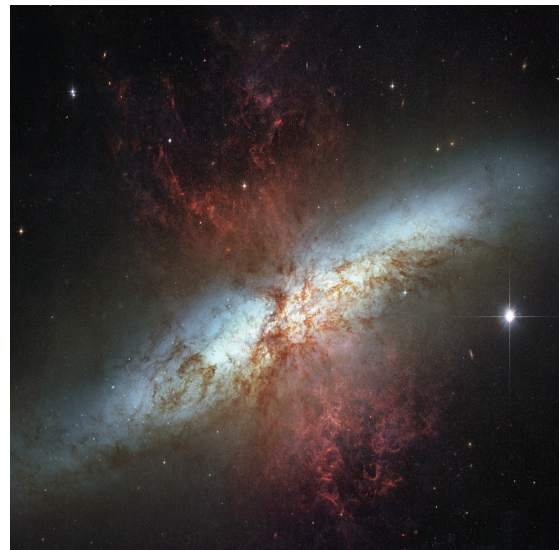
(C) Composite image of M82 from Chandra, HST and Spitzer data. Image credits are X-ray: NASA/CXC/JHU/D.Strickland; Optical: NASA/ESA/STScI/AURA/The Hubble Heritage Team; IR: NASA/JPL-Caltech/Univ. of AZ/C. Engelbracht

FIGURE E.1: Bubbles in other galaxies.
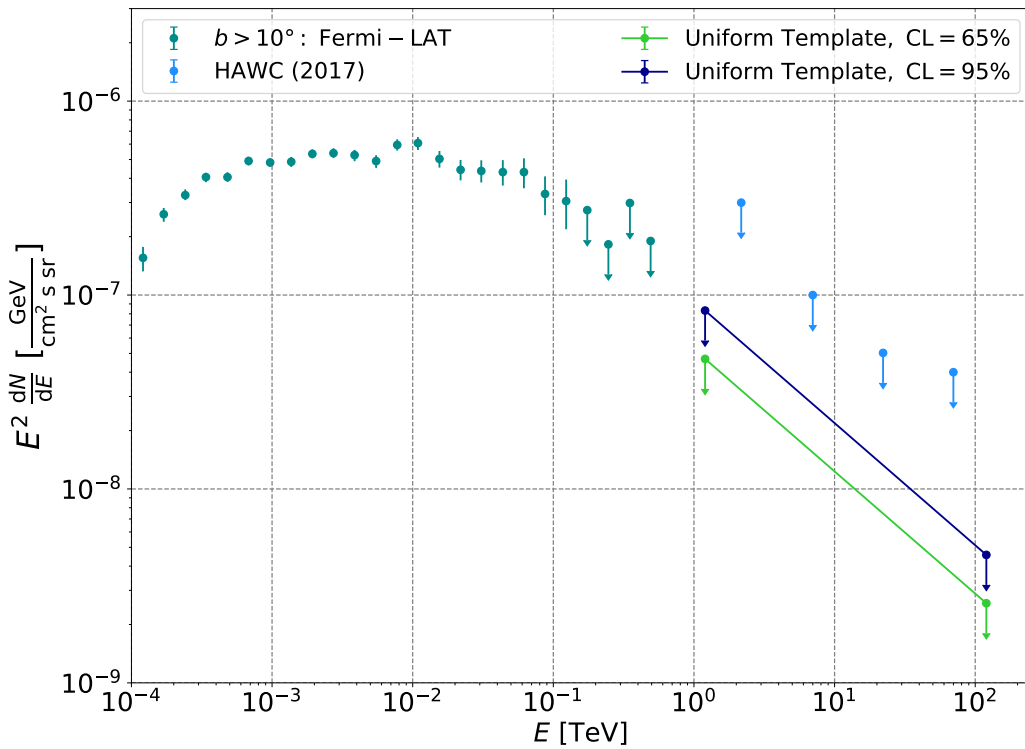
FIGURE E.2: Flux upper limit comparison for different confidence levels.
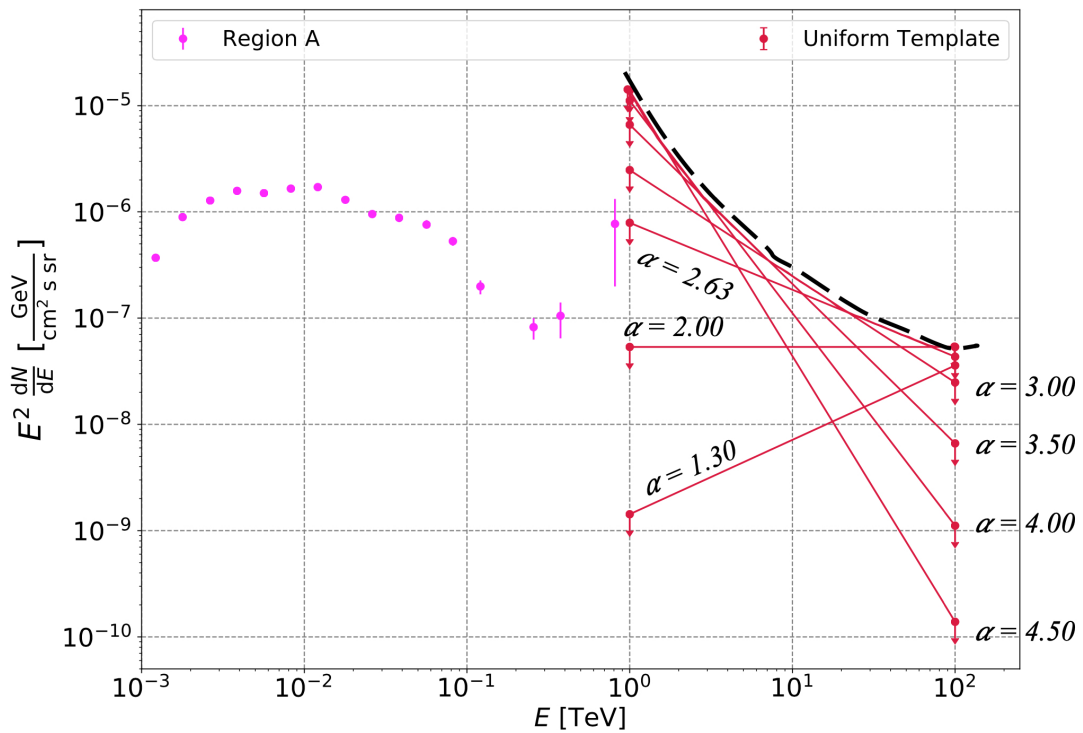
FIGURE E.3: Extracting integral flux upper limits using 95% confidence level upper limits from different spectral indices.

Bibliography

Agostinelli, S. et al. (2003). "Geant4 — A Simulation Toolkit". In: *Nuclear Instruments and Methods in Physics Research Section A: Accelerators, Spectrometers, Detectors and Associated Equipment* 506 (3), p. 250.

Aharonian, F. and S. Casanova (2018). "Selected Topics in Gamma-Ray Astronomy: Very High Energy Gamma-Rays as Tracers of Galactic Cosmic-Rays". In: *Multiple Messengers and Challenges in Astroparticle Physics*. Ed. by R. Aloiso, E. Coccia, and F. Vissani, pp. 97–143. DOI: 10.1007/978-3-319-65425-6_2.

Aharonian, F. et al. (2008). "High energy astrophysics with ground-based gamma ray detectors". In: *Reports on Progress in Physics* 71.9, p. 096901. DOI: 10.1088/0034-4885/71/9/096901.

Aharonian, F. A. (2004). *Very high energy cosmic gamma radiation : a crucial window on the extreme Universe*. DOI: 10.1142/4657.

Aharonian, F. A., A. M. Atoyan, and T. Kifune (1997). "Inverse Compton gamma radiation of faint synchrotron X-ray nebulae around pulsars". In: MNRAS 291.1, pp. 162–176. DOI: 10.1093/mnras/291.1.162.

Allison, J. et al. (2006). "Geant4 Developments and Applications". In: *IEEE Transactions on Nuclear Science* 53, p. 270.

Allison, J. et al. (2016). "Recent Developments in Geant4". In: *Nuclear Instruments and Methods in Physics Research Section A: Accelerators, Spectrometers, Detectors and Associated Equipment* 835, p. 186.

Amenomori, M. et al. (1992). "Search for steady emission of 10-TeV gamma rays from the Crab Nebula, Cygnus X-3, and Hercules X-1 using the Tibet Air Shower Array". In: *Physical Review Letters* 69, pp. 2468–2471. DOI: 10.1103/PhysRevLett.69.2468.

Anchordoqui, L. A., G. E. Romero, and J. A. Combi (1999). "Heavy nuclei at the end of the cosmic-ray spectrum?" In: Phys. Rev. D 60.10, p. 103001. DOI: 10.1103/PhysRevD.60.103001. arXiv: astro-ph/9903145 [astro-ph].

Antonelli, L. A. et al. (2009). "The Next Generation of Cherenkov Telescopes. A White Paper for the Italian National Institute for Astrophysics (INAF)". In: *arXiv e-prints*, arXiv:0906.4114. arXiv: 0906.4114 [astro-ph.IM].

ARGO-YBJ Collaboration et al. (2002). "Results from the ARGO-YBJ test experiment". In: *Astroparticle Physics* 17, pp. 151–165.

Arons, J. (2003). "Magnetars in the Metagalaxy: An Origin for Ultra-High-Energy Cosmic Rays in the Nearby Universe". In: ApJ 589.2, pp. 871–892. DOI: 10.1086/374776. arXiv: astro-ph/0208444 [astro-ph].

Atkins, R. et al. (2003). "Observation of TeV Gamma Rays from the Crab Nebula with Milagro Using a New Background Rejection Technique". In: ApJ 595.2, pp. 803–811. DOI: 10.1086/377498. arXiv: astro-ph/0305308 [astro-ph].

Atwood, W. B. et al. (2009). "The Large Area Telescope on the Fermi Gamma-Ray Space Telescope Mission". In: ApJ 697.2, pp. 1071–1102. DOI: 10.1088/0004-637X/697/2/1071. arXiv: 0902.1089 [astro-ph.IM].

Axford, W. I., E. Leer, and G. Skadron (1977). "The Acceleration of Cosmic Rays by Shock Waves". In: *International Cosmic Ray Conference*. Vol. 11. International Cosmic Ray Conference, p. 132.

Baixeras, C. (2003). "The MAGIC telescope". In: *Nuclear Physics B Proceedings Supplements* 114, pp. 247–252. DOI: 10.1016/S0920-5632(02)01910-2.

Baughman, B. (2011). "Gamma/Hadron Separation as a function of nHit". In: *HAWC Internal documentation*. URL: https://private.hawc-observatory.org/hawc.umd.edu/internal/db/2105_01.pdf.

Baughman, B. and A. Smith (2010). "Requirements and Baseline Design WBS 5.4 - Detector Simulation". In: *HAWC Internal documentation*. URL: https://private.hawc-observatory.org/hawc.umd.edu/internal/db/2019_05.pdf.

Bauleo, P. M. and J. Rodríguez Martino (2009). "The dawn of the particle astronomy era in ultra-high-energy cosmic rays". In: Nature 458.7240, pp. 847–851. DOI: 10.1038/nature07948.

Bell, A. R. (1978a). "The acceleration of cosmic rays in shock fronts - I." In: MNRAS 182, pp. 147–156. DOI: 10.1093/mnras/182.2.147.

— (1978b). "The acceleration of cosmic rays in shock fronts - II." In: MNRAS 182, pp. 443–455. DOI: 10.1093/mnras/182.3.443.

Berge, D., S. Funk, and J. Hinton (2007). "Background modelling in very-high-energy γ-ray astronomy". In: A&A 466.3, pp. 1219–1229. DOI: 10.1051/0004-6361:20066674. arXiv: astro-ph/0610959 [astro-ph].

Berkhuijsen, E. M. (1973). "Galactic continuum loops and the diameter-surface brightness relation for supernova remnants." In: A&A 24, pp. 143–147.

Bernlöhr, K. (2018). "High energy astrophysics". In: *Lecture notes, Universität Heidelberg*.

Bhabha, H. J. and W. Heitler (1937). "The Passage of Fast Electrons and the Theory of Cosmic Showers". In: *Proceedings of the Royal Society of London Series A* 159.898, pp. 432–458. DOI: 10.1098/rspa.1937.0082.

Biland, A. (2018). "Astro-particle physics". In: *Lecture notes, ETH Zurich*.

Bilous, A. V. et al. (2016). "A LOFAR census of non-recycled pulsars: average profiles, dispersion measures, flux densities, and spectra". In: A&A 591, A134, A134. DOI: 10.1051/0004-6361/201527702. arXiv: 1511.01767 [astro-ph.SR].

Bingham, R. G. (1967). "Magnetic fields in the galactic spurs". In: MNRAS 137, p. 157. DOI: 10.1093/mnras/137.2.157.

Blandford, R. D. and J. P. Ostriker (1978). "Particle acceleration by astrophysical shocks." In: ApJ 221, pp. L29–L32. DOI: 10.1086/182658.

Blasi, P. (2013). "Theoretical challenges in acceleration and transport of ultra high energy cosmic rays: A review". In: *European Physical Journal Web of Conferences*. Vol. 53. European Physical Journal Web of Conferences, p. 01002. DOI: 10.1051/epjconf/20135301002. arXiv: 1208.1682 [astro-ph.HE].

Blasi, P., R. I. Epstein, and A. V. Olinto (2000). "Ultra-High-Energy Cosmic Rays from Young Neutron Star Winds". In: ApJ 533.2, pp. L123–L126. DOI: 10.1086/312626. arXiv: astro-ph/9912240 [astro-ph].

Blumenthal, G. R. and R. J. Gould (1970). "Bremsstrahlung, Synchrotron Radiation, and Compton Scattering of High-Energy Electrons Traversing Dilute Gases". In: *Rev. Mod. Phys.* 42 (2), pp. 237–270. DOI: 10.1103/RevModPhys.42.237. URL: https://link.aps.org/doi/10.1103/RevModPhys.42.237.

Blümer, J. and K. H. Kampart (2000). "Search for the sources of cosmic radiation". In: *Physikalische Blätter* 56N3, p. 39.

Bothe, W. and W. Kolhörster (1929). "Das Wesen der Höhenstrahlung". In: *Zeitschrift fur Physik* 56.11-12, pp. 751–777. DOI: 10.1007/BF01340137.

Carretti, E. et al. (2013). "Giant magnetized outflows from the centre of the Milky Way". In: Nature 493.7430, pp. 66–69. DOI: 10.1038/nature11734. arXiv: 1301.0512 [astro-ph.GA].

Casandjian, J. M. and I. Grenier (2009). "High Energy Gamma-Ray Emission from the Loop I region". In: *arXiv e-prints*, arXiv:0912.3478, arXiv:0912.3478. arXiv: 0912.3478 [astro-ph.HE].

Casandjian, Jean-Marc (2015). "The Fermi-LAT model of interstellar emission for standard point source analysis". In: *arXiv e-prints*, arXiv:1502.07210, arXiv:1502.07210. arXiv: 1502.07210 [astro-ph.HE].

Casanova, S. et al. (2010). "Molecular Clouds as Cosmic-Ray Barometers". In: PASJ 62, p. 769. DOI: 10.1093/pasj/62.3.769. arXiv: 0904.2887 [astro-ph.HE].

Cash, W. (1979). "Parameter estimation in astronomy through application of the likelihood ratio." In: ApJ 228, pp. 939–947. DOI: 10.1086/156922.

Cherenkov, PA (1934). "Visible luminescence of pure liquids under the influence of γ-radiation". In: *Usp. Fiz. Nauk* 93.AEC-tr-2358, pp. 385–388.

Cherenkov Telescope Array Consortium et al. (2019). *Science with the Cherenkov Telescope Array*. DOI: 10.1142/10986.

Chudakov, A. E. and N. M. Nesterova (1958). "Cherenkov radiation of extensive air showers". In: *Il Nuovo Cimento* 8, pp. 606–611. DOI: 10.1007/BF02962580.

Cocconi, G. (1960). "An air shower telescope and the detection of 10^{12} eV photon sources". In: *International Cosmic Ray Conference* 2, p. 309.

COESA (1976). *US Standard Atmosphere 1976*.

Crocker, R. M. and F. Aharonian (2011). "Fermi Bubbles: Giant, Multibillion-Year-Old Reservoirs of Galactic Center Cosmic Rays". In: Phys. Rev. Lett. 106.10, p. 101102. DOI: 10.1103/PhysRevLett.106.101102. arXiv: 1008.2658 [astro-ph.GA].

Crocker, R. M. et al. (2015). "A Unified Model of the Fermi Bubbles, Microwave Haze, and Polarized Radio Lobes: Reverse Shocks in the Galactic Center's Giant Outflows". In: ApJ 808.2, p. 107. DOI: 10.1088/0004-637X/808/2/107. arXiv: 1412.7510 [astro-ph.HE].

Dame, T. M., Dap Hartmann, and P. Thaddeus (2001). "The Milky Way in Molecular Clouds: A New Complete CO Survey". In: ApJ 547.2, pp. 792–813. DOI: 10.1086/318388. arXiv: astro-ph/0009217 [astro-ph].

De Angelis, A., N. Giglietto, and S. Stramaglia (2010). "Domenico Pacini, the forgotten pioneer of the discovery of cosmic rays". In: *arXiv e-prints*, arXiv:1002.2888. arXiv: 1002.2888 [physics.hist-ph].

De Angelis, A. and M. Mallamaci (2018). "Gamma-ray astrophysics". In: *European Physical Journal Plus* 133.8, p. 324. DOI: 10.1140/epjp/i2018-12181-0. arXiv: 1805.05642 [astro-ph.HE].

de Gouveia Dal Pino, E. M. and A. Lazarian (2000). "Ultra-High-Energy Cosmic-Ray Acceleration by Magnetic Reconnection in Newborn Accretion-induced Collapse Pulsars". In: ApJ 536.1, pp. L31–L34. DOI: 10.1086/312730. arXiv: astro-ph/0002155 [astro-ph].

de Mink, S. E. et al. (2014). "The Incidence of Stellar Mergers and Mass Gainers among Massive Stars". In: ApJ 782.1, p. 7. DOI: 10.1088/0004-637X/782/1/7. arXiv: 1312.3650 [astro-ph.SR].

Di Sciascio, G. (2019a). "Detection of Cosmic Rays from ground: an Introduction". In: *Journal of Physics Conference Series*. Vol. 1263. Journal of Physics Conference Series, p. 012002. DOI: 10.1088/1742-6596/1263/1/012002. arXiv: 1904.08344 [astro-ph.HE].

— (2019b). "Ground-based Gamma-Ray Astronomy: an Introduction". In: *arXiv e-prints*. arXiv: 1904.06218 [astro-ph.IM].

Di Sciascio, G. and LHAASO Collaboration (2016). "The LHAASO experiment: From Gamma-Ray Astronomy to Cosmic Rays". In: *Nuclear and Particle Physics Proceedings* 279, pp. 166–173. DOI: 10.1016/j.nuclphysbps.2016.10.024. arXiv: 1602.07600 [astro-ph.HE].

Dickinson, C. (2018). "Large-Scale Features of the Radio Sky and a Model for Loop I". In: *Galaxies* 6, p. 56. DOI: 10.3390/galaxies6020056.

Diehl, R., N. Prantzos, and P. von Ballmoos (2006). "Astrophysical constraints from gamma-ray spectroscopy". In: Nucl. Phys. A 777, pp. 70–97. DOI: 10.1016/j.nuclphysa.2005.02.155. arXiv: astro-ph/0502324 [astro-ph].

Dobler, G. et al. (2010). "The Fermi Haze: A Gamma-ray Counterpart to the Microwave Haze". In: ApJ 717.2, pp. 825–842. DOI: 10.1088/0004-637X/717/2/825. arXiv: 0910.4583 [astro-ph.HE].

Donahue, R. J. and W. R. Nelson (1991). "Alternative Positron-Target Design for Electron-Positron Colliders". In:

Dubus, G. (2013). "Gamma-ray binaries and related systems". In: A&A Rev. 21, p. 64. DOI: 10.1007/s00159-013-0064-5. arXiv: 1307.7083 [astro-ph.HE].

Egger, Roland J. and Bernd Aschenbach (1995). "Interaction of the Loop I supershell with the Local Hot Bubble." In: A&A 294, pp. L25–L28. arXiv: astro-ph/9412086 [astro-ph].

Fabian, A. C. (2012). "Observational Evidence of Active Galactic Nuclei Feedback". In: ARA&A 50, pp. 455–489. DOI: 10.1146/annurev-astro-081811-125521. arXiv: 1204.4114 [astro-ph.CO].

Fang, K. and K. Murase (2018). "Linking high-energy cosmic particles by black-hole jets embedded in large-scale structures". In: *Nature Physics* 14.4, pp. 396–398. DOI: 10.1038/s41567-017-0025-4. arXiv: 1704.00015 [astro-ph.HE].

Fang, K. and A. V. Olinto (2016). "High-energy Neutrinos from Sources in Clusters of Galaxies". In: ApJ 828.1, p. 37. DOI: 10.3847/0004-637X/828/1/37. arXiv: 1607.00380 [astro-ph.HE].

Fermi, E. (1949). "On the Origin of the Cosmic Radiation". In: *Physical Review* 75.8, pp. 1169–1174. DOI: 10.1103/PhysRev.75.1169.

Fermi-LAT Collaboration et al. (2009). "Fermi Observations of High-Energy Gamma-Ray Emission from GRB 080916C". In: *Science* 323.5922, p. 1688. DOI: 10.1126/science.1169101.

Fermi-LAT Collaboration et al. (2012). "Fermi-LAT Observations of the Diffuse γ-Ray Emission: Implications for Cosmic Rays and the Interstellar Medium". In: ApJ 750.1, p. 3. DOI: 10.1088/0004-637X/750/1/3. arXiv: 1202.4039 [astro-ph.HE].

Fermi-LAT Collaboration et al. (2014a). "Fermi-LAT Observations of the Gamma-Ray Burst GRB 130427A". In: *Science* 343.6166, pp. 42–47. DOI: 10.1126/science.1242353. arXiv: 1311.5623 [astro-ph.HE].

Fermi-LAT Collaboration et al. (2014b). "The Spectrum and Morphology of the Fermi Bubbles". In: ApJ 793.1, 64, p. 64. DOI: 10.1088/0004-637X/793/1/64. arXiv: 1407.7905 [astro-ph.HE].

Fermi-LAT Collaboration et al. (2015). "Fermi Large Area Telescope Third Source Catalog". In: ApJS 218.2, 23, p. 23. DOI: 10.1088/0067-0049/218/2/23. arXiv: 1501.02003 [astro-ph.HE].

Fermi LAT Collaboration et al. (2017). "The Fermi Galactic Center GeV Excess and Implications for Dark Matter". In: ApJ 840.1, 43, p. 43. DOI: 10.3847/1538-4357/aa6cab. arXiv: 1704.03910 [astro-ph.HE].

Fichtel, C. E. et al. (1993). "Results from the energetic gamma-ray experiment telescope (EGRET) on the Compton Observatory". In: *Advances in Space Research* 13. DOI: 10.1016/0273-1177(93)90175-B.

Finkbeiner, D. P. (2003). "A Full-Sky Hα Template for Microwave Foreground Prediction". In: ApJS 146.2, pp. 407–415. DOI: 10.1086/374411. arXiv: astro-ph/0301558 [astro-ph].

— (2004). "Microwave Interstellar Medium Emission Observed by the Wilkinson Microwave Anisotropy Probe". In: ApJ 614.1, pp. 186–193. DOI: 10.1086/423482. arXiv: astro-ph/0311547 [astro-ph].

Finkbeiner, D. P., G. I. Langston, and A. H. Minter (2004). "Microwave Interstellar Medium Emission in the Green Bank Galactic Plane Survey: Evidence for Spinning Dust". In: ApJ 617.1, pp. 350–359. DOI: 10.1086/425165. arXiv: astro-ph/0408292 [astro-ph].

Fiorino, D. (2016). "HAWC Observatory Map Making Reference". In: *HAWC Internal documentation*. URL: http://private.hawc-observatory.org/hawc.umd.edu/internal/db/2128_12.pdf.

— (2017). "Chunks". In: *HAWC Internal documentation*. URL: https://private.hawc-observatory.org/hawc.umd.edu/internal/db/2368_02.pdf.

Fishman, G. J. et al. (1992). "The BATSE experiment on the Compton Gamma Ray Observatory: status and some early results." In: *NASA Conference Publication*. Vol. 3137, pp. 26–34.

Frank, I. M. and I. E. Tamm (1937). "Coherent visible radiation of fast electrons passing through matter". In: *Compt. Rend. Acad. Sci. URSS* 14.3. [Usp. Fiz. Nauk93,no.2,388(1967)], pp. 109–114. DOI: 10.1007/978-3-642-74626-0_2, 10.3367/UFNr.0093.196710o.0388.

Fujita, Y., Y. Ohira, and R. Yamazaki (2014). "A Hadronic-leptonic Model for the Fermi Bubbles: Cosmic-Rays in the Galactic Halo and Radio Emission". In: ApJ 789.1, 67, p. 67. DOI: 10.1088/0004-637X/789/1/67. arXiv: 1405.5214 [astro-ph.HE].

Funk, S. (2015). "Ground- and Space-Based Gamma-Ray Astronomy". In: *Annual Review of Nuclear and Particle Science* 65, pp. 245–277. DOI: 10.1146/annurev-nucl-102014-022036. arXiv: 1508.05190 [astro-ph.HE].

Gabici, S., F. A. Aharonian, and S. Casanova (2009). "Broad-band non-thermal emission from molecular clouds illuminated by cosmic rays from nearby supernova remnants". In: MNRAS 396.3, pp. 1629–1639. DOI: 10.1111/j.1365-2966.2009.14832.x. arXiv: 0901.4549 [astro-ph.HE].

Gaisser, T. K., R. J. Protheroe, and Todor Stanev (1998). "Gamma-Ray Production in Supernova Remnants". In: ApJ 492.1, pp. 219–227. DOI: 10.1086/305011. arXiv: astro-ph/9609044 [astro-ph].

Galbraith, W. and J. V. Jelley (1953). "Light Pulses from the Night Sky associated with Cosmic Rays". In: Nature 171, pp. 349–350. DOI: 10.1038/171349a0.

Gehrels, N., E. Chipman, and D. Kniffen (1994). "The Compton Gamma Ray Observatory". In: ApJS 92, p. 351. DOI: 10.1086/191978.

Gehrels, N. et al. (1993). "The Compton gamma ray observatory". In: *Scientific American* 269.6, pp. 68–77.

Ginzburg, V. L. and S. I. Syrovatskii (1964). *The Origin of Cosmic Rays*.

Goodenough, L. and D. Hooper (2009). "Possible Evidence For Dark Matter Annihilation In The Inner Milky Way From The Fermi Gamma Ray Space Telescope". In: *arXiv e-prints*, arXiv:0910.2998, arXiv:0910.2998. arXiv: 0910.2998 [hep-ph].

Górski, K. M. et al. (2005). "HEALPix: A Framework for High-Resolution Discretization and Fast Analysis of Data Distributed on the Sphere". In: ApJ 622, pp. 759–771. DOI: 10.1086/427976. eprint: astro-ph/0409513.

Greisen, K. (1966). "End to the Cosmic-Ray Spectrum?" In: Phys. Rev. Lett. 16.17, pp. 748–750. DOI: 10.1103/PhysRevLett.16.748.

Guo, F. and W. G. Mathews (2012). "The Fermi Bubbles. I. Possible Evidence for Recent AGN Jet Activity in the Galaxy". In: ApJ 756.2, 181, p. 181. DOI: 10.1088/0004-637X/756/2/181. arXiv: 1103.0055 [astro-ph.HE].

Hampel-Arias, Z. (2017). "Cosmic Ray Observations at the TeV Scale with the HAWC Observatory". PhD thesis. University of Wisconsin-Madison.

Hartman, R. C. et al. (1999). "The Third EGRET Catalog of High-Energy Gamma-Ray Sources". In: ApJS 123, pp. 79–202. DOI: 10.1086/313231.

Haslam, C. G. T. et al. (1982). "A 408 MHz all-sky continuum survey. II. The atlas of contour maps." In: A&AS 47, pp. 1–143.

HAWC Collaboration et al. (2013). "Sensitivity of the high altitude water Cherenkov detector to sources of multi-TeV gamma rays". In: *Astroparticle Physics* 50, pp. 26–32. DOI: 10.1016/j.astropartphys.2013.08.002. arXiv: 1306.5800 [astro-ph.HE].

HAWC Collaboration et al. (2017a). "Daily Monitoring of TeV Gamma-Ray Emission from Mrk 421, Mrk 501, and the Crab Nebula with HAWC". In: ApJ 841.2, 100, p. 100. DOI: 10.3847/1538-4357/aa729e. arXiv: 1703.06968 [astro-ph.HE].

HAWC Collaboration et al. (2017b). "Extended gamma-ray sources around pulsars constrain the origin of the positron flux at Earth". In: *Science* 358.6365, pp. 911–914. DOI: 10.1126/science.aan4880. arXiv: 1711.06223 [astro-ph.HE].

HAWC Collaboration et al. (2017c). "Observation of the Crab Nebula with the HAWC Gamma-Ray Observatory". In: ApJ 843.1, p. 39. DOI: 10.3847/1538-4357/aa7555. arXiv: 1701.01778 [astro-ph.HE].

HAWC Collaboration et al. (2017d). "Search for Very High-energy Gamma Rays from the Northern Fermi Bubble Region with HAWC". In: ApJ 842.2, 85, p. 85. DOI: 10.3847/1538-4357/aa751a. arXiv: 1703.01344 [astro-ph.HE].

HAWC Collaboration et al. (2017e). "The 2HWC HAWC Observatory Gamma-Ray Catalog". In: ApJ 843.1, p. 40. DOI: 10.3847/1538-4357/aa7556. arXiv: 1702.02992 [astro-ph.HE].

HAWC Collaboration et al. (2018a). "Observation of Anisotropy of TeV Cosmic Rays with Two Years of HAWC". In: ApJ 865.1, 57, p. 57. DOI: 10.3847/1538-4357/aad90c. arXiv: 1805.01847 [astro-ph.HE].

HAWC Collaboration et al. (2018b). "Very high energy particle acceleration powered by the jets of the microquasar SS 433". In: *arXiv e-prints*, arXiv:1810.01892. arXiv: 1810.01892 [astro-ph.HE].

HAWC Collaboration et al. (2019). "Measurement of the Crab Nebula Spectrum Past 100 TeV with HAWC". In: ApJ 881.2, p. 134. DOI: 10.3847/1538-4357/ab2f7d. URL: https://doi.org/10.3847\%2F1538-4357\%2Fab2f7d.

HAWC Collaboration et al. (2020). "Multiple Galactic Sources with Emission Above 56 TeV Detected by HAWC". In: *Phys. Rev. Lett.* 124 (2), p. 021102. DOI: 10.1103/PhysRevLett.124.021102. arXiv: 1909.08609 [astro-ph.HE].

Heck, D. et al. (1998). *CORSIKA: a Monte Carlo code to simulate extensive air showers.*

Heiles, C. et al. (1980). "A new look at the north Polar Spur". In: ApJ 242, pp. 533–540. DOI: 10.1086/158487.

Herold, L. and D. Malyshev (2019). "Hard and bright gamma-ray emission at the base of the Fermi bubbles". In: A&A 625, A110, A110. DOI: 10.1051/0004-6361/201834670. arXiv: 1904.01454 [astro-ph.HE].

Hess, V. F. (1912). "Aus der Abteilung für geophysik Meteorologie und Erdmagnetismus". In: *Phys. Z* 13, p. 1084.

H.E.S.S. Collaboration et al. (2004). "High-energy particle acceleration in the shell of a supernova remnant". In: Nature 432.7013, pp. 75–77. DOI: 10.1038/nature02960. arXiv: astro-ph/0411533 [astro-ph].

H.E.S.S. Collaboration et al. (2016). "Acceleration of petaelectronvolt protons in the Galactic Centre". In: Nature 531.7595, pp. 476–479. DOI: 10.1038/nature17147. arXiv: 1603.07730 [astro-ph.HE].

H.E.S.S. Collaboration et al. (2019a). "A very-high-energy component deep in the γ-ray burst afterglow". In: Nature 575.7783, pp. 464–467. DOI: 10.1038/s41586-019-1743-9. arXiv: 1911.08961 [astro-ph.HE].

H.E.S.S. Collaboration et al. (2019b). "Resolving the Crab pulsar wind nebula at teraelectronvolt energies". In: *Nature Astronomy*, p. 476. DOI: 10.1038/s41550-019-0910-0. arXiv: 1909.09494 [astro-ph.HE].

Hester, J. J. (2008). "The Crab Nebula : an astrophysical chimera." In: ARA&A 46, pp. 127–155. DOI: 10.1146/annurev.astro.45.051806.110608.

Hewish, A. et al. (1968). "Observation of a Rapidly Pulsating Radio Source". In: Nature 217.5130, pp. 709–713. DOI: 10.1038/217709a0.

Hillas, A. M. (1984). "The Origin of Ultra-High-Energy Cosmic Rays". In: ARA&A 22, pp. 425–444. DOI: 10.1146/annurev.aa.22.090184.002233.

— (1985). "Cerenkov light images of EAS produced by primary gamma". In: *International Cosmic Ray Conference* 3.

— (2013). "Evolution of ground-based gamma-ray astronomy from the early days to the Cherenkov Telescope Arrays". In: *Astroparticle Physics* 43, pp. 19–43. DOI: 10.1016/j.astropartphys.2012.06.002.

Hofmann, W. (2000). "The high energy stereoscopic system (HESS) project". In: *AIP Conference Proceedings* 515.1, pp. 500–509. DOI: 10.1063/1.1291416. eprint: https://aip.scitation.org/doi/pdf/10.1063/1.1291416. URL: https://aip.scitation.org/doi/abs/10.1063/1.1291416.

Jardin-Blicq, A. (2019). "The TeV gamma-ray emission of the Galactic Plane". PhD thesis. Ruperto-Carola University of Heidelberg.

Johnson, W. N. et al. (1993). "The Oriented Scintillation Spectrometer Experiment: Instrument Description". In: ApJS 86, p. 693. DOI: 10.1086/191795.

Joshi, V. (2019). "Reconstruction and Analysis of Highest Energy γ-Rays and its Application to Pulsar Wind Nebulae". PhD thesis. Ruperto-Carola University of Heidelberg.

Kang, H., J. P. Rachen, and P. L. Biermann (1997). "Contributions to the Cosmic Ray Flux above the Ankle: Clusters of Galaxies". In: MNRAS 286.2, pp. 257–267. DOI: 10.1093/mnras/286.2.257. arXiv: astro-ph/9608071 [astro-ph].

Kappes, A. et al. (2007). "Potential Neutrino Signals from Galactic γ-Ray Sources". In: ApJ 656.2, pp. 870–878. DOI: 10.1086/508936. arXiv: astro-ph/0607286 [astro-ph].

Kargaltsev, O. et al. (2008). "X-Ray Observations of Parsec-scale Tails behind Two Middle-Aged Pulsars". In: ApJ 684.1, pp. 542–557. DOI: 10.1086/589145. arXiv: 0802.2963 [astro-ph].

Karim, M. T. et al. (2018). "Probing the Southern Fermi Bubble in Ultraviolet Absorption Using Distant AGNs". In: ApJ 860.2, 98, p. 98. DOI: 10.3847/1538-4357/aac167. arXiv: 1804.10617 [astro-ph.GA].

Kataoka, J. et al. (2018). "X-Ray and Gamma-Ray Observations of the Fermi Bubbles and NPS/Loop I Structures". In: *Galaxies* 6.1, p. 27. DOI: 10.3390/galaxies6010027. arXiv: 1802.07463 [astro-ph.HE].

Kifune, T. (1996). "Ground-based gamma-ray astronomy: general remarks." In: *Nuovo Cimento C Geophysics Space Physics C* 19C, pp. 953–957. DOI: 10.1007/BF02508136.

Klein, O. and T. Nishina (1929). "Über die Streuung von Strahlung durch freie Elektronen nach der neuen relativistischen Quantendynamik von Dirac". In: *Zeitschrift fur Physik* 52.11-12, pp. 853–868. DOI: 10.1007/BF01366453.

Kotera, K. and M. Lemoine (2008). "Inhomogeneous extragalactic magnetic fields and the second knee in the cosmic ray spectrum". In: Phys. Rev. D 77.2, p. 023005. DOI: 10.1103/PhysRevD.77.023005. arXiv: 0706.1891 [astro-ph].

Kotera, K. et al. (2009). "Propagation of Ultrahigh Energy Nuclei in Clusters of Galaxies: Resulting Composition and Secondary Emissions". In: ApJ 707.1, pp. 370–386. DOI: 10.1088/0004-637X/707/1/370. arXiv: 0907.2433 [astro-ph.HE].

Kozlovsky, B., R. J. Murphy, and R. Ramaty (2002). "Nuclear Deexcitation Gamma-Ray Lines from Accelerated Particle Interactions". In: ApJS 141.2, pp. 523–541. DOI: 10.1086/340545.

Kronberg, P. P. (1994). "Extragalactic magnetic fields". In: *Reports on Progress in Physics* 57.4, pp. 325–382. DOI: 10.1088/0034-4885/57/4/001.

Krymskii, G. F. (1977). "A regular mechanism for the acceleration of charged particles on the front of a shock wave". In: *Soviet Physics Doklady* 22, p. 327.

Kubo, H. et al. (2004). "Status of the CANGAROO-III project". In: *New Astronomy Reviews* 48.5-6, pp. 323–329.

Kumar, P. and B. Zhang (2015). "The physics of gamma-ray bursts & relativistic jets". In: Phys. Rep. 561, pp. 1–109. DOI: 10.1016/j.physrep.2014.09.008. arXiv: 1410.0679 [astro-ph.HE].

Law, C. J. (2010). "A Multiwavelength View of a Mass Outflow from the Galactic Center". In: ApJ 708.1, pp. 474–484. DOI: 10.1088/0004-637X/708/1/474. arXiv: 0911.2061 [astro-ph.GA].

Lemoine, M. (2005). "Extragalactic magnetic fields and the second knee in the cosmic-ray spectrum". In: Phys. Rev. D 71.8, p. 083007. DOI: 10.1103/PhysRevD.71.083007. arXiv: astro-ph/0411173 [astro-ph].

Li, T. P. and Y. Q. Ma (1983). "Analysis methods for results in gamma-ray astronomy". In: ApJ 272, pp. 317–324. DOI: 10.1086/161295.

Longair, M. S. (2011). *High Energy Astrophysics*.

López-Coto, R. (2015). "Very-high-energy γ-ray observations of pulsar wind nebulae and cataclysmic variable stars with MAGIC and development of trigger systems for IACTs". PhD thesis. Universitat Autònoma de Barcelona.

Lorenz, E. and R. Wagner (2012). "Very-high energy gamma-ray astronomy. A 23-year success story in high-energy astroparticle physics". In: *European Physical Journal H* 37.3, pp. 459–513. DOI: 10.1140/epjh/e2012-30016-x. arXiv: 1207.6003 [physics.hist-ph].

Madsen, Kristin K. et al. (2015). "Broadband X-ray Imaging and Spectroscopy of the Crab Nebula and Pulsar with NuSTAR". In: ApJ 801.1, 66, p. 66. DOI: 10.1088/0004-637X/801/1/66. arXiv: 1502.07765 [astro-ph.HE].

MAGIC Collaboration et al. (2008). "Observation of Pulsed γ-Rays Above 25 GeV from the Crab Pulsar with MAGIC". In: *Science* 322.5905, p. 1221. DOI: 10.1126/science.1164718. arXiv: 0809.2998 [astro-ph].

MAGIC Collaboration et al. (2019). "Teraelectronvolt emission from the γ-ray burst GRB 190114C". In: Nature 575.7783, pp. 455–458. DOI: 10.1038/s41586-019-1750-x.

Maier, G. et al. (2019). "Performance of the Cherenkov Telescope Array". In: *arXiv e-prints*, arXiv:1907.08171. arXiv: 1907.08171 [astro-ph.IM].

Manchester, R. N. et al. (2005). "VizieR Online Data Catalog: ATNF Pulsar Catalog (Manchester+, 2005)". In: *VizieR Online Data Catalog*, VII/245, pp. VII/245.

Marinelli, S. (2016). "Neural-Net Energy Reconstruction". In: *HAWC Internal documentation*. URL: https://private.hawc-observatory.org/hawc.umd.edu/internal/db/2332_02.pdf.

Martin, B. and G. P. Shaw (2008). *Particle Physics, Third Edition*.

Martinez-Castellanos, I. (2016). "Background calculation for low statistics analysis bins". In: *HAWC Internal documentation*. URL: https://private.hawc-observatory.org/hawc.umd.edu/internal/db/2347_04.pdf.

Matsubara, T. et al. (2012). "Evaluation of 400 low background 10-in. photo-multiplier tubes for the Double Chooz experiment". In: *Nuclear Instruments and Methods in Physics Research A* 661.1, pp. 16–25. DOI: 10.1016/j.nima.2011.09.023. arXiv: 1104.0786 [physics.ins-det].

Matthews, J. (2005). "A Heitler model of extensive air showers". In: *Astroparticle Physics* 22.5-6, pp. 387–397. DOI: 10.1016/j.astropartphys.2004.09.003.

Mazin, D. (2019). "The Cherenkov Telescope Array". In: *arXiv e-prints*, arXiv:1907.08530. arXiv: 1907.08530 [astro-ph.IM].

McLaughlin, M., J. M. Cordes, and Z. Arzoumanian (2000). "Searching for FAST Pulsars". In: *IAU Colloq. 177: Pulsar Astronomy - 2000 and Beyond*. Ed. by M. Kramer, N. Wex, and R. Wielebinski. Vol. 202. Astronomical Society of the Pacific Conference Series, p. 41.

McLaughlin, M. A. et al. (2002). "PSR J1740+1000: A Young Pulsar Well Out of the Galactic Plane". In: ApJ 564.1, pp. 333–342. DOI: 10.1086/324151. arXiv: astro-ph/0106371 [astro-ph].

Meegan, C. et al. (2009). "The Fermi Gamma-ray Burst Monitor". In: ApJ 702.1, pp. 791–804. DOI: 10.1088/0004-637X/702/1/791. arXiv: 0908.0450 [astro-ph.IM].

Mertsch, P. and S. Sarkar (2011). "Fermi Gamma-Ray "Bubbles" from Stochastic Acceleration of Electrons". In: Phys. Rev. Lett. 107.9, 091101, p. 091101. DOI: 10.1103/PhysRevLett.107.091101. arXiv: 1104.3585 [astro-ph.HE].

Mirzoyan, R. et al. (1994). "The first telescope of the HEGRA air Cherenkov imaging telescope array". In: *Nuclear Instruments and Methods in Physics Research A* 351, pp. 513–526. DOI: 10.1016/0168-9002(94)91381-1.

Murase, K., S. Inoue, and S. Nagataki (2008). "Cosmic Rays above the Second Knee from Clusters of Galaxies and Associated High-Energy Neutrino Emission". In: ApJ 689.2, p. L105. DOI: 10.1086/595882. arXiv: 0805.0104 [astro-ph].

Naito, T. and F. Takahara (1994). "High energy gamma-ray emission from supernova remnants". In: *Journal of Physics G Nuclear Physics* 20.3, pp. 477–486. DOI: 10.1088/0954-3899/20/3/009.

Netzer, H. (2015). "Revisiting the Unified Model of Active Galactic Nuclei". In: ARA&A 53, pp. 365–408. DOI: 10.1146/annurev-astro-082214-122302. arXiv: 1505.00811 [astro-ph.GA].

Ohm, S. (2016). "Starburst galaxies as seen by gamma-ray telescopes". In: *Comptes Rendus Physique* 17.6, pp. 585–593. DOI: 10.1016/j.crhy.2016.04.003. arXiv: 1601.06386 [astro-ph.HE].

Owen, E. R. et al. (2019). "Starburst and post-starburst high-redshift protogalaxies. The feedback impact of high energy cosmic rays". In: A&A 626, A85, A85. DOI: 10.1051/0004-6361/201834350. arXiv: 1905.00338 [astro-ph.GA].

Parsons, R. D. and H. Schoorlemmer (2019). "Systematic differences due to high energy hadronic interaction models in air shower simulations in the 100 GeV-100 TeV range". In: *Phys. Rev. D* 100 (2), p. 023010. DOI: 10.1103/PhysRevD.100.023010. URL: https://link.aps.org/doi/10.1103/PhysRevD.100.023010.

Particle Data Group et al. (2012). "Review of Particle Physics". In: *Phys. Rev. D* 86 (1), p. 010001. DOI: 10.1103/PhysRevD.86.010001. URL: https://link.aps.org/doi/10.1103/PhysRevD.86.010001.

Particle Data Group et al. (2018). "Review of Particle Physics". In: *Phys. Rev. D* 98 (3), p. 030001. DOI: 10.1103/PhysRevD.98.030001. URL: https://link.aps.org/doi/10.1103/PhysRevD.98.030001.

Planck Collaboration et al. (2014). "Planck 2013 results. XI. All-sky model of thermal dust emission". In: A&A 571, A11, A11. DOI: 10.1051/0004-6361/201323195. arXiv: 1312.1300 [astro-ph.GA].

Ponti, G. et al. (2019). "An X-ray chimney extending hundreds of parsecs above and below the Galactic Centre". In: Nature 567.7748, pp. 347–350. DOI: 10.1038/s41586-019-1009-6. arXiv: 1904.05969 [astro-ph.HE].

Protheroe, R. J. (1999). "Acceleration and interaction of ultra high energy cosmic rays". In: *Topics in Cosmic-Ray Astrophysics*. Ed. by Michael A. Duvernois. Vol. 230, p. 247. arXiv: astro-ph/9812055 [astro-ph].

Remazeilles, M. et al. (2015). "An improved source-subtracted and destriped 408-MHz all-sky map". In: MNRAS 451.4, pp. 4311–4327. DOI: 10.1093/mnras/stv1274. arXiv: 1411.3628 [astro-ph.IM].

Rybicki, George B. and Alan P. Lightman (1986). *Radiative Processes in Astrophysics*.

Ryu, D. et al. (2003). "Cosmological Shock Waves and Their Role in the Large-Scale Structure of the Universe". In: ApJ 593.2, pp. 599–610. DOI: 10.1086/376723. arXiv: astro-ph/0305164 [astro-ph].

Salter, C. J. (1983). "Loop-I the North Polar Spur - a Major Feature of the Local Interstellar Environment". In: *Bulletin of the Astronomical Society of India* 11, p. 1.

Sarkar, K. C. (2019). "Possible connection between the asymmetry of the North Polar Spur and Loop I and Fermi bubbles". In: MNRAS 482.4, pp. 4813–4823. DOI: 10.1093/mnras/sty2944. arXiv: 1804.05634 [astro-ph.GA].

Saz Parkinson, P. M. et al. (2010). "Eight γ-ray Pulsars Discovered in Blind Frequency Searches of Fermi LAT Data". In: ApJ 725.1, pp. 571–584. DOI: 10.1088/0004-637X/725/1/571. arXiv: 1006.2134 [astro-ph.HE].

Schlickeiser, R. (2002). *Cosmic Ray Astrophysics*.

Schoenfelder, V. et al. (1993). "Instrument Description and Performance of the Imaging Gamma-Ray Telescope COMPTEL aboard the Compton Gamma-Ray Observatory". In: ApJS 86, p. 657. DOI: 10.1086/191794.

Scott, P. et al. (2010). "Direct constraints on minimal supersymmetry from Fermi-LAT observations of the dwarf galaxy Segue 1". In: J. Cosmology Astropart. Phys. 2010.1, 031, p. 031. DOI: 10.1088/1475-7516/2010/01/031. arXiv: 0909.3300 [astro-ph.CO].

SGSO Collaboration et al. (2019). "Science Case for a Wide Field-of-View Very-High-Energy Gamma-Ray Observatory in the Southern Hemisphere". In: *arXiv e-prints*, arXiv:1902.0842 arXiv:1902.08429. arXiv: 1902.08429 [astro-ph.HE].

Sherf, N., U. Keshet, and I. Gurwich (2017). "IceCube Constraints on the Fermi Bubbles". In: ApJ 847.2, 95, p. 95. DOI: 10.3847/1538-4357/aa894f. arXiv: 1705.06665 [astro-ph.HE].

Singer, C. (2013). *A short history of science to the nineteenth century*. Courier Corporation.

Snowden, S. L. et al. (1997). "ROSAT Survey Diffuse X-Ray Background Maps. II." In: ApJ 485.1, pp. 125–135. DOI: 10.1086/304399.

Stanev, T. (2010). "Cosmic Rays and Extensive Air Showers". In: *CERN document server*. URL: https://cds.cern.ch/record/1247048/files/p272.pdf.

Stothers, Richard and Jay A. Frogel (1974). "The local complex of O and B stars. I. Distribution of stars and interstellar dust". In: AJ 79, p. 456. DOI: 10.1086/111565.

Su, M., T. R. Slatyer, and D. P. Finkbeiner (2010). "Giant Gamma-ray Bubbles from Fermi-LAT: Active Galactic Nucleus Activity or Bipolar Galactic Wind?" In: ApJ 724.2, pp. 1044–1082. DOI: 10.1088/0004-637X/724/2/1044. arXiv: 1005.5480 [astro-ph.HE].

Swanenburg, B. N. et al. (1981). "Second COS B catalog of high-energy gamma-ray sources". In: ApJ 243, pp. L69–L73. DOI: 10.1086/183445.

SWGO Collaboration et al. (2019). "The Southern Wide-Field Gamma-Ray Observatory (SWGO): A Next-Generation Ground-Based Survey Instrument for VHE Gamma-Ray Astronomy". In: *arXiv e-prints*, arXiv:1907.07737. arXiv: 1907.07737 [astro-ph.IM].

Teegarden, B. J. and S. J. Sturner (1999). "INTEGRAL Observations of Gamma-Ray Bursts". In: *AAS/High Energy Astrophysics Division #4*. Vol. 31. Bulletin of the American Astronomical Society, p. 717.

The Milagro Collaboration (2004). "TeV Gamma-Ray Survey of the Northern Hemisphere Sky Using the Milagro Observatory". In: *arXiv e-prints*, astro–ph/0403097. arXiv: astro-ph/0403097 [astro-ph].

Thompson, D. J. (2019). "The Fourth Fermi LAT Source Catalog (4FGL)". In: *AAS/High Energy Astrophysics Division*. AAS/High Energy Astrophysics Division, p. 109.33.

Tluczykont, M. et al. (2014). "The HiSCORE concept for gamma-ray and cosmic-ray astrophysics beyond 10 TeV". In: *Astroparticle Physics* 56, pp. 42–53. DOI: 10.1016/j.astropartphys.2014.03.004. arXiv: 1403.5688 [astro-ph.IM].

VERITAS Collaboration et al. (2012). "VERITAS deep observations of the dwarf spheroidal galaxy Segue 1". In: Phys. Rev. D 85.6, 062001, p. 062001. DOI: 10.1103/PhysRevD.85.062001. arXiv: 1202.2144 [astro-ph.HE].

Vietri, M. (1995). "The Acceleration of Ultra–High-Energy Cosmic Rays in Gamma-Ray Bursts". In: ApJ 453, p. 883. DOI: 10.1086/176448. arXiv: astro-ph/9506081 [astro-ph].

Vitale, V. and A. Morselli (2009). "Indirect Search for Dark Matter from the center of the Milky Way with the Fermi-Large Area Telescope". In: *arXiv e-prints*, arXiv:0912.3828, arXiv:0912.3828. arXiv: 0912.3828 [astro-ph.HE].

Waxman, E. (1995). "Cosmological Gamma-Ray Bursts and the Highest Energy Cosmic Rays". In: Phys. Rev. Lett. 75 (3), pp. 386–389. DOI: `10.1103/PhysRevLett.75.386`. URL: `https://link.aps.org/doi/10.1103/PhysRevLett.75.386`.

Weekes, T. C. (1981). "a Fast Large Aperture Camera for Very High Energy Gamma-Ray Astronomy". In: *International Cosmic Ray Conference* 8, p. 34.

Weekes, T. C. et al. (1989). "Observation of TeV gamma rays from the Crab nebula using the atmospheric Cerenkov imaging technique". In: ApJ 342, pp. 379–395. DOI: `10.1086/167599`.

Weekes, T. C. et al. (2002). "VERITAS: the Very Energetic Radiation Imaging Telescope Array System". In: *Astroparticle Physics* 17, pp. 221–243. DOI: `10.1016/S0927-6505(01)00152-9`. eprint: `astro-ph/0108478`.

Williams, J. P., L. Blitz, and C. F. McKee (2000). "The Structure and Evolution of Molecular Clouds: from Clumps to Cores to the IMF". In: *Protostars and Planets IV*. Ed. by V. Mannings, A. P. Boss, and S. S. Russell, p. 97. arXiv: `astro-ph/9902246 [astro-ph]`.

Wood, J. R. (2016). "An all-sky search for bursts of verh high energy gamma-rays with HAWC". PhD thesis. University of Maryland.

Yang, H. Y. K. and M. Ruszkowski (2017). "The Spatially Uniform Spectrum of the Fermi Bubbles: The Leptonic Active Galactic Nucleus Jet Scenario". In: ApJ 850.1, 2, p. 2. DOI: `10.3847/1538-4357/aa9434`. arXiv: `1706.05025 [astro-ph.HE]`.

Yang, R., E. de Oña Wilhelmi, and F. Aharonian (2014). "Probing cosmic rays in nearby giant molecular clouds with the Fermi Large Area Telescope". In: A&A 566, A142. DOI: `10.1051/0004-6361/201321044`. arXiv: `1303.7323 [astro-ph.HE]`.

Yoast-Hull, T. M., III Gallagher J. S., and E. G. Zweibel (2014). "The Cosmic-Ray Population of the Galactic Central Molecular Zone". In: ApJ 790.2, p. 86. DOI: `10.1088/0004-637X/790/2/86`. arXiv: `1405.7059 [astro-ph.HE]`.

Zatsepin, G. T. and A. E. Chudakov (1961). "On the methods for searching local sources of high energy photons". In: *Zhur. Eksptl'. i Teoret. Fiz.* 41.

Zatsepin, G. T. and V. A. Kuz'min (1966). "Upper Limit of the Spectrum of Cosmic Rays". In: *Soviet Journal of Experimental and Theoretical Physics Letters* 4, p. 78.

Zhou, H. (2015). "Search for TeV gamma-ray sources in the Galactic Plane with the HAWC observatory". PhD thesis. Michigan Technological University.